Pathways towards single-polariton nonlinearity: from ground state exciton-polariton condensates in GaAs to Rydberg exciton-polaritons in Cu_2O

Konstantinos Orfanakis

A Thesis Submitted for the Degree of PhD
at the
University of St Andrews

2023

Identifiers to use to cite or link to this thesis:

DOI: https://doi.org/10.17630/sta/363
http://hdl.handle.net/10023/27247

Pathways towards single-polariton nonlinearity: from ground state exciton-polariton condensates in GaAs to Rydberg exciton-polaritons in Cu_2O

Konstantinos Orfanakis

University of
St Andrews

This thesis is submitted in partial fulfilment for the degree of
Doctor of Philosophy (PhD)
at the University of St Andrews

March 2023

Abstract

This work explores several routes towards achieving single-polariton nonlinearity. Exciton-polaritons are part-light part-matter quasiparticles arising from the strong coupling of excitons and cavity photons in micron-sized optical cavities. Owing to their excitonic component, polaritons can be described as “dressed photons” with nonlinear interactions several orders of magnitude larger than in typical optical materials. However, interactions between microcavity polaritons have remained weak, with the single-polariton nonlinearity being much smaller than the cavity linewidth. In this thesis, two approaches are studied as a way of circumventing this limitation and entering the nonlinear regime. The first approach involves narrowing the emission linewidth of a polariton condensate through optical confinement so that the linewidth approaches the interaction constant. The second approach involves exploiting the giant nonlinearities of Rydberg excitons in cuprous oxide, first in nanoparticles to study the effect of quantum confinement and then inside a microcavity to create highly nonlinear Rydberg exciton-polaritons.

The main result presented in this thesis are: (1) An optically trapped polariton condensate in a state-of-the-art GaAs-based microcavity approaches but still remains away from the regime of single-polariton nonlinearity. The condensate is characterised by an ultra-narrow linewidth as evidenced by the temporal decay of its coherence. The latter also exhibits an oscillatory behaviour originating from a beating between two condensate modes. (2) Rydberg excitons states are resolved up to principal quantum number $n = 6$ in the absorption spectrum of clusters of cuprous oxide nanoparticles. Rydberg excitons are also resolved for single nanoparticles; however, the spectrum is dominated by effects inherent to the nanoparticle system, thus hindering the study of the nonlinearity of Rydberg excitons in this quantum-confined structure. (3) Strong coupling between cavity photons and Rydberg excitons can be achieved by embedding a thin cuprous oxide crystal as the active layer of an optical microcavity. Even though the microcavity is below the nonlinear regime for all strongly coupled Rydberg states, non-classical light can be observed by reducing the mode volume and suppressing the phonon-background of cuprous oxide in future microcavities.

This thesis is a major step towards realising single-polariton nonlinearity for future quantum applications. The results presented in this work highlight the limitations of traditional GaAs-based semiconductor microcavities while establishing Rydberg polaritons with their huge nonlinearities as a promising route for achieving a scalable, strongly correlated photonic platform.

Candidate's declaration

I, Konstantinos Orfanakis, do hereby certify that this thesis, submitted for the degree of PhD, which is approximately 45,000 words in length, has been written by me, and that it is the record of work carried out by me, or principally by myself in collaboration with others as acknowledged, and that it has not been submitted in any previous application for any degree. I confirm that any appendices included in my thesis contain only material permitted by the "Assessment of Postgraduate Research Students" policy.

I was admitted as a research student at the University of St Andrews in August 2018.

I received funding from an organisation or institution and have acknowledged the funder(s) in the full text of my thesis.

Date: 10 - 03 - 2023 Signature of candidate

Supervisor's declaration

I hereby certify that the candidate has fulfilled the conditions of the Resolution and Regulations appropriate for the degree of PhD in the University of St Andrews and that the candidate is qualified to submit this thesis in application for that degree. I confirm that any appendices included in the thesis contain only material permitted by the "Assessment of Postgraduate Research Students" policy.

Date: 10 - 03 - 2023 Signature of supervisor

Permission for publication

In submitting this thesis to the University of St Andrews we understand that we are giving permission for it to be made available for use in accordance with the regulations of the University Library for the time being in force, subject to any copyright vested in the work not being affected thereby. We also understand, unless exempt by an award of an embargo as requested below, that the title and the abstract will be published, and that a copy of the work may be made and supplied to any bona fide library or research worker, that this thesis will be electronically accessible for personal or research use and that the library has the right to migrate this thesis into new electronic forms as required to ensure continued access to the thesis.

I, Konstantinos Orfanakis, have obtained, or am in the process of obtaining, third-party copyright permissions that are required or have requested the appropriate embargo below.

The following is an agreed request by candidate and supervisor regarding the publication of this thesis:

Printed copy

No embargo on print copy.

Electronic copy

No embargo on electronic copy.

Date: 10 - 03 - 2023 Signature of candidate

Date: 10 - 03 - 2023 Signature of supervisor

Underpinning Research Data or Digital Outputs

Candidate's declaration

I, Konstantinos Orfanakis, understand that by declaring that I have original research data or digital outputs, I should make every effort in meeting the University's and research funders' requirements on the deposit and sharing of research data or research digital outputs.

Date: 10 - 03 - 2023 Signature of candidate

Permission for publication of underpinning research data or digital outputs

We understand that for any original research data or digital outputs which are deposited, we are giving permission for them to be made available for use in accordance with the requirements of the University and research funders, for the time being in force.

We also understand that the title and the description will be published, and that the underpinning research data or digital outputs will be electronically accessible for use in accordance with the license specified at the point of deposit, unless exempt by award of an embargo as requested below.

The following is an agreed request by candidate and supervisor regarding the publication of underpinning research data or digital outputs:

No embargo on underpinning research data or digital outputs.

Date: 10 - 03 - 2023 Signature of candidate

Date: 10 - 03 - 2023 Signature of supervisor

Acknowledgements

A PhD is not an individual effort, and there are many people I need to thank. First, I would like to express my sincere and heartily gratitude to my supervisor Hamid Ohadi for his continuous support, patience, enthusiasm, and encouragement. I warmly thank him for giving me the opportunity to be involved in setting up a new laboratory and for guiding me throughout my degree. His immense knowledge helped me hone my skills in many areas of research and expand my horizons in multiple directions.

It is my pleasure to acknowledge and thank our collaborators, Pavlos Savvidis, David Petrosyan, Andreas Tzortzakakis, Sylwia Zielińska-Raczyńska, Gerard Czajkowski, Karol Karpiński, David Ziemkiewicz, Valentin Walther, Thomas Volz, and Thomas Pohl for fruitful discussions on my results and for providing valuable theoretical support for this work.

I am grateful to the past and present members of the group, namely Sai Rajendran and Anindya Paul, for the useful discussions and the nice collaboration we shared during this work. My gratitude also goes to all members of our department's cryogenic, mechanical, and electrical workshops for the technical support provided throughout my degree. A special thanks go to Debra Thompson, Julie Massey, and Chris Hooley for building an amazing community of CDT students, organising enjoyable events, and always being there for moral support.

I would like to heartily thank my friends Thanasis, Will, Carolina, Kristín, Januka, Teresa, and Josh for the continuous support and for all the amazing moments we have spent together.

I am forever grateful to my parents, Olga and Nikos, and my brother Yiannis for their continuous support and love. Most importantly, I deeply thank my partner Gemma who has encouraged and supported me throughout this process. I would not have managed it without you!

Funding

This work was supported by EPSRC grant number EP/L015110/1.

Research Data/Digital Outputs Access Statement

Research data underpinning this thesis are available at:

- https://doi.org/10.17630/cb6784fd-521e-46c6-a4fa-c8936cab4f4b
- https://doi.org/10.17630/633aa0f8-bf54-43e4-ad11-417ef94549d9
- https://doi.org/10.17630/4f4e4d92-8309-45db-bade-26b147696138
- https://doi.org/10.17630/6ee1310d-0559-4ad1-b32d-d0b9906dac29

This page is intentionally left blank.

Contents

Abbreviations

a.u.	arbitrary units
AOM	acousto-optic modulator
bcc	body-centered cubic
BEC	Bose-Einstein condensation
BF	bright-field
BS	beam splitter
CB	conduction band
CCD	charge-coupled device
CMOS	complementary metal-oxide-semiconductor
DBR	distributed Bragg reflectors
DF	dark-field
DOS	density of states
ECDL	external cavity diode laser
EIT	electromagnetically induced transparency
fcc	face-centered cubic
FSR	free spectral range
FWHM	full width half maximum
GPE	Gross-Pitaevskii equation
LCOS	liquid crystal on silicon
LED	light emitting diode
Li	i^{th} lens
LP	lower polariton
MBE	molecular beam epitaxy
Mi	i^{th} mirror

MRAF	mixed-region amplitude freedom
NA	numerical aperture
NNP	natural nanoparticle
NP	nanoparticle
PL	photoluminescence
QCSE	quantum confined Stark effect
QD	quantum dot
QW	quantum well
RDMA	real density matrix approach
RF	radio frequency
RPM	revolutions per minute
RR	retroreflector
SAW	surface-acoustic wave
sCMOS	scientific CMOS
SEM	scanning electron microscopy
SHG	second harmonic generation
SLM	spatial light modulator
SNP	synthetic nanoparticle
TA	tapered amplifier
TMM	transfer matrix method
UP	upper polariton
UV	ultraviolet
VB	valence band
VCSEL	vertical-cavity surface-emitting laser
XRD	x-ray diffraction

List of Publications

- **Konstantinos Orfanakis**, Andreas F. Tzortzakakis, David Petrosyan, Pavlos G. Savvidis, and Hamid Ohadi. **Ultralong temporal coherence in optically trapped exciton-polariton condensates**. *Physical Review B*, 103(23):235313, June 2021. doi: 10.1103/PhysRevB.103.235313. URL
- **Konstantinos Orfanakis**, Sai Kiran Rajendran, Hamid Ohadi, Sylwia Zielińska-Raczyńska, Gerard Czajkowski, Karol Karpiński, and David Ziemkiewicz. **Quantum confined Rydberg excitons in Cu_2O nanoparticles**. *Physical Review B*, 103(24):245426, June 2021. doi: 10.1103/PhysRevB.103.245426.
- **Konstantinos Orfanakis**, Sai Kiran Rajendran, Valentin Walther, Thomas Volz, Thomas Pohl, and Hamid Ohadi. **Rydberg exciton-polaritons in a Cu_2O microcavity**. *Nature Materials*, 21(7):767-772, July 2022. doi: 10.1038/s41563-022-01230-4.

This page is intentionally left blank.

Chapter 1

Introduction

1.1 Motivation

A long-standing goal in quantum photonics has been the realisation of strong interactions (nonlinearities) between individual photons. In the ultimate limit of single-photon nonlinearity, the system enters a regime where individual photons interact so strongly with one another that the propagation of light pulses consisting of one, two, or more photons varies significantly with photon number. The regime of single-photon nonlinearity would thus permit controlling the response of a quantum system to an external drive, for example, through the presence of a single photon in a quantum optical device [1–5]. This capability would propel the field of integrated quantum photonics, which suffers from weak photon interactions as typical optical nonlinearities are too small to go beyond linear optical interaction, even in the best nonlinear crystals. Achieving and utilising strong single-photon nonlinearities could enhance the performance of classical nonlinear devices, enabling, for instance, ultrafast energy-efficient all-optical transistors [3]. Additionally, nonlinear optical switches activated by single photons could enable optical quantum information processing [6] and communication [7], while a scalable network of strongly correlated photons, where interactions between neighbours can be individually tuned, is essential for quantum simulations [8].

However, even though light fields can interact inside nonlinear optical media, the nonlinearity in conventional materials is insignificant at the light powers associated with individual photons. Despite this limitation, the potential payoff of realising nonlinear single-photon devices is significant. Therefore, considerable effort has been dedicated to achieving single-photon nonlinearity across a wide range of materials with platforms ranging from single atoms in optical resonators [9–12] to ultracold atomic ensembles [13–15]. Interestingly, instead of using real atoms, it is also possible to use artificial atoms in a solid-state system, such as quantum dots in semiconductors [4, 16–18] or nitrogen-vacancy centres in diamond [19–21]. One of the main advantages of using a solid-state platform is the possibility of integrating single-photon nonlinearities in nanophotonic circuits in a single chip for quantum technologies. However, current implementations, e.g., quantum dot systems, while being very successful at the single-particle level, have been unsuccessful at reconfigurability, which is only achievable through fabricating a new system.

An interesting system for realising correlated and highly-interacting photons is exciton-polariton, or simply polariton, in an optical microcavity. Polaritons - hybrid light-matter quasi-particles emerging from the strong coupling of excitons and cavity photons in micron-sized semiconductor structures - can interact nonlinearly due to their excitonic component and can travel fast due to their photonic component. They can be used to create reconfigurable systems by means such as optical excitation, and networks can be made by etching [22] or optical patterning of a microcavity chip [23–25]. An additional feature is the ability to create and manipulate polariton condensates, quantum objects characterised by a macroscopic occupation of a single quantum state with extended temporal and spatial coherence [26]. The nonlinear character of polariton condensates leads to a wealth of fascinating phenomena, including superfluidity [27] and the formation of quantised vortices [28] and dark solitons [29].

So far, interactions between microcavity polaritons have been weak, i.e. the single-polariton nonlinearity has been much smaller than the cavity linewidth. There are two approaches to overcoming this challenge and achieving single-polariton nonlinearity: manufacturing higher quality microcavities or enhancing the polariton-polariton interactions. The first approach, i.e., improving the quality of the microcavity structure, results in a reduction of losses from the cavity, manifested as an increase in the photon and polariton lifetimes and a simultaneous cavity linewidth narrowing. If the improvement is good enough, an ultranarrow cavity linewidth will approach the nonlinearity constant, and the system will enter the nonlinear regime. Fabricating higher quality microcavities can reduce cavity losses but improving the current well-established semiconductor growth technology is a major technological hurdle. In the current state-of-the-art semiconductor microcavities, such as those based on Gallium-Arsenide (GaAs), the polariton-polariton nonlinearity is several orders of magnitude smaller than the polariton decay rate.

The second approach towards achieving single-polariton nonlinearity involves improving the nonlinear interaction of polaritons by enhancing the interaction of the underlying excitons. One candidate system capable of providing enhanced exciton-exciton interactions is cuprous oxide (Cu_2O). Cuprous oxide is an abundant direct-bandgap semiconductor in which excitons were first discovered [30, 31]. In 2014, a seminal work by Kazimierczuk et al. [32] demonstrated that Cu_2O can host giant Rydberg excitons because of its large Rydberg energy ($R_x \approx 100$ meV, which is ∼25 times larger than GaAs). Rydberg excitons are highly excited states with a principal quantum number $n > 1$, similar to Rydberg atoms. These excited states have giant wavefunction extensions as the average distance between the electron and the hole constituents can extend to thousands of lattice sites, as large as a micron. Such extensions are 100 times larger than that of the ground state exciton in GaAs, almost five times larger than the optical wavelength of the exciting photon, and comparable to the size of the current micropillar microcavities ($\sim$2 μm). Moreover, Rydberg excitons have narrower linewidth compared to GaAs.

The unique properties of Rydberg excitons lead to the emergence of nonlinear phenomena. Owing to their giant dimensions, Rydberg excitons repel each other strongly due to the repulsion of their electron clouds and become highly nonlinear at much smaller densities than other traditional semiconductors. In a process called the "Rydberg blockade" effect, the strong dipole-dipole interaction between such excitons could become so large that the presence of one exciton prevents the excitation of another in its vicinity due to the strong "blueshift" of the exciton transition [32]. This "antibunching" behaviour is commonly used in single-photon sources [33]. Theoretical calculations demonstrate that the polariton-polariton interaction strength g in Cu_2O for medium Rydberg states ($6 \leqslant n \leqslant 15$) is three to five orders of magnitude stronger than in the state-of-the-art quantum wells such as GaAs ($g(\text{GaAs}) \approx 6$ μeV/μm^2 for the ground state) [34].

The aim of this work is to explore these two approaches towards achieving single-polariton nonlinearity. The first approach is implemented by realising an ultranarrow polariton condensate in a state-of-the-art GaAs-based microcavity. The condensate will be decoupled from the decoherence-inducing exciton reservoir by optical trapping, i.e., by spatial patterning the excitation laser so that the condensate is confined within an optical potential. This practice aims to reduce the condensate linewidth to values approaching the interaction constant. The second approach involves exploiting the giant nonlinearities of Cu_2O Rydberg excitons in two systems. First, quantum confined Rydberg excitons will be studied in nanoparticles of Cu_2O. The nanoparticle system enables the study of the effect of quantum confinement on these giant excitons and constitutes a scalable system through nanofabrication techniques like focused ion beam and etching. Second, hybridising Rydberg excitons with photons to form highly nonlinear polaritons in Cu_2O will be studied as an additional route towards achieving strong interactions. Since the nonlinearity of Rydberg excitons in Cu_2O is more than three orders of magnitude stronger than that of the GaAs exciton, the weakly correlated polariton system is expected to enter the strong correlation regime for the first time in a semiconductor system. The nonlinearity associated with Rydberg exciton-polaritons is strong enough to achieve the holy grail of polaritonics, i.e., single polariton nonlinearity, a long-standing goal with both fundamental and technological significance [35].

1.2 Thesis Structure

This thesis is organised as follows: First, Chapter 2 introduces the basic concepts of polariton physics and Rydberg excitons, starting with an in-depth discussion on excitons (Section 2.1) and cavity photons (Section 2.2). The coupling between the latter leads to the notions of exciton-polaritons (Section 2.3) and polariton condensates (Section 2.4). This chapter finished by presenting an introduction to the newly-emerged field of Rydberg excitons (Section 2.5). In Chapter 3, the experimental methods used in this work are presented. This includes details on the sample preparation (Section 3.1) along with details on the optical spectroscopy and interferometry setups (Section 3.2). Chapters 4, 5 and 6 present the results obtained in the course of this work. The temporal coherence of an optically trapped condensate is studied in Chapter 4 as a way of probing the condensate linewidth. Chapter 5 details the observation of quantum confined Rydberg exciton in nanoparticles of Cu_2O. Chapter 6 demonstrates the ability to realise Rydberg exciton-polaritons by embedding a thin Cu_2O crystal inside an optical microcavity. Finally, Chapter 7 summarises the obtained results and provides an outlook for future projects.

Chapter 2

Concepts

In this chapter, the concepts most important to this work are presented in more detail. First, the idea of the exciton is introduced in Section 2.1, followed by a discussion of semiconductor-based microcavities in Section 2.2. Then, the strong coupling between quantum well excitons and cavity photons is addressed in Section 2.3, followed by a discussion of polariton condensation in Section 2.4. Finally, Section 2.5 reviews the most relevant concepts related to Rydberg excitons in cuprous oxide.

2.1 Excitons

Simply put, a polariton is a mixed light-matter excitation arising in semiconductors. There are many candidate excitations that can form the matter component of polaritons, but the most commonly used one is the exciton. Excitons in semiconductors are correlated electron-hole pairs that travel across the crystal, bound by the Coulomb interaction, similar to a positronium atom. They are the elementary electronic excitations in semiconductors and appear as sharp peaks in the photoluminescence (PL) spectrum. A model system for the study of excitons is the semiconductor quantum well, which is a thin layer of semiconductor material confining excitons to length scales of the order of their de Broglie wavelength in one dimension (the growth direction), thus inducing quantisation effects.

In Section 2.1.1, a basic hydrogenic picture of excitons will be presented; a more thorough description can be found in Chapter 4 of Ref. [36] and Chapter 6 of Ref. [37]. Then, Section 2.1.2 discusses the effect of exciton confinement in semiconductor quantum wells.

2.1.1 Excitons in Bulk Semiconductors

The quantum mechanical description of electrons in solid-state crystals requires the solution of the Schrödinger equation in the case of the spatially periodic crystal lattice. The most important consequence of this theoretical approach is that the energy spectrum consists of allowed and forbidden energy bands[1] and that an electron state can be characterised by its quasi-momentum $\mathbf{p}$ (or quasi-wavevector $\mathbf{k} = \mathbf{p}/\hbar$). The energy in an allowed band is a periodic function of $\mathbf{k}$, so it may be considered only in a certain region of $\mathbf{k}$-space known as the first Brillouin zone.

In the ground state of a semiconductor, a certain number of the lowest allowed bands are completely filled with electrons (populated according to the Pauli principle), while higher bands are empty. In most cases, only the upper filled band and the first empty band are of interest. These bands are known as the valence band (VB) and the conduction band (CB), respectively. The conduction and valence bands are separated by a forbidden energy gap E_g. This energy gap is also known as the bandgap of the semiconductor. In most semiconductors, the value of E_g is of the order of 1-3 eV. For GaAs $E_g \approx 1.52$ eV [38] and for Cu_2O $E_g \approx 2.172$ eV [32, 39] at cryogenic temperatures.

Exciting an electron in the valence band to the conduction band requires energy equal to or higher than the energy gap. As the electron is excited, an unoccupied state in the valence band is left behind. This state is modelled as a new quasiparticle termed *electron hole* (or simply *hole*) and has similar properties to the electron, namely inverse charge, same momentum magnitude but opposite sign, and a different effective mass. External perturbation, such as optical excitation, can therefore create these free electron-hole pairs that represent the primary electronic excitation in a semiconductor and are commonly utilised in photovoltaic solar cells or CMOS and CCD cameras.

However, under certain conditions, the subsequent Coulomb attraction between the negatively charged electron and the positively charged hole results in a bound electron-hole state - a bosonic quasiparticle with a neutral charge consisting of two fermions of opposite charge. This quasiparticle, named *exciton*, can be regarded as the solid-state analogue of the hydrogen atom, where the role of the proton is played here by the hole. Therefore, excited exciton states, labelled by an integer quantum number n, appear as discrete energy levels below the bandgap and can be optically excited directly from the valence band. The ground state exciton ($n = 1$) represents the lowest electronic excitation in a semiconductor. Excitons are usually excited optically and can either decay non-radiatively or emit a photon spontaneously by radiative recombination of their electron and hole on the time scale of their lifetime. Typical exciton lifetimes are of the

---

[1] Instead of discrete energy levels associated with individual atoms.

order of 1 ns [40].

Excitons have been studied in two limiting cases, depending on the properties of the material in question [36, 37]. In materials with a small dielectric constant, the screening of the electron-hole interaction is limited, and the pair is strongly bound to each other within the same or nearest-neighbour unit cells [See Fig. 2.1(a)]. The binding energies of such excitons, termed *Frenkel* or *tightly bound excitons*, are in the order of 0.1 to 1 eV and are typically found in organic semiconductor [41].

On the other hand, when the dielectric constant is larger, the Coulomb interaction is strongly screened by the valence electrons. The result is a weekly bound electron-hole pair, known as *Wannier-Mott exciton* [42, 43], with a radius exceeding the dimensions of the crystal unit cell [See Fig. 2.1(b)]. Wannier-Mott exciton can move freely through the crystal; hence the alternative name of "free" excitons. The binding energy of Wannier-Mott excitons is typically in the order of tens of meV. Wannier-Mott excitons are commonly encountered in inorganic semiconductors, such as GaAs and Cu_2O.

In this thesis, we will limit ourselves to Wannier-Mott excitons since they are the exciton type typically encountered in most semiconductors, including GaAs and Cu_2O. On the other hand, Frenkel excitons can be found in insulators and organic crystals. A detailed theoretical treatment of Frenkel excitons can be found in Ref. [44].

The properties of Wannier excitons can be calculated with the effective mass approximation based on Refs. [45–47]. We consider a semiconductor with a non-degenerate valence and conduction band dispersions assumed to be approximately parabolic and separated by the bandgap

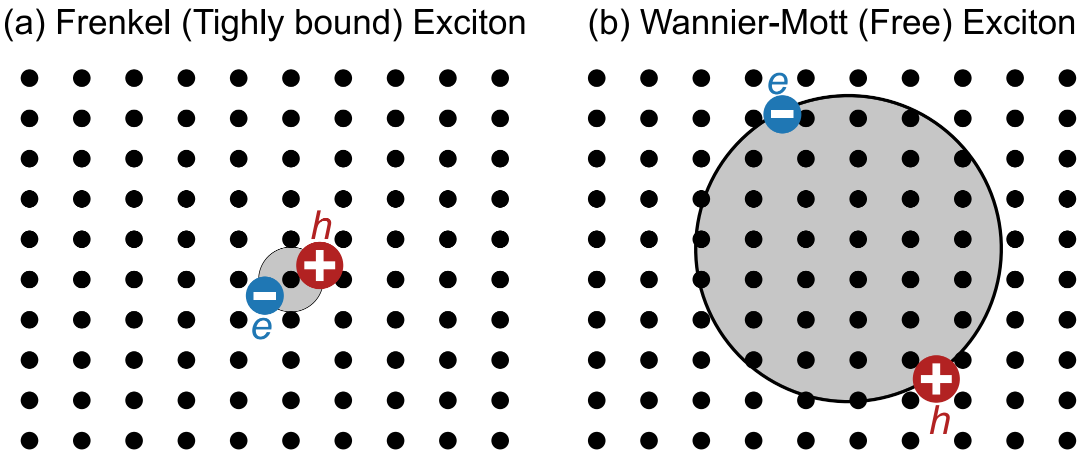

Figure 2.1: Schematic diagram of (a) a Frenkel exciton, also called a tightly bound exciton, and (b) a Wannier-Mott exciton, also called a free exciton, in the host's crystal lattice (black dots). The negatively charged electron e and the positively charged hole h are marked by the blue and red dots, respectively.

energy E_g close to the centre of the Brillouin zone (band extrema being located at $\mathbf{k} = 0$). Within the effective mass approximation, the periodic crystal potential is neglected, and electrons and holes are considered free particles with effective masses m_e^* and m_h^*, given by the curvature of the relevant energy bands. The electron-hole interaction is screened with respect to the vacuum case due to the relative permittivity ϵ_r of the dielectric material. Assuming spherical symmetry, the Hamiltonian describing an exciton H_x is given by the sum of the electron and hole energies plus the potential energy of their interaction:

$$H_x = E_g - \frac{\hbar^2}{2m_e^*}\nabla_e^2 - \frac{\hbar^2}{2m_h^*}\nabla_h^2 - \frac{e^2}{4\pi\epsilon_0\epsilon_r|\mathbf{r}_e - \mathbf{r}_h|}\,, \tag{2.1}$$

where ∇_e^2 and ∇_h^2 refer to the spatial derivative with respect to the electron and hole coordinates $\mathbf{r}_e$ and $\mathbf{r}_h$, respectively, e is the elementary charge, and ϵ_0 the vacuum permittivity. As in any two-particle system, the exciton motion can be decomposed into a centre-of-mass motion and a relative motion of the two particles about the centre-of-mass [37]. Therefore, H_x can be expressed in terms of the relative electron-hole position $\mathbf{r}$, centre-of-mass $\mathbf{R}$, reduced mass μ^*, and total effective mass m_x^*, where:

$$\mathbf{r} = \mathbf{r}_e - \mathbf{r}_h\,, \qquad \mathbf{R} = \frac{m_e^*\mathbf{r}_e + m_h^*\mathbf{r}_h}{m_e^* + m_h^*}\,, \tag{2.2}$$

$$\mu^* = \frac{m_e^* m_h^*}{m_e^* + m_h^*}\,, \qquad m_x^* = m_e^* + m_h^*\,. \tag{2.3}$$

After this coordinate transformation, the exciton Hamiltonian of Eq. 2.1 may be written as:

$$H_x = E_g + \frac{\hbar^2}{2m_x^*}\nabla_{\mathbf{R}}^2 + \frac{\hbar^2}{2\mu^*}\nabla_{\mathbf{r}}^2 - \frac{e^2}{4\pi\epsilon_0\epsilon_r|\mathbf{r}|}\,. \tag{2.4}$$

The exciton Hamiltonian H_x can then be expressed as the sum of the Hamiltonians corresponding to the centre-of-mass and relative motion of electron and hole, $H_x = H_{\text{cen}} + H_{\text{rel}}$, with:

$$H_{\text{cen}} = E_g + \frac{\hbar^2}{2m_x^*}\nabla_{\mathbf{R}}^2\,, \qquad H_{\text{rel}} = \frac{\hbar^2}{2\mu^*}\nabla_{\mathbf{r}}^2 - \frac{e^2}{4\pi\epsilon_0\epsilon_r|\mathbf{r}|}\,. \tag{2.5}$$

These two terms commute with each other (as one depends only on $\mathbf{R}$, and the other on $\mathbf{r}$). Thus, the eigenstates of H_x take the form:

$$\Psi_{\mathbf{k},n}(\mathbf{R},\mathbf{r}) = \frac{1}{\sqrt{V}}e^{i\mathbf{k}\mathbf{R}}\phi_n(\mathbf{r})\,. \tag{2.6}$$

The form is the product of a plane wave with wavevector $\mathbf{k} = \mathbf{k}_e + \mathbf{k}_h$, eigenstate of H_{cen}, and an envelope function $\phi_n(\mathbf{r})$, eigenstate of H_{rel}. V refers to the volume of the system and acts as a normalisation factor. The eigenvalues of H_{cen} are given by:

$$E_{\text{cen}} = E_g + \frac{\hbar^2 k^2}{2m_x^*} \,. \tag{2.7}$$

As this corresponds to a free particle equation, it describes the overall centre-of-mass propagation of the exciton through the crystal lattice with quasi-momentum $\hbar k$ and kinetic energy $E_{kin} = \hbar^2 k^2 / 2(m_e^* + m_h^*)$.

The relative motion of the electron and the hole in the exciton is similar to that of the electron and the proton inside the hydrogen atom. The solutions of H_{rel} (Eq. 2.5) are well-known as they correspond to the state of the hydrogen atom with the addition of the screening of the electron-hole interaction due to the semiconductor. Therefore, the eigenvalues are given by:

$$E_{\text{rel},n} = -\frac{\mu^* e^4}{2\hbar^2 (4\pi\epsilon_0\epsilon_r)^2} \frac{1}{n^2} \,, \tag{2.8}$$

where n is the principal quantum number of the hydrogen-like orbitals of the exciton wavefunction. Eq. 2.8 represents the *exciton binding energy* E_b, which scales with the principal quantum number as n^{-2}, similar to the case of hydrogen. Due to the exciton binding energy, excitons are the lowest energy electronic excitations of a semiconductors, appearing as sharp lines below the bandgap in the photoluminescence spectrum. The binding energy can be rewritten as:

$$E_{\text{rel},n} \equiv E_{b,n} = -\frac{\mu^*}{m_e \epsilon_r^2} R_H \frac{1}{n^2} = -\frac{R_x^*}{n^2} \,, \tag{2.9}$$

where m_e is the free electron mass, $R_H \approx 13.6$ eV is the Rydberg constant for hydrogen, and R_x^* is the excitonic Rydberg constant. The latter corresponds to the binding energy of the ground state ($n = 1$):

$$R_x^* \equiv |E_{b,n=1}| = \frac{\mu^*}{m_e \epsilon_r^2} R_H \,. \tag{2.10}$$

The main contributions to the excitonic Rydberg constant come from the dielectric screening of the Coulomb potential and lower reduced mass of the exciton. Considering typical values $\epsilon_r \approx 10$ and $\mu^*/m_e \approx 0.1$ for semiconductors, a typical value of the Rydberg constant R_x^* thus amounts to $E_b \approx (0.1/10^2) \cdot 13.6$ eV ≈ 13 meV, i.e. of the order of tens of meV [48]. For GaAs, $R_x^* \approx 4.1$ meV, while for Cu_2O $R_x^* \approx 100$ meV. Stable exciton formation is achieved only if the attractive potential is sufficient to prevent the exciton from breaking up after collisions with phonons. Since the maximum energy of a thermally excited phonon at temperature T is $\sim k_B T$, where k_B is Boltzmann's constant, the binding energy must thus be higher than $\sim k_B T$.

Consequently, Wannier-Mott excitons are usually studied at cryogenic temperatures owing to their small binding energy [36]. In addition to low temperatures, also sufficient crystal purity is essential for the existence of free excitons. Impurity atoms and defects can trap free excitons propagating through the crystal, which then get localised at the impurity sites losing their kinetic energy, and *bound excitons* are formed [48]. Charged impurities can also induce statistically distributed Stark shifts and ionisation broadening for high-n excitonic states in cuprous oxide [49].

In summary, the total exciton energy, including its centre-of-mass kinetic energy, is:

$$E_x(n,k) = E_g + E_{kin} + E_b = E_g + \frac{\hbar^2 k^2}{2m_x^*} - \frac{R_x^*}{n^2}\,. \tag{2.11}$$

The above equation describes a quasiparticle that moves freely within the crystal (first two terms), while the relative motion of the electron and hole is similar to that of the electron and proton in the case of the hydrogen atom (last term). The first four exciton states are schematically illustrated in Fig 2.2.

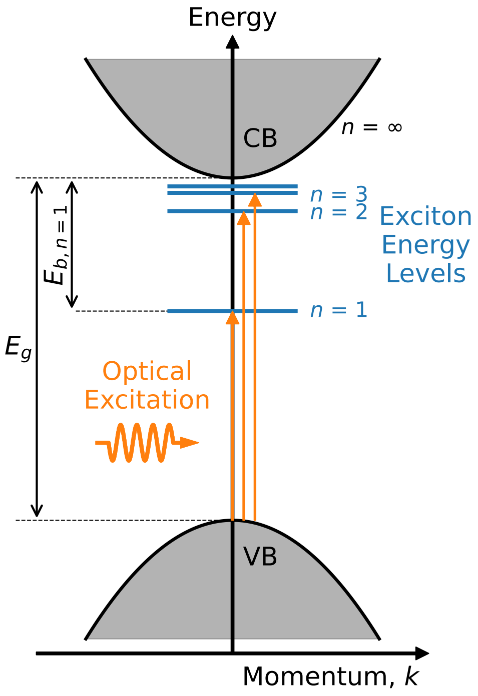

Figure 2.2: Schematic exciton levels (blue lines) for the $n = 1, ..., 4$ states in a semiconductor with a direct bandgap of width E_g. The binding energy of the ground state exciton $E_{b,n=1}$ is highlighted. Optical absorption transitions for the first three exciton states are marked by orange arrows. In the effective mass approximation, excitons have a parabolic dispersion given by their kinetic energy $\hbar^2 k^2/2(m_e^* + m_h^*)$.

Similar to the case of the hydrogen atom, an effective Bohr radius can be defined by quantifying exciton extension, i.e. the mean separation of electron and hole:

$$\alpha_x = \frac{\hbar^2 4\pi\epsilon_0\epsilon_r}{\mu^* e^2} n^2 = \frac{\epsilon_r}{(\mu^*/m_e)} \alpha_B n^2 \,, \tag{2.12}$$

where α_B is the ground state Bohr radius of the hydrogen atom. Assuming typical values for conventional semiconductors, the ground state radius for Wannier-Mott excitons is of the order of $r_{n=1} \approx 100\ \alpha_B \approx 50$ Å [48].

In Eq. 2.6, the envelope function $\phi_n(\mathbf{r})$ is the eigenstate of H_{rel}, which is a hydrogen-like Hamiltonian. Consequently, the relative motion of the electron and hole is described using the same envelope functions as the hydrogen atom, $\phi_n(\mathbf{r}) = \phi_{nlm}(\mathbf{r})$. These envelope functions contain the spherical harmonics, and so the relative motion of electron and hole is classified by angular momentum quantum numbers l and m, with $l = 0, 1, 2, ..., n-1$ and can be described by S-, P-, D-...like states. In reality, however, the non-spherical symmetry of the crystal lattice means that angular momentum is not a good quantum number, and the relative motion has to be described in terms of the irreducible symmetry representations of the lattice. Nonetheless, the excitonic states are usually labelled by their corresponding spherical counterpart.

The negatively charged electron and the positively charged hole in an exciton form an electric dipole, which can interact with electromagnetic radiation. The interaction between an exciton dipole $\mathbf{D}$ and an electric field $\mathbf{E}$ may lead to a transition between the exciton ground state (electron in the valence band, $|g\rangle$) and the first excited state (electron in the valence band, $|e\rangle$). The probability of this transition can be obtained by applying Fermi's golden rule and is conventionally described by a dimensionless quantity called the oscillator strength f_{osc}. For an exciton gas in a quantum well, the oscillator strength is defined as [40]:

$$f_{\text{osc}} \propto |\langle e|\mathbf{D}\cdot\mathbf{E}|g\rangle|^2 \frac{V}{\pi\alpha_B^3} \,. \tag{2.13}$$

Here V is the quantisation volume. $V/\pi\alpha_B^3$ reflects the enhancement of the interaction due to enhanced electron-hole overlap in an exciton compared to a pair of unbound electron and hole. Equation 2.13 defines the oscillator strength as an extensive property of a QW; the intensive equivalent is the oscillator strength per unit area. For S states, the oscillator strength of allowed transitions drops as the third power of the principal quantum number [48]:

$$f_{\text{osc},S} \propto n^{-3} \,. \tag{2.14}$$

For P states, the oscillator strength is modified [32]:

$$f_{\mathrm{osc},P} \propto \frac{n^2-1}{n^5}\,. \tag{2.15}$$

As a result, exciton lines related to higher states $n = 2, 3, 4, \ldots$ rapidly fade away, as can be clearly observed in the absorption and emission spectra of semiconductors [32, 48].

2.1.2 Excitons in Quantum Wells

Semiconductor quantum wells (QWs) are examples of heterostructure devices, i.e. devices that contain layers of different materials grown on top of a thicker substrate crystal [36]. A quantum well consists of a thin narrow bandgap semiconductor, such as GaAs, sandwiched between two wider-bandgap semiconductors, such as Al$_x$Ga$_{1-x}$As. The thickness of the thin potential well is typically comparable to the exciton Bohr radius. The difference in bandgap energy between the quantum well and barrier region creates an effective potential well for the electrons and holes. QWs represent a finite quantum-mechanical potential well for excitons that confine the centre of mass motion of the exciton to the QW plane (1D confinement), thus leading to a quantisation of the exciton energy (See Fig. 2.3) Therefore, QWs behave as two-dimensional (2D) materials since the degree of freedom for motion in space is reduced from 3D in bulk to 2D.

The wavefunctions and energy spectrum of quantum-confined excitons can be strongly different from their bulk counterparts. The two-particle Hamiltonian (Eq. 2.1) contains an additional term describing the QW confinement potential V_{conf} [48]:

$$H_x = E_g - \frac{\hbar^2}{2m_e^*}\nabla_e^2 - \frac{\hbar^2}{2m_h^*}\nabla_h^2 - \frac{e^2}{4\pi\epsilon_0\epsilon_r|\mathbf{r}_e - \mathbf{r}_h|} + V_{\mathrm{conf}}\,. \tag{2.16}$$

The confinement potential describes the depth of the well separately for electrons and holes as these values may significantly differ from each other depending on the semiconductor materials forming the well and the barriers. Equation 2.16 can be simplified by exploiting the so-called strong quantum confinement limit, where the effect of the Coulomb interaction on the exciton energy in the growth direction z is assumed to be negligible compared to the manifestation of quantum confinement [48]. Therefore, excitonic effects manifest themselves only in the 2D plane. Under these conditions, solving the Schrödinger equation with the Hamiltonian of Eq. 2.16 yields

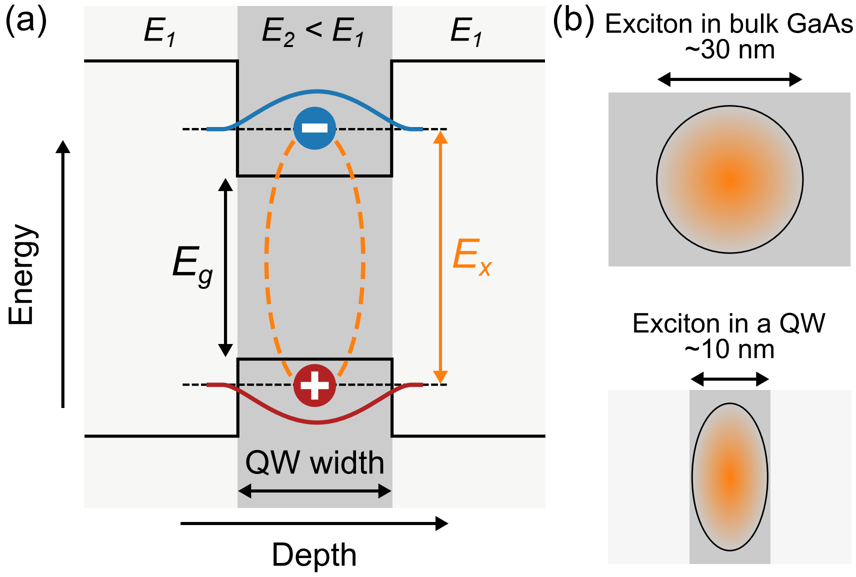

Figure 2.3: (a) Schematic band structure of a quantum well with quantised energy levels for the electron and hole. The bandgap energy E_g of the layer material is smaller than that of the surrounding medium, forming a potential trap for both electrons and holes. If the QW width is comparable to the exciton extension, schematically sketched in panel (b), the exciton energy is quantised.

the energy levels (denoted by j)[2] of excitons in a 2D QW as [48]:

$$E_n^{2\mathrm{D}} = E_g - \frac{R_x^*}{(n_j - 1/2)^2} + \frac{\hbar^2 \pi^2 j^2}{2\mu^* d_z^2}, \qquad n_j = 1, 2, 3, \dots, \tag{2.17}$$

where d_z is the well thickness. Using Eqs 2.9 and 2.17, we can compare the binding energies of excitonic levels in 3D and 2D structures of the same material (referred to the bottom of the conduction band):

$$\frac{E_b^{2\mathrm{D}}}{E_b^{3\mathrm{D}}} = \frac{n^2}{(n - 1/2)^2} > 1\,. \tag{2.18}$$

In 2D structures, exciton states are always deeper in the bandgap, indicating that the exciton binding energy is increased compared to the bulk. Since the squared exciton Bohr radius α_x^2 scales with the inverse of the exciton binding energy E_b ($\alpha_x^2 \sim 1/E_x$, See Eqs. 2.9 and 2.12), the exciton Bohr radius in 2D structures decreases compared to 3D crystals:

$$\frac{\alpha_x^{2\mathrm{D}}}{\alpha_x^{3\mathrm{D}}} = \frac{(n - 1/2)}{n} < 1\,. \tag{2.19}$$

---

[2] Each localised state of the electron-hole pair in a quantum well, described by a quantum number j, has a series of excitonic states $n_j = 1, 2, 3, \dots$ For the sake of simplicity, the subscript j is omitted in the following description.

This result implies that confinement decreases the Bohr radius as the electron and hole are "squeezed" closer together in a 2D well. Finally, the third characteristic parameter of an excitonic transitions is its oscillator strength f_{osc}, which scales reciprocally with the third power of n (Eq. 2.14):

$$f_{\mathrm{osc}}^{\mathrm{3D}} \approx n^{-3}, \quad f_{\mathrm{osc}}^{\mathrm{2D}} \approx (n-1/2)^{-3} \quad \Rightarrow \quad \frac{f_{\mathrm{osc}}^{\mathrm{2D}}}{f_{\mathrm{osc}}^{\mathrm{3D}}} = \frac{n^3}{(n-1/2)^3} > 1\,. \tag{2.20}$$

$$\text{For } n = 1: \quad \frac{f_{\mathrm{osc}}^{\mathrm{2D}}}{f_{\mathrm{osc}}^{\mathrm{3D}}} = \frac{1}{(1-1/2)^3} = \frac{1}{1/8} = 8\,. \tag{2.21}$$

Therefore, a 2D ground state ($n = 1$) exciton experiences an eightfold increase in the oscillator strength compared to a bulk exciton. In summary, quantum confinement reduces the extension of the electron and hole wavefunctions compared to the bulk case, leading to an increased electron-hole overlap and larger binding energies, which, in turn, increase the oscillator strength. On the downside, however, the overlap between the exciton wavefunction and external light field is subsequently decreased. To counteract this decrease, the light field needs to be confined as well, for example, in an optical cavity [40], as discussed in the following section (See Section 2.2).

As a last remark, it should be noted that excitons can only be considered as "good" bosons in the low-density regime when the fermionic character of their constituents is negligible. As quasi-particles consisting of two fermions, excitons always have an integer total spin $S = 0$ or 1 and can thus be considered bosonic quasi-particles. This assumption remains valid as long as the spacing between individual excitons exceeds the spacing between the constituent electron and holes, i.e. $\rho_x \ll \alpha_x^{-3}$, where ρ_x corresponds to the exciton density. At higher densities, increased electronic screening from free and other bound carriers leads to a reduction of the exciton binding energy. Above a critical density, excitons, as bound electron-hole pairs, cease to exist, and the system undergoes a transition from an insulating state (bosonic) to a metallic electron-hole plasma (fermionic) - an effect referred to as the Mott transition [40, 50]. For an InGaAs/GaAs QW, the critical density above which a Mott transition occurs, also termed as Mott density, has been calculated as 10×10^{10} to 10×10^{11} cm^{-2} at carrier temperatures of ∼30 K [51]. In $\mathrm{Cu_2O}$, the plasma density where the 1S exciton vanishes in the continuum, is approximately 3×10^{18} cm^{-3} at 4 K [52].

2.2 Confinement of Light in Optical Cavities

An optical cavity, or optical resonator, is defined by two or more reflectors arranged such that only specific light frequencies are allowed to exist within the cavity. Depending on the technological application and building material, several geometries of microresonators have been developed, including micropillar cavities, microtoroid resonators, whispering gallery cavities, and photonic crystal cavities [53, 54]. However, the most common microcavity design is the planar cavity comprising two parallel flat mirrors [53].

In the following, the concept of the semiconductor microcavity will be introduced, starting with a short discussion of the idealised case of the Fabry-Pérot interferometer in Section 2.2.1. Then, the main properties commonly used to describe resonators are presented in Section 2.2.2, followed by a discussion of the dispersion of photons inside a cavity in Section 2.2.3. The developed ideas in these sections will be applied to the case of semiconductor structures such as distributed Bragg reflectors in Section 2.2.4 and semiconductor microcavities in Section 2.2.5.

2.2.1 Fabry-Pérot Interferometer

Most of the properties of optical microcavities can be understood from the simple Fabry-Pérot interferometer. A Fabry-Pérot interferometer, also called Fabry-Pérot etalon, consists of two partially reflective mirrors arranged parallel to each other to form a cavity. The mirrors are separated by a layer of length d and refractive index n_c and are surrounded by a medium of refractive index n_{ext}.

The working principle behind the Fabry-Pérot interferometer is schematically illustrated in Fig. 2.4(a). A light ray (i.e. a wave whose wavefronts are normal to the given ray) is incident on the first of the two partially reflecting mirrors. Some light enters the space between the mirrors, where it is repeatedly reflected, with a small fraction transmitted at each encounter with a mirror. This leads to an interference of the electromagnetic waves, and a standing wave pattern of the light field is formed within the structure. The partial reflection and transmission of light incident from the “external” medium to the Fabry-Pérot are determined by the coefficients r_1 and t_1, respectively. The opposite scenario, where light is incident within the cavity to the external medium, is described by the reflection and transmission coefficients r_2 and t_2.

The total transmitted field U_{out} can be calculated by adding the contributions from each of the transmitted waves U_1, U_2, U_3, etc. To carry out this sum, we need to know their relative phases and amplitudes. The amplitude of the first transmitted beam U_1 is calculated by multiplying the amplitude of the incident wave U_0 with the transmission coefficients t_1 and t_2, i.e. $U_1 = U_0 t_1 t_2$. The second transmitted beam is reflected two times within the Etalon and is,

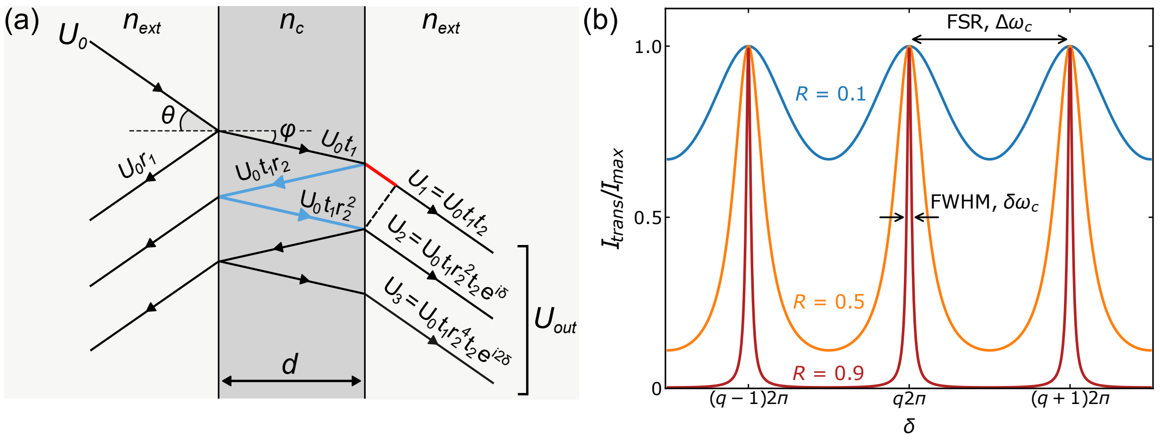

Figure 2.4: (a) Working principle of a Fabry-Pérot interferometer. A medium of refractive index n_c and width d is surrounded by regions of material with refractive index n_{ext}. An incident beam with amplitude U_0 is partially reflected and partially transmitted at the two reflective interfaces. The overall transmission of the structure is given by the sum of the amplitudes of all transmitted beams U_i. The optical path difference between two successive transmitted beams is given by the difference between the blue and the red lines. (b) A graph of the normalised transmitted intensity, $I_{\text{trans}}/I_{\text{max}}$, plotted against the phase shift δ for three value of mirror reflectivity, $R = 0.1$ (blue curve), $R = 0.5$ (orange), and $R = 0.9$ (red). The full width at half-maximum (FWHM) for one resonance mode and the FSR are highlighted in the graph.

therefore, given by $U_2 = U_0 t_1 r_2 r_2 t_2 e^{ik2n_c d\cos(\theta)} = U_0 t_1 r_2^2 t_2 e^{i\delta}$, where the phase factor $e^{i\delta}$ arises due to optical path difference between U_1 and U_2. The optical path difference corresponds to the difference between the red and blue lines in Fig. 2.4(a) and amounts to a total phase lag between successive transmitted beams given by [55]:

$$\delta = k2n_c d\cos(\phi)\,, \tag{2.22}$$

with ϕ being the internal angle of reflection. The total amplitude transmitted through the Fabry-Pérot U_{out} is given by:

$$U_{\text{out}} = U_0 t_1 t_2 \{1 + Re^{i\delta} + R^2 e^{i2\delta} + ...\} = \frac{U_0 t_1 t_2}{1 - Re^{i\delta}}\,, \tag{2.23}$$

where $R = |r_2|^2$ is the “internal” reflectivity of the mirrors. The transmittance T of the Fabry-Pérot interferometer is given by the ratio between the transmitted and incident intensities:

$$T = \frac{I_{\text{transmitted}}}{I_{\text{incident}}} = \frac{|U_{\text{out}}|^2}{|U_0|^2} = \left(\frac{|t_1 t_2|}{1 - R}\right)^2 \left[1 + \frac{4R}{(1-R)^2 \sin^2(\delta/2)}\right]^{-1}. \tag{2.24}$$

The prefactor $|t_1 t_2|/(1-R)$ is of little interest and can be absorbed into the maximum transmitted intensity I_{max}. Additionally, a useful property for interferometers, the *finesse*, can be defined as $\mathscr{F} = \pi\sqrt{R}/(1-R)$. Therefore, Eq. 2.24 can be rewritten in the form of an Airy function:

$$\frac{I_{\text{trans}}}{I_{\text{max}}} = \frac{1}{1 + (4\mathscr{F}^2/\pi^2)\sin^2(\delta/2)}\,. \tag{2.25}$$

Figure 2.4(b) shows the normalised transmitted intensity $I_{\text{trans}}/I_{\text{max}}$ as a function of δ for three different values of reflectivity R. The peaks get narrower as the mirror reflectivity, and therefore the coefficient of finesse $\mathscr{F}$, increases. Figure 2.4(b) also shows that the intensity transmitted by a Fabry-Pérot, given by Eq. 2.25, has peaks that occur where $\sin(\delta/2) = 0$, which occurs when $\delta = q \cdot 2\pi$, with q is an integer, corresponding to constructive interference between the multiple transmitted waves from the cavity. In other words, a Fabry-Pérot cavity only transmits discrete modes, labelled with integer q. Assuming normal incidence ($\cos(\phi) = 0$ in Eq. 2.22), the *resonance condition* of the interferometer, expressed in terms of wavelength, is given by:

$$n_c d = q\frac{\lambda_c}{2}\,, \tag{2.26}$$

where λ_c denotes the resonance wavelength of the cavity. Eq. 2.26 permits the Fabry-Pérot to act as a very narrow band-pass filter for fixed cavity length d.

2.2.2 Optical Properties of Resonators

Several optical quantities can characterise the operation of a Fabry-Pérot interferometer. The ones most relevant to this work are the quality factor, the free-spectral range, and the finesse. The *quality factor*, or *Q factor*, is a measure of the rate at which optical energy decays from within the cavity through mechanisms such as absorption, scattering, or leakage through the imperfect ($R < 1$) mirrors. It is defined as the ratio of a resonant cavity frequency ω_c, to the linewidth of the cavity mode $\delta\omega_c$, quantified by the full width at half maximum (FWHM) [See Fig. 2.4(b)]:

$$Q = \frac{\omega_c}{\delta\omega_c}\,. \tag{2.27}$$

Q^{-1} is the fraction of energy lost in a single round-trip around the cavity. Equivalently, the exponentially decaying photon number has a lifetime given by $\tau = Q/\omega_c$. Q factor is thus a measure of the lifetime of the cavity photons [47].

A Fabry-Pérot resonator supports modes whose wavelength is a multiple of twice the length of the cavity (Eq. 2.26), thus fulfilling the 2π-phase criterion. Consequently, several modes exist within the resonator apart from the fundamental wavelength, as shown in Fig. 2.4(b). The mode spacing, commonly referred to as the *free spectral range* (FSR), is determined by the cavity length, or equivalently, by one full round trip of a photon around the resonator. The FSR in terms of phase δ will always be 2π. The FSR, expressed in terms of angular frequency, is given by:

$$\Delta\omega_c = \frac{2\pi c}{nL}\,, \tag{2.28}$$

where c is the speed of light in vacuum, n the refractive index of the medium, and L the round trip physical length, i.e. $L = 2d$. Normal incidence is assumed in Eq. 2.28. The mode separation is inversely proportional to the cavity length. Thus, microcavities have far fewer optical modes in each region of the spectrum than macroscopic cavities. Therefore, precise tuning of the cavity mode to a particular emission wavelength becomes more important than in large cavities.

The transmission peaks in Fig. 2.4(b) are not infinitely sharp as mirrors cannot be made perfectly reflecting ($R < 1$). This limitation reduces the resonator's spectral resolution, i.e. its ability to distinguish two closely spaced wavelengths (or frequencies) apart. The *finesse* parameterises the spectral resolution, or resolving power, of the cavity and is defined as the ratio of free spectral range (the frequency separation between successive longitudinal cavity modes) to the linewidth (FWHM) of a cavity mode.

$$\mathscr{F} = \frac{\Delta\omega_c}{\delta\omega_c} = \frac{\pi\sqrt{R}}{1-R}\,. \tag{2.29}$$

Equations 2.27 and 2.29 demonstrate that improving the mirror reflectivity leads to a reduction of the modes' linewidth, which, in turn, result is a higher finesse and Q factor. The finesse is solely affected by the resonator losses, as the greater the loss, the broader the resonance and the lower the finesse. On the other hand, the Q factor is affected by both the frequency of the mode and the cavity loss.

2.2.3 Photonic Dispersion in Planar Microcavities

Photons in (3D) vacuum follow a linear dispersion relation $E_c = \hbar\omega(k) = \hbar c|\mathbf{k}|$, with c the vacuum speed of light and $\mathbf{k}$ the wavevector. In planar cavities, however, photons are strongly confined in the longitudinal direction (perpendicular to the mirror plane), while transverse propagation remains unrestricted. Consequently, the wavevector inside the resonator is expressed in terms of its in-plane $\mathbf{k}_{||}$ and out-of-plane $\mathbf{k}_{\perp}$ components as $\mathbf{k} = \mathbf{k}_{||} + \mathbf{k}_{\perp}$. The energy dispersion of a confined cavity photon in a planar Fabry-Pérot resonator can be obtained by expressing $\mathbf{k}$ in terms of its $k_{\perp}$ and $k_{||}$ components, and including the non-zero refractive index of the medium [40]:

$$E_c(\mathbf{k}) = \frac{\hbar c}{n_c}|\mathbf{k}| = \frac{\hbar c}{n_c}\sqrt{k_\perp^2 + k_{||}^2}\,. \tag{2.30}$$

For small in-plane wavevectors $k_{||} \ll k_\perp$, the energy dispersion of cavity photons can be approximated[3] as:

$$E_c(\mathbf{k}) \approx \frac{\hbar c}{n_c}k_\perp(1 + \frac{k_{||}^2}{2k_\perp^2}) = E_c(k_{||} = 0) + \frac{\hbar^2 k_{||}^2}{2m_c^*}\,. \tag{2.31}$$

The first term in Eq. 2.31 represents the confinement energy or equivalently the ground state energy of cavity photons, while the second defines the in-plane kinetic energy expressed as a parabolic dispersion $\frac{\hbar^2 k_{||}^2}{2m_c^*}$, where m_c^* is the *cavity photon effective mass*, given by:

$$m_c^* = \frac{E_c(k_{||} = 0)}{c^2/n_c^2}\,. \tag{2.32}$$

This mass is typically small compared to the mass of exciton ($\sim 10^{-4} m_x^*$) or electrons ($\sim 10^{-5} m_e$). As a result, the excitonic dispersion appears virtually flat when it is plotted with the cavity dispersion for the same in-plane momenta. The in-plane wavevector $k_{||}$ is related to the angle θ, under which light is emitted from the cavity structure, with[4]:

$$k_{||} = \frac{E_c(k_{||} = 0)}{\hbar c}\sin(\theta) \approx \frac{E_c}{\hbar c}\theta\,. \tag{2.33}$$

From an experimental point of view, Eq. 2.33 is of paramount importance as it allows us to retrieve the true dispersion curves of exciton-polaritons by measuring the angle dependence of their transmission spectrum [40, 56].

2.2.4 Distributed Bragg Reflectors

Distributed Bragg reflectors (DBRs) are critical components in several devices such as vertical cavity surface emitting lasers (VCSELs) [57], fibre lasers [58], and other types of narrow-linewidth laser diodes such as distributed feedback lasers [59]. A DBR, also known as Bragg mirror or Bragg reflector, is a periodic structure consisting of alternating layers of dielectric or semiconductor materials with different refractive indices, n_1 and n_2. The physical thickness of each layer d_i is designed so that the corresponding optical thickness is equal to a quarter of the wavelength in vacuum λ_c, i.e. $n_1 d_1 = n_2 d_2 = \lambda_c/4$. If this condition is satisfied, all the beams transmitted through the DBR interfere destructively, whereas all beams reflected by the

---

[3] $\sqrt{a^2 + b^2} = a\sqrt{a + b^2/a^2} \approx a(1 + b^2/2a^2 + ...)$

[4] The derivation uses the geometric relation $|\mathbf{k}_{||}| = |\mathbf{k}_{ext}|\sin\theta$ and the photon dispersion $E_c = \hbar c|\mathbf{k}| = \hbar c|\mathbf{k}_{ext}|/n_{ext}$ with $n_{ext} = 1$ for air as the external medium.

structure are in phase [47].

The transmission and reflection properties of periodic structures, including DBRs, can be simulated using the transfer matrix method (TMM) [60, 61]. Figure 2.5(a) presents the TMM simulations for a DBR mirror consisting of 20 $\mathrm{Al_{0.15}Ga_{0.85}As/AlAs}$ pairs. The reflectivity spectrum is characterised by a broad and flat region of high reflectivity around its design wavelength $\lambda_c = 800$ nm, commonly termed the DBR *photonic gap* or "*stopband*". Reflectivity drops off in an oscillating fashion on either side of the stopband and exhibits low-reflectivity regions called *Bragg modes*. Reflectivity in the stopband is approximately constant, and its maximum value, occurring at λ_c, is given by [47, 62]:

$$R_{\max} = R(\lambda_c) = \left(\frac{n_0(n_2)^{2N} - n_s(n_1)^{2N}}{n_0(n_2)^{2N} + n_s(n_1)^{2N}} \right)^2 , \tag{2.34}$$

where n_0, n_s are the refractive indices of the originating and the terminating medium, respectively, and N is the number of alternating layers of refractive index n_1 and n_2, with $n_1 < n_2$. Consequently, the maximum reflectivity of the mirror improves by increasing either the refractive index contrast ($\Delta n = n_2 - n_1$) between the constituent materials or the total number of pairs in the DBR. A further important characteristic of a DBR mirror is the width of its stopband given by [47, 63]:

$$\Delta\lambda_{\max} = \frac{4\lambda_c}{\pi} \sin^{-1}\left(\frac{\Delta n}{n_2 + n_1} \right) . \tag{2.35}$$

The $\Delta\lambda_{\max}$ given in Eq. 2.35 specifies the full width at half maxima of the reflectivity when the number of pairs approaches infinity. $\Delta\lambda_{\max}$ is proportional to the resonance wavelength λ_c and is sensitively affected by the refractive index contrast Δn. Thus, a higher Δn is very desirable in DBR fabrication for both a high peak reflectance (Eq. 2.34) and a wide stopband width (Eq. 2.35) [63].

The electric field distribution inside the DBR can also be simulated and is shown in Fig. 2.5(b) for two incident waves. For the wave with a wavelength equal to the stopband centre (orange curve), destructive interference of the transmitted beams leads to an exponential decay in its intensity as a function of the DBR depth. The non-negligible penetration of the electric field into the DBR is caused by the inability to fabricate DBRs with 100% reflectivity in an experimental setting. The penetration depth can be reduced by increasing the refractive index contrast between the layers. On the other hand, a wave tuned to the first Bragg mode (red curve) experiences high transmittance and the corresponding field distribution is concentrated within the mirror structure.

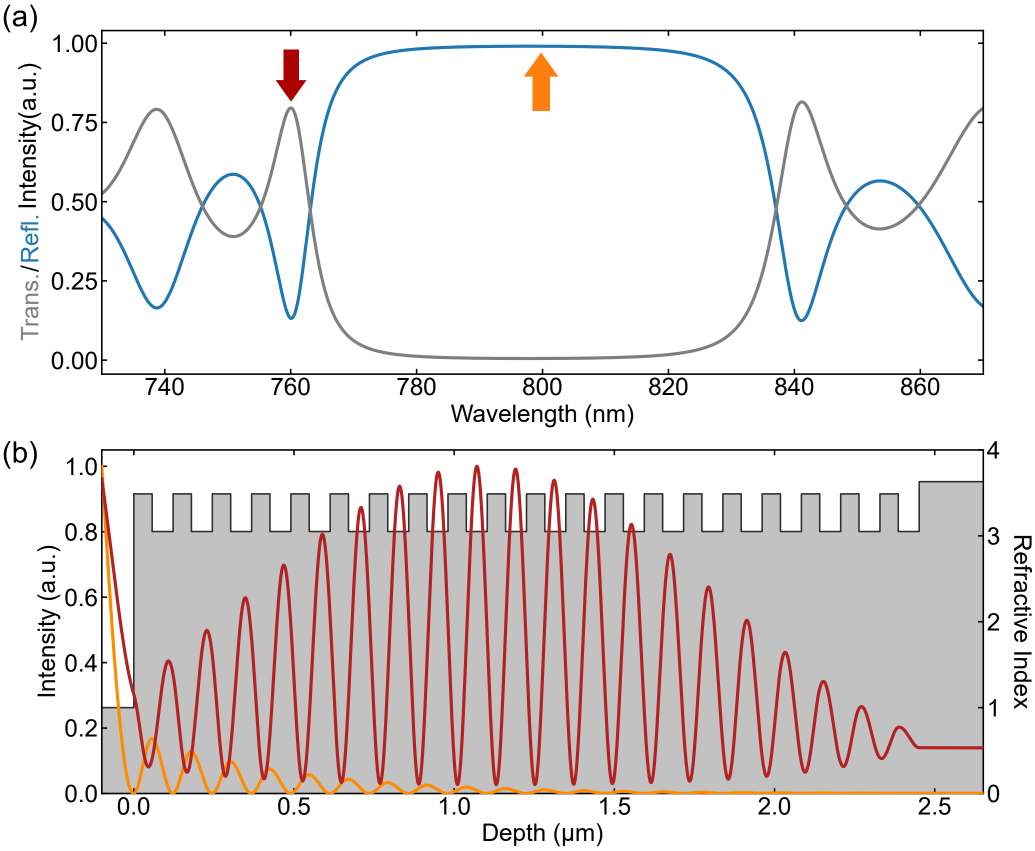

Figure 2.5: Transfer matrix simulations of a distributed Bragg reflector consisting of 20 pairs of $Al_{0.15}Ga_{0.85}As/AlAs$. (a) Reflectivity and transmittivity spectra. (b) Electric field distribution of two incident fields at 760 nm (red line) corresponding to the first Bragg mode and 800 nm (orange line) corresponding to the centre of the stopband centre, as indicated by the red and orange arrows in (a). The incident intensity is normalised to one in both cases. The simulations were performed using the `tmm` Python package [64].

2.2.5 Semiconductor Microcavities

A planar semiconductor microcavity can be formed by fabricating two opposing DBR mirrors encapsulating a cavity space layer. This design is essentially a monolithic Fabry-Pérot microresonator and all concepts discussed in Section 2.2 are applicable. For such Fabry-Pérot cavity, the cavity thickness d, has to be an integer multiple q of the resonance wavelength (Eq. 2.26). While this condition still holds, the non-negligible penetration of the electric field into the mirrors must be considered when designing the semiconductor microcavity. Specifically, the Fabry-Pérot cavity length has to be replaced by a larger effective cavity length $d_{\text{eff}} = d + d_{\text{DBR1}} + d_{\text{DBR2}}$, where the penetration length into the DBRs d_{DBR}, can be approximated as [65]:

$$d_{\text{DBR}} = \frac{\lambda_c}{2} \frac{n_1 n_2}{n_c(n_2 - n_1)} \qquad (n_1 < n_2)\,, \tag{2.36}$$

where λ_c is the resonance wavelength and n_c the refractive index of the cavity material. For typical GaAs/AlAs structures, $d_{\text{DBR}} \sim (3-4)d$ [66].

The simulated reflectivity spectrum and field distribution for a microcavity consisting of a GaAs spacer layer encapsulated inside two 20-pair $\text{Al}_{0.15}\text{Ga}_{0.85}\text{As/AlAs}$ DBR mirrors is shown in Fig. 2.6(a). The reflectivity spectrum exhibits a broad stopband surrounded by Bragg modes, similar to the case of a single DBR. Nevertheless, the stopband features a pronounced reflectivity minimum at the resonance wavelength λ_c, corresponding to a high transmittance of the Fabry-

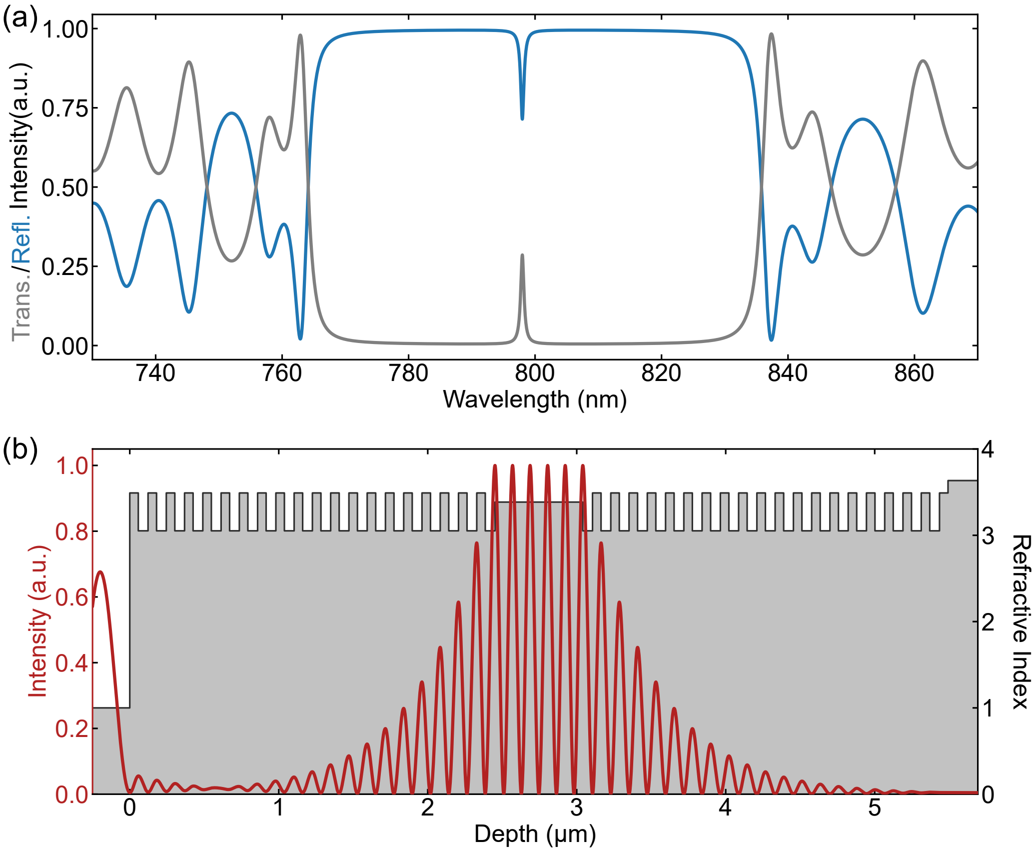

Figure 2.6: Transfer matrix simulation of a microcavity consisting of two 20 pair $\text{Al}_{0.15}\text{Ga}_{0.85}\text{As/AlAs}$ DBRs and a $5\lambda_c/2$ GaAs cavity layer. (a) Reflectivity and transmittivity spectra reveal a sharp resonance at the centre of the stopband at $\lambda_c = 800$ nm. (b) Distribution of the electric field inside the structure at the resonance wavelength λ_c. The antinode intensity is normalised to one. The simulations were performed using the `tmm` Python package [64].

Pérot structure at this wavelength. The corresponding electric field distribution for the resonance wavelength, presented in Fig. 2.6(b), shows a strong enhancement of the field inside the cavity accompanied by an exponential decay in each Bragg mirror. Additionally, maxima of the intra-cavity intensity, or anti-nodes, are formed at the two mirror-cavity interfaces and inside the cavity. This observation is important for the design of microcavities. Specifically, placing QWs at the anti-nodes of the electric field inside the cavity increases the overlap between the cavity photon field and QW excitons, thus increasing the strength of the light-matter interaction. For N QWs, the light-matter coupling is enhanced by a factor $\sqrt{N}$ [67]. Furthermore, using several QWs allows the total exciton density to be distributed over the QWs to avoid reaching the Mott density while simultaneously enhancing the cavity coupling [68]. As a convention, a $q\lambda_c/2$ cavity contains $q-1$ antinodes separated by $\lambda_c/2$.

2.3 Polaritons

Embedding semiconductor QWs inside a microresonator constitutes a powerful tool for studying light-matter interaction. The general practice involves placing multiple QWs at the antinodes of the light field inside the microcavity, with the QW-exciton transition in resonance with one of the cavity modes. The energetic and spatial overlap between the exciton and photon modes enhances the interaction between the two systems, and if the right conditions are satisfied, the so-called strong-coupling regime of light-matter interaction is realised. In this regime, the elementary excitations of the system are no longer the bare excitons and photon modes but a new type of quasiparticles called exciton-polaritons.

In the following, the concept of the polariton will be introduced more thoroughly and its properties will be discussed. First, the difference between weak and strong coupling is discussed in Section 2.3.1. Then, a simple mathematical model describing the coupling between QW excitons and cavity photons as well as other key concepts of polariton physics are presented in Section 2.3.2. The discussion is complemented by a few remarks regarding practical aspects of the creation and of polaritons in Section 2.3.3.

2.3.1 Light-Matter Coupling

The resonant light-matter interaction in optical cavities can be described in terms of either the weak or strong coupling regimes, depending on the coupling strength between cavity photons and a quantum emitter [69]. In our case, the emitter is a quantum well embedded in a microcavity, with the exciton transition coinciding with one of the resonant modes of the cavity. In this scenario, the interaction between the exciton and the light field will be strongly affected since the exciton and cavity can exchange photons coherently. At resonance, the relative strength of the exciton-cavity interaction is determined by three parameters: the photon decay rate of the cavity γ_c, the exciton decay rate γ_x, and the exciton-photon coupling parameter g. These three parameters each define a characteristic time-scale for the dynamics of the coupled exciton-photon system [69].

The interaction is said to be in the *weak coupling regime* when dissipation dominates over the coupling between the resonant exciton and photon modes. In this regime, the two coupled systems essentially retain their uncoupled properties under the influence of interaction between them, allowing a perturbative treatment for the dynamics of the system [47]. One of the hallmarks of weak coupling is the so-called *Purcell effect*, which describes the enhancement (or suppression) of a quantum system's spontaneous emission rate due to the changes in the density of photonic states of the surrounding medium [70]. Intuitively, if a dipole is resonant with the cavity mode, the photon density of states seen by the dipole is increased with respect to the vacuum density of states. The spontaneous emission rate is subsequently enhanced as the dipole decays radiatively faster than in the vacuum, and the photons are emitted in the cavity mode[5] [47]. The control of spontaneous emission through the Purcell effect is routinely utilised in semiconductor-based emitters like vertical-cavity surface-emitting lasers (VCSELs) [54] and quantum dot-based single-photon sources [71, 72].

On the other hand, if the exciton-photon coupling strength prevails over the different damping factors (loss rates), the perturbative weak-coupling regime breaks, and instead, the so-called *strong coupling* takes place. In a simplified picture, the radiative decay of an exciton becomes reversible and periodic, given the periodic re-absorption of the emitted photon during its lifetime inside the cavity [69]. The frequency of this energy exchange is referred to as the *vacuum Rabi frequency*. In the strong coupling regime, the eigenstates of the coupled system are no longer the bare exciton and photon modes but hybrid light-matter eigenstates, the upper and lower polariton modes, which are spectrally separated by the *vacuum Rabi splitting*. This splitting is the signature of periodic energy exchange between light and matter; the stronger the coupling, the larger the splitting. Another signature of strong coupling is a characteristic *avoided crossing*, also know as *anticrossing*, observed in the reflection (transmission) spectra when the light mode crosses the exciton resonance or vice versa.

The first theoretical discussion of the strong coupling regime in a solid state system was made by Hopfield in 1958 [73]. Following early studies on atoms in the microwave regime [74] and the first successful demonstration of the strong coupling of a single atom in an optical cavity [75],

---

[5] The opposite effect is also possible: if the dipole is placed out of resonance, the photon density of states seen by the dipole is smaller than in vacuum and the spontaneous emission rate is reduced.

the strong coupling regime in semiconductor microcavities was first identified by Weisbuch et al. in 1992 [76], marking the experimental discovery of cavity polaritons.

2.3.2 Quantum Description of Polaritons

The interaction between light and matter in a microcavity system containing QWs can be described using the so-called coupled *harmonic oscillator model*. This model treats both the exciton and the cavity photon modes as harmonic oscillators with resonance energies $E_x(k_{||})$ and $E_c(k_{||})$ that are coupled by a coupling constant g. The model assumes operation in the low-density limit, where exciton-exciton interactions can be neglected. Since only excitonic and photonic states with the same in-plane momentum are allowed to couple, g is nonzero only between modes with the same $k_{||}$. This constant quantifies the strength of the exciton-photon interaction, and for the case of a QW inside a cavity, it is given by [77, 78]:

$$g = e\hbar\sqrt{\frac{f_{\mathrm{osc}}/A}{8\epsilon d_{\mathrm{QW}} m_e}} \int d^3\mathbf{r}\psi_x(\mathbf{r})\psi_c(\mathbf{r})\,, \tag{2.37}$$

where e is the elementary charge, f_{osc}/A the exciton oscillator strength per surface area, ϵ the dielectric constant of the QW material, d_{QW} the quantum well thickness, and m_e the electron mass. The integral in Eq. 2.37 represents the overlap between the exciton and photon wavefunctions ψ_x and ψ_c, indicating that the coupling strength is increased by placing the QW at an antinode of the cavity light field. Additionally, g scales as $\sqrt{f_{\mathrm{osc}}}$ and thereby on the number of quantum wells inside the cavity (See Section 2.2.5). Therefore, multiple QWs can be placed at the antinode of the cavity field to increase the exciton-photon coupling strength.

The linear Hamiltonian of the coupled system, written within the framework of second quantisation[6], reads:

$$\begin{aligned} \hat{H}_{\mathrm{pol}} &= \hat{H}_c + \hat{H}_x + \hat{H}_I \\ &= \sum E_c(k_{||})\hat{\alpha}^\dagger_{\boldsymbol{k}_{||}}\hat{\alpha}_{\boldsymbol{k}_{||}} + \sum E_x(k_{||})\hat{b}^\dagger_{\boldsymbol{k}_{||}}\hat{b}_{\boldsymbol{k}_{||}} + \sum g(\hat{\alpha}^\dagger_{\boldsymbol{k}_{||}}\hat{b}_{\boldsymbol{k}_{||}} + \hat{\alpha}_{\boldsymbol{k}_{||}}\hat{b}^\dagger_{\boldsymbol{k}_{||}})\,, \end{aligned} \tag{2.38}$$

where $\hat{\alpha}^\dagger_{\boldsymbol{k}_{||}}$, $\hat{\alpha}_{\boldsymbol{k}_{||}}$ ($\hat{b}^\dagger_{\boldsymbol{k}_{||}}$, $\hat{b}_{\boldsymbol{k}_{||}}$) denote the creation and annihilation operators for a photon (exciton) with in-plane wavevector $k_{||}$. For simplicity, the longitudinal component of the photon wavevector is omitted. In Eq. 2.38, the first two terms describe the exciton and photon oscillator modes, while the last term represents the interaction between those two modes. The

---

[6] Second quantisation is a mathematical formalism largely used in quantum field theory and quantum optics where physical processes are described in terms of creation and annihilation operators.

Hamiltonian of Eq. 2.38 can be diagonalised by the following unitary transformation:

$$\begin{aligned} \hat{l}_{\boldsymbol{k}_{||}} &= X_{\boldsymbol{k}_{||}} \hat{b}_{\boldsymbol{k}_{||}} + C_{\boldsymbol{k}_{||}} \hat{\alpha}_{\boldsymbol{k}_{||}} , \\ \hat{u}_{\boldsymbol{k}_{||}} &= -C_{\boldsymbol{k}_{||}} \hat{b}_{\boldsymbol{k}_{||}} + X_{\boldsymbol{k}_{||}} \hat{\alpha}_{\boldsymbol{k}_{||}} . \end{aligned} \tag{2.39}$$

The resulting Hamiltonian in the new basis becomes:

$$\hat{H}_{\text{pol}} = \sum E_{\text{LP}}(k_{||}) \hat{l}^{\dagger}_{\boldsymbol{k}_{||}} \hat{l}_{\boldsymbol{k}_{||}} + \sum E_{\text{UP}}(k_{||}) \hat{u}^{\dagger}_{\boldsymbol{k}_{||}} \hat{u}_{\boldsymbol{k}_{||}} . \tag{2.40}$$

This equation reflects the formation of two new eigenmodes in the coupled system, with creation and annihilation operators $\hat{l}^{\dagger}_{\boldsymbol{k}_{||}}/\hat{u}^{\dagger}_{\boldsymbol{k}_{||}}$ and $\hat{l}_{\boldsymbol{k}_{||}}/\hat{u}_{\boldsymbol{k}_{||}}$, respectively. These eigenmodes describe the quasi-particles referred to as lower (LP) and upper polariton (UP). Thus, a polariton can be conceptualised as a linear superposition of an exciton and a photon with the same in-plane wave number $k_{||}$. The exciton and photon fractions in each polariton branch are given by the amplitude squared of $X_{\boldsymbol{k}_{||}}$ and $C_{\boldsymbol{k}_{||}}$, which are referred to as the Hopfield coefficients [73]:

$$\begin{aligned} |X_{\boldsymbol{k}_{||}}|^2 &= \frac{1}{2}\left(1 + \frac{\Delta(k_{||})}{\sqrt{\Delta(k_{||})^2 + 4g^2}}\right) , \\ |C_{\boldsymbol{k}_{||}}|^2 &= \frac{1}{2}\left(1 - \frac{\Delta(k_{||})}{\sqrt{\Delta(k_{||})^2 + 4g^2}}\right) , \end{aligned} \tag{2.41}$$

where $\Delta(k_{||}) = E_c(k_{||}) - E_x(k_{||})$ is the detuning between the bare cavity and exciton modes. $|X|^2$ and $|C|^2$ yield the exciton and photon fraction of the LP (photon and exciton fraction of the UP), respectively, and they always add up to unity: $|X|^2 + |C|^2 = 1$.

Neglecting dissipation, the energies of the coupled system, E_{UP} and E_{LP}, are the eigenenergies of the diagonalised Hamiltonian of Eq. 2.40 and are deduced as:

$$E_{\text{LP,UP}} = \frac{1}{2}(E_x + E_c \pm \sqrt{4g^2 + (E_x - E_c)^2}) . \tag{2.42}$$

These give the upper and lower polariton $k_{||}$-dependent dispersion curves, which are of paramount importance in the characterisation of polariton systems in microresonator systems.

The coupled harmonic oscillator model can be extended to account for the finite lifetime of excitons and cavity photons due to dissipation. This is achieved by considering the complex energies $E_x(k_{||}) - i\gamma_x$ and $E_c(k_{||}) - i\gamma_c$ for the exciton and cavity modes in the Hamiltonian of Eq. 2.38. The parameters γ_c and γ_x denote the homogeneous linewidth of the two modes, which are directly linked to the corresponding lifetimes via Heisenberg's uncertainty principle

$\tau = \hbar/\gamma$. The decay rate of excitons $1/\tau_x = \gamma_x/\hbar$ is governed by radiative and non-radiative decay channels, whereas the out-coupling decay rate of photons $1/\tau_c = \gamma_c/\hbar$ is determined by the cavity losses (absorption and leakage), i.e. the Q-factor [79]. When decay is taken into account, the UP and LP dispersion curves of Eq. 2.42 are modified as:

$$E_{\mathrm{LP,UP}}(k_{||}) = \frac{1}{2}\left[E_x + E_c - i(\gamma_x + \gamma_c) \pm \sqrt{4g^2 + [E_x - E_c - i(\gamma_x - \gamma_c)]^2}\right]. \tag{2.43}$$

The real parts of Eq. 2.43 correspond to the polariton dispersion curves, while the imaginary parts characterise the polariton linewidths.

The detuning $\Delta(k_{||})$ between the photon and exciton modes is a key parameter in systems designed for strong light-matter coupling, as the polariton dispersion and the corresponding Hopfield coefficients are strongly dependent on its magnitude. The lower and upper polariton energies are plotted in Fig. 2.7(a) as a function of detuning. Due to the coupling between the exciton and photon modes, the new polariton energies anticross when the cavity energy is tuned across the exciton energy. This avoided-crossing behaviour is one of the signatures of the strong coupling regime, commonly used to prove experimentally that the system operates in this regime. The minimal energy splitting between the lower and upper branches $\hbar\Omega$ is the vacuum Rabi splitting, discussed in Section 2.3.1, and occurs at zero detuning, i.e. when the photon and exciton modes are in resonance $E_c(k_{||}) = E_x(k_{||})$. The vacuum Rabi splitting is related to light-matter coupling constant g by $\hbar\Omega = 2g$. Note that for zero detuning, both Hopfield coefficients (Eq. 2.41) become 1/2, indicating that the UP and LP are exactly half-light half-matter quasiparticles.

Anticrossing behaviour can also be observed in the polariton energy dispersions at nonzero $k_{||}$-vectors. This phenomenon is demonstrated in Fig. 2.7(b-d) where the polariton dispersions and Hopfield coefficients are plotted for negative, zero, and positive detuning of the cavity mode at $k_{||} = 0$. In all cases, the wavevector-dependent detuning not only changes the form of the upper and lower polariton dispersions, but also affects the excitonic or photonic character of the polaritons. For instance, in Fig. 2.7(b), the LP is highly photonic at $k_{||} = 0$, as shown in the composition graph ($C > X$). At wavevector values ∼2.5 $\mu\mathrm{m}^{-1}$, the exciton and photon modes cross, and both polariton branches are half light, half exciton. Finally, at very high $k_{||}$, the lower polariton is predominantly excitonic ($X >> C$) and hence their PL emission is expected to be very weak. Although the dispersions of the individual photonic and excitonic modes cross over each other for zero or negative detuning, the polariton modes show a clear anticrossing at $k_{||}$ such that $\Delta(k_{||}) \approx 0$. At this point, the lower and upper polariton "exchange" their excitonic or photonic nature. Samples with zero or negative detuning at $k_{||} = 0$ are usually preferable to polariton studies since only those exhibit avoided crossing of the two modes (at $\Delta(k_{||}) \approx 0$).

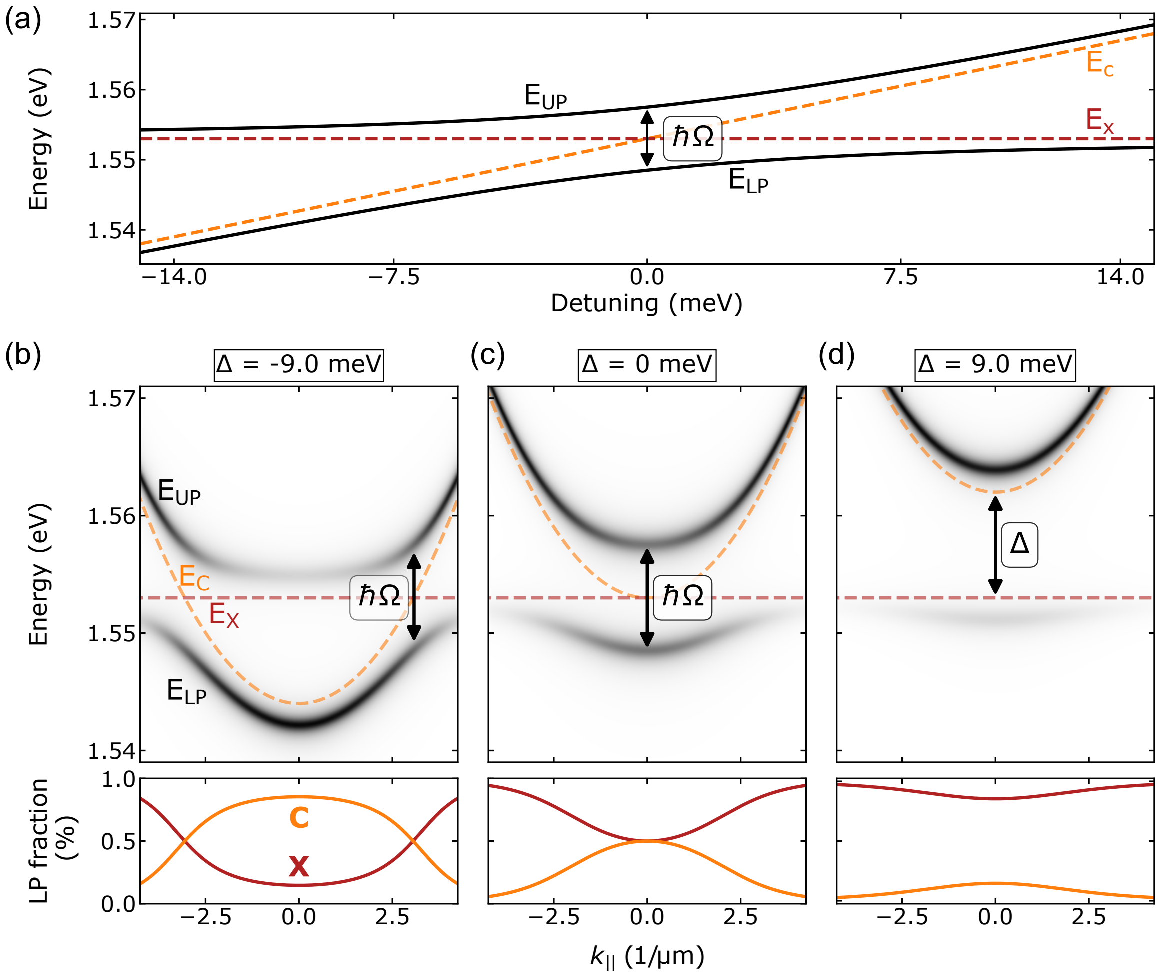

Figure 2.7: (a) Upper and lower polariton energy at $k_{||} = 0$ (solid black lines) for a range of exciton photon detunings. Even though the dispersion of the individual exciton (red dashed line) and photon (orange dashed line) cross over each other at zero detuning, the two polariton dispersions show a clear avoided crossing behaviour, characteristic of strong coupling. (b-d) Polariton dispersion curves for negative, zero, and positive detuning of the cavity mode at $k_{||} = 0$, symbolised by Δ. The grey-scale codes the photon fraction (proportional to the light intensity emitted from the cavity), and the line thickness represent the linewidth of the polariton. The lower row shows the composition of the LP. The vacuum Rabi splitting $\hbar\Omega$ is highlighted in (b) and (c). Simulation parameters: $E_x = 1.553$ eV, $m_c = 3.6 \cdot 10^{-35}$ kg, $\hbar\Omega = 9$ meV; linewidths $\gamma_x = 1$ meV, $\gamma_c = 0.5$ meV.

Equation 2.43 can be used to derive a quantitative criterion to separate the weak and strong coupling regimes, namely if the square root is imaginary or not. Specialising to the resonance case ($E_x = E_c$), the criterion is:

$$2g \equiv \hbar\Omega \lessgtr |\gamma_c - \gamma_x| \quad \text{for} \quad \begin{cases} \text{weak} \\ \text{strong} \end{cases} \text{coupling}\,. \tag{2.44}$$

From an experimentalist point of view, this criterion has the following caveat: it predicts operation in the strong coupling regime even if both linewidths are equal with each other and larger than the Rabi frequency: $\gamma_c = \gamma_x > \Omega$, where there would be no visible splitting in the spectrum [80]. Hence, a more stringent criterion is usually implemented where we look for two peaks that are clearly separated by a splitting S at the resonance point. This criterion reads as:

$$S \lesseqgtr \gamma_{\mathrm{LP}} + \gamma_{\mathrm{UP}} \quad \text{for} \quad \begin{cases} \text{weak} \\ \text{strong} \end{cases} \text{coupling}\,. \tag{2.45}$$

The system is in the strong coupling regime when the modes are clearly split in the spectrum (at the resonance point) [54, 80]. The implementation of this criterion is schematically illustrated in Fig. 2.8, which shows the transition from Purcell enhancement of spontaneous emission to vacuum Rabi splitting in a two-level system for increasing quality factor Q. The eigenenergies of the system, which are initially degenerate, exhibit a splitting as the quality factor is increased above a characteristic value Q_{split}, and the emission spectrum becomes a doublet, split by $\hbar\Omega = 2g$. This transition is manifested in the emission spectrum of the system as a transition from a single Lorentzian to a double-peaked structure. The clearly resolved case occur at $S \geqslant \gamma_{\mathrm{LP}} + \gamma_{\mathrm{UP}}$ for quality factors $Q \geqslant Q_{\mathrm{split}}$, as shown in Fig. 2.8.

The polariton effective masses, m^*_{UP} and m^*_{LP}, can be derived from the UP and LP dispersion curves. For wavevectors where $\hbar^2 k_{||}^2/2m_c \ll 2g$, both dispersions can be approximated by a parabola:

$$E_{\mathrm{LP,UP}}(k_{||}) \approx E_{\mathrm{LP,UP}}(k_{||} = 0) + \frac{\hbar^2 k_{||}^2}{2m^*_{\mathrm{LP,UP}}}\,. \tag{2.46}$$

The polariton effective mass is the weighted harmonic mean of the mass of its exciton and photon components, as determined by the Hopfield coefficients of Eq. 2.41:

$$\begin{aligned} \frac{1}{m^*_{\mathrm{LP}}} &= \frac{|X|^2}{m^*_x} + \frac{|C|^2}{m^*_c}\,, \\ \frac{1}{m^*_{\mathrm{UP}}} &= \frac{|C|^2}{m^*_x} + \frac{|X|^2}{m^*_c}\,, \end{aligned} \tag{2.47}$$

where m^*_x is the effective exciton mass of its centre-of-mass motion and m_c is the effective cavity-photon mass given by Eq. 2.32. As discussed in Section 2.2.3, the effective photon mass is typically four orders of magnitude smaller than that of bare excitons, so Eqs. 2.47 can be approximated as:

$$\begin{aligned} m^*_{\mathrm{LP}}(k_{||} \approx 0) &\approx m^*_c/|C|^2 \sim 10^{-4} m^*_x\,, \\ m^*_{\mathrm{UP}}(k_{||} \approx 0) &\approx m^*_c/|X|^2\,. \end{aligned} \tag{2.48}$$

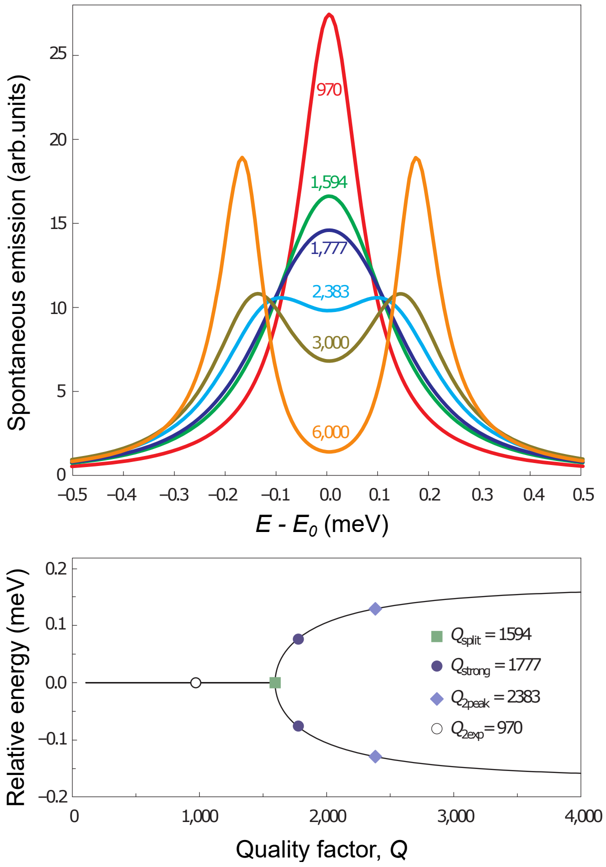

Figure 2.8: Illustration of the transition from Purcell enhancement of spontaneous emission to vacuum Rabi splitting in a two-level system: (a) spontaneous emission spectra and (b) eigenenergies for different values of quality factor Q. The numbers adjacent to each curve denote the quality factor value for each spectrum. For $Q > Q_{\text{split}}$, the eigenenergies split from an initially degenerate state. Reproduced with permission from Ref. [54].

The very small effective mass of LPs at $k_{||} \sim 0$ make LP polaritons great candidates for polariton condensation [40], as discussed in Section 2.4.2.

Lastly, the decay rate, and hence the lifetime, of the polariton modes are determined by those of the exciton and photon components as:

$$\begin{aligned} \gamma_{\text{LP}} &= |X|^2\gamma_x + |C|^2\gamma_c \,, \\ \gamma_{\text{UP}} &= |C|^2\gamma_x + |X|^2\gamma_c \,. \end{aligned} \tag{2.49}$$

In general, the lifetime of cavity photons is about two orders of magnitude smaller than the QW-excitons in the case of the ground state. Therefore, polariton decay is primarily determined by their photonic component and the LP lifetime can be estimated as:

$$\tau_{\mathrm{LP}} = \hbar/\gamma_{\mathrm{LP}} \approx \hbar/(|C|^2\gamma_c) \approx \tau_c/|C|^2 \,. \tag{2.50}$$

Typical values for photon and polariton lifetimes are of the order of tens of ps, although very long lifetimes around ~200 ps are possible in high-Q microcavities [81]. Conservation of energy, momentum, and phase dictates that polaritons decay via photon emission with the same $k_{||}$ and total energy $\hbar\omega = E_{\mathrm{LP,UP}}$ [40]. Therefore, the internal polariton mode and the externally out-coupled light are directly related to each other, facilitating experimental access to polariton energy dispersion via optical spectroscopy.

2.3.3 Excitation

The first step in any experimental study on polariton physics is the creation of polaritons. In general, this can be achieved primarily by resonant [82] or non-resonant [81, 83, 84] optical pumping, as well as by electrical injection [85, 86]. Here, only non-resonant pumping is reviewed since it is the only pumping method used in this thesis. A complete discussion is presented in Chapter 8 of Ref. [47].

In the case of non-resonant optical pumping (See Fig. 2.9), the pumping laser is blue-detuned to an energy above the stopband of the DBRs, typically to the first or second Bragg mode (See Section 2.2.4). Therefore, no direct excitation of polaritons is achieved. Instead, the laser energy is converted into a population of free, hot electron-hole pairs, which self-thermalise in ps time scales to the high-$k_{||}$ of the LP branch via the emission of longitudinal optical phonons. There, the peculiar shape of the dispersion relation plays a critical role in the polariton relaxation dynamics [47].

Specifically, LP-LP scattering due to Coulomb exchange interactions of the LP's excitonic component thermalises the polariton gas. Such polariton-polariton interactions strongly affect polariton relaxation but do not dissipate energy. Instead, a dissipative cooling mechanism for the polariton gas is provided via the emission of longitudinal acoustic phonons. This cooling happens efficiently down to momenta such that the detuning between the exciton and photon modes is of the order of the Rabi splitting, where the photonic component of LPs becomes more prominent. At this momentum, the polariton lifetime is greatly reduced, so less time is available for cooling. Simultaneously, the decreasing excitonic component reduces the phonon density of states, thus making the cooling less efficient. These effects lead to an accumulation of polaritons at the k-space region around the inflexion point of the LP dispersion owing to a relaxation time towards low momentum states typically one order of magnitude larger than the polariton

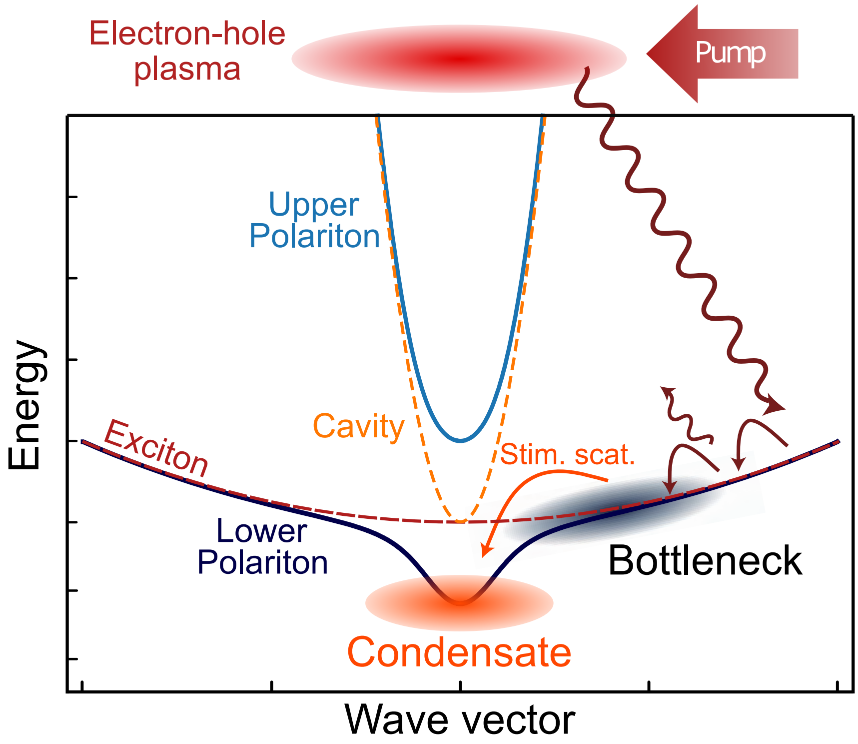

Figure 2.9: Schematic illustration of the polariton relaxation process after non-resonant pumping. The pump laser initially excites high-energy excitons (red cloud), which cools via phonon emission towards the bottleneck region (black cloud). Excitons in the bottleneck region then scatter into the condensate (orange cloud) via stimulated scattering. Adapted from Ref. [68].

lifetime at this point [47, 68]. This phenomenon is termed as the *bottleneck effect* [87–89].

The bottleneck effect can be overcome via final-state stimulated scattering, an effect originating from the bosonic nature of polaritons, where the presence of N particles in a final quantum state enhances the scattering rate into the final state by a factor $N + 1$ [40, 68]. If the pumping power is increased sufficiently enough, final state stimulation can significantly accelerate the relaxation of polaritons towards the low-momentum states and overcome the relaxation bottleneck [40, 90]. The first experimental demonstration of bosonic stimulation in a polariton system was the optical parametric amplifier [91]. Also, final-state stimulation is the underlying process of gain in lasers, where the macroscopic occupation of photons in the lasing mode stimulates the emission of more photons into it [40].

As a final remark, note that the “smoking gun” for the demonstration of polariton condensation, introduced in a following section (See Section 2.4.3), is the spontaneous build-up of coherence in the condensate as a result of spontaneous symmetry breaking [26]. Therefore, the coherence of the pump laser needs to be washed out of the final, relaxed polariton population to demonstrate the emergence of coherence as a result of condensation. This is achieved through non-resonant pumping as the initial coherence of the pump is lost after the multiple scattering interactions until polaritons reach the bottom of the LP branch [92].

2.4 Polariton Condensation

Polaritons are composite, weakly interacting quasiparticles known to behave as *good bosons* at sufficiently low densities [90, 91, 93]. Therefore, polaritons are suitable candidates for realising solid-state Bose-Einstein condensation (BEC). Additionally, since the polariton effective mass at the bottom of the LP dispersion branch is about four to five orders of magnitude smaller than that of the bare exciton and about eight orders of magnitude smaller than the mass of a Rubidium atom, polariton condensation at temperatures much higher than for the case of atomic BEC is achievable [40].

The following section introduces the topic of polariton condensation, starting with a discussion on the general concept of BEC in Section 2.4.1 followed by a short history of BEC in Section 2.4.2. The unique properties of polariton condensates are then discussed, starting with the experimental signatures (Section 2.4.3) and the differences with atomic BECs and photon lasers (Section 2.4.4). The next section introduces the generalised Gross-Pitaevskii equation as a tool for the theoretical description of polariton condensates (Section 2.4.5), followed by a discussion on polariton coherence (Section 2.4.6). Finally, several techniques commonly used for polariton potential landscape engineering are reviewed in Section 2.4.7.

2.4.1 Bose-Einstein Condensation

The term Bose-Einstein condensation (BEC) refers to a phase transition in which an incoherent (possessing no phase relation) ensemble of bosons “condenses” into a highly-ordered macroscopic quantum state. This state, termed *Bose-Einstein condensate*, exhibits long-range coherence as the individual bosons have the same relative phase, and the overall system is described by a single macroscopic wavefunction.

BEC occurs when a large number of bosons, initially possessing no phase relation, all become coherent once a system parameter, such as temperature or density, crosses a threshold. The physical mechanism underlying the formation of a BEC is qualitatively illustrated in Fig. 2.10. In a simplified picture, individual bosons in an ensemble may be regarded as quantum-mechanical wavepackets with an extent of the order of their thermal de Broglie wavelength $\lambda_{\mathrm{dB}} = h/p$, where p is the boson’s momentum. At high temperatures or, equivalently, low densities, the

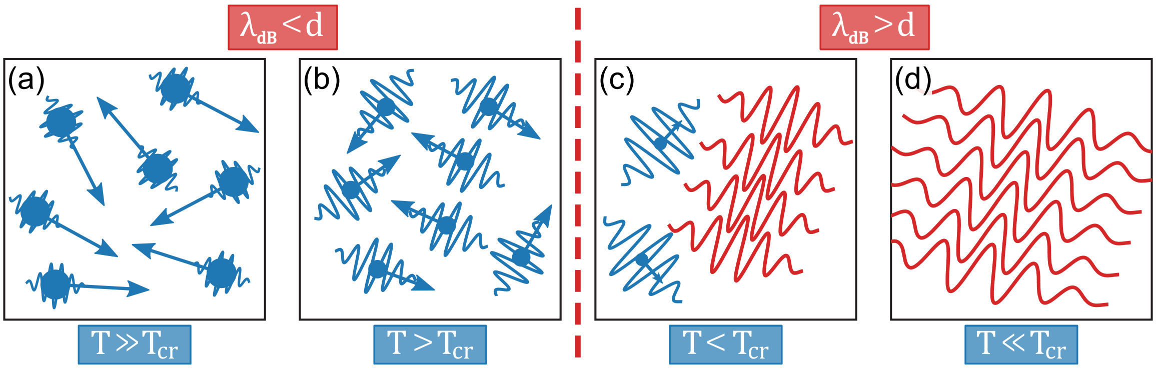

Figure 2.10: Schematic illustration of the Bose-Einstein condensation process. As the temperature of the system is lowered (a → d), the wave nature of the bosons in (d) dominates over the particle properties in (a). Below the threshold temperature T_{cr} (red dashed line), the individual matter waves overlap, leading to the emergence of a common phase in the system. A coherent matter cloud is formed in the lowest energy state of the system, the Bose-Einstein condensate (red curves). Adapted from Ref. [80].

ensemble of bosons behaves like a classical ideal gas comprising bosons with well-defined trajectories and large momenta. As the temperature is lowered, the individual bosons lose kinetic energy, and their spatial position becomes less and less well-defined. In other words, their de Broglie wavelength increases, and their bosonic wave nature becomes progressively more prominent. When cooled below a critical temperature T_{cr}, the system exhibits a transition from a classical gas to a BEC, where the individual bosons are sufficiently delocalised to overlap with each other, and consequently, their phases become correlated. This transition to condensate is evidenced by the build-up of a macroscopic, coherent matter wave [94] and is associated with the appearance of a macroscopic condensate order parameter $\psi(\mathbf{r})$, which has a nonzero mean value [47]:

$$\langle\psi(\mathbf{r})\rangle = \sqrt{\rho_{\text{cond}}(\mathbf{r})}e^{i\theta(\mathbf{r})}, \tag{2.51}$$

where $\langle\psi(\mathbf{r})\rangle$ is the order parameter for this phase transition. It is a complex number with an amplitude - the square root of the condensate density ρ_{cond} - and a phase θ. Note that the BEC transition spontaneously breaks the system's symmetry since the condensate phase is randomly selected and is fixed throughout the whole condensate [47].

2.4.2 Short History of BEC

The history of Bose-Einstein condensation started with the seminal work of Satyendra Bose and Albert Einstein in the mid-1920s [95, 96]. In 1925, after generalising Bose's work on the statistics of a monoatomic ideal gas, Einstein predicted that, at sufficiently low temperatures, a gas of a certain type of identical integer-spin particles, now called bosons, would condense into the system's lowest energy state - a phenomenon now termed *Bose-Einstein condensation* [97]. It is one of the fundamental consequences of quantum mechanics that leads - among others - to significant phenomena like superfluidity and superconductivity. In the following decades, a lot of effort was put into achieving BEC in various systems. However, the experimental verification of Einstein's prediction proved a challenging task, requiring decades of experimental efforts. The main problem associated with realising BEC is achieving quantum degeneracy, i.e. cooling or "densifying" a boson gas until the matter waves begin to overlap and form a coherent condensate. Analytic expressions for the critical temperature T_{cr} and density ρ_{cr} are derived in most standard quantum mechanics textbooks on the topic [97, 98]. For the purpose of this thesis, it suffices to say that the critical temperature for BEC for an ideal (non-interacting and at thermal equilibrium) bosonic gas in three dimensions occurs when:

$$\rho \lambda_{\mathrm{dB}}^3 = 2.62\,, \tag{2.52}$$

where ρ is the density of bosons and λ_{dB} the de Broglie wavelength, which can be written as:

$$\lambda_{\mathrm{dB}} = \sqrt{\frac{2\pi\hbar^2}{m k_{\mathrm{B}} T}}\,, \tag{2.53}$$

where m is the mass of the bosons, k_{B} is Boltzmann's constant, and T is the temperature [68]. This criterion can intuitively be thought of as that BEC phrase transition occurs either by increasing the density of particles at a constant temperature or reducing the temperature of an ensemble of particles at a given density. By combining Eqs. 2.52 and 2.53 and solving for T, we can derive an expression for the critical temperature T_{cr}:

$$T_{\mathrm{cr}} = \frac{2\pi\hbar^2}{k_{\mathrm{B}} m}\left(\frac{\rho}{2.612}\right)^{2/3}. \tag{2.54}$$

The mass dependence of T_{cr} indicates that (for a fixed density ρ) it is easier to produce Bose-Einstein condensates for light mass particles [26, 68]. Consequently, atomic BEC requires temperatures below 1 μK owing to the comparatively high particle mass involved ($\sim 10^3 m_e$). With the advent of laser cooling and magneto-optical trapping, the first unambiguous experimental realisation of BEC came in 1995, seven decades after the theoretical formulation, in two different atomic systems. The first condensate was reported by Eric Cornell and Carl Wieman's team in a very dilute and cold rubidium atomic gas at a temperature of 170 nK [99]. Later the same year, Wolfgang Ketterle and colleagues produced a BEC in a gas of sodium atoms cooled to ∼2 μK [100]. For their pioneering work in achieving BEC in dilute gases of alkali atoms and early fundamental studies of the properties of the condensates, Eric Cornell, Wolfgang Ketterle and Carl Wieman were jointly awarded the Nobel Prize in Physics in 2001 [101].

The prediction of BEC was preceded by the discovery of superconductivity by K. Onnes in 1911 [102]; however, the relationship between the two phenomena was properly understood much later, after the developments of the Bardeen, Cooper, and Schiffer (BCS) theory in the 1950s [103]. Superconductivity is nowadays understood as a Bose-Einstein condensation of the so-called Cooper pairs, which are bound states of two electrons with a total spin of 0 or 1 [47, 97]. Bose-Einstein condensation is also linked with the phenomenon of superfluidity, first reported in Helium-4 by P. Kapitza in 1938 [104]. A few months after this discovery, F. London first proposed the interpretation of this phenomenon as a manifestation of BEC [105].

Starting from the 1960s, the search for BEC in solid-state systems, particularly semiconductor excitons, received significant attention. Excitons were known to behave as weakly interacting Bose[7] gases at low densities and low temperatures and are, therefore, good candidates for observation of BEC. Owing to their light effective mass ($\sim 10^{-1} m_e$), the critical temperature is expected in the range of mK to a few Kelvin, about six orders of magnitude higher than the critical temperature for atomic BEC. The idea was independently proposed by Moskalenko [106] and Blatt et al. [107] in 1962 and was followed by a large number of theoretical and experimental works on excitonic condensation and superfluidity. Several publications reported condensation in excitonic systems such as biexcitons in CuCl [108, 109] and CuBr [110], excitons in Cu_2O [111–113] and indirect excitons in coupled QWs [114, 115]. However, none of these reports has been accepted as unambiguous evidence of excitonic BEC [116, 117].

A new candidate system for high-temperature Bose-Einstein condensation became available in 1992 when Weisbuch et al. [76] observed strong coupling between light and excitons in a semiconductor microcavity. Experiments such as the parametric scattering [91] have demonstrated that polaritons behave as good bosons up to densities large enough to obtain quantum degeneracy and despite of their composite nature. Additionally, microcavity polaritons, owing to their low effective mass ($\sim 10^{-5} m_e$) - inherited from the photonic component -, were expected to form Bose-Einstein condensates at elevated temperatures, easily achieved with standard cryogenic techniques and even up to room temperature. These reasons make microcavity polaritons as ideal candidates for the observation of BEC in solids. This idea was put forward by A. Immamoglu et al. [118] and was experimentally demonstrated a decade later in a CdTe-based microcavity with the seminal publication of J. Kasprzak et al. [83]. There, the authors reported various experimental signatures of BEC above a critical density, mainly massive occupation

---

[7] Exciton, as quasi-particles consisting of two fermions, always have an integer total spin ($S = 0$ or 1).

of the ground state ($k_{||} = 0$), narrowing of the momentum distribution, increase in temporal and long-range spatial coherence accompanied by linear polarisation build-up. The condensate formed at a temperature of 19 K, which is six to nine orders of magnitude larger than atomic BECs, as expected. This work has sparked the interest in polaritons as a suitable system to study the physics of dilute Bose gases. Since them, polariton condensates have been used to study a plethora of fundamental physical phenomena like superfluidity [27, 119], quantised vortices [28, 120], solitons [121, 122], optical Josephson oscillations [123], long-range spatial and temporal coherence [83, 124], and polariton fluids in lattices [25, 125, 126].

Additionally, polariton condensation and related phenomena have been demonstrated in a wide variety of material systems, such as inorganic semiconductors (e.g. GaAs [81, 124, 127–129], CdTe [83], GaN [130–132], ZnO [133, 134]) organic materials (e.g. conjugated polymers [135], biologically produced fluorescent proteins [136], molecular dyes [137], transition metal dichalcogenides [138], and perovskites [139]. In fact, condensation up to room temperature has been reported [131, 140]. It is worth noting that the observation of BEC in optical microcavities has not been limited to light-matter systems in the strong-coupling regime. Indeed, Bose-Einstein condensation of photons in an optical microcavity was reported by Klaers et al. in 2020 [141]. Lastly, polaritons are not the only solid-state quasi-particle system in which condensation has been realised as magnon condensation has been reported in ferromagnetic insulators [142–144].

2.4.3 Experimental Signatures of Polariton Condensation

Polariton condensation is the appearance of long-range spatial order in a cloud of polaritons. A typical experiment on polariton condensation involves non-resonant pumping at energies above the exciton, creating an initial population of dark excitons that subsequently relax into polariton states (See Section 2.3.3). The basic idea of condensation refers to the macroscopic occupation of a single quantum mechanical state. A polariton condensate exhibits distinct signatures related to the specific properties of polariton condensates, some of which coincide with those of atomic BECs, while others differ. A general criterion for BEC was proposed by Penrose and Onsager [145], based on the single-particle density matrix, $\hat{\rho}(\mathbf{r},\mathbf{r}') = \langle\hat{\psi}^\dagger(\mathbf{r})\hat{\psi}(\mathbf{r}')\rangle$ [47, 97]. The criterion states that the presence of the condensate is shown by the off-diagonal elements of the system's density matrix approaching a constant, nonzero value as $|\mathbf{r}-\mathbf{r}'| \to \infty$:

$$\langle\hat{\psi}^\dagger(\mathbf{r})\hat{\psi}(\mathbf{r}')\rangle \to \rho_0 \,, \tag{2.55}$$

where $\hat{\psi}^\dagger(\mathbf{r})$ and $\hat{\psi}(\mathbf{r})$ are the creation and annihilation bosonic field operators at a point $\mathbf{r}$ and n_0 is the density of the macroscopically occupied state. This criterion, often referred to as *off-*

diagonal long-range order, is directly related to the macroscopic occupation of a single-particle state. In a simple picture, it can be interpreted as follows: in a condensate, the annihilation of a particle at position $\mathbf{r}$ and the creation of a particle at $\mathbf{r}'$ is coherent, even when the points $\mathbf{r}$ and $\mathbf{r}'$ are separated arbitrarily far apart. In contrast, this process would be incoherent in a normal liquid except when $\mathbf{r}$ and $\mathbf{r}'$ are close together [97]. Experimentally, this criterion corresponds to extended spatial first-order coherence $g^{(1)}(r)$ across the condensates above threshold, but short-range correlations below threshold [68]. Measuring spatial correlation functions requires a variant of the Michelson or Mach-Zender interferometer (See Section 2.4.6), as confirmed by Refs. [83, 146].

Moreover, a strong spectral narrowing of both the energy and k-space distributions is expected in the emission from the system above the critical excitation density, signalling the macroscopic occupation of a quantum state and spontaneous formation of a coherent phase. The reduced linewidth and k-space distribution indicate increased temporal coherence. The corresponding temporal correlation function can be measured using a standard Michelson interferometer.

Another signature of polariton condensation is given by measuring the power dependence of the microcavity-PL emission [147–150]. The total emitted light is recorded as a function of the pump power and is typically presented in a double-logarithmic scale, as in the example of Fig. 2.11(a). The resulting curve is characterised by three distinct regimes. The low-power regime corresponds to the sub-threshold polariton PL, where the polariton emission signal increases linearly with the pump power. A condensate is formed at the threshold-power P_{th} when the system reaches its critical density. This transition is manifested as a strongly non-linear response of the emission intensity, marked by the onset of stimulated scattering into a single condensate state. At pumping powers considerably above the condensation threshold, a second transition occurs at a threshold P_{ph}, where strong coupling is lost, and the system enters the regime of conventional photon lasing. There, the emission is still coherent but originates from the bare cavity mode instead of the bottom of the LP branch. This transition to the weak coupling regime, marked by another non-linear increase in PL emission, originates from the increased Coulomb screening and the subsequent diminishing of the exciton oscillator strength due to the onset of the Mott transition (See Section 2.1.2). Note that these transitions can also be observed in the E-$k_{||}$ dispersion curve [See Fig. 2.11(b)], where emission from a polariton condensate can be differentiated from photon lasing if it appears on the blue-shifted LP branch, as opposed to the uncoupled cavity parabola at even higher energy.

A third indicator commonly used to prove the formation of a polariton condensate is the observation of a strong degree of polarisation in the microcavity emission above threshold. As outlined in Section 2.4.1, an uncondensed polariton population possesses no long-range coherence

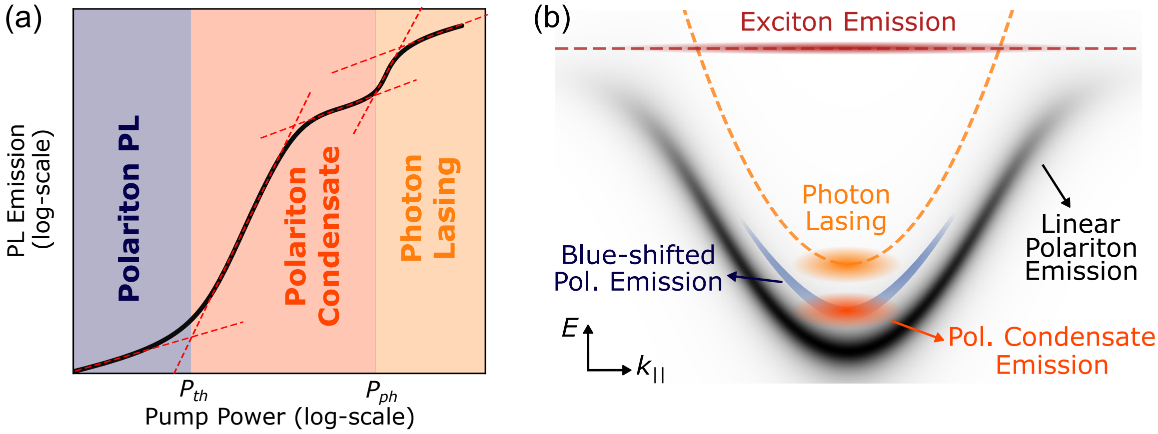

Figure 2.11: (a) Power dependence of the PL emission of a non-resonantly pumped microcavity, where two thresholds can be identified as power increases: first, the condensation threshold (blue to orange), followed by the photon lasing threshold (orange to yellow). Red dashed lines are guides to the eye, illustrating where the emission grows linearly with the pump. (b) Dispersion curves illustrating the spectral differences between polariton condensation and photon lasing in an E-$k_{||}$ diagram. Condensate emission originates from the blue-shifted LP branch (orange cloud), whereas photon lasing stems from the bare cavity mode (yellow cloud). Adapted from Ref. [80].

as individual polaritons are uncorrelated with each other, and their phases are chosen randomly. Therefore, the overall degree of polarisation is expected to average to zero. On the other hand, a condensed fraction should be described by a single wavefunction and a stationary phase across the whole condensate. As a result, the polarisation of all emitted photons should be identical, leading to condensate emission with a strong degree of polarisation. Polaritons in quantum-well microcavities have two projections of their total angular momentum along the growth axis of the structure, $J_z \pm 1$ (spin-up or spin-down), which correspond to right- and left-circularly polarised photons emitted by the cavity, respectively. Under linear excitation, the populations of spin-up and spin-down reservoir excitons are balanced. In perfectly isotropic cavities, an initially spin-balanced exciton reservoir is expected to give a condensate with a stochastic linear polarisation due to spontaneous symmetry breaking. The orientation of the linear polarisation would be chosen spontaneously by the system and would randomly change between different realisations of the experiment [92]. However, linear polarisation is generally pinned to one of the crystallography axes, and a fixed polarisation angle is observed in most real cavities [83, 127].

2.4.4 Polariton Condensates, Atomic BECS, and Photon Lasers

Despite the similarities in the underlying physical mechanisms and concepts, polariton condensates significantly differ from their atomic counterparts in a number of aspects. One of the most significant differences between a polariton condensate and an atomic BEC is that the former is not in thermal equilibrium, which is an essential property of BEC. Microcavities are open systems as polaritons have a finite lifetime (of the order of ps), after which they decay as externally emitted photons. Therefore, continuous external pumping is required to maintain a condensate population for an extended period of time. A non-equilibrium steady state of continuous decay and replenishment arises, yielding a dynamical quasi-equilibrium condensate and has to be accounted for in any theoretical treatment of the system [151, 152]. Small intensity fluctuations in the pump laser can be transferred to and amplified in the condensate. Specifically, a fluctuating pumping intensity will lead to variations in the condensate population and hence the blueshift potential. The latter affects the energy of the condensate and hence its temporal coherence (See Section 2.4.6). Therefore, a stable and single-mode laser should be ideally used for pumping and to improve temporal stability [153].

Exciton-polariton condensates form in effectively two-dimensional structures, as opposed to the three-dimensional atomic BEC. The reduced dimensionality further complicates the situation. In a uniform two-dimensional Bose gas, true long-range order associated with Bose-Einstein condensation is precluded at any finite/nonzero temperature [154]. However, if a Bose gas is further confined within the two-dimensional plane, for instance, due to some form of potential trap, then the possibility of BEC is recovered [155, 156]. In this case, one often speaks of a finite-sized condensation. A more thorough discussion on this topic can be found in Chapter 8 of Ref. [47].

Another important distinction between polariton condensates and atomic BECs is that polaritons are interacting bosons. The ability to interact, stemming from their exciton component, renormalises the polariton dispersion, leading to a continuous *blueshift* to higher emission energies as the polariton density increases [81, 157].

A condensate of polaritons behaves as a weakly interacting Bose gas when the density is low. At high densities, polaritons lose their bosonic character due to excitons undergoing a Mott transition to a fermionic electron-hole plasma [51, 158] (See Section 2.1.2). The increased Coulomb screening due to fermionic exchange interaction decreases the oscillator strength and deteriorates the coherence properties of the condensate [159].

Owing to their photonic component, the experimental requirements for probing the macroscopic condensate wavefunction are significantly better for polariton condensate. Indeed, coherence measurements of polariton condensates are much easier than the ones with atomic BECs. Polaritons decay by leaking outside the DBR mirrors, emerging as photons carrying the same energy, momentum, and phase as the polaritons in the cavity. The energy can be measured by spectroscopic means, while the momentum can be found from the angular direction of the photon propagation. Therefore, the condensate cloud can be imaged directly, with full access to the k-space dynamics.

Another key distinction is that, by definition, atomic BECs are formed by the macroscopic occupation of a single quantum state, namely the ground state of the system. On the other hand, macroscopic coherence in a quantum fluid of polaritons can arise at the ground state ($k_{||} = 0$) as well as states with higher energy ($k_{||} > 0$). Interestingly, multiple polariton states can show coherence simultaneously [160–163] and even in the same spatial location [164].

The term *polariton condensate* is often used in literature, instead of *polariton BEC*, to emphasise the specific properties of macroscopic quantum states based on polaritons compared to atomic BECs. This convention is adopted for the remaining of this thesis.

A second careful distinction needs to be made between polariton condensates and photon lasers. VCSELs in particular, are heterostructure devices typically comprising a set of QWs embedded in a high-quality cavity formed by DBR mirrors. Therefore, VCSELs are structurally identical to microcavities commonly used for polariton condensation studies. In a standard VCSEL, electrons and holes act as the gain medium, and lasing occurs via population inversion. Coherent light is emitted by the stimulated emission mechanism, where the light in the cavity is amplified by the recombination of electron-hole pairs [68]. They are, therefore, open systems that require continuous pumping to support the electron-hole population, just like polariton condensates. Additionally, they show threshold behaviour, an increase of first-order coherence, appearance of spatial order and linewidth narrowing, characteristics shared with polariton condensates [26]. These similarities pose the question of whether condensation of polaritons is the same as photon lasing.

The key difference between a photon laser and polariton condensate is the absence or presence of strong coupling [68]. This can be verified by studying the dispersion curve of the system. An example is provided in Fig. 2.11(b), where the various emission mechanisms present in a microcavity system are illustrated. Photon lasing corresponds to coherent light emission from the bare uncoupled cavity mode (shown in yellow), located at an energy higher than the LP branch. Similarly, exciton emission originates from the exciton line (red) and proves that the system is in the weak coupling regime.

In contrast, coherent photoluminescence from a polariton condensate stems from the state at which the condensate is formed, usually the bottom of the LP curve (shown in orange). Note that lower polaritons experience repulsive interactions, and the energy of the low momentum states (near $k_{||}$) is expected to increase with increasing pumping power. However, near the threshold, the blueshift of the lower polariton is much smaller than the Rabi splitting, and the excitations of the system are indeed polaritons. In summary, emission from a polariton condensate can be differentiated from photon lasing if it originates from the blue-shifted LP curve, as opposed to the uncoupled cavity branch at even higher energy.

Additionally, the pump power dependence of the emission intensity shows a transition from an uncondensed polariton population to a polariton condensate followed by the photon lasing regime, as discussed in Session 2.4.3. The observation of two thresholds is often used as proof that the first one is associated with polariton condensate.

As a last remark, note that the conventional lasing condition in semiconductors is the so-called *Bernard-Durraffourg condition* for population inversion [165]. Laser-like emission by the polariton condensate occurs at particle densities orders of magnitude below the Bernard-Durraffourg density (similar to the Mott density), thus reducing the power consumption of the microcavity [26]. This explains the attractiveness of polariton lasers as a source of coherent light with an ultra-low operation threshold [166].

2.4.5 Theoretical Description of Polariton Condensates

The dynamics of polariton condensates and their non-equilibrium character can be described theoretically by the so-called generalised Gross-Pitaevskii equation (GPE), a type of non-linear Schrödinger equation. The non-linearity accounts for polariton self-interactions, whereas pumping and dissipation terms are added to describe the gain and decay of the open-dissipative condensate [47].

One approach for describing the case of a non-resonantly excited condensate - which is the case most relevant for this work (See Section 2.3.3) - was initially proposed by M. Wouters and I. Carusotto [167] and later used under several versions [168–171]. The time evolution of the condensate order parameter $\psi(\mathbf{r}, t)$ is described by a non-linear second-order partial differential equation as follows:

$$i\hbar \frac{\partial \psi(\mathbf{r}, t)}{\partial t} = \left\{ -\frac{\hbar^2}{2m^*} \nabla_{\mathbf{r}}^2 + V(\mathbf{r}) + \frac{i\hbar}{2} \Big[R(\rho_R(\mathbf{r})) - \Gamma \Big] + \hbar \alpha_R \rho_R(\mathbf{r}) + \hbar \alpha |\psi(\mathbf{r}, t)|^2 \right\} \psi(\mathbf{r}, t) \, , \quad (2.56)$$

where m^* is the effective polariton mass and $V(\mathbf{r})$ an external potential [172]. The condensate decays with a polariton loss-rate Γ and is replenished at a gain-rate of $R(\rho_R(\mathbf{r}))$. The latter represents the stimulated scattering rate and is a monotonously increasing function of the reservoir density $\rho_R(\mathbf{r})$. The last two terms quantify the shifts in the condensate energy due to interactions between condensate and reservoir (with interaction constant α_R) as well as polariton-polariton interactions (with interaction constant α) [78, 167, 173].

The condensate evolution (Eq. 2.56) is coupled to a rate equation describing the dynamics of the incoherent reservoir. This rate equation describes the balance between the non-resonant pumping, the loss from the reservoir and stimulated scattering into the condensate states. It is given by:

$$\frac{\partial \rho_R(\mathbf{r},t)}{\partial t} = P_R(\mathbf{r}) - \gamma_R \rho_R(\mathbf{r}) - R(\rho_R(\mathbf{r}))|\psi(\mathbf{r},t)|^2 + D\nabla^2 \rho_R \,. \tag{2.57}$$

Here $P_R(\mathbf{r})$ is the gain-rate of the excitonic reservoir as a result of the non-resonant pumping and γ_R the reservoir loss. The last term in Eq. 2.57 parameterises the gain of the condensate due to the stimulated scattering from the excitonic reservoir into the lower polariton states. It is proportional to the condensate density $|\psi|^2$ due to stimulated scattering [168]. The last term describes the spatial diffusion of reservoir polaritons with a rate D [167] and is frequently omitted [168].

Note that a second approach for the theoretical description of non-resonant excitation has been proposed by Jonathan Keeling and Natalia G. Berloff [174], where the reservoir dynamics are not explicitly formulated. Instead, a saturable gain term is included directly in the GPE describing the evolution of the condensate. As this approach is not implemented for modelling the optically trapped polariton condensates in Chapter 4, it will not be presented here. More information is available in Ref. [174, 175].

2.4.6 Coherence

An important consequence of Bose-Einstein condensation is the appearance of coherence associated with the phase of the order parameter (Eq. 2.51). The macroscopic occupation of a single quantum state and the build-up of phase correlations among the condensed bosons give rise to long-term temporal and spatial coherence, which are considered key features of polariton devices.

Coherence can be described as a "*collection of correlations*" arising from the macroscopic multiparticle wavefunction of the condensate. In a classical picture, coherence measures the amount of perturbation - or noise - in a wave and describes the stability of the emitted light. Namely, coherence refers to the ability to infer a wave at remote locations, in space or time, from its knowledge at a given point [47]. The small size of the polariton condensate in the experiments of Chapter 4 makes it difficult to extract useful information about the decay of spatial coherence. Therefore, the rest of this discussion focuses on temporal coherence.

The quantitative description of coherence can be achieved through correlation functions, i.e., functions which specify the degree of correlation as a function of temporal (or spatial) distance [69]. The first-order coherence expresses the phase fluctuations of a light field $E(t)$, and, with that, the associated decrease in its ability to interfere. It is quantified by the first-order correlation function $g^{(1)}(t)$, defined by:

$$g^{(1)}(t) = g^{(1)}(t', t'+t) = \frac{\langle E^*(t')E(t'+t)\rangle}{\langle |E(t')|^2\rangle}\,. \tag{2.58}$$

The symbol $\langle ...\rangle$ indicates an average over a long time interval. $g^{(1)}(t)$ describes the degree of first-order temporal coherence between the electric fields at two times separated by a time delay t, and takes the values $0 \leq |g^{(1)}(t)| \leq 1$ for all light sources. $g^{(1)}(t)$ is called the first-order correlation function because it is based on the properties of the first power of the electric field [69].

According to Eq. 2.58, $g^{(1)} = 1$ at zero time delay in all cases. However, its evolution is highly dependent on the degree of coherence of the source. The idealised scenario of a perfectly coherent source is characterised by $|g^1(t)| = 1$ for all values of t. On the other hand, a perfectly incoherent source displays $|g^1(t)| = 0$. Between these two extremes, partially coherent light sources exhibit a decay in $g^{(1)}(t)$ from 1 to 0 over a time scale of the order of the so-called *coherence time* τ_c. The coherence time is defined as the maximum relative time delay that two interfering waves can have so that they still display interference. A general formula for the coherence time of a wave of spectral width $\Delta\lambda$ centred about a wavelength λ is given by:

$$\tau_c = \frac{\lambda^2}{c\Delta\lambda} \approx \frac{1}{\Delta\omega}\,, \tag{2.59}$$

where λ is the central wavelength of the source, $\Delta\lambda$ and $\Delta\omega$ are the spectral width of the source in units of wavelength and angular frequency, respectively [47]. The result in Eq. 2.59 shows that the coherence time is determined by the spectral width of the light. A perfectly monochromatic source with $\Delta\omega = 0$ has an infinite coherence time, or equivalently perfect coherence, while the white light emitted by a thermal source has a very short coherence time. Most importantly, Eq. 2.59 explains the emergence of high coherence in a polariton condensate as a result of the spectral narrowing observed at threshold.

Coherence correlations can be extended up to arbitrary orders [176]. While the first-order coherence function $g^{(1)}(t)$, which is the correlator of field amplitudes at different times (Eq. 2.58), reflects the coherence of the emitted light, its second-order counterpart quantifies intensity correlations and gives insights into emission statistics. Higher-order correlation functions describe still more subtle details and are out of the scope of this thesis.

As mentioned in Section 2.4.3, the reduced linewidth and k-space distribution above threshold indicate increased temporal and spatial coherence in the condensate phase. Probing coherence requires interferometry to measure the first-order field correlation function. Since the emitted photons preserve the phase information of the polariton condensate, interferometric measurements can be performed on the emitted light from the cavity.

Specifically, the first-order (temporal) correlation function $g^{(1)}$ can be measured by overlapping the real-space image of the polariton emission spot with its reflected version in a standard Michelson-interferometer setup [83]. The simplest version of a Michelson interferometer, schematically illustrated in Fig. 2.12(a), consists of a 50:50 beam splitter (BS) and two mirrors, M1 and M2, one at each of the two so-called arms of the interferometer. Emitted light from the microcavity is incident on the beam splitter, where it is divided and directed towards the two mirrors. The light reflected off M1 and M2 recombines at the BS, producing an interference pattern at the output port where a detector, such as a CCD camera, is placed. The path length of one of the arms can be varied by translating one of the mirrors (say M2) in the direction parallel to the beam [69]. Changing the length of one arm of the interferometer results in a relative phase shift between the two split beams. Since the two recombined beams project the mirrored images of the emitter on the detector, the intensity measured at one particular pixel shows a sinusoidal modulation as a function of the arm's movement determined by the phase relation at that point. Using such data, one can extract the phase difference between the overlapped images at a particular pixel point as well as the fringe visibility. The latter quantity is proportional to the first-order correlation function [173]. By continuously varying the length of the moving arm, or equivalently, the time delay t between the two beams, the modulation of intensity can be recorded for each pixel based on the temporal coherence of the condensate emission.

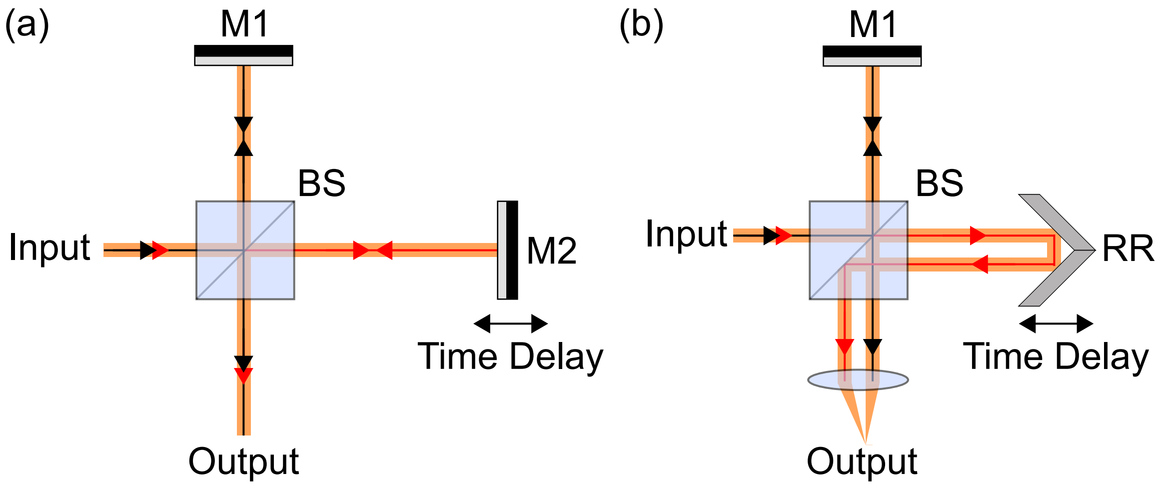

Figure 2.12: (a) Schematic illustration of a typical Michelson interferometer setup. The apparatus consists of a 50:50 beam splitter (BS) and two mirrors, M1 and M2. Interference fringes are observed at the output port as the length of one of the arms (arm 2 in this case) is varied. (b) By replacing the mirror M2 (the mirror in the moving arm) with a retroreflector (RR), this interferometric setup can be used to measure spatial correlations.

Measuring spatial correlation functions usually requires a variant of the Michelson interferometer [See Fig. 2.12(b)]. Specifically, the Michelson interferometer is modified by replacing the mirror in one arm with a retroreflector, which inverts the image so that each point $\mathbf{r}$ of the interferogram is related to the correlation function between the field at $\mathbf{r}$ and $\mathbf{r}' = -\mathbf{r}$ [83]. For the emission from a polariton condensate, this leads to correlation effects between different spots across the emission spot, as outlined by the Penrose and Onsager criterion (See Section 2.4.3). The correlation function is then obtained via the fringe visibility [177, 178]. For the spatial distribution of visibilities, only interference data at $t = 0$ is of interest. Additionally, spatial correlation functions can be measured using a Mach-Zender interferometer or its variants [179, 180]. All experiments presented in Chapter 4 involve a microcavity structure consisting of multiple QWs. The treatment of such systems is the same as a single-well system, as coherence between multiple wells is established via the cavity mode.

Since a polariton condensate emits coherent light, it is of interest to characterise this coherence. The emergence of temporal coherence was interpreted as a signature of condensation in the first demonstration of polariton condensation [83]. There, the authors reported a significant spectral narrowing in the polariton emission accompanied by an increase in coherence time from 1.5 ps to 6 ps as the system entered the condensed phase. A similar observation was reported a year later for a polariton condensate in a trap [127]. Both studies used a multi-mode laser excitation, which induced fluctuations of the energy of the condensate, thus broadening its linewidth. The reduction of intensity noise in the pump laser revealed a Gaussian decay of $g^{(1)}(t)$ with an improved coherence time of $\sim$150 ps [153]. Additionally, the temporal decay in a polariton laser with shot-noise-limited intensity stability displayed a transition from exponential to Gaussian with increasing condensation population, attributed to strong interactions within the condensate [181]. Recently, we demonstrated temporal coherence beyond 1 ns in an optically trapped polariton condensate, spatially decoupled from the decoherence-inducing exciton reservoir [124]. Besides temporal coherence, many publications report on spatial coherence in a variety of materials and structures [146, 177, 179, 182].

2.4.7 Polariton Potential Landscape Engineering

Significant experimental efforts have been directed towards engineering efficient and non-destructive potential landscapes for polaritons and polariton condensates. The possibility of engineering polariton trapping potentials is a key to controlling, shaping, and directing the flow of polariton within the cavity, in addition to tuning the overall spectral properties of the emission. Therefore, sophisticated potential landscapes are of high importance for optoelectronic applications, such as highly nonlinear photonic integrated circuits and polariton logic elements [183, 184], as they allow for the manipulation of polariton populations on a chip. Moreover, polariton confinement has triggered the interest in using polariton systems for fundamental studies, including the interaction between multiple spatially separated condensates in a lattice and quantum emulation of complex many-body phenomena, such as the physics of high-temperature superconductors, graphene, or frustrated spin lattices [185–187].

Several techniques have been implemented to engineer potential landscapes for polaritons. Being hybrid light-matter quasiparticles, polaritons can be confined via their excitonic as well as photonic component, which leads to a wide range of highly complementary trapping techniques. Here some of these techniques are briefly presented. A more comprehensive review can be found in Ref. [188].

One of the first techniques used for tuning the energy of the exciton mode is the application of mechanical stress by pressing a sharp metal tip of radius ∼50 μm against the microcavity. The compressive strain locally affects the energy of the QW exciton via the stress-depending bandgap. This induces a parabolic potential for QW excitons, which, in turn, creates a potential minimum for polaritons [127, 189]. The implementation of this technique led to the first demonstration of polariton condensation in a trap by Balili et al. [127].

A somewhat similar technique, that also exploits a modification of the local strain, is modulation with surface-acoustic waves (SAWs). The application of SAWs creates a periodic modulation of the exciton energy due to the periodic deformation in the crystal, as shown in Fig. 2.13(a). As a result, this periodic modulation is responsible for folding of the polariton dispersion along the SAW propagation direction and allows for the controlled transport of polariton in the QW plane. Note that the application of SAWs also affects the photonic component of polaritons by modifying the thickness and refractive index of the cavity layer, but the amplitude of the energy shift is weaker compared to the excitonic component [188]. This method has been used for realising polariton condensation in 1D and 2D dynamical acoustic lattices [190–192].

Electrostatic trapping is another set of techniques which rely on applying electric fields to semiconductor QWs to tune the exciton energy via the quantum confined Stark effect (QCSE). A major advantage of electrostatic trapping is the ability to dynamically tune the polariton energy by adjusting the external field; however, an intrinsic limit to the tuning range of the exciton energy is the carrier tunnelling out of the finite QW barriers. A possible scheme for the fabrication of electrostatic polariton traps involves the deposition of electrical contacts on top and bottom of the microcavity - for instance, in a Schottky [196] or conventional diode configuration, as shown in Fig. 2.13(b) [193]. In such devices, both red-shifts in polariton energy due to the QCSE [196] and blueshifts due to the reduction of the Rabi splitting[8] [193] have been reported. Additionally, electrostatic trapping has been successfully used to localise indirect excitons in

---

[8] The reduction of the Rabi splitting was caused by a tunnelling-induced charge buildup and fractional bleaching of QWs, which reduced the exciton oscillator strength

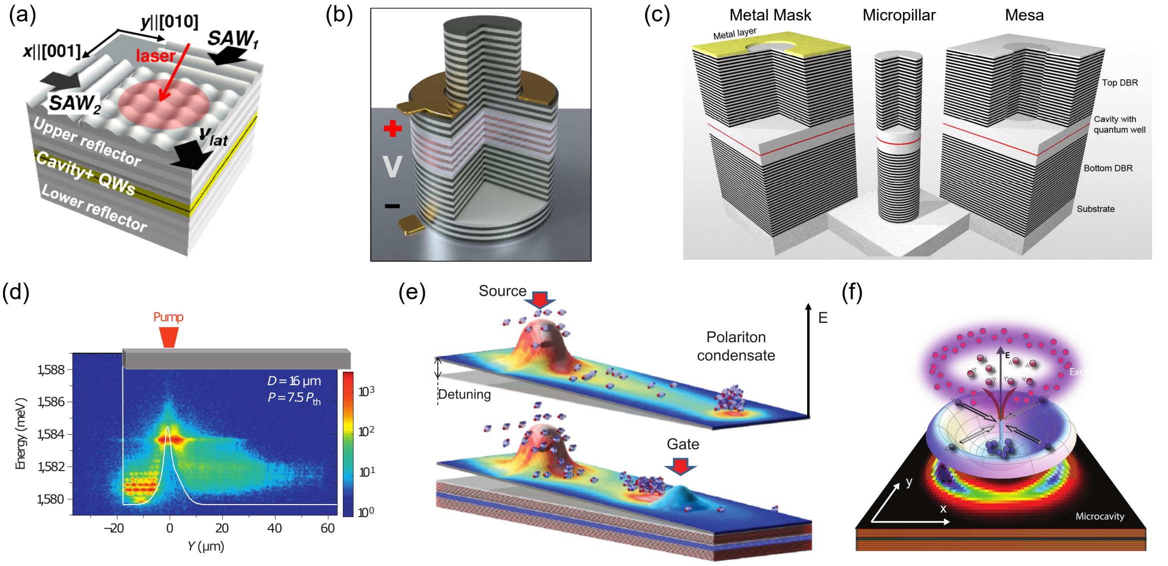

Figure 2.13: Examples of polariton potential engineering from the literature: (a) Surface Acoustic Waves [192], (b) electrostatic trapping [193], (c) depositing a metal mask (left panel), etching a micropillar (middle), and defining a shallow mesa in a cavity (right) [188], (d) 1D microwire [194], (e) all-optical polariton transistor [195], and (f) ring-shaped excitation laser spot [84]. All images are reproduced with permission from the corresponding sources.

coupled quantum wells and study cold exciton gases in the presence of confinement [197, 198].

Considerable research interest has been dedicated to developing methods that act not on the excitonic but on the photonic component of polaritons. One such approach is the so-called *metal mask* technique, where a patterned thin metallic layer is deposited onto the top DBR, as displayed in the left panel of Fig. 2.13(c). Effective photonic confinement is achieved as this layer changes the boundary conditions for the electromagnetic field with respect to the semiconductor-air interface, resulting in a modest shift in the energy of the optical resonance (typically on the order of 0.1-1 meV [188]). This simple yet efficient technique has been used to realise 1D and 2D periodic potential landscapes [125, 185, 186, 199].

A similar approach involves lithographical structuring to modify the cavity thickness locally. This is achieved during sample fabrication by patterning small mesa structures into the cavity layer before growing the top DBR. The buried mesas, schematically shown in right panel of Fig. 2.13(c), provide optical confinement that is sufficiently strong to localise polaritons with the advantage of stronger modulations of the polariton potential [200–203].

An alternative method for photonic confinement involves permanently modifying the microcavity by deep etching the microcavity through all its layers (top mirror, QW(s), and bottom mirror) down to the substrate, as shown in the middle panel of Fig. 2.13(c). This geometry creates “hard walls” for polaritons as the optical field is laterally confined by the semiconductor-air interface[9]. The main advantage of this method is scalability, as it enables the realisation of structures with almost arbitrary geometry, such as 1D and 2D channels, coupled pillar structures, and large-scaled honey-comb lattices [187, 194, 204, 205]. Moreover, this approach has already led to the first generation of polaritonic logic devices, including switches [195], interferometers [180], and tunnelling diodes [206].

Another set of techniques for photonic confinement is based on hybrid cavities, where the top and bottom mirrors are of different natures. One example involves replacing the top DBR mirror with a highly reflecting sub-wavelength high contrast grating, which is a broadband crystal mirror. In-plane optical confinement of polariton is achieved as strong coupling conditions can only be maintained underneath the finite-sized grating [207]. Another hybrid approach relies on open cavities, where the top mirror is a concave DBR deposited at the end of an optical fibre tip. The fibre is attached to piezo actuators, which allow for tuning of the physical cavity length, hence the cavity energy. Optical confinement is introduced through the concaveness of the DBR [208].

Lastly, there is a third approach to engineering the polariton potential landscape that does not target the underlying excitonic and photonic components. Instead, this approach relies on the direct polariton-polariton and polariton-exciton interactions. These interactions, which are usually repulsive in nature [172, 209, 210], renormalise the polariton dispersion, leading to a continuous blue shift to higher emission energies as the polariton density increases - an effect often referred to as the blueshift potential [81]. In the case of non-resonant optical excitation, a large cloud of high-energy excitons is formed in the vicinity of the pump spot, in addition to the resulting polariton density. This so-called exciton reservoir repels polaritons, driving them away from the location of their creation. A second effect is the direct self-repulsion among the condensed polaritons, which is manifested as a spreading of the wavefunction to fill out as much of the trap as possible while retaining good spatial overlap with the pump spot. Therefore, these repulsive interactions blue shift the entire polariton dispersion around the pump spot compared to areas of low polariton and exciton density. The gradient of the exciton density translated to a diminishing blueshift potential the polaritons experience as they move outwards and resulting in the formation of a radially expanding polariton condensate [194, 211, 212]. As polaritons are expelled from the excitation area, the blueshift potential energy is converted to kinetic energy, indicating that polaritons accelerate in a manner analogous to a ball rolling down the slope of a hill [194, 213]. Overall, the mechanism of optical confinement can be summarised as follows: each pump spot injects an optically inactive reservoir composed of a hot electron-hole plasma and dark excitons that repel and diffuse in all directions. During this diffusion, the optically “inactive” reservoir relaxes in energy and forms an optically “active” reservoir of excitons, which

---

[9] This is due to the high refraction index contrast between the semiconductor (e.g. $n \approx 3.5$ for GaAs) and air ($n \approx 1$)

subsequently couple to cavity photons and form polaritons in the middle of the trap.

The effects of the density-induced blueshift potential are clearly observable in experiments. However, some aspects of the underlying physical mechanism are still under debate, most notably which contribution to the blueshift potential dominates. The influence of the exciton reservoir [214] seems to dominate in freely expanding 1D and 2D polariton condensates [194, 211], whereas for tightly trapped polaritons and in situations where the polariton condensate is spatially separated from the exciton reservoir the polariton non-linearities prevail [129, 161, 172, 215].

Engineering blueshift potentials induced by non-resonant as well as resonant optical excitation has proved an efficient way to confine, manipulate, and steer polariton condensates. The initial demonstration of this effect was performed in a deeply etched wire cavity where polaritons became confined in all spatial directions close to the edge of the wire, as shown in Fig. 2.13(d) [194]. The authors also demonstrated tunnelling-induced coupling of extended condensates separated by a repulsive potential, with a tunable tunnelling strength determined by the power of the excitation. Another example is the implementation of an all-optical polariton transistor switch based on the optical gating of polariton condensate flow on a ridge [See Fig. 2.13(e)] [195]. Moreover, polaritons can be confined all-optically by patterning smart geometries of the excitation laser beam, for example, using a spatial light modulator. As a result, almost arbitrarily complex potential landscapes can be realised, such as ring-shaped confinements [See Fig. 2.13(f)] [84, 161], confinements created by multiple pump spots [24, 160, 161, 216, 217], and controlled flow patterns in more complex landscapes [218].

The remaining of this chapter is dedicated to the semiconductor cuprous oxide and the newly emerged field of Rydberg excitons.

2.5 Rydberg Excitons in Cuprous Oxide

Cuprous oxide (Cu_2O) is one of the principal oxides of copper, found in nature as the red-coloured mineral cuprite. Cu_2O has been at the forefront of multiple fields of semiconductor research since the first observation of its photoconductivity by A. Pfund in 1916 [219]. It was one of the first semiconducting materials used in electronics devices, like rectifiers [220, 221], before silicon emerged as the semiconductor of choice for most microelectronic applications. Cu_2O has also been considered a photovoltaic material suitable for low-cost solar cells, owing to the abundance and non-toxicity of its constituent elements along with a high absorption coefficient in the visible region [222–224].

However, cuprous oxide does not currently have many technological applications, primarily due to its fairly brittle texture, low durability, and lack of efficiency as an electrical component compared to other semiconductors. An additional hindrance is the inability to fabricate high-quality samples. Even though there have been some recent advances in growing high-quality synthetic Cu_2O [225, 226], the highest quality samples still originate from natural gemstones.

Despite the lack of technological applications, Cu_2O is one of the most significant materials for research on excitons in semiconductors. While the concept of excitons was already developed theoretically in the 1930s, the first experimental demonstration of excitons was achieved in Cu_2O in the early 1950s when E. Gross and N. Karryev observed hydrogen-like spectra near the bandgap absorption edge [30, 227]. The same discovery was made independently by M. Hayashi and K. Katsuki [31] in the same year. The early spectroscopic studies on excitons in Cu_2O are summarised in review articles by Agekyan [228] and Nikitine [229]. After examining the linear optical properties and their dependencies on perturbations, such as electric and magnetic fields (See Ref. [228] and references therein) or strain [230, 231], research concentrated on the lowest exciton series, the yellow series, and its long-lived 1S ground state. Starting from 1980s, this state was considered a prime candidate for the realisation of Bose-Einstein condensation (BEC) in excitonic systems [106]. Even though numerous claims of such collective exciton coherence have been published [111–113, 232, 233], no unambiguous proof of condensation of excitons has been given [116, 117].

In recent years, interest in Cu_2O was renewed when the yellow exciton series was extended up to a large principal quantum number of $n = 25$ [32]. This discovery has opened up the research field of giant Rydberg excitons and led to a variety of new experimental and theoretical investigations [234–250].

In the following sections, several topics related to Cu_2O and Rydberg exciton are discussed, starting with the crystal structure (Section 2.5.1) and band structure (Section 2.5.2) of Cu_2O. Next, the selection rules for optical excitation are reviewed in Section 2.5.3, followed by a discussion on the absorption (Section 2.5.4) and photoluminescence (Section 2.5.5) spectra of Cu_2O.

2.5.1 Crystal Structure

Cuprous oxide is one of the stable phases of three well-established copper oxide compounds; the others are cupric oxide and paramelaconite, with chemical formulas CuO and Cu_4O_3 [251]. Natural crystals of Cu_2O can be found worldwide, with high-quality and low defect density crystals primarily originating from African countries, such as Zaire [252] and Namibia [32, 247]. An example of a natural gemstone next to a µm-thin slab is shown in Fig. 2.14(a,b).

Unstressed cuprous oxide crystallises in a cubic structure and can be described according to symmetry operations of the point group O_h [251]. The unit cell consists of four copper ions and two oxygen ions, as shown in Fig. 2.14(c). Inside the unit cell, the O atom are arranged in a body-centered cubic (bcc) sublattice with the Cu atoms superimposed in a face-centered cubic (fcc) sublattice. The two sublattices are shifted by a quarter of the lattice diagonal, leading to oxygen atoms being fourfold coordinated with copper atoms as nearest neighbours and copper atoms being linearly coordinated with two oxygen atoms as nearest neighbours. This structure is centrosymmetric, i.e. has inversion symmetry [253]. The lattice constant is $\alpha = 4.27$ Å [254].

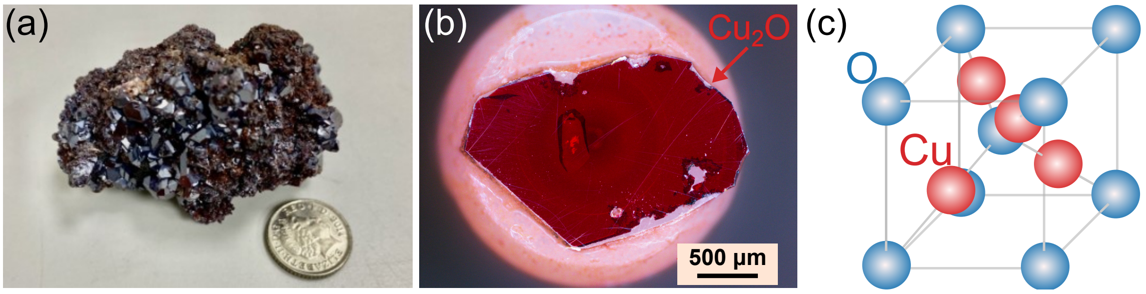

Figure 2.14: (a) Image of a natural gemstone of Cu_2O. (b) Optical microscope image of a polished thin crystal (approximately 50 µm thick). (c) The unit cell of Cu_2O with the origin on an oxygen site. Red spheres represent copper atoms in an fcc lattice, blue spheres represent oxygen atoms in a bcc lattice.

2.5.2 Band Structure

The main properties of the electronic band structure will be summarised here. A complete description is presented in Refs. [253, 255–259]. The optical properties considered in this work result from the electronic properties of the valence and conduction bands around the centre of the Brillouin zone (Γ point). At this point, cuprous oxide is a direct gap semiconductor at the Γ point with a bandgap energy of approximately 2.172 eV at the yellow region of the visible spectrum.

A schematic representation of the relevant electronic bands, after considering the effects of the crystal field and spin-orbit interaction, is shown in Fig. 2.15. The symmetry of the bands is assigned by the irreducible representations $\Gamma_i^{\pm}$ of the point group O_h, where ± refers to the parity [260]. The valence bands are predominantly d-like in character built up from the Cu 3d orbitals split by spin-orbit interaction (Γ_7^+ - Upper VB, Γ_8^+ - Lower VB). The conduction bands originate from Cu 4s electrons (Γ_6^+ - Lower CB), and Cu 4p electrons (Γ_8^- - Upper CB) [257, 258].

By considering all possible transitions from the valence bands to the conduction bands shown

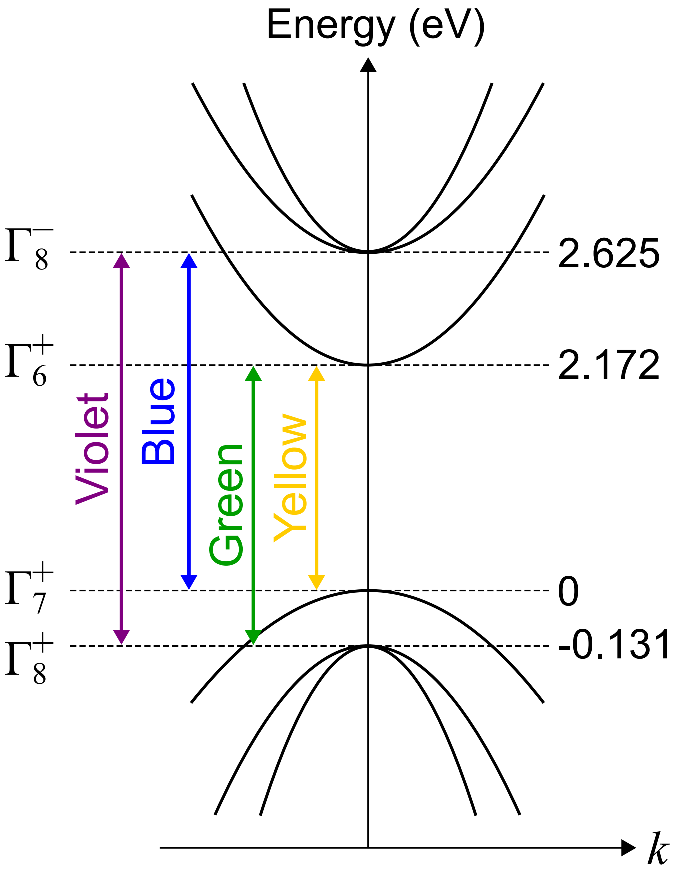

Figure 2.15: Schematic band structure of Cu_2O around the centre of the Brillouin zone and corresponding band-to-band transitions. The terms of the form $\Gamma_i^\pm$ denote the symmetry of the wavefunctions in the different energy bands. The transition energies are: yellow ($\Gamma_6^+ \rightarrow \Gamma_7^+$) at 2.17208 eV [32], green ($\Gamma_6^+ \rightarrow \Gamma_8^+$) at 2.3023 eV [264], blue ($\Gamma_8^- \rightarrow \Gamma_7^+$) at 2.6336 eV [243], and violet-indigo ($\Gamma_8^- \rightarrow \Gamma_8^+$) at 2.756 eV [266].

in Fig. 2.15, four exciton series are obtained. These exciton series are labelled after the colour of the corresponding wavelength region and are known as the yellow, green, blue, and violet series. Transitions from the uppermost valence band to the lowest conduction band belong to the yellow series with a bandgap of ~2.17208 eV at cryogenic temperatures [32, 261]. The yellow series was the first exciton series observed and the one where giant Rydberg excitons were first realised [32]. Even though most of the experimental and theoretical interest has been focused on the yellow series, the other three series have attracted considerable attention in recent years [243, 244, 262–265].

The remaining of this thesis focuses entirely on the yellow series. The yellow exciton series in cuprous oxide has the record for the highest principal quantum number of excitons ever observed, i.e. $n = 25$ in an absorption experiment [32] and $n = 30$ using photoluminescence excitation spectroscopy [247]. One factor contributing to such a robust exciton series is the high exciton

Rydberg constant. The effective masses of the electron and hole are found to be $m_e^* = 0.99m_e$ and $m_h^* = 0.58m_e$ [267, 268], resulting in an effective mass of $\sim$0.366m_e. Assuming a relative permittivity of $\epsilon_r \approx 7.5$ [267], the Rydberg energy is approximately 90 meV, which is in good agreement with the experimentally measured values [32, 247, 269]. This Rydberg energy is significantly higher than other conventional direct bandgap semiconductors [47], such as 4.2 meV for GaAs [270], which is often considered the prototypical semiconductor for exciton studies.

The highly excited Rydberg yellow exciton states are accompanied by a large spatial extension due to the radius of the exciton wavefunction scaling as n^2 (Eq. 2.12). The average exciton radius using a hydrogen relation that accounts for the principal quantum number n and angular momentum l of an orbital is [32]:

$$\langle r_n \rangle = \frac{1}{2}\alpha_B(3n^2 - l(l+1))\,, \tag{2.60}$$

where $\alpha_B = 1.11$ nm [271] for the P excitons in Cu_2O and $l = 1$ for P states. Therefore, $\langle r_{\mathrm{n}=25} \rangle = 1.04$ µm for $n = 25$, corresponding to a huge exciton extension of more than 2 µm, about ten times the light wavelength required to create this exciton. This finding underlies the role of Rydberg excitons in bringing quantum phenomena to microscopic dimensions, orders of magnitude higher than the lattice constant.

Apart from the spatial extension, several other properties scale with n. For instance, the dipole moment follows the exciton radius scaling law and scales as n^2, the spacing between Rydberg levels scales as n^{-3} [272], whereas the polarizability and natural line width scale as n^7 and n^{-3}, respectively. These characteristic scaling laws imply that highly excited Rydberg excitons possess exaggerated properties such as huge interactions between Rydberg states and significant sensitivity to external fields. The interactions between two Rydberg states separated by R, in particular, scales as n^{11}/R^6 and n^4/R^3 for van der Waals and dipole-dipole interactions, respectively. The former is more relevant for large separations, while the latter better describes the interactions at small distances [32, 273].

The large dipole-dipole interactions between Rydberg excitons lead to a Rydberg blockade effect, similar to the one observed for Rydberg atoms [274], which is manifested as a drop in the oscillator strength of high-n states. The physical mechanism behind the Rydberg blockade effect is as follows: when a Rydberg exciton is created, the energy needed to excite a second exciton in its vicinity to a Rydberg state is shifted by the dipole interaction energy away from the narrow undisturbed absorption line. As a result, resonant absorption and exciton creation are suppressed inside the blockade volume V_{blockade} in which the dipole interaction energy is larger than the absorption line width Γ_n. Interestingly, the Blockade effect occurs not only for excitons with the same n but also for different n [32]. Potential applications of the blockade effect with Rydberg excitons include nonlocal all-optical switching and mesoscopic single-photon devices [32, 246].

The giant interactions between excitons in Rydberg states and the resultant Rydberg blockade effect motivated proposals suggesting the use of Rydberg excitons to strongly enhance optical nonlinearities and induce nonlinear processes at the level of single photons [34, 275]. These nonlinearities can be further harnessed by quantum confinement of the excitons in low-dimensional semiconductor structures such as quantum wells and quantum dots [245, 249, 276]. Chapter 5 introduces Cu_2O nanoparticles as a suitable system for quantum confinement and an exciting platform for realising quantum technologies with Rydberg excitons.

2.5.3 Selection Rules

As discussed in Section 2.5.2, the highest valence and lowest conduction bands arise, respectively, from the 3d and 4s orbitals of the Cu atoms and are the origin of the yellow exciton series. Since both bands share the same (positive) parity, direct transitions between them may seem dipole forbidden. However, transitions from the ground state (full valence band, empty conduction band) to exciton states acquire the angular momentum of the relative motion between electrons and holes as an additional degree of freedom. The total parity of an exciton level is thus determined by the product of the parities of the valence band, the conduction band, and the exciton envelope wavefunction.

For an excitonic S state, the parity is positive, and the transition to the ground state is dipole forbidden but quadrupole allowed. For a P state, the parity is negative, and the transition to the ground state is dipole allowed. In general, exciton states in Cu_2O fall into one of two categories: The dipole-active exciton states of negative parity and odd angular momentum, which can be observed in one-photon absorption and the exciton states of positive parity and even angular momentum, which can be observed in two-photon absorption.

For one-photon absorption, the dominant states observed have P-type symmetry. Since P states exist for $n > 1$, there is no dipole emission from the lowest energy exciton states with $n = 1$. Therefore, Cu_2O is a semiconductor with a so-called forbidden direct bandgap [228]. However, one-photon excitations of S excitons are allowed in terms of a quadrupole transition [243].

Due to its small radius, the 1S exciton in Cu_2O is an intermediate between a Frenkel and a Wannier exciton [44, 239], which results in an enhancement of its binding energy to about $\sim$150 meV and significant deviations from the typical hydrogen-like spectrum. To describe these states theoretically, the so-called central-cell corrections have to be included as outlined in Refs. [237, 239, 271].

Moreover, spin-orbit (exchange) interaction splits the 1S state into a triply degenerate orthoexciton state (total angular momentum $J = 1$) and a singlet paraexciton state ($J = 0$), found 12 meV below the orthoexciton [261, 277, 278]. Hence, the 1S paraexciton is actually the lowest exciton level of Cu_2O.

For 1S orthoexcitons, decay to the ground state is quadrupole allowed. However, the lifetime of 1S orthoexcitons is mainly limited by the transition to the lower lying paraexciton state, which is ~1 ns [279–281]. Optical decay from the paraexciton state is forbidden to all orders of perturbation since transitions between levels can be made when $\Delta J = \pm 1$. Thus, the lowest energy exciton state in Cu_2O is a dark state, and its lifetime is expected to be long. Practically, the lifetime of the paraexciton state is limited by nonradiative recombination at crystal impurities and defects and can reach several microseconds [279]. The splitting into orthoexciton and paraexciton states is also present in other S excitons, though it is most prominent for the 1S [261].

Due to its long lifetime and its small radius, the 1S paraexciton in Cu_2O is considered a promising candidate for excitonic Bose-Einstein condensation [115]. Despite the numerous attempts [111–113, 232, 233] to verify the existence of such condensate, there is still no unambiguous proof of it [116, 117]. The main limiting factor is the two-exciton Auger recombination decay, in which one exciton recombines non-radiatively, giving its energy to a second exciton and ionising it [117]. Consequently, the Auger decay mechanism, which is pronounced in Cu_2O, hinders the formation of an excitonic condensate by reducing the density of excitons and simultaneously by heating the crystal [115, 282].

2.5.4 Absorption Spectrum

The whole one-photon absorption spectrum of the yellow exciton series, measured with a high-resolution setup at a temperature of 1.35 K [283], is presented in Fig. 2.16. The absorption spectrum exhibits a beautiful hydrogenic series of P exciton absorption lines. The series starts with the prominent 2P line and extends up to $n = 22$ in this case, having a hydrogenic energy ladder following an n^{-2} dependence, as expected from theory (Eq. 2.9). Apart from the prominent P states, higher angular momentum negative-parity states are visible, with the F states appearing as small shoulders on the high energy side of the P states (See inset III for a zoomed-in version of the F states near the 4P line). Higher angular momentum states, such as H states ($l = 5$), have also been reported [234]. The 6H state is highlighted in the inset IV of Fig. 2.16.

Interestingly, the spectrum begins with the sharp quadrupole transition of the 1S orthoexciton at 2.03279 eV. A zoomed-up version of this peak, shown in the inset I in the upper panel

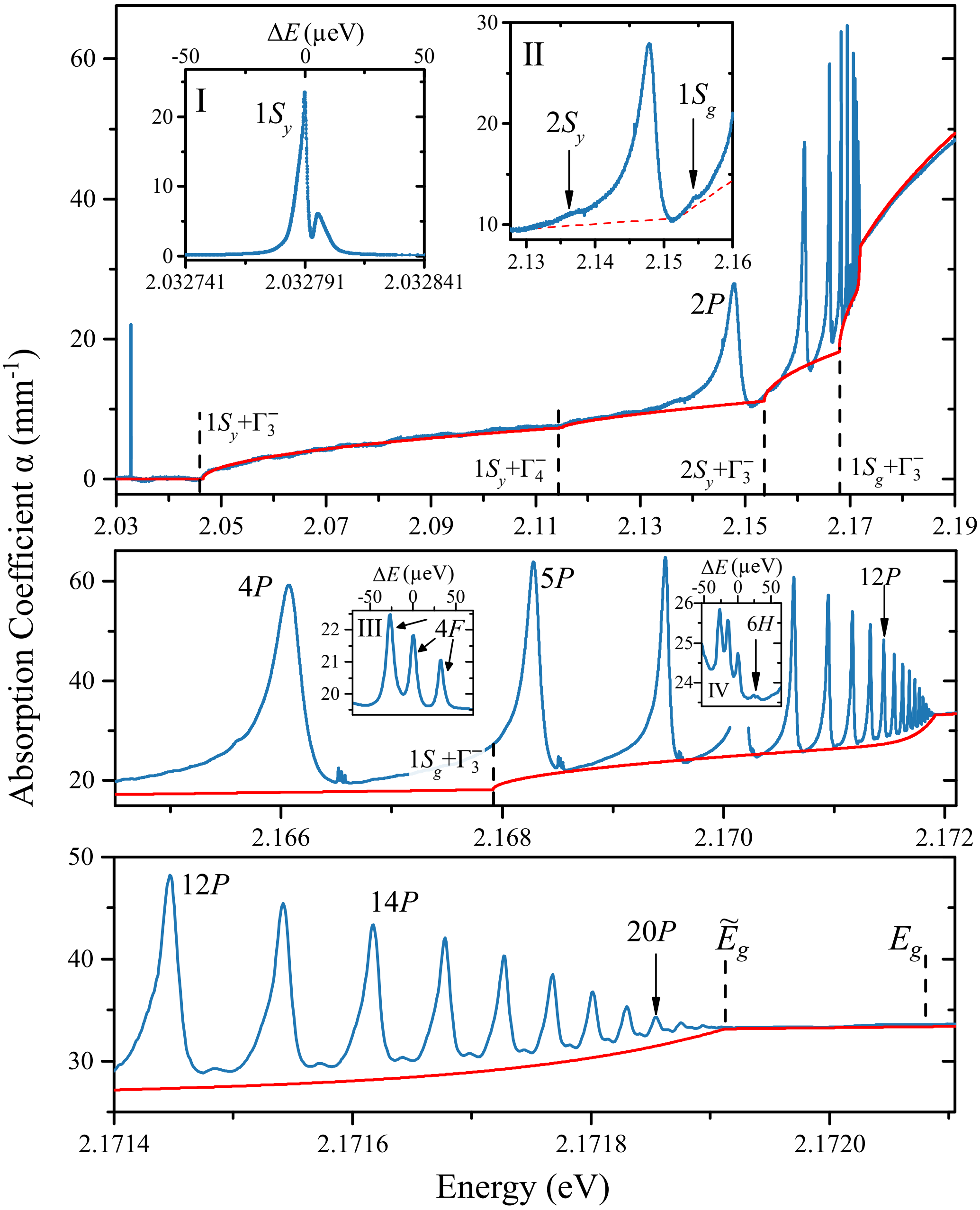

Figure 2.16: High-resolution absorption spectrum of the yellow exciton series of Cu_2O measured with a probe power of 1 μW at $T = 1.35$ K. The red line denotes the background absorption, whereas the dashed vertical lines mark the beginning of a phonon branch. $\tilde{E}_g$ indicates the end of the exciton series and the transition into the continuum at about 172 μeV below E_g, the latter being the nominal bandgap at 2.172087 eV obtained by a fit to the energies. Insets show zooms into regions of S, F and H angular momentum states. Reproduced with permission from Ref. [283].

of Fig. 2.16, reveals a split into two resonances with linewidths of ∼4 μeV and ∼2 μeV. This splitting was attributed to deviations from parabolicity in the valence band structure seen by an exciton with finite total momentum $\hbar\mathbf{k}$ [237, 283].

Note that the green exciton series overlaps with the energy range of the yellow series. Specifically, the green 1S exciton, marked as $1S_g$ in the inset II of Fig. 2.16, is between the 2P and the 3P resonances of the yellow series at an energy ∼2.1544 eV [239, 243, 261]. The higher lying green excitons are all found above the bandgap of the yellow series.

The exciton absorption lines are superimposed on top of a continuously increasing broad absorption background, originating from phonon-assisted processes. Despite their positive parity, S orthoexcitons can be produced by absorption of one photon under simultaneous emission of a longitudinal optical (LO) phonon with negative parity. In Cu_2O, the most relevant phonon is the optical Γ_3^- at an energy of $E_{\text{phon}}^{\Gamma_3^-} = 13.6$ meV, followed by the Γ_4^- LO phonon with energy $E_{\text{phon}}^{\Gamma_4^-} = 82.1$ meV [240, 263]. This phonon-assisted absorption occurs through a virtual intermediate dipole-allowed state, with such virtual states consisting of blue/violet S-exciton states (depending on the final state being yellow or green, respectively) [240]. By this process, an exciton with an almost arbitrary wavenumber can be formed. The absorption coefficient is thus proportional to the density of final exciton states, which, in turn, is proportional to the square root of the excess energy. A phonon-assisted process manifests itself as a distinct absorption onset that follows the expected square root dependence starting at one LO phonon energy above the 1S exciton resonance energy. Several phonon-assisted transitions to the 1S excitons of the green and yellow series are possible and form the continuous background on which the series of Rydberg exciton states are overlaid [240]. The onsets of the relevant branches are indicated by dashed vertical lines in Fig. 2.16.

Additionally, the background exhibits an exponential increase in absorption starting from about $n = 10$ until the bandgap energy $E_g \approx 2.172$ eV, where the yellow exciton series ends, and the absorption spectrum smoothly transforms into a continuum. This exponential increase is known as the Urbach tail and is attributed to the existence of a static electric microfield distribution in the crystal, caused by charged impurities, that ionises the highest Rydberg states [49].

The P-exciton resonances show a characteristic asymmetric line shape. An individual absorption peak can be described by an asymmetric Lorentzian curve of the form [284, 285]:

$$\alpha_n(E) = C_n \frac{\frac{\Gamma_n}{2} + 2q_n(E - E_n)}{(\frac{\Gamma_n}{2})^2 + (E - E_n)^2}, \tag{2.61}$$

where C_n denotes the resonance amplitude that is proportional to the oscillator strength, Γ_n represents the linewidth of the nP state, q_n the asymmetry parameter, and E_n the resonance energy. Note that the value of E_n does not necessarily coincide with the peak of the absorption line due to the asymmetry quantified by the q_n parameter.

The cause of this asymmetry is a matter of debate in the literature. Initially, Toyozawa attributed the asymmetry to interband scattering between different exciton bands caused by optical phonons [284, 285]. However, a later theoretical study [286] showed that the experimentally observed asymmetries are larger than what Toyozawa's theory predicts and have to be attributed to a Fano interference effect [287] between the discrete exciton states and the continuous phonon-assisted background. In a Fano resonance, two paths - one direct from the discrete state and the other mediated by the continuum - interfere to produce the asymmetric Fano profile given by:

$$f(\epsilon) = \frac{(q+\epsilon)^2}{1+\epsilon^2}\,, \tag{2.62}$$

where $\epsilon = (E - E_0)/\gamma$ is the dimensionless resonant channel detuning with resonance energy E_0, $\gamma = \Gamma/2$ is the linewidth of the Fano resonance with damping parameter Γ, and q is the asymmetry parameter [287, 288]. In our case, the coupling of the Rydberg excitons to the phonon background provides an interfering excitation pathway, thus creating a Fano resonance. This interpretation is disputed in Ref. [289], where authors argue that exciton-phonon scattering processes alone can explain the asymmetric line shape of the P-exciton states. It should be noted that, within this work, the exact origin of the line asymmetry is not of major importance as it does not affect the outcome of the experiments of Chapters 5 and 6.

As a last remark, the resonance energies of Cu_2O extracted from absorption measurements exhibit a small but systematic deviation from the ideal Rydberg series. Consequently, a quantum defect model is often used to describe the n-dependence of the resonance energy [32, 237, 290], in close analogy to atomic physics [291]. In this model, a quantum defect parameter $\delta_{n,l}$ is incorporated in the binding energy relation (Eq. 2.9), giving the corrected energy dispersion:

$$E_{b,n} = -\frac{R_x^*}{(n-\delta_{n,l})^2}\,. \tag{2.63}$$

The quantum defect in alkali atoms shows a weak dependence on energy. Similarly, an n-dependence has been applied to describe the quantum defects of Cu_2O excitons [290, 292]. However, for the purpose of this thesis, any n-dependence of the quantum defect will be neglected.

2.5.5 Photoluminescence Spectrum

Figure 2.17 shows a PL spectrum of Cu_2O measured at 6 K in the energy range most relevant to this work [243]. In pure Cu_2O samples, the lowest energy exciton state is the 1S paraexciton. Even though the yellow 1S exciton is dipole-forbidden, the direct luminescence of the 1S orthoexciton is the most dominant radiative recombination process via electric quadrupole transitions [243]. The 1S orthoexciton peak appears at ∼2.033 eV (∼609.8 nm), accompanied by several phonon-assisted lines, the most prominent of which is the Γ_3^--phonon-assisted 1S orthoexciton emission at ∼2.020 eV. This fact provides evidence of the strong interaction between the Γ_3^- phonon and 1S exciton, as discussed in Section 2.5.4. Emission originating from the paraexciton is manifested as the weak Γ_5^--phonon-assisted peak at approximately 2.011 eV (∼616.64 nm), the observation of which can be used to confirm the high quality of the crystal [248].

An additional emission mechanism present in Cu_2O is the up-conversion of the yellow paraexcitons into higher Rydberg states, manifested as several peaks at the low-energy side of the phonon-assisted 1S yellow lines (Not shown in Fig. 2.17) [243]. The mechanism involves the collision of two 1S excitons, either two paraexcitons or one paraexciton and one orthoexciton states. After the collision, one of these excitons is excited up to a higher-energy Rydberg nP state, where it can then decay radiatively. The other exciton is transferred to a lower state where it radiatively emits, creating a series of peaks between ∼1.88 to ∼1.91 eV. Both energy and momentum are conserved during this process. However, despite this up-conversion mechanism, photoluminescence from P-exciton states is three orders of magnitude weaker than the 1S orthoexciton line and has been observed in high-resolution measurements involving high-purity samples [243, 247]. The yellow P-exciton series has been extended up to $n = 10$ in a PL experiment [243].

Another radiative channel in Cu_2O is bound excitons. Crystal defects, such as atomic-scale impurities and dislocations, can lead to captured excitons becoming bound at the defect site, leading to several sharp spectral features at energies lower than the 1S paraexciton, approximately between 1.99 to 2.01 eV [293], assigned to phonon-assisted processes involving orthoex-

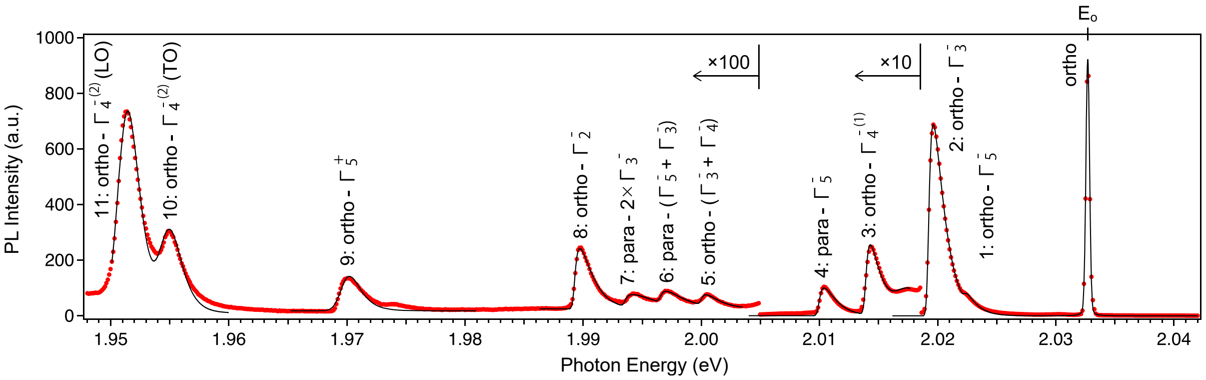

Figure 2.17: Phonon-assisted luminescence of orthoexcitons and paraexcitons of the 1S yellow state in Cu_2O at 6 K. The black lines represent a fit to the spectrum. Reproduced with permission from Ref. [243].

citons and paraexcitons [243].

In addition to defects, copper and oxygen vacancies form traps for free excitons, resulting in broad spectral features at much lower energy than the 1S excitons (Not shown in Fig. 2.17) [294–296]. Specifically, a broad peak centred around ~1.72 eV is attributed to the luminescence of excitons trapped at doubly ionised oxygen vacancies (V_O^{++}). Another broad peak near ~1.53 eV is the luminescence band of excitons trapped at singly ionised oxygen vacancies (V_O^{+}). Lastly, a third feature at around ~1.4 eV corresponds to copper vacancies (V_{Cu}^{-}) [294]. The amplitude of these peaks depends on the composition of vacancies in the sample and varies in the literature. A recent work [247] reported a nearly complete absence of broad emission at 1.7 eV, indicating the absence of oxygen vacancies within the probed sample volume.

This page is intentionally left blank.

Chapter 3

Experimental Methods

This chapter is dedicated to the technical aspects of the experiments presented in this thesis. First, Section 3.1 presents the fabrication processes used to prepare the systems studied in this work, namely the Cu_2O thin bulk crystal, the Cu_2O nanoparticles, and the GaAs- and Cu_2O-based microcavities. Then, Section 3.2 introduces the experimental setups for optical spectroscopy and interferometry measurements, along with other techniques used for material characterisation.

3.1 Sample Preparation

3.1.1 Natural Crystal Thinning and Polishing

Most studies on the optical properties of Cu_2O are based on a mined natural crystal [32, 243, 247, 248], with only a few recent publications using a synthetic crystal [225, 226]. Raw natural crystals usually undergo a thinning and polishing procedure that renders them suitable for optical measurements. The goal is to fabricate a thin crystal with a few tens of micron thickness having high-quality polished surfaces.

In this thesis, all Cu_2O samples originate from the same mother crystal, mined in the Tsumeb mine in Namibia and sourced from the commercial gemstone and mineral market. We start by cutting a small (∼1-2 mm in all dimensions) piece from this crystal. The piece is selected so that at least one surface is aligned with one of the crystallographic axes of the Cu_2O crystal lattice, which is evidenced by a smooth, highly reflective, metallic-like surface. This assessment is performed by eye, and XRD is not performed at this stage. One flat end of a ceramic fibre ferrule is coated with an ethanol-soluble fast-acting adhesive (Loctite Super Glue). The sample is then mounted on the ferrule with its natural facet side on top of the adhesive-coated ferrule surface. This practice ensures that the final sample will be aligned with one crystallographic axis after the polishing procedure.

All polishing steps described here are performed on top of a glass polishing plate (Thorlabs CTG913) that provides a hard, flat surface. For thinning and polishing, we use lapping (polishing) film sheets commonly used for polishing optical fibres. Lapping sheets are typically composed of tiny particles acting as the abrasive material, glued to a substrate of polyester with a non-pressure-sensitive adhesive. By moving the sample over the polishing film, excess material is removed and the sample surface is polished. Different grades of lapping sheets, from 30 µm down to 0.3 µm, were used in successive polishing cycles, with each polishing cycle using a finer grit paper. Specifically, six grit sizes were used: 30 and 12 µm grits using aluminum oxide (3M 50023 and 50022), 5 µm grit using silicon carbide (Thorlabs LF5P), 1 and 3 µm grits using aluminum oxide (Thorlabs LF1P and LF3P), and 0.3 µm grit using calcined alumina (Thorlabs LF03P).

The ferrule is inserted into the central pinhole of a polishing puck (Thorlabs D50-F), which ensures that it is held perpendicular to the lapping sheet surface. By moving the puck over the sheet, while the Cu_2O sample is held in contact with the lapping sheet, excess material from the crystal surface is removed. The puck is moved in a figure of 8 pattern, which causes the direction of polishing to move around in all directions on the end of the ferrule, ensuring even polishing and preventing marks from polishing in only one or two directions. Additionally, the random, uneven nature of the figure eight motion moves the sample over more surface on the polishing sheet, thus avoiding polishing on top of areas with residue from earlier polishing strokes. The last observation is particularly important during the final stages, when using finer grit sizes, since residual powder on the lapping sheet can induce marks and scratches.

The sample undergoes multiple polishing cycles, followed by inspection under a commercial optical microscope (See Section 3.2.4.1). The bright-field (BF) and dark-field (DF) optical microscopy images of a Cu_2O sample polished with three lapping sheets of different sizes are shown in Fig 3.1(a-c). It is clear that moving from coarse to finer grits, the size of surface defects is reduced, leading to high-quality surfaces with a small number of scratches and defects. Polishing is halted when the desired surface quality [similar to Fig. 3.1(c)] is achieved.

Once polishing of the first surface is complete, the sample is submerged into a solution of either ethanol or acetone to dissolve the glue and separate the ferrule from the Cu_2O crystal. The sample is again mounted on the ferrule, but now, from its polished side. The polishing procedure described above is repeated until we obtain a thin sample (thickness ∼50 µm, verified by optical microscopy), with both the bottom and top surfaces polished to a high quality. Figure 3.1(d) shows one of the polished surfaces of the Cu_2O sample used in the experiments of Chapters 5 and 6. The final sample is again submerged into a solvent solution to dissolve the glue and separate the ferrule. Then, both surfaces are gently wiped with a lens cleaning tissue soaked in

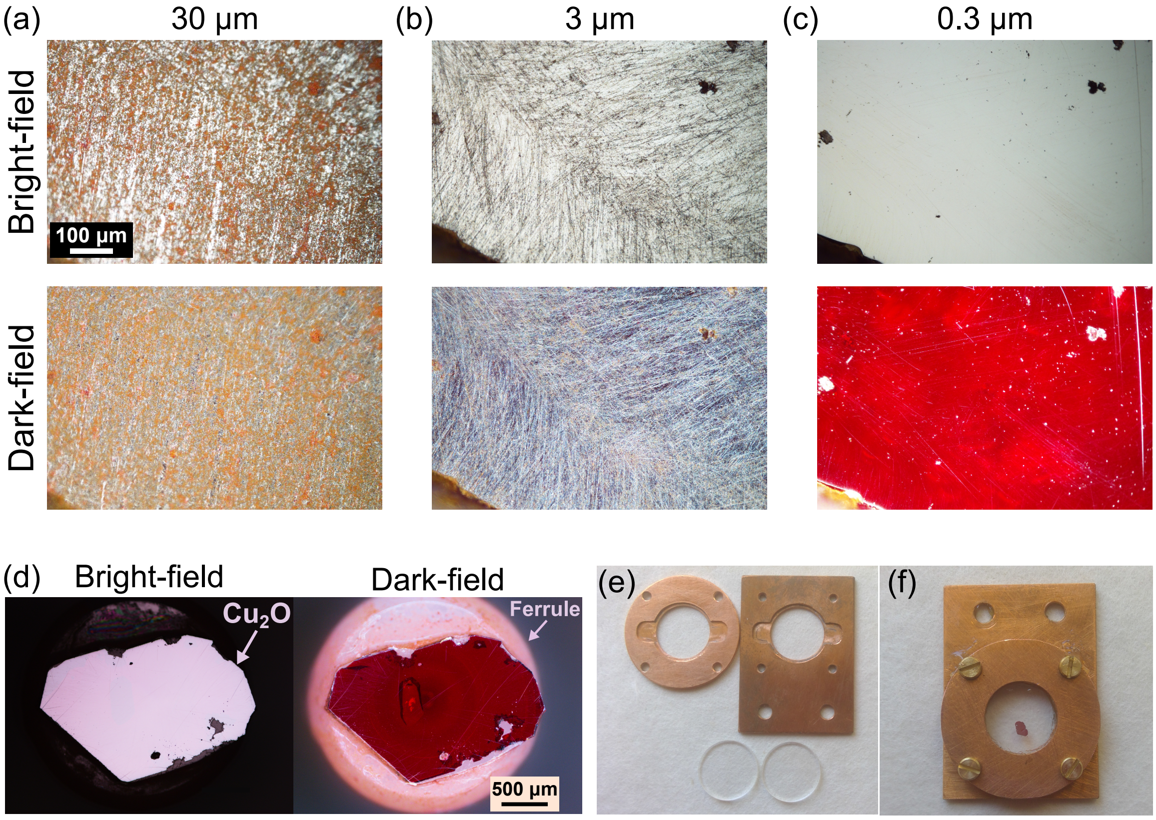

Figure 3.1: (a-c) Bright-field (top panel) and dark-field (bottom panel) optical microscopy images of the surface of a Cu_2O sample after several rounds of polishing with lapping sheets of (a) 30 µm, (b) 3 µm, and (c) 0.3 µm. All images are taken at roughly the same sample region with the same magnification (20x). (d) Bright-field (left panel) and dark-field (right panel) optical microscopy images of the Cu_2O sample used in the experiments of Chapter 5. (e) Image of the copper holder assembly parts. (f) Image of Cu_2O bulk crystal inside the assembly.

methanol. After that, the sample is dusted off using either an air duster or a nitrogen gun.

Previous studies have shown that Cu_2O crystals glued to a substrate are strained when they cool. This strain distorts the crystal lattice and thus influences the optical absorption spectrum [297, 298]. To prevent this, the crystal is kept inside a pocket formed by two transparent CaF_2 substrates (10 mm diameter and 1 mm thickness, UQG Optics WCF-111). This assembly is subsequently placed between two copper holders, which are held together by four screws [See Fig. 3.1(e,f)]. This holder assembly is mounted on the cold finger of the cryostat for optical measurements at cryogenic temperatures. To improve the thermal contact between components, a small amount of thermal paste (Apiezon N Grease) is applied on the edges of the two CaF_2 windows, between the two copper holders, and between the holder assembly and the cold finger of the cryostat. We use CaF_2 substrates due to their excellent thermal conductivity at cryogenic temperatures and transparency in the visible spectrum [299].

3.1.2 Nanoparticles

Samples of Cu_2O particles were prepared by implementing the solvent evaporation technique. Specifically, a suspension of Cu_2O powder ($\sim$80 mg) in water or ethanol is formed, and then part of it is deposited onto the target CaF_2 substrate in the form of a droplet. Evaporation of the solvent in ambient conditions leads to the formation of different self-organised microstructures of Cu_2O particles in the region of the droplet.

The first kind of Cu_2O powder used for fabrication is the extracted residual powder from polishing a natural mined crystal. We refer to these particles as natural nanoparticles (NNPs). Additionally, we used commercial synthetic powder (Nanografi) with an average size distribution of $\sim$0.6 µm. We refer to these as synthetic nanoparticles (SNPs).

Scanning electron microscopy (See Section 3.2.4.2) reveals that Cu_2O particles tend to aggregate and form clusters of different sizes due to Van der Waals forces as the particles redistribute during solvent evaporation [See Fig. 3.2(a,b)]. The particles are of various sizes and shapes. The distribution of NNPs is characterised by an average and median diameter size of $\sim$1.1 and $\sim$0.7 µm, respectively. DF optical microscopy (See Section 3.2.4.1) enables the optical

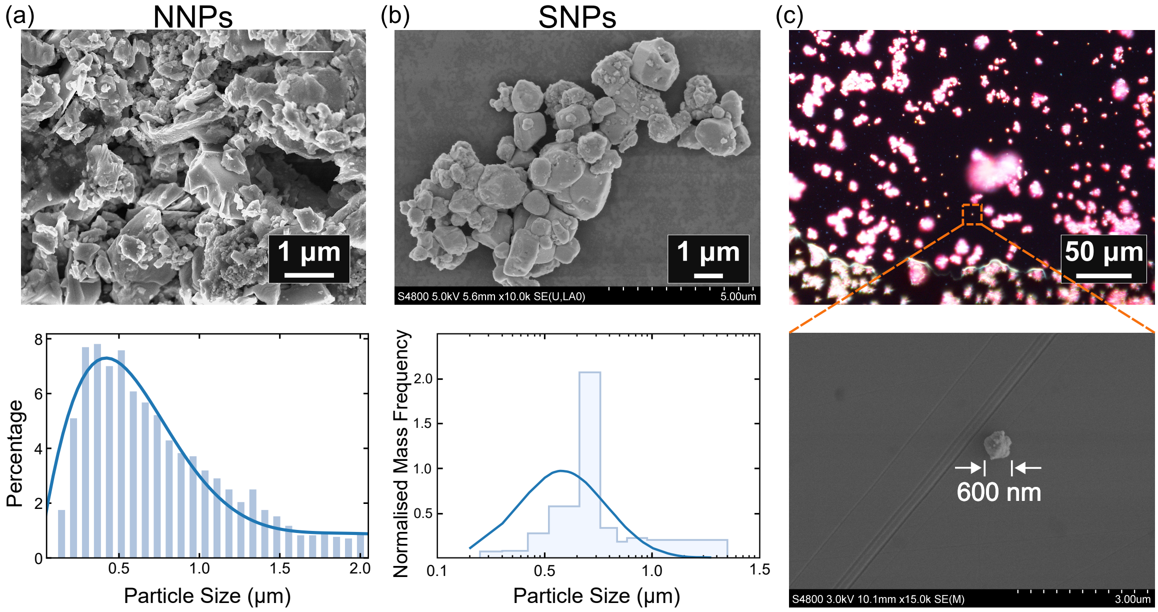

Figure 3.2: (a,b) SEM image (top panel) and corresponding size distribution (bottom panel) for a sample of (a) NNPs and (b) SNPs. The size distribution of SNPs, expressed as the normalised mass frequency, is courtesy of the manufacturer (Nanografi) and is reproduced with permission. (c) Dark-field optical microscopy image of an area containing clusters of SNPs (top panel) and an SEM image of the single SNP (bottom panel) marked in the square orange region of the optical microscopy image.

characterisation of these nanoparticles. We can identify single nanoparticles by SEM and observe them as diffraction-limited spots under DF microscopy [See Fig. 3.2(c)]. Substrates with deposited particle samples were mounted directly onto the cold finger of the cryostat using silver conductive paint (RS PRO Conductive Lacquer).

3.1.3 Microcavities

3.1.3.1 Gallium Arsenide

The GaAs microcavity sample studied in this work was grown, processed, and initially characterised in the group of Pavlos G. Savvidis at the University of Crete. A thorough characterisation of the sample is presented in Ref. [150], while additional publications include Refs [160, 161, 211, 216, 217, 300].

The microcavity is a stack of almost a hundred single-crystalline layers of $Al_xGa_{1-x}As$ alloys grown by molecular beam epitaxy (MBE). MBE is a widely used technique for epitaxial (layer-by-layer) atomically precise growth of single-crystal thin films and multi-layered structures such as quantum wells and superlattices [301]. Material growth takes place under ultra-high vacuum conditions on a heated crystalline substrate by the interaction of adsorbed species supplied by atomic or molecular beams. The beams generally have thermal energy and are produced by evaporation or sublimation of suitable materials contained in separate ultra-pure crucibles [302]. In our case, the material choice ($Al_xGa_{1-x}As$) allows us to grow structures with a large number of layers without strain buildup due to lattice mismatch since GaAs and AlAs have only a small lattice mismatch ($\sim$0.15 %) [303].

Figure 3.3 shows cross-sectional SEM images of the sample used for the experiments presented in Chapter 4. The microcavity is formed by two highly reflective DBR mirrors with 32 (top) and 35 (bottom) alternating pairs of $Al_{0.15}Ga_{0.85}As/AlAs$ layers of thickness 57.2/65.4 nm. The cavity active layer has an effective optical length of $\frac{5}{2}\frac{\lambda_c}{n_c}$, where $\lambda_c = 805$ nm is the design wavelength of the microcavity. A set of three 10 nm GaAs QWs, separated by 10 nm $Al_{0.3}Ga_{0.7}As$ spacer layers, is placed at each one of the four antinodes of the cavity electric field to enhance the coupling of excitons to the photonic mode. A wedge in the cavity thickness gives access to a tunable cavity-exciton detuning parameter Δ, with negative detunings up to -9.7 meV previously observed [150].

The experimental quality factor of the sample exceeds $Q > 16,000$, yielding cavity-phonon lifetimes of $\tau_c > 7$ ps. Strong coupling between the cavity and exciton modes has been achieved with a Rabi splitting of $\hbar\Omega = 9$ meV. Polariton condensation under non-resonant optical pumping in this sample has been previously observed [217, 300].

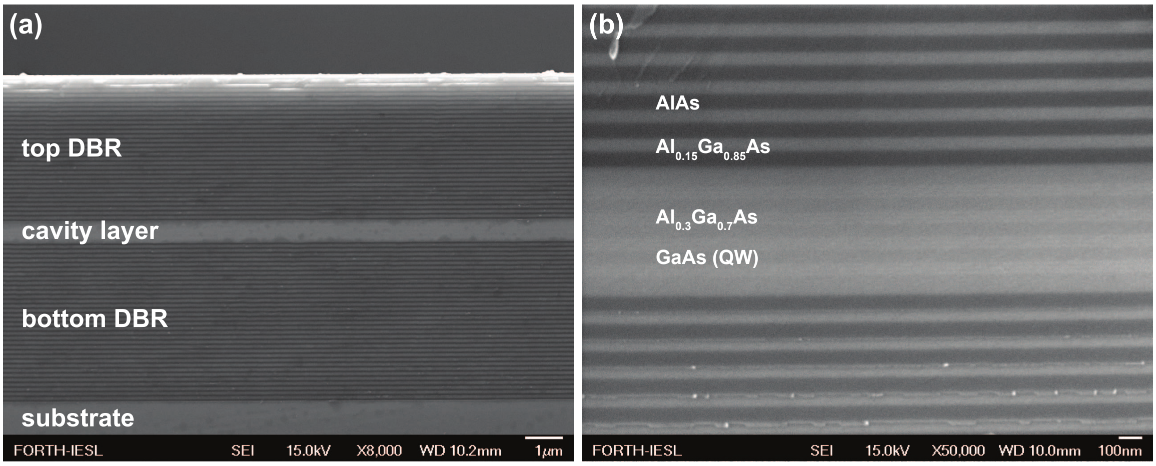

Figure 3.3: Cross-sectional SEM image of the microcavity structure formed on a GaAs substrate by layers of different $Al_xGa_{1-x}As$ alloys. (a) Full cavity structure. (b) Close-up of the cavity layer with its 4 x 3 QWs positioned at the electric field antinodes. Image courtesy of Pavlos Savvidis, reproduced with permission.

Transfer matrix simulations of the microcavity sample are shown in Fig. 3.4. The microcavity was excited non-resonantly in the second Bragg mode at the high-energy side of the stopband, marked by the red arrow in Fig. 3.4(a). All reported experiments were performed at sample positions where the cavity mode is detuned about 6-7 meV below the exciton energy at $k_{||} = 0$.

3.1.3.2 Cuprous Oxide

The second microcavity sample studied in this thesis uses Cu_2O as the active layer. I thinned and polished of the Cu_2O crystal while DBR design and deposition were performed by Sai K. Rajendran. X-ray diffraction measurements were performed by Y. Nanao and S. K. Rajendran.

A schematic of the fabrication process is presented in Fig. 3.5. It starts by mounting a small piece of natural Cu_2O crystal on a fibre ferrule with its natural facet side on top of the ferrule, as outlined in Section 3.1.1. Once polishing of the top surface is complete, we separate the crystal from the ferrule. The polished side of the Cu_2O crystal is subsequently mounted on top of a DBR-coated CaF_2 window using an ultraviolet-cured epoxy. The epoxy (Norland Optical Adhesive, NOA61) is transparent in the visible region and is used commercially for bonding optical elements. The epoxy was spin-coated (3000 RPM for 30 seconds) to ensure the thinnest possible layer. To further reduce its thickness, the sample is gently pushed onto the epoxy before UV curing. Due to its small thickness compared to the Cu_2O layer and its high transparency in the yellow region, the epoxy layer is neglected in all simulations of Chapter 6, even though it is a part of the active layer of the microcavity. The second surface of the crystal is thinned down to a

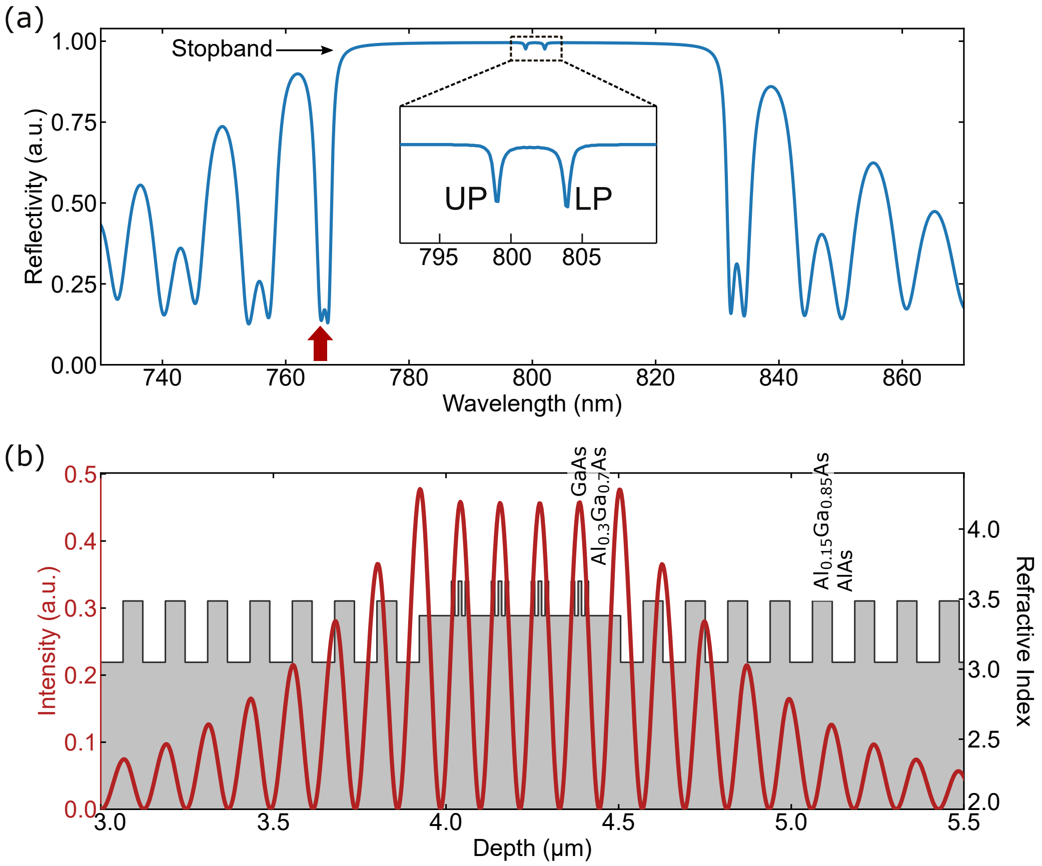

Figure 3.4: Transfer matrix simulations of the GaAs cavity studied in this thesis. (a) Calculated reflectivity spectrum showing the upper and lower polariton modes with a Rabi splitting of ∼9 meV. The red upward indicates the excitation wavelength during measurements. Inset is a close-up of the two polariton modes. (b) Refractive index profile (grey step graph) and light field intensity distribution (red line) around the central part of the microcavity with the top and bottom DBR mirrors (left and right) and the $5/2\lambda_c$ cavity with four sets of three QWs. The simulations were performed using the `tmm` Python package [64].

thickness ∼30 μm and polished with the finest grit (0.3 μm). The final step involves depositing the top DBR directly on the Cu_2O crystal to form a cavity. The bright-field reflectivity images in Fig. 3.5 show the sample before and after the deposition of the top mirror, confirming the successful integration of the DBRs with the Cu_2O layer in the microcavity.

The DBR mirrors were fabricated by RF sputtering alternating layers of SiO_2/Ta_2O_5 at room temperature to obtain maximum reflectivity near 575 nm, i.e. at the wavelength region of yellow P excitons of Cu_2O. The top (bottom) mirror contains 13 (10) pairs of alternating 67.6-nm-thick SiO_2 and 98.9-nm-thick Ta_2O_5 layers. However, there can be up to 5% variation in thickness depending on the position of the substrate in the chamber.

The transmission spectra of a 10- and 13-pair DBR were measured using an ellipsometer at normal incidence and are presented in Fig. 3.6(a). These DBRs were fabricated on separate

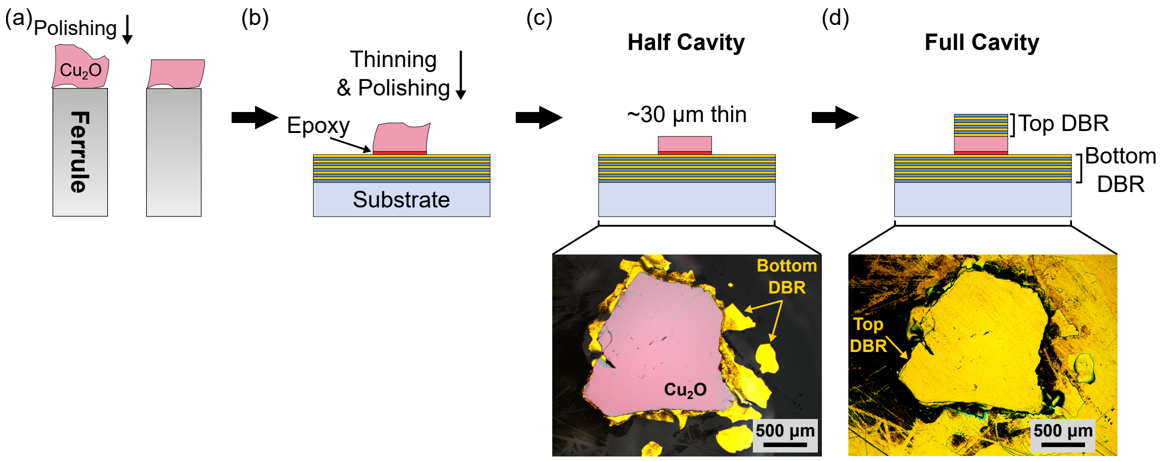

Figure 3.5: Schematic illustration of the process used to fabricate the Cu$_2$O microcavity: (a) A bulk Cu$_2$O crystal, cut from a natural stone, is mounted on a ferrule and its top side is polished. (b) The polished side of the crystal is mounted on a DBR-coated CaF$_2$ substrate using an ultraviolet-cured epoxy. (c) The other surface is thinned down to a thickness of ∼30 µm and is polished as outlined in Section 3.1.1. (d) The top mirror is grown on top of the Cu$_2$O crystal to form the cavity. Optical microscopy images of the half cavity (c) and full cavity (d) are provided below the corresponding steps.

CaF$_2$ substrates and were co-deposited at the same run as the ones in the microcavity sample to ensure same sputtering conditions. There is good agreement between designed and experimentally characterised transmission spectra through the DBRs with a stopband of ∼140 nm. The mismatch in the position of the stopband is assigned to a difference in the experimentally realised and theoretical thickness of the deposited layers. The calculated transmittivity minima are 0.25 (0.27)% and 0.08 (0.03)% for the 10 (13) pair DBR. This small mismatch is assigned to scattering losses in the substrates (60/40 scratch/dig) and mirrors when measured over a 2 mm spot diameter with an ellipsometer. These effects can lead to a drop in the measured DBR transmission minimum and resultant quality factor by about 10%.

Figure 3.6(a) also shows the calculated transmission spectrum through a microcavity with a 32 µm thick transparent layer of refractive index 3 (same as Cu$_2$O [304]), demonstrating the expected free spectral range and cavity linewidth of such microcavity. The absorption coefficient of a 75 µm thick Cu$_2$O crystal measured with a large bandwidth low resolution (150 l/mm) grating is overlaid on the same figure to demonstrate the overlap between the DBR bandgap and the absorption of the yellow P excitons.

To confirm that the Cu$_2$O crystal is cut along the crystal planes of the crystal lattice, we performed X-ray diffraction (XRD) (See Section 3.2.4.3). The microcavity sample was mounted on the sample stage in an X-ray diffractometer, and a $\theta - 2\theta$ scan was performed to extract the XRD spectrum of the Cu$_2$O crystal [See Fig. 3.6(b)]. Reference calculated XRD intensity and

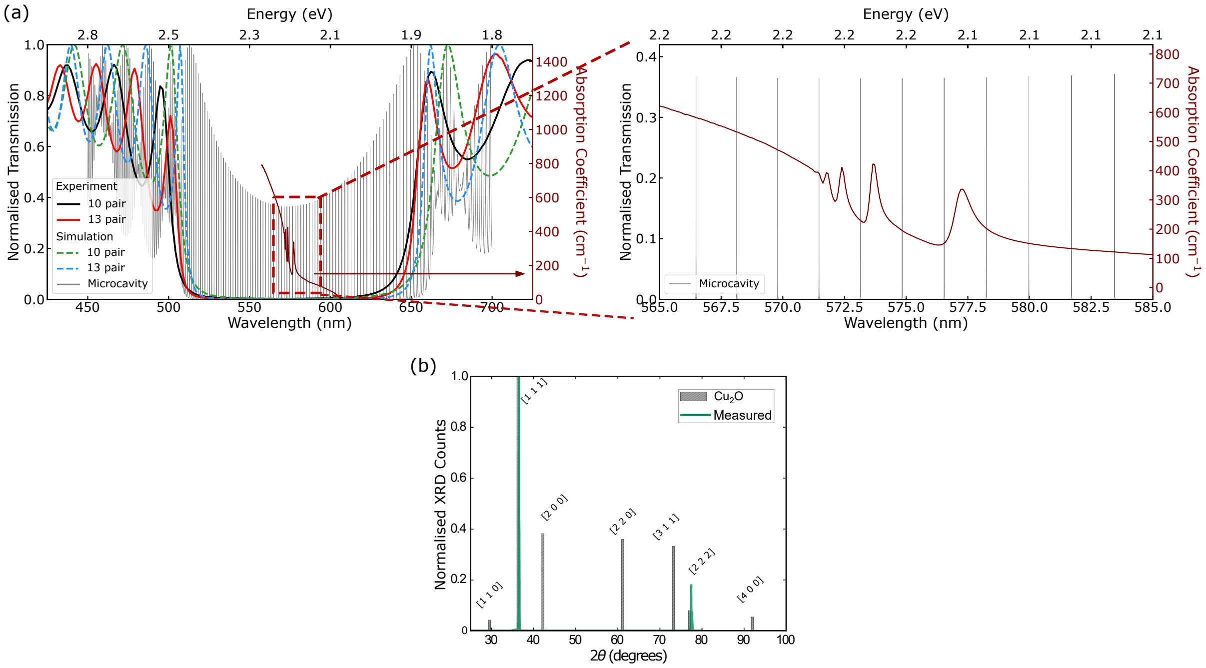

Figure 3.6: (a) Left panel: Experimental (solid lines) and TMM simulated transmission (dashed lines) through a 10- and 13-pair DBR and a cavity (solid grey line). An experimental absorption spectrum of a 75 µm thick Cu_2O crystal taken in a low spectral resolution broadband measurement (solid maroon line) is also overlaid (right axis). Right panel: Zoomed-in version at the vicinity of the yellow P excitons of Cu_2O. (b) Experimental X-ray diffraction spectra of the Cu_2O crystal in the microcavity (green) overlaid on a theoretical spectrum from cubic Cu_2O (grey) extracted from literature [305].

peak positions from a cubic Cu_2O crystal [305] (shown as grey bars in Fig. 3.6) confirm that the Cu_2O crystal was cut and polished along the [111] crystal axis.

3.2 Experimental Setup

3.2.1 Optical Spectroscopy

Optical spectroscopy is a powerful tool for probing the electronic and optical properties of materials. It is at the core of light-matter interaction research as it enables studying the optical response of the electronic structure of a material. Two spectroscopic techniques were mainly used in this work: absorption and photoluminescence. Absorption of spectrally-broad light is determined by the spectral features (resonance energy, lineshape, etc.) of optical transitions and hence can give insights into the electronic and phonon structure of a material. Complementary to the information obtained via absorption, photoluminescence spectroscopy investigates the emission properties. The following five sections describe the implementation of these two techniques in the experiments of Chapters 5 and 6.

3.2.1.1 Absorption Spectroscopy

The absorption of light by an optical medium is quantified by its absorption coefficient, defined as the fraction of the power absorbed in a unit length inside the medium. In this thesis, the absorption coefficient of bulk and NPs of Cu_2O was measured using broadband absorption spectroscopy. Specifically, light of a specific wavelength range is directed onto the sample, and the transmitted light is recorded and spectrally analysed by a spectrometer at the other end. Neglecting reflection, the transmission through a material T can be modelled with the Beer's law [36]:

$$T = \frac{I}{I_0} = e^{-\alpha \cdot d}\,, \tag{3.1}$$

where $\alpha = \alpha(\lambda)$ is the wavelength-dependent absorption coefficient, d is the thickness of the material, I is the transmitted intensity, and I_0 is the input intensity. Equation 3.1 assumes weak optical nonlinearities and therefore it is only valid for low intensities [36]. The intensity I_0 can be approximated by measuring the transmitted intensity at a position away but close to the sample. Losses due to reflectance at the air$-$$Cu_2O$ (first) and $Cu_2O$$-$air (second) interfaces should be taken into account by considering the reflectance at the interface R_{intf}, between two lossless media with refractive indices n_1 and n_2 at normal incidence [306]:

$$R_{\mathrm{intf}} = \left(\frac{n_2 - n_1}{n_2 + n_1}\right)^2 . \tag{3.2}$$

For air ($n_{\mathrm{air}} \approx 1$) and Cu_2O ($n_{\mathrm{Cu_2O}} \approx 3$ [304]), reflectance is estimated $R_{\mathrm{intf}} \approx 0.25$. The corresponding transmittance is $T_{\mathrm{intf}} \approx 0.75$. Therefore, there is ~25% loss of intensity at each interface due to reflection, or, equivalengtly, only ~75% of the incident intensity is trasmitted. Equation 3.1 now reads:

$$T = \frac{I}{I_0} = T_{\mathrm{intf}} \cdot e^{-\alpha \cdot d} \cdot T_{\mathrm{intf}} = T_{\mathrm{intf}}^2 \cdot e^{-\alpha \cdot d} = 0.75^2 \cdot e^{-\alpha \cdot d} \approx 0.56 e^{-\alpha \cdot d}\,. \tag{3.3}$$

3.2.1.2 Photoluminescence Spectroscopy

Photoluminescence (PL) is the emission of light from a material under optical excitation of higher energy. Photoluminescence spectroscopy is a powerful tool for characterising the opto-electronic properties of semiconductors. Analysing the spectrum of the emitted light can provide information about the band structure of a material, its composition, overall quality (impurity and defect levels) and other carrier-related phenomena such as transport, relaxation, recombination, and exciton formation.

In a typical photoluminescence experiment, a probe light beam of relatively high-energy photons is focused on the sample, and the emitted photons, usually at lower energy, are collected and analysed by a spectrometer. The optical path layout of a photoluminescence measurement is, therefore, quite similar to an absorption measurement. A critical difference between the two spectroscopic methods is that the emitted photons during photoluminescence can be collected from any side of the sample, either the front side where the probing light incidents, the back side, or the edges. As outlined in Section 3.2.1.5 and Fig. 3.8, in this work, photoluminescence is collected in a backscattering geometry, i.e. from the same side as the excitation radiation.

The physical process behind photoluminescence in a direct gap semiconductor, illustrated in Fig. 3.7(a), consists of the following three major steps [36, 37, 48, 306]:

1. **Excitation**: An external photon with energy $\hbar\omega'$, usually higher than the bandgap E_g of the semiconductor, excites an electron from its initially occupied valence band state to an empty conduction band state, thus forming an electron-hole pair.

2. **Thermalisation**: The photoexcited electron and hole relax towards lower energy states before reaching quasi-thermal equilibrium with the lattice close to the CB and VB edge states. This process is depicted as a cascade of transitions with the bands in Fig. 3.7(a). Each step corresponds to the emission of a phonon with the appropriate energy and momentum to satisfy the conservation laws.

3. **Radiative recombination**: The energy-relaxed electron and hole recombine as the electron at the CB edge state transits to the empty VB edge state, radiatively emitting a photon with energy approximately equal to the bandgap energy $\hbar\omega \approx E_g$.

The electron-phonon coupling in most solids is very strong, and electron-hole pairs thermalise on time scales as short as ~100 fs. Radiative lifetimes are in the nanosecond range; therefore, carriers are able to relax by phonon emission before recombination [36].

The optical wavelength $\lambda = c/f \approx 300 - 700$ nm is orders of magnitude larger than the lattice constant α, which is usually of the order of a few Å. Consequently, the magnitude of the photon wavevector $2\pi/\lambda$ is negligible compared to the characteristic dimension of the Brillouin zone $2\pi/\alpha$. As a result, the momentum of the emitted photon can be neglected. Conservation of momentum dictates that the electron and hole that recombine must have the same $\mathbf{k}$ vector; that is why the transition is represented by a downward vertical arrow on the band diagram of Fig. 3.7(a).

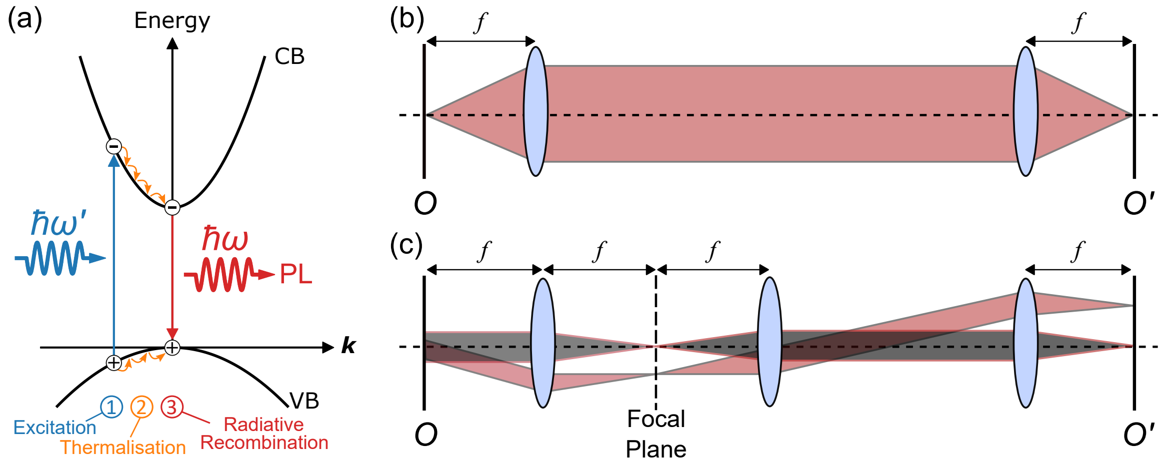

Figure 3.7: Schematic illustration of (a) The photoluminescence in a direct gap semiconductor. A probing photon with energy $\hbar\omega'$ excites an electron to the CB, leaving behind a hole in the VB (Excitation step, shown in blue). The photo-excited electron and hole relax to their respective band edge states (Thermalisation step, shown in orange). The energy-relaxed electron and hole recombine radiatively to emit a photon with energy $\hbar\omega < \hbar\omega'$ (Thermalisation step, shown in red). (b) Real-space imaging, where a position at the object plane O corresponds to a position at the imaging plane O' and (c) Fourier-space imaging, where a direction at the object plane O corresponds to a position at the imaging plane O'.

In reality, however, the recombination of the electron-hole pair can also be non-radiative, such that the energy from the electron-hole recombination is transferred to the crystal lattice. Materials contain defect levels within the bandgap due to intentional or unintentional doping agents, crystal defects, and dislocations. These defect energy levels have a strong tendency to capture carriers temporarily as an intermediate step before the completion of the recombination process; a carrier is first captured at this energy level and then makes an annihilating transition to the opposite band. When captured electrons and holes recombine radiatively at these levels, defect luminescence is manifested as additional, usually broad in linewidth, lines in the PL spectrum. Such defects are known as radiative recombination centres; otherwise, they are referred to as non-radiative traps. In the latter case, the excess energy is released as thermal energy (heat), or equivalently, phonons are emitted [37]. Additionally, during an Auger-type process, excess energy can be transferred to a third carrier which is then excited to higher energy levels within its respective band. This highly energetic carrier then thermalises back down to the band edge through collisions with the semiconductor lattice. Overall, the eventual luminescence power of a semiconductor is the result of the interplay between radiative and non-radiative recombinations of the electron-hole pairs. If non-radiative processes occur at a faster rate than radiative transitions, very little light will eventually be emitted [36, 306].

In this work, two configurations were routinely used to map sample surfaces (imaging) or analyse light signals (spectroscopy and interferometry): real-space and k-space imaging and spectroscopy, as described below.

3.2.1.3 Real-Space Imaging and Spectroscopy

In a typical setup for real-space imaging (or similarly spectroscopy), as schematically illustrated in Fig. 3.7(b), the excitation beam is focused on the sample surface with a lens (usually an objective). The same lens is also used for collecting the emitted signal. The collected light is then sent to the imaging lens, which focuses the image of the sample surface on the entrance slit of a spectrometer or to a camera. As shown in Fig. 3.7(b), a position at the sample surface plane O corresponds to a position at the imaging plane O'.

3.2.1.4 k-Space Imaging and Spectroscopy

k-space, also called Fourier- or momentum-space, imaging is a commonly used technique for characterising polariton modes in microresonator systems. A schematic picture of this experimental setup is presented in Fig. 3.7(c). Simple ray tracing arguments show that when using a lens for imaging the surface of a sample, the back focal plane of this lens corresponds to the Fourier Plane. This plane has the characteristic property that each point corresponds to one specific angle of emission, independently of the exact real-space origin in O.

As mentioned in Section 2.2.3, the angle of photon emission out of a cavity (angle with respect to the surface normal) directly corresponds to the in-plane momentum of its emitter inside the cavity (Eq. 2.33). Additionally, the energy of the emitted photons is equal to the energy of the intracavity polaritons due to energy conservation laws. Consequently, studying k-space emission allows us to access all this information and measure the dispersion of polariton modes.

Note that imaging the Fourier plane requires one more lens of focal length f compared to the setup used for the real-space imaging, which has to be placed at a distance f from the Fourier plane.

3.2.1.5 Optical Setup

The optical setup used for the absorption and photoluminescence measurements of Chapters 5 and 6 is schematically illustrated in Fig. 3.8(a). It was used for measurements on bulk and NPs of Cu_2O as well as the Cu_2O microcavity. Part of this setup was used for measuring the coherence of exciton-polaritons in the GaAs microcavity (See Section 3.2.2 for a full description of the interferometry setup).

To measure the absorption coefficient of Cu_2O (both in bulk and nanoparticle form), we used

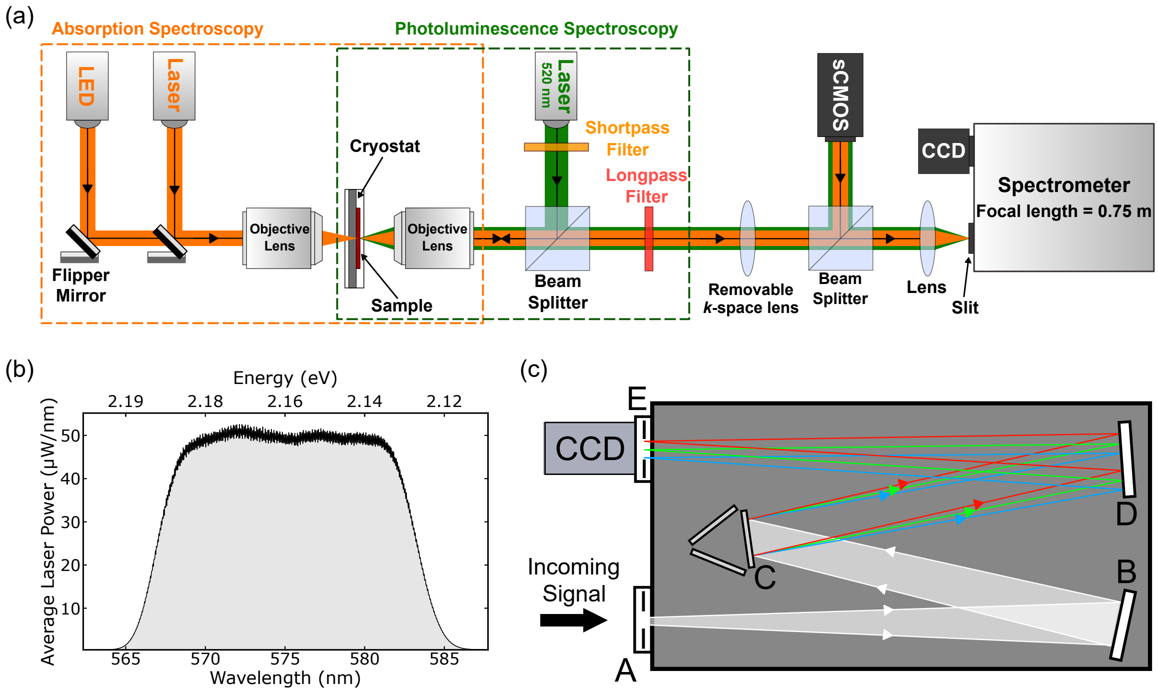

Figure 3.8: (a) Schematic representation of the optical setup used for absorption and photoluminescence measurements. Distances are not drawn to scale. (b) The average power of the broadband NKT laser expressed in µW/nm. (c) Schematic representation of a Czerny-Turner configuration, adapted with permission from Andor.

a broadband green-yellow light-emitting diode (LED) with a centre wavelength of 554 nm (Thorlabs MINTF4). The LED is coupled with a 200 µm optical fibre (Thorlabs M25L02 - Ø200 µm, 0.22 NA), resulting in a typical output power of ~8.5 mW.

For all measurements on the Cu_2O microcavity sample, a broadband femtosecond white laser (NKT Laser SuperK EXTREME EXU-6) was used. The laser was spectrally filtered by an acousto-optic modulator (See Section 3.2.2.3) run at 10% amplitude to create a top-hat excitation from 568 to 582 nm in wavelength [See Fig. 3.8(b)]. Specifically, wavelength tuning is electrically controlled through the application of radio-frequency (RF) signals. When a sinusoidal RF input signal is applied to the modulator, diffraction is limited to a narrow range of optical frequencies, where a phase-matching condition involving both optical and acoustic waves is fulfilled. The filter essentially works in two ways: the diffracted light functions as a bandpass filter, while the non-diffracted light acts as a notch filter. In this work, a NKT SuperK SELECT was used a multi-channel tunable filter, giving access to up to eight simultaneous, freely tunable wavelength channels. The laser has a repetition rate of 78.1 MHz and ~5 ps pulse duration.

For PL studies, a green laser diode (Osram Opto PLT5 520B 80mW) emitting at 520 nm is used in a back-reflection geometry, in which photoluminescence is collected from the same spot on which the exciting beam is focused by an objective lens. A short pass filter with a cut-off wavelength of 550 nm is placed right after the laser diode to block unwanted, higher-in-energy laser lines. A long pass filter with a cut-off wavelength of 550 nm is used to block the back-reflected laser emission at 520 nm from entering the spectrometer.

For absorption spectroscopy, an objective lens (20x Mitutoyo Plan Apo, NA = 0.42) focuses the excitation light to a spot on the sample (~100 µm diameter for the LED, ~1.5 µm for the NKT). For real-space spectroscopy of the cavity, a planoconvex lens with $f = 25$ mm was used, creating an excitation spot ~3 µm. In all cases, an objective lens (Mitutoyo BD Plan Apo 20x, NA = 0.42) collects and collimates the transmitted light from our sample.

The emitted signal from all samples in this work is collected, dispersed, and analysed using an Andor Shamrock 750 spectrometer. It has a 750 mm focal length (f/9.7 aperture) and is equipped with three diffraction gratings on its turret: 150 g/mm, 1200 g/mm, and 1800 l/mm. The vast majority of spectra used in this thesis were obtained using the 1800 l/mm grating, which gives the highest spectral resolution. This grating is optimised for the wavelength range 350-900 nm, and its resolution at the yellow exciton transitions is 0.03 nm (~112 µeV). The wavelength accuracy is ±0.016 nm.

The geometry of the spectrometer is shown in Fig. 3.8(c). It is a standard Czerny-Turner design, where the incoming signal is focused at the entrance slit (A). The slit is placed at the focal point of a parabolic mirror (B) that collimates the divergent incoming light (focused at infinity). The collimated light is then diffracted from a reflective grating (C) and is collected by a second parabolic mirror (D), which refocuses the dispersed light on the exit slit (E). In all measurements, the slit was kept as closed as possible (~10 µm) to obtain the highest spectral resolution achievable.

A deep cooled Andor Newton (DU971P-BV) charge-coupled device (CCD) is attached to the exit of the monochromator. The camera utilises the thermoelectric effect to operate at −60 °C for a high signal-to-noise ratio. The CCD sensor contains 1600 (H) × 400 (V) pixels with a pixel size of 16 µm × 16 µm. The camera has a quantum efficiency >90% in the spectral range from 500 nm to 700 nm, with maximum quantum efficiency (>95%) at ~575 nm.

The Andor Newton CCD can also be used for imaging a sample surface or emission signal, without spectral analysis, by keeping the spectrometer slit open and using the zeroth-order mode of the diffraction grating. This mode of operation does not provide any angular dispersion (change in angle with change in wavelength) and is manifested as a typical surface reflection.

However, the spectrometer and the CCD are primarily used for spectral analysis, and a second camera is added for imaging. For this purpose, a beam splitter is placed in the setup so that 50% of the incident light is transmitted towards the spectrometer, and the remaining 50% is reflected to a scientific CMOS (sCMOS) camera (Thorlabs Quantalux CS2100M-

USB). The number of active pixels is 1920 (H) × 1080 (V) pixels, and the pixel dimension is 5.04 µm x 5.04 µm. The camera's quantum efficiency is approximately 60% in the wavelength region from 525 to 625 nm, with a peak quantum efficiency of 61% at 600 nm.

3.2.2 Interferometry

3.2.2.1 Setup Overview

The experimental setup used for the interference measurements of Chapter 4 is schematically presented in Fig. 3.9. It can be conceptionally divided into four main parts:

1. **Laser pattern generation**: A home-made tapered amplifier laser system emitting at 765 nm generates the pump laser beam (shown as a red line throughout the schematic), which is directed onto an acousto-optic modulator (AOM) for amplitude modulation. The final key component is a spatial light modulator (SLM), whose function is to generate the optical potentials for trapping polariton condensates.

2. **Microcavity imaging and emission collection**: A telescope formed by a spherical lens (L4) and a microscope objective is implemented to scale the laser excitation pattern down to micrometre dimensions and project it onto the microcavity sample mounted inside the cryostat. Polariton emission is then collected from the same objective (backscattering geometry) and is directed towards the interferometer. A bandpass filter centred at 800 nm (FWHM = 40 nm) is used to filter out the laser radiation from entering the interferometer and, ultimately, the spectrometer. A removable lens (L5) is included for k-space measurements.

3. **Interferometer**: Temporal coherence measurements are performed by implementing a Michelson interferometer in the mirror-retroreflector configuration. The retroreflector is mounted on a motorised linear translation stage (Thorlabs LTS300/M) equipped with an integrated stepper motor controller, which facilitates the automated movement of the retroreflector for up to 30 cm of translation.

4. **Direct imaging and spectral analysis of real- and k-space**: The last part of the setup allows for the direct imaging (onto the sCMOS camera) and spectral analysis (through the spectrometer) of the two-dimensional real-space or k-space emission from the sample. The spectral resolution of the spectrometer is ∼0.03 nm (∼60 µeV) at the spectral region of the polariton modes (∼800 nm).

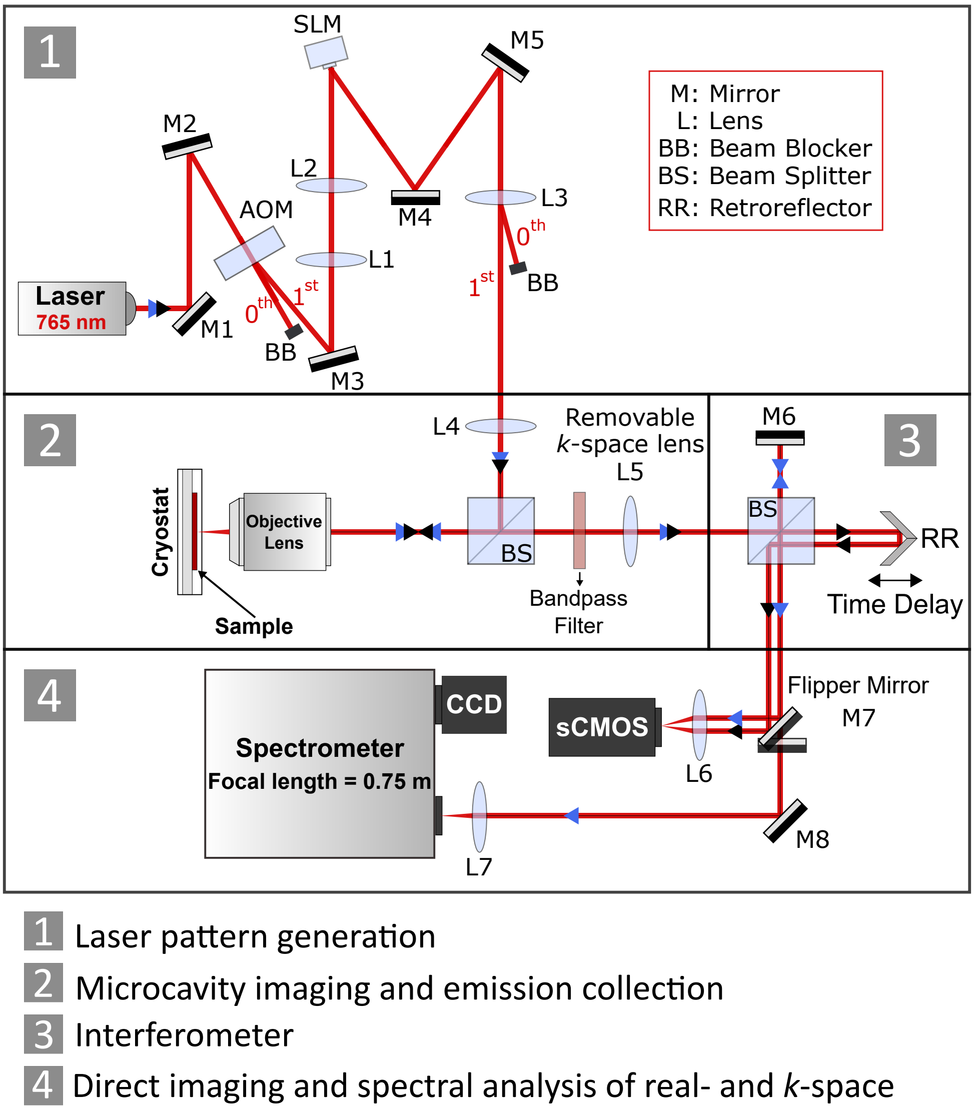

Figure 3.9: Experimental setup for real- and k-space analysis of polariton condensates. The focal length of each lens is: L1 - $f_1 = 50$ mm, L2 - $f_2 = 300$ mm, L3 - $f_3 = 400$ mm, L4 - $f_4 = 200$ mm, L5 (k-space) - $f_5 = 300$ mm, L6 - $f_6 = 700$ mm, and L7 - $f_7 = 200$ mm. For the AOM and SLM, 0^{th} and 1^{st} correspond to the zeroth- and first-order transmission and reflection beams, respectively. The bandpass filter (Throlabs FBH800-40) is centred at 800 nm with a full width at half maximum of 40 nm and is used to filter out the laser radiation at 765 nm. Distances are not drawn to scale.

3.2.2.2 External Cavity Diode Laser and Tapered Amplifier Laser System

The laser system used to optically excite the GaAs-based microcavity sample is schematically illustrated in Fig. 3.10(a). It emits at 765 nm with a linewidth of ~10 MHz and a maximum output of ~2 W. The laser was designed by Dr H. Ohadi and was assembled by the author with the assistance of Dr H. Ohadi.

The system consists of an external cavity diode laser (ECDL) coupled with a tapered amplifier [307–309], mounted on a single baseplate with an enclosure. Specifically, a laser diode emitting at 760 nm (Eagleyard Photonics EYP-RWE-0760-02010-1500-SOT12-0000) is initially mounted in a tube equipped with an aspheric collimation lens with a focal length $f = 4.51$ mm [denoted as L1 in Fig. 3.10(a)]. The external cavity is implemented in a modified Littrow configuration, where the collimated beam is reflected by a diffraction grating, with the first-order diffraction mode retroreflected back into the diode and the zeroth-order used as output [310, 311]. Optical feedback with a narrow-linewidth laser output is thus established between the end facet of the laser diode and the diffraction grating, which form an external cavity.

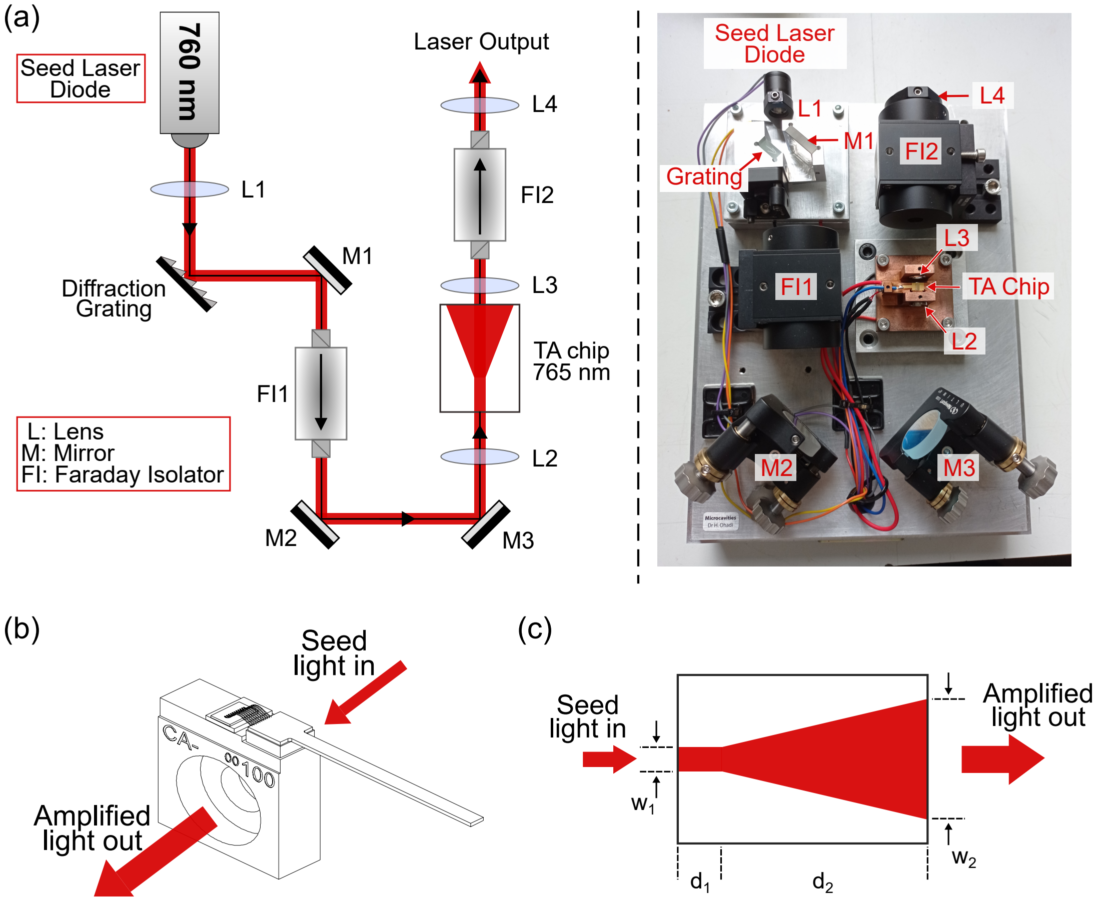

Figure 3.10: (a) Schematic illustration (left) and image (right panel) of the TA laser system. The focal length of the three aspheric lenses L1-3 is $f = 4.51$ mm. For the cylindrical lens L4 $f = 50$ mm. The diffraction grating is a reflective holographic grating with 1800 grooves/mm. (b) Schematic drawing of the TA chip. Image courtesy of Eagleyard Photonics, reproduced with permission. (c) Schematic drawing of the top-view of the TA chip where the straight, index-guided section of the chip of length d_1 and width w_1, and the tapered, gain-guided section of length d_2 and output width w_2 are depicted. Typical values are: $d_1 \approx 0.5$ mm, $d_2 \approx 1.5 - 3$ mm, $w_1 \approx 1 - 3$ µm and $w_2 \approx 200$µm [307].

Moreover, only a narrow range of wavelengths reflects back to the diode for amplification because of the wavelength-selective reflectivity of the grating. However, as the wavelength is tuned, the direction of the output beam changes. For this reason, a mirror (M1) is placed on the same stage as the grating to compensate for grating adjustments. Besides tunability and narrow linewidth, an ECDL constitutes a low-cost and compact laser device offering high stability [312, 313].

Single-mode operation requires that the transverse dimension of the laser diode to be of the order of the optical wavelength, which limits the output power of the ECDL (∼100 mW). This restriction was circumvented by coupling the ECDL to a tapered amplifier (TA). This device amplifies the low output of the seed ECDL, while simultaneously preserving its spectral properties (wavelength, linewidth etc.) [307, 314]. The seed laser beam is initially inserted from a narrow aperture into a short, straight, index-guided section in the TA chip (Eagleyard Photonics EYP-TPA-0765-02000-4006-CMT04-0000) [See Fig. 3.10(b,c)]. The narrow transverse dimension of this region allows for the excitation of only the fundamental transverse mode, thus ensuring a high beam quality. The light radiation is then guided into a longer, tapered, gain-guided region for optical amplification. This region is typically made of a III-V semiconductor (AlGaAs in our case). While in operation, carrier population inversion is established through uniform electrical pumping of the tapered region. Consequently, optical amplification of the propagating beam is achieved through the mechanism of stimulated emission from electron-hole recombination, just as in conventional lasing. An essential requirement for optical amplification is that the wavelength of the tapered amplifier matches the wavelength of the seed laser. For this purpose, a TA chip with a centre wavelength of 765 nm is used for amplifying the ECDL. The laser after the TA has a maximum output of ∼2 W.

The design of the TA chip is such that the propagating beam is freely diverging in the tapered plane until it is emitted through the much wider aperture at the end of the tapered section [See Fig. 3.10(c)]. An aspheric lens (f = 4.51 mm) is placed on either side of the TA chip, the first (L2) for focusing the input and the other (L3) for collimating the vertical component of the output beam. Apart from high divergence, the output beam is highly astigmatic. Therefore, an additional lens with a cylindrical shape (L4) is placed after L3 for collimating the horizontal component of the beam.

A small portion of the amplified radiation is reflected back from the front facet of the TA chip and could disturb the single-mode operation of the seed laser diode. A Faraday isolator (Qioptiq FI-780-5SV, denoted as FI1) is placed between the ECDL and the TA in order to suppress this back-reflected radiation. Furthermore, back-reflections from optical components after the laser system can potentially cause permanent damage to TA chip. To prevent this, another Faraday isolator (FI2) is placed after the TA chip.

Stable operation requires the temperature regulation. Maintaining the temperature of the seed laser diode constant guarantees power and frequency stability. Additionally, the TA chip needs to be actively cooled since ∼10 W of power is electrically pumped into the chip (I = 3.8 A, V = 2.9 V), but only ∼2 W of optical power is extracted. For this purpose, a thermoelectric cooling device is placed below the mounts for both the diode and the TA chip.

Finally, our laser system offers several advantages compared to other lasers commonly used within the polariton community, e.g., Ti:sapphire [125, 217, 300, 315, 316]. Most importantly, low-intensity noise operation makes it an ideal laser system for interferometric measurements. Because random fluctuations in the laser power are minimised, the dephasing induced by our apparatus is minimised as well. This, in fact, has been demonstrated using a solid-state laser diode pump [153]. Moreover, the ECDL coupled with the TA laser is a compact device (all components mounted on the same enclosable baseplate) with a low construction cost (∼£7500) and low maintenance. On the flip side, its tuning range (∼10 nm) is considerably less than that offered by Ti:sapphire lasers (∼100 nm) [317].

3.2.2.3 Acousto-Optic Modulator

The purpose of the acousto-optic modulator (AOM) in our setup is twofold: it acts both as a beam-chopper for pulsed operation and as an intensity modulator for electronically controlling the pump power. Its operation is largely dependent on an external driver, which generates a radio-frequency (RF) signal that is converted to an acoustic wave within the crystal of the AOM, propagating perpendicularly to the laser beam. The mechanical stress induced by the acoustic wave leads to the formation of a grating pattern in the refractive index profile of the AOM crystal, at which light can experience Bragg diffraction [318]. For our measurement, the first-diffraction order is selected with a diffraction efficiency ∼85% [319].

During pulsed operation, exciting the sample and recording its emission requires the combined operation of three components: the AOM (AA Opto-Electronic MT80-A1.5-IR) and its driver (AA Opto-Electronic MODA80-B4-34), a function generator, and the camera. The AOM driver is connected to the output terminal of a function generator, which is set to produce rectangular waveforms [See Fig. 3.11(a)]. Its amplitude regulates the pump power, and its duty cycle acts as a chopper, producing pulses of defined duration (usually ∼50 µs in our experiments). Moreover, the function generator has an external trigger input terminal connected to the sCMOS camera. When set to capture an image, the camera sends an input signal to the function generator used to trigger its output. Once the trigger signal is sent, the camera will stay active for the whole duration of the input pulse; hence the whole polariton emission will be recorded. The rise time of the AOM is measured to be ∼40 ns [See Fig. 3.11(b)].

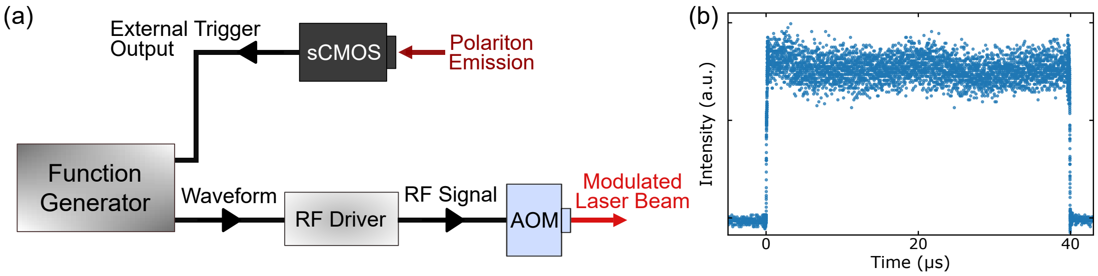

Figure 3.11: (a) Schematic representation of the triggering mechanism. (b) Laser pulse (blue dots) with a duration equal to 40 μs. The rise time of the pulse is calculated ∼40 ns.

3.2.2.4 Spatial Light Modulator

A spatial light modulator (SLM) is implemented to phase-shape the pump laser beam and therefore produce arbitrary intensity patterns on the sample. In this work, the SLM (Hamamatsu LCOS-SLM X10468) is based on liquid crystal on silicon (LCOS) technology (LCOS-SLM) and consists of an array of voltage-controlled liquid crystal cells, each constituting a pixel in an 800 × 600 pixel display. The birefringent molecules are initially parallelised but tilt according to an electric field which can be controlled pixel by pixel. A difference in tilt angles results in a change in refractive index. This, in turn, changes the optical path length in the liquid crystal layer; therefore, the light will experience a voltage-dependent phase shift [320]. Because all pixels can be addressed individually, spatially varying phase patterns can be imprinted on the pump laser.

Modulating the phase of the pump laser with an SLM causes it to be diffracted, similar to a conventional grating. A Fourier lens, i.e. a lens which is separated by its focal length f from both the SLM and the desired image (sample) plane (See Section 3.2.1.4), is then used to focus light with a specific angle of incidence to a corresponding spot in the image plane, thus translating diffraction angles (reciprocal space) to spatial position (real space).

In this work, the so-called *mixed-region amplitude freedom* (MRAF) algorithm [321] was used to create the laser pattern. This algorithm allows the generation of clean, high-resolution laser patterns (∼2 μm on the sample surface), at the cost of a relatively low efficiency (∼20% of the incident laser power). A computer program to control the SLM based on the MRAF algorithm, originally implemented by Dr H. Ohadi, is used to shape the excitation pattern.

3.2.3 Cryogenic System

Temperature is an important factor when studying excitonic/optoelectronic mechanisms in semiconductors. At elevated temperatures (>80 K), PL emission is usually broad in width, and its intensity is thermally quenched. Performing PL measurements at cryogenic temperatures can yield information about excitonic states that would otherwise be hidden by thermal effects at elevated temperatures [36].

For these reasons, the optical setup described in Sections 3.2.1.5 and 3.2.2.1 was coupled with a cryogenic system to perform optical measurements at 4 K. The cryogenic system, schematically illustrated in Fig. 3.12, consists of five main parts: the cryostat (Oxford Instruments MicrostatHe), the transfer line (Oxford Instruments LLT700/13 - Transfer Tube: 1.3m Dewar Leg. 1.3m Flexible Section), a liquid helium storage dewar (Wessington Cryogenics CH-120), the temperature controller (Oxford Instruments MercuryiTC), and the recovery system.

The cryostat is a continuous helium-flow cryostat that performs in the temperature range from 3.2 K to 500 K. The cryostat has a short working distance (as low as 4.5 mm) and is configured for reflectance and transmission measurements. Liquid helium is continuously transferred through a high-efficiency superinsulated line to a copper sample mount inside the cryostat vacuum space. A needle valve is incorporated in the transfer line and is used to regulate the flow of cryogens to the sample mount. One end of the transfer line is inserted into the cryostat, while the other end is inserted into the He storage dewar. The dewar consists of a He reservoir, surrounded by a vacuum jacket, which isolates the reservoir from the ambient conditions of the room. Helium flow through the system is controlled through a flow meter (Oxford Instruments VCU Helium and Nitrogen Gas Flow Controller). Vaporised helium used in the process is recaptured and directed to a helium recovery system for reliquification.

Proper operation of the cooling system requires that the cryostat is in a vacuum. Vacuum inside the cryostat provides effective thermal insulation, resulting in shorter cooldown times, lower temperatures in the sample mount and lower He consumption. For this purpose, a turbo pump (Adixen MDP 5011) is used to evacuate the cryostat chamber to a pressure $< 10^{-5}$ mbar before the start of cooling. The temperature of the sample holder can be live-tracked and controlled with the MercuryiTC temperature controller.

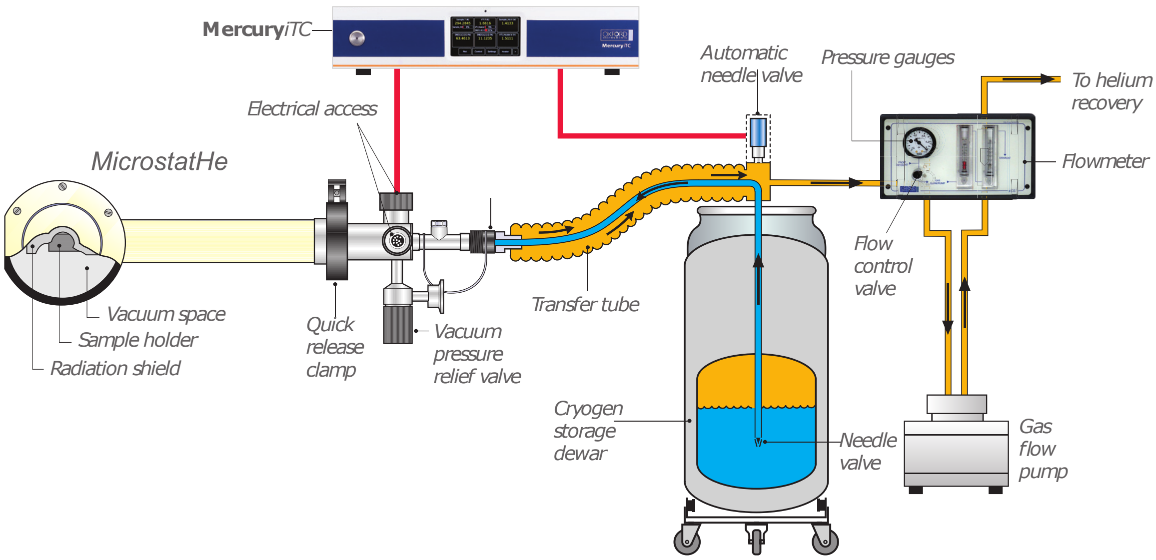

Figure 3.12: Schematic illustration of the cryogenic system. The main components are the cryostat (MicrostatHe), helium storage dewar, temperature controller (MercuryiTC), and gas flow pump. Image courtesy of Andor, reproduced with permission.

3.2.4 Miscellaneous

3.2.4.1 Optical Microscopy

Optical microscopy is an imaging technique that uses visible light and a system of lenses to generate magnified images of objects. Optical microscopy was routinely used during polishing (described in Section 3.1.1) to assess the surface quality and thickness of Cu_2O crystals [See Fig. 3.1(a-d)], as well as imaging clusters and single Cu_2O particles [See Figs. 3.2(c)]. All images in this work were taken from a commercial microscope (Nikon Eclipse LV100ND) using a reflected light microscopy configuration, where the sample is illuminated by light passing through an objective and light reflected by the sample surface re-enters the objective to be directed to the eyepieces or a camera.

Conventional optical microscopes are usually equipped with a white light source (wavelengths in the visible range from 400 to 700 nm). Consequently, the limited resolving power of visible light makes optical microscopes incapable of resolving features below $\sim$0.5 µm - depending on the wavelength and refractive index of the sample or the media. The maximum magnification achievable with our optical microscope is $\sim$100x.

Two illumination techniques were implemented: bright-field (BF) and dark-field (DF) spectroscopy. In BF microscopy, the simplest of all illumination techniques, illumination light is focused on the sample, and the reflected signal is collected by the same objective lens. Optical contrast is generated due to different reflection properties between the different features of the sample or between sample and substrate.

On the other hand, DF spectroscopy operates by removing the zeroth order, unscattered reflection and collecting only the backscattered light (by reflection, refraction, or diffraction) from the sample. Object detail responsible for the scattering appears bright on a dark background [322].

DF microscopy was used during polishing to better visualise surface features, such as scratches and surface defects, as these entities scatter more light than the surrounding smooth polished surface. Additionally, DF microscopy enhances the signal contrast, thus allowing us to probe single Cu_2O nanoparticles, which would otherwise be impossible to detect due to their small size.

3.2.4.2 Scanning Electron Microscopy

Scanning electron microscopy is an electron imaging technique used to characterise the morphology and microstructure of bulk materials. A scanning electron microscope (SEM) projects and scans a focused stream of electrons over a surface to create a high-resolution image. The electrons are scattered by the interactions with the atoms in the sample, producing various signals that can be used to obtain information about surface topography and composition.

SEM enables higher magnification and imaging resolution than optical microscopes since electrons have a much shorter wavelength than visible light, thus allowing smaller details to be resolved. The most sophisticated SEMs can achieve magnifications of around 100,000x and sub-nanometre resolutions [323, 324].

SEM (Hitachi S-4800) was used to acquire high-resolution close-up images of nanoparticle clusters, as in Fig. 3.2(a,b). A cross-sectional SEM image of the GaAs-microcavity, taken at the group of Pavlos Savvidis at the IESL-FORTH, is shown in Fig. 3.3.

3.2.4.3 X-Ray Diffraction

X-ray diffraction (XRD) is a technique used to determine the crystallographic structure of materials. Specifically, it can reveal structural information, such as chemical composition, crystal structure, crystallite size, strain, preferred orientation, and layer thickness.

XRD is based on the constructive interference of monochromatic X-rays and a crystalline material. Specifically, X-rays are collimated and directed onto a sample, where they are subsequently scattered by electrons of atoms present in the sample. Since X-rays have wavelengths (between 0.2 and 10 nm) comparable to the interatomic spacing of a crystalline solid, the incident X-ray beam diffracts in specific directions and constructively interferes, as predicted by Bragg's law. The intensity of the diffracted rays scattered at different angles of material is detected, processed, and plotted to display a diffraction pattern [325, 326].

XRD measurements presented in Fig. 3.6(b) were recorded on a Bruker D8 Advance X-Ray diffractometer with a Cu Kα anode (λ = 0.1542 nm) operating at 40 kV and 30 mA. The diffraction patterns were collected at room temperature and over an angular range of 25 to 80° with a step size of 0.02° per step and at a scan rate of 2.75° 2θ per minute.

This page is intentionally left blank.

Chapter 4

Ultralong Temporal Coherence in Optically Trapped Exciton-Polariton Condensates

The topic of this chapter is the temporal coherence of an optically trapped polariton condensate in a GaAs-based microcavity. Quantum coherence is the defining feature of lasers and light sources in general. Linewidth and intensity noise are two basic parameters of a laser, corresponding to the temporal first- and second-order coherence functions, respectively. The first-order coherence function, which is the most relevant for this work, characterises the phase coherence and quantifies how the phase of the electric field fluctuates in time. Coherent light emission from a polariton condensate, a coherent, thermodynamically favoured many-body state occurs at a much lower carrier density than the population inversion density required for conventional lasers. Additionally, spatial confinement of the condensate in an optical trap is expected to increase temporal coherence as the condensate is largely decoupled from the thermal, decoherence-inducing exciton reservoir. A direct result of this decoupling is a reduction of noise accompanied by linewidth narrowing of the condensate emission. If the narrowing is strong enough, the condensate linewidth may approach the nonlinearity constant, and the system may enter the single-polariton nonlinear regime, provided the cavity linewidth is narrow enough.

First, the mechanism of optical trapping and its implementation are discussed in Section 4.1. Then, the PL emission of the microcavity is studied in Section 4.2, demonstrating that light emission in this work originates from a polariton condensate rather than a photon laser. The temporal evolution of coherence from a trapped condensate is compared to the untrapped case in Section 4.3. Interestingly, due to the reduction of the spatial overlap with the thermal reservoir of excitons, the coherence time of the trapped condensate is more than an order of magnitude longer than that of an untrapped condensate, accompanied by periodic beats of the field correlation function. A theoretical model for the description of coherence stemming from trapped condensates is developed in Section 4.4, assuming the existence of two energy-degenerate condensate modes responsible for the periodic beating of the correlation function. Achieving single-polariton nonlinearity in the optical confined condensate system is discussed in Section 4.5. The existence of the two condensate modes is further studied experimentally through polarisation-resolved measurements in Section 4.6, while the temporal decay of coherence in different sample positions is briefly discussed in Section 4.7. Finally, Section 4.8 gives a summary of the experimental and theoretical findings.

The experiments presented in this chapter were performed by the author under the supervision of Dr H. Ohadi and have been published in Ref. [124]. The microcavity was fabricated by P. G. Savvidis at the University of Crete. The theoretical model was developed by A. F. Tzortzakakis and D. Petrosyan.

4.1 The Optical Trap

The sample used for probing the coherence of optically trapped polariton condensates was the $5\lambda/2$ GaAs microcavity described in Section 3.1.3.1, where polariton condensation under nonresonant optical pumping was previously observed [150, 217, 300]. The excitation source in this work was the single-mode quasi-continuous-wave diode laser system composed of an external cavity diode laser seeding a tapered amplifier (see Section 3.2.2.2). The excitation wavelength is blue-detuned by ∼100 meV from the first Bragg mode of the microcavity's stopband. The AOM is used for laser power modulation and generation of 60-µs-long pulses (See Fig. 3.11). The pulse duration is much longer than the rise/fall time of the AOM (∼40 ns) and is significantly longer than the condensate formation time (∼100 ps) so that the condensate can be treated as stationary. The excitation duration is much shorter than typical vibration time scales (∼1 ms), indicating that active stabilisation of the interferometer is not required [28].

The optical trap is implemented by patterning the laser radiation on the microcavity using an SLM (See Section 3.2.2.4), similar to previous works [24, 84, 217, 300]. Specifically, the trap consists of six individual pump spots shaped into a hexagonal pattern of diameter ∼7.5 µm [shown as dashed orange circles in Fig. 4.1(a,b)]. The mechanism of optical confinement was presented in Section 2.4.7. When the polariton density exceeds the condensation threshold, a macroscopically coherent condensate in the ground state of the momentum space forms in the centre of the trap. The advantage of this method is that it results in a small overlap between the condensate and the hot reservoir at the pump spots. This decoupling of the condensate from the decoherence-

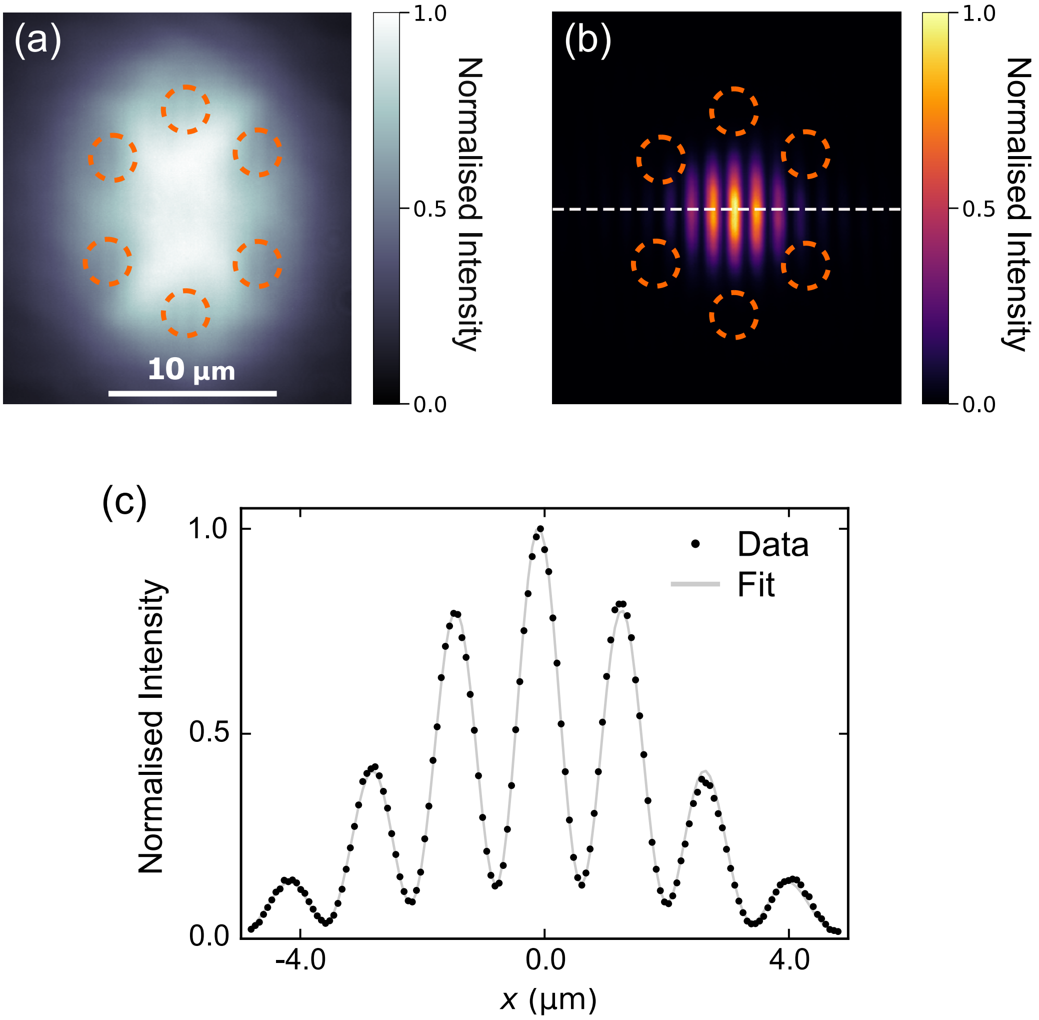

Figure 4.1: Single-shot real-space interferograms (a) below threshold ($\sim 0.75 P_{\mathrm{th}}$) and (b) above threshold ($\sim 2.50 P_{\mathrm{th}}$). The six pump spots of diameter 2.5 µm are shown as orange dashed circles. (c) Horizontal line profile across the dashed line of the interference pattern in (b). The gray line shows the theoretical fit using Eq. 4.1.

inducing reservoir consequently yields a narrower linewidth in optically confined condensates compared to their unconfined counterparts [84]. It is also expected to lead to a higher degree of optical coherence. To realise an untrapped condensate, the pump consists of only one spot and the condensate is formed on top of the reservoir. Note that the optical trap in Fig. 4.1(a) appears slightly elongated towards the vertical axis, even though the MRAF algorithm is set to produce a symmetric hexagon after the SLM. This asymmetry is attributed to astigmatism as the input beam is incident to the SLM at an oblique angle. The asymmetry can be corrected by adjusting the MRAF algorithm to produce an initially elongated beam towards the horizontal direction in a way that counteracts the induced asymmetry towards the vertical axis. However, such correction does not affect the observed temporal decay of coherence in all cases studied and was not implemented for the sake of simplicity.

The coherence of polariton condensates is studied using a Michelson interferometer in the mirror-retroreflector configuration (See the discussion in Section 2.4.6 and a schematic of the optical setup in Section 3.2.2.1). By varying the position of the moving arm and superimposing the image from each arm, interferograms are formed for various time delays. Below the condensation threshold, the emission is incoherent, and no interference fringes are observed, as shown in the interferogram of Fig. 4.1(a). Note that emission from uncondensed polariton originates from the middle of the trap and, interestingly, between the pump spots (orange dashed circles), highlighting the diffusion of excitons and the coupling away from the pump spots. Above threshold, a macroscopically coherent state appears in the centre of the trap, attested by the presence of interference fringes at zero delay[1] [See Fig. 4.1(b)]. The overlap between the pump spots and the interferogram is minimal, proving that the condensate is largely decoupled from the reservoir.

4.2 k-space Imaging of the Condensate

The dependence of photoluminescence on the pump power exhibits three distinct regimes, as shown in Fig. 4.2(a). The low-power regime corresponds to below-threshold, linear polariton emission and shows a linear dependence on the excitation power. The second regime is the onset of condensation at a critical power threshold P_{th}. This transition is manifested as a nonlinear increase in the emission up until $\sim 2P_{\mathrm{th}}$, followed by a sublinear third regime. The power dependence of the PL emission proves that the microcavity does not reach the photon lasing regime and PL emission stems from polariton condensation for the pump powers used in this work (See Section 2.4.3). An interesting feature of this system is the sublinear behaviour of the third regime, contrary to what has been observed for untrapped polariton condensates in the same cavity [150].

The $E(k_{||})$ dispersion curves for three pump powers are shown in Fig. 4.2(b-d). The dispersion curves are measured at a position close to where interferometry measurements were performed and are all normalised to unity. Below the threshold, at a pumping power $P \approx 0.6P_{\mathrm{th}}$ [See Fig. 4.2(b)], emission originates predominantly from the LP branch at non-zero wavevectors, indicating that polaritons do not thermalise completely to the bottom of the LP branch. Interestingly, hints of polariton condensation are shown at $k_{||}$ near zero and blueshifted by ∼0.85 meV relative to the bottom of the LP branch due to polariton self-interactions within the condensate

---

[1] Zero delay corresponds to the case when both arms of the interferometer have equal length.

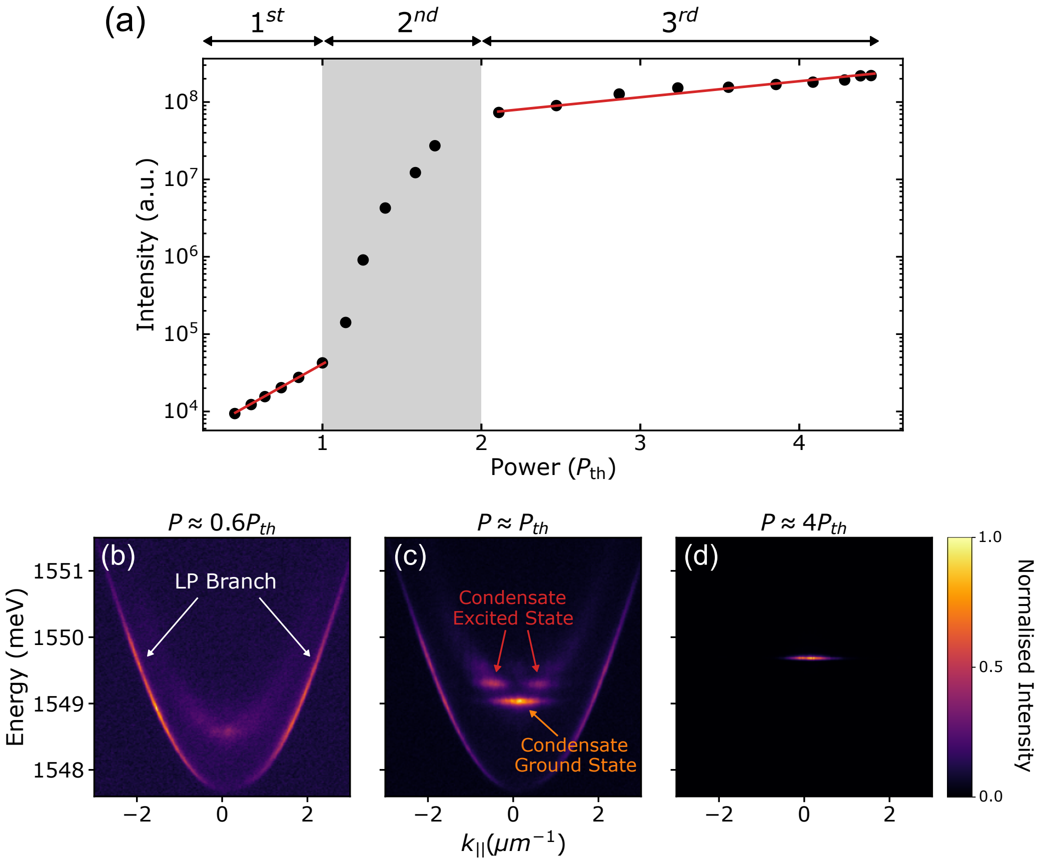

Figure 4.2: (a) Power dependence of the PL emission from the microcavity. Red lines serve as a guide for the eye, illustrating where the emission intensity increases linearly with the pump power, while the gray-shaded area denotes the nonlinear response of the PL emission associated with the onset of polariton condensation. (b-d) Dispersion curves for three pump powers: (b) below threshold at $P_{\text{th}} \approx 0.6P_{\text{th}}$, (c) at threshold $P \approx P_{\text{th}}$, and (d) above threshold $P_{\text{th}} \approx 4P_{\text{th}}$, illustrating all light-emitting entities in the microcavity sample. The intensity in each dispersion curve is independently normalised to one.

mode and polariton interactions with the exciton reservoir [147]. At threshold [See Fig. 4.2(c)], most of the emission comes from the condensed polariton population, which is blueshifted by ∼1.3 meV relative to the bottom of the LP branch. Uncondensed higher-$k_{||}$ polaritons also contribute to the emission from the cavity. Near threshold, the first excited condensate mode can be observed at energies ∼0.3 meV above the ground state one, although much weaker. Note that the energy splitting between the ground state and the excited state is two orders of magnitude larger than the energy splitting responsible for the coherence oscillations discussed in the remaining of this chapter. For higher excitation powers above threshold, mode competition favours condensation on the lowest energy polariton state. At a power $P \approx 4P_{\text{th}}$ [See Fig. 4.2(d)], emission comes exclusively from the condensate, which is further blueshifted by ∼2 meV from the bottom of the LP curve.

4.3 Measuring Coherence of an Optically Trapped Condensated

A line profile across the centre of an interferogram can be fit by a Gaussian function, representing the condensate mode profile, multiplied by a cosine to acquire the fringe contrast [181]:

$$f(x) = A\mathrm{exp}\Big(-\frac{(x-x_0)^2}{2w^2}\Big)(\alpha\mathrm{cos}(kx+\phi)+1)\,, \tag{4.1}$$

where parameters A, x_0, and w are the amplitude, the centre, and the width of the Gaussian function. The parameter α corresponds to the fringe contrast, k to the wavenumber, and ϕ to the phase. Figure 4.1(c) demonstrates an example where the fitted line using Eq. 4.1 perfectly describes the experimental line profile (dots) across the centre of the interferogram of Fig. 4.1(b) (represented by the white dashed line). The fringe contrast is equal to the magnitude of the first-order correlation function $|g^{(1)}(t)|$, where t is the time delay. Since the condensate mode is small, the spatial dependence in the correlation function can be neglected. This observation is attested by the fact that Eq. 4.1 fits the experimental data exceptionally. In the opposite scenario where spatial dependence had to be accounted for, Eq. 4.1 would require an additional factor for the exponential spatial decay of the condensate coherence. To acquire the temporal dependence of the correlation function, the fringe contrast was recorded while changing the time delay. Five realisations of interferograms are averaged for each time delay.

The position of the moving arm that corresponds to zero delay is determined by first creating a polariton cloud slightly below the condensation threshold [$\sim 0.9P_{\mathrm{th}}$, similar to Fig. 4.1(a)], where the emission linewidth is broad, and coherence length is very short (of the order of a few ps). When the two arms of the interferometer have a different length, i.e. away from zero delay, no fringes are observed owing to the small coherence length of the polariton population. On the other hand, the position of zero delay is manifested by the appearance of interference fringes in the middle of the polariton cloud. The fringe pattern appears faint and not as clear as in Fig. 4.1(b) due to the small correlation length below the condensation threshold.

The effect of optical confinement on polariton coherence is revealed by comparing the decay of temporal coherence in the trapped and untrapped condensates, as shown in Fig. 4.3. The latter case is characterised by a rapid decay of the correlation function $g^{(1)}(t)$ (black curve in Fig. 4.3) with a decay time[2] $\tau_G \approx 20$ ps. On the other hand, the temporal correlation function of the trapped polariton condensate (orange curve in Fig. 4.3) does not exhibit a monotonous decay as previously reported for untrapped condensates [153, 181]. Instead, it exhibits a periodic oscillatory decay with a period of ~200 ps. The contrast initially decays rapidly to nearly 0 after 150 ps, but then it recovers to 0.35 after ~100 ps. The insets in Fig. 4.3 illustrate that the

---

[2] The decay time is defined as $1/e$ of fringe contrast.

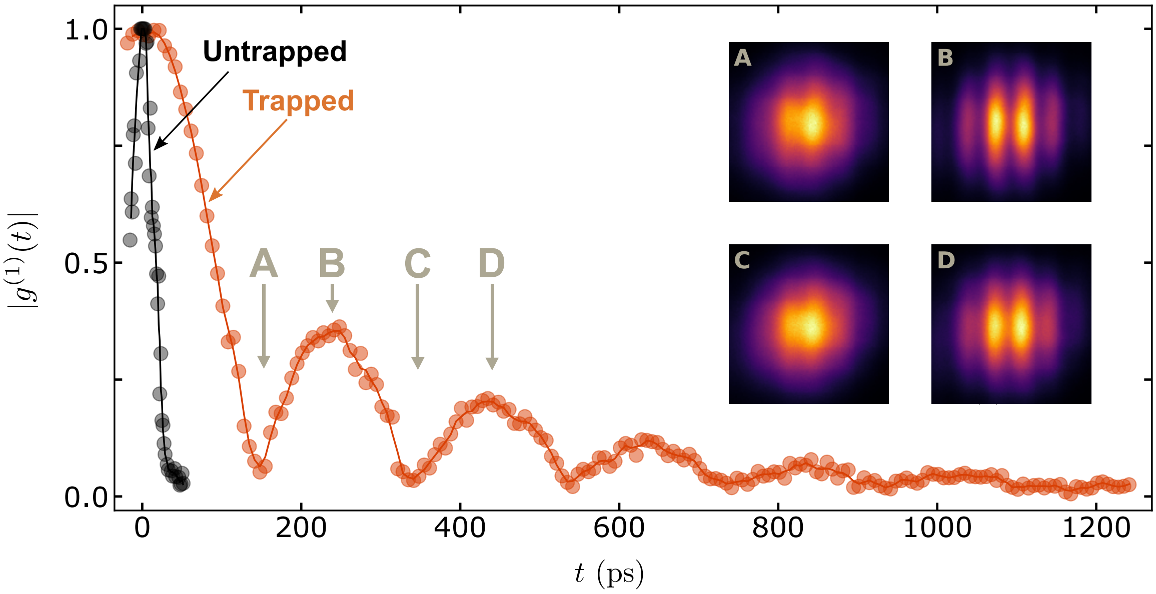

Figure 4.3: Temporal evolution of $|g^{(1)}|$ for an untrapped $P \approx 1.27P_{\text{th}}$ (black circles) and a trapped condensate $P \approx 3.9P_{\text{th}}$ (orange circles). Solid lines are guides to the eye. Inset: interferograms for four time delays (150, 250, 340 and 435 ps), denoted as A, B, C and D.

interferograms corresponding to the first two minima (A and C) have much lower fringe contrast than those corresponding to the first two maxima (B and D). A total of five peaks of $g^{(1)}(t)$ can be observed for up to $t = 1$ ns, approaching the exciton lifetime [327, 328]. Interestingly, a nonzero contrast is observed even for time delays above 1 ns. The coherence time for the trapped condensate τ_{ph} is more than an order of magnitude longer than that for the untrapped condensate, which is due to the significant reduction of the spatial overlap between the trapped condensate and the thermal reservoir of excitons.

The experiments presented here are similar to the ones performed in Ref. [84], where a pump profile shaped into a ring was used to form the optical trap for polaritons. However, the condensate linewidth merely drops from ∼250 µeV in the untrapped condensate to the ∼200 µeV in the trapped case. From the measured linewidth (∼200 µeV) in Ref [84], the coherence time would be ∼20 ps, which is more than an order of magnitude smaller than in the experiments of this work. Additionally, no coherence oscillations are observed in Ref. [84]. This discrepancy is attributed to the different pump laser sources between the two works. In Ref. [84], the laser source was a Ti:sapphire laser, which operates with a high-intensity noise as it is pumped by another external laser. In this work, the ECDL coupled with the TA is associated with a low-intensity noise, which, in turn, minimises the dephasing induced by the apparatus. Consequently, it enables the observation of ultralong coherence times and periodic oscillations of coherence. Moreover, Ref. [84] is probably limited by the resolution of the spectrometer, whereas here a much higher resolution is achieved due to time-domain interferometry and long-time integration.

The temporal decay of the correlation function and the period of oscillations depend on the excitation power, as evidenced in Fig. 4.4(a). The temporal decay of fringe contrast has a similar profile for all pumping powers exhibiting the periodic oscillatory decay behaviour described above. However, increasing the pump power from $2.5P_{\mathrm{th}}$ to $4.3P_{\mathrm{th}}$ leads to decrease in the frequency of oscillations Δ and the dephasing rate $\kappa = 1/\tau_{\mathrm{ph}}$. These two parameters will be later used to develop a theoretical model and explain the temporal evolution of $|g^{(1)}(t)|$ (See Section 4.4).

The power dependence of the coherence time was also measured for the case of an untrapped condensate [see black points in Fig. 4.4(b)]. Specifically, the coherence time is equal to 12 ps just above threshold and almost triples for a pumping power $\sim 2P_{\mathrm{th}}$. This coherence time is more than an order of magnitude smaller than that for trapped condensates at all powers [see blue points in Fig. 4.4(b)].

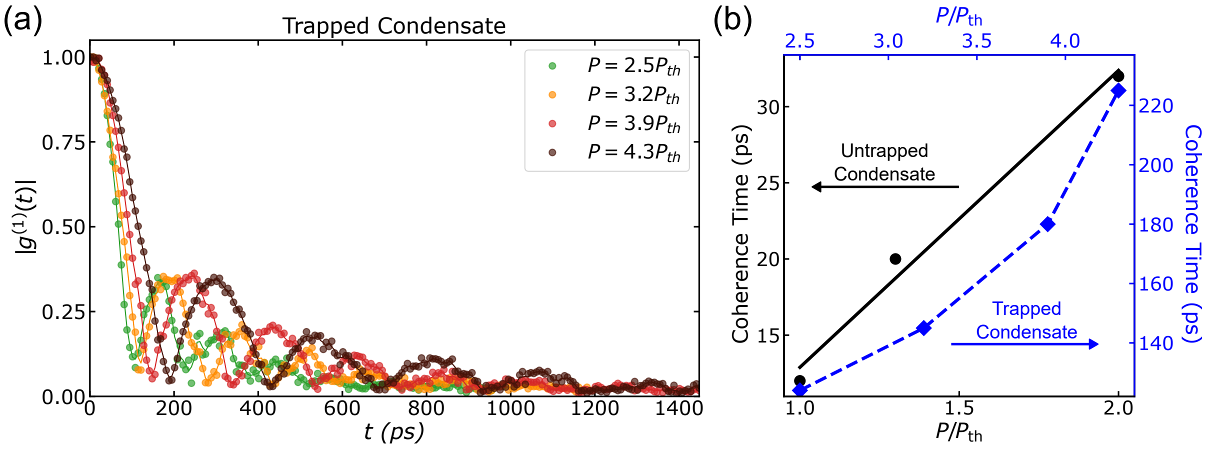

Figure 4.4: (a) Temporal decay of fringe contrast for four pumping powers: $P = 2.5P_{\mathrm{th}}$, $3.2P_{\mathrm{th}}$, $3.9P_{\mathrm{th}}$, and $4.3P_{\mathrm{th}}$. Circles represent experimental points, while solid lines are used as guides for the eye. (b) Power dependence of the coherence time τ_G for the untrapped (black points) and trapped condensate (blue point). The coherence time of the trapped condensate is discussed later in Section 4.4. The lines are used as guides for the eye.

4.4 Theoretical Desciption of Trapped Polariton Condensate Coherence

The theoretical model developed to describe the coherence of optically trapped condensates is based on the presence of an energy splitting between two linear polarisation modes of the condensate. This splitting is attributed to MBE growth-related strain across the microcavity structure and can reach values as large as ∼30 μeV, as previously observed in the present cavity [300]. Additionally, the splitting is tunable by electric fields and is of the order of a few μeV at zero fields [329]. However, direct observation of such splitting is below the current spectrometer sensitivity and requires the interferometry techniques used in this work.

In the circular polarisation basis, the polariton condensate has two energy-degenerate modes ψ_1 and ψ_2 of the polariton condensate with orthogonal circular polarisations $\boldsymbol{\varepsilon}_1$ and $\boldsymbol{\varepsilon}_2$ ($\boldsymbol{\varepsilon}_1 \cdot \boldsymbol{\varepsilon}_2 = 0$) that are coupled via a Josephson coupling. Specifically, the energy splitting between the two polarisation modes in the linear basis becomes a Josephson-type coupling in the circular basis [24, 217]. The field $\boldsymbol{E}(r,t)$ is proportional to the polariton condensate wavefunction, and in this case, is given by $\boldsymbol{E}(r,t) \propto \boldsymbol{\varepsilon}_1\psi_1(t) + \boldsymbol{\varepsilon}_2\psi_2(t)$. Substituting this in the equation for the first-order field correlation function (Eq. 2.58) yields:

$$g^{(1)}(t) = \frac{\langle \psi_1(t+t')\psi_1^*(t') + \psi_2(t+t')\psi_2^*(t')\rangle}{\sqrt{\langle |\psi_1(t')|^2 + |\psi_2(t')|^2\rangle \langle |\psi_1(t+t')|^2 + |\psi_2(t+t')|^2\rangle}} \,. \tag{4.2}$$

The two polariton modes can be described by the generalised Gross-Pitaevskii equation (See Section 2.4.5) as:

$$\partial_t\psi_1 = \frac{1}{2}(R_1N_1 - \gamma_1)\psi_1 - i[\epsilon_1(t) + u_{11}|\psi_1|^2 + u_{12}|\psi_2|^2]\psi_1 + iJ\psi_2 \,, \tag{4.3a}$$

$$\partial_t\psi_2 = \frac{1}{2}(R_2N_2 - \gamma_2)\psi_2 - i[\epsilon_2(t) + u_{21}|\psi_1|^2 + u_{22}|\psi_2|^2]\psi_2 + iJ^*\psi_1 \,, \tag{4.3b}$$

where R_jN_j is the pumping rate of the jth polariton from the reservoir of N_j excitons, γ_j is the polariton decay rate, ϵ_j are the single-particle energies, u_{ij} are the non-linear self ($i = j$) and cross ($i \neq j$) interactions rates, and J is the Josephson coupling between the two modes due to the linear polarisation splitting [330]. As discussed in Section 2.4.5, the above equations are coupled to rate equations describing the dynamics of the incoherent reservoir:

$$\partial_t N_j = P_j - \Gamma_j N_j - R_j N_j |\psi_j|^2 \,, \tag{4.4}$$

where P_j is the thermal exciton pumping rate, Γ_j is the decay (recombination) rate, and R_j is the scattering rate of the excitons into the condensate of polaritons. At steady state, $\partial_t N_j = 0$ yielding $N_j = \frac{P_j}{\Gamma_j + R_j|\psi_j|^2}$. Upon substituting into the polariton equations and demanding that $R_j N_j - \gamma_j \geq 0$, the threshold pumping rate $P_j \geq \gamma_j \Gamma_j / R_j$ can be obtained for non-zero polariton intensity $|\psi_j|^2 > 0$. Above threshold and while neglecting the coupling between the two polariton modes, the average polariton intensity at steady state is then $\bar{n}_j \simeq \frac{P_j}{\gamma_j} - \frac{\Gamma_j}{R_j}$, while the exciton number is $N_j \simeq \frac{\gamma_j}{R_j}$.

Each polariton mode is assumed to be subject to phase fluctuations with a rate $\kappa = 1/\tau_{\mathrm{ph}}$, which would correspond to an exponential decay of polariton coherence. These phase fluctuations are modelled by a Wiener process [331]. Specifically, $\epsilon_j(t)$ in Eqs. (4.3) are assumed to be Gaussian stochastic variables with mean $\langle \epsilon_{1,2} \rangle = 0$ and variance $\sigma_\epsilon^2 = 2\kappa/\delta t$, where δt is the time increment in the simulations of the system dynamics. The polariton modes in Eq. 4.3 are simulated numerically starting with small random seed amplitudes $\psi_{1,2} \neq 0$ at some time t_0. The simulation parameters, all expressed in unit of 1/ps, are $\gamma_{1,2} = 1$, $\Gamma_{1,2} = 0.3$, $R_{1,2} = 0.001$, yielding $P_{\mathrm{th}} = \gamma\Gamma/R = 300$, and thus $P = 2.5P_{\mathrm{th}},\ 3.2P_{\mathrm{th}},\ 3.9P_{\mathrm{th}},\ 4.3P_{\mathrm{th}}$ leading to $\bar{n}_{1,2} = 450,\ 660,\ 870$, and 990 after a short transient. All the nonlinear self- and cross-interaction coefficients are set the same $u_{ij} \equiv u = 2 \times 10^{-4}$, which shifts the mean energy of the polariton condensate but does not change the energy difference between the two polariton modes. The remaining fitting parameters are $J = \Delta/2$, where Δ is the frequency of oscillations, and the dephasing rate κ. The initial values of the seed are unimportant, as after a short transient, a few tens of picoseconds in duration, the polariton populations attain close to the steady-state values $\bar{n} \simeq \frac{P}{\gamma} - \frac{\Gamma}{R}$ determined by the exciton pumping rate (provided $P \geq P_{\mathrm{th}} = \gamma\Gamma/R$).

The correlation functions (Eq. 4.2) are then obtained upon long-time averaging over the system dynamics. The experimental data in Fig. 4.4(a) are fit by setting $J \simeq \Delta/2$ and choosing an appropriate dephasing rate κ for each pumping rate P_j. Therefore, the developed theoretical model in this work has only two fitting parameters, the Josephson coupling strength between the two polarisation modes and the coherence relaxation rate due to phase fluctuations, which reproduce the experimental results remarkably well, as shown in Fig. 4.5(a). The periodic oscillations of the field correlation function correspond to the *beating* of the two eigenmodes split by $\pm J$ and broadened by κ. This is illustrated by the power spectrum of the polariton field $S(\omega)$ given by the Fourier transform of $g^{(1)}(t)$ [See insets in Fig. 4.5(a)]. The spectrum $S(\omega)$ is centered at frequency $u(\bar{n}_1 + \bar{n}_2)$ and split by $\pm J$.

The extraordinarily long coherence time of the trapped polariton condensate allows the observation of energy splittings as small as 16 μeV, which is five orders of magnitude smaller than the energy (chemical potential, 1.54 eV) of the condensate. Our result thus enables high-resolution spectroscopy of polariton condensates, which can be applied to precision tuning of the condensates energies in optical lattices [23, 24] and polariton simulators [332]. The observed

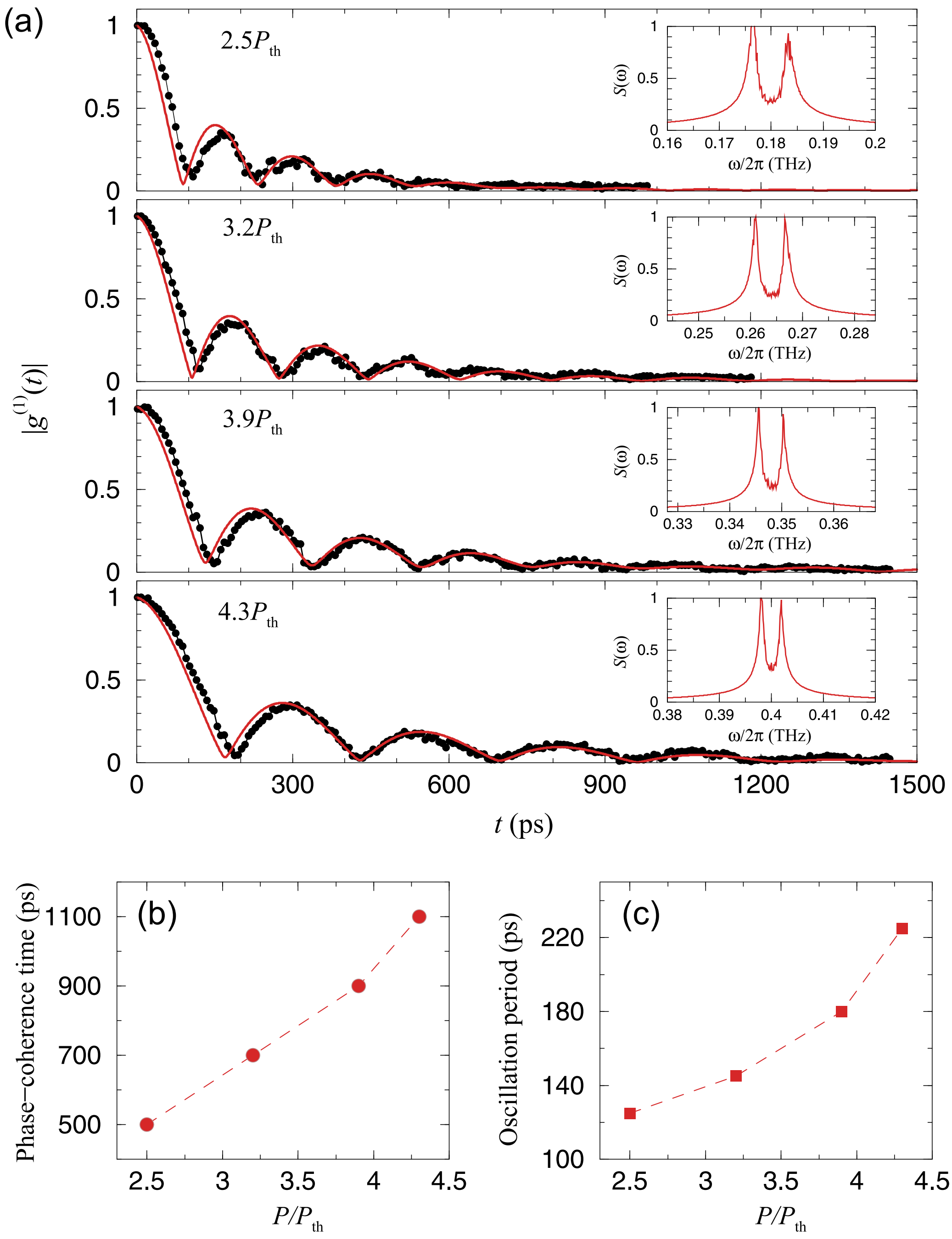

Figure 4.5: Temporal decay of fringe contrast for four pumping powers: $P = 2.5P_{\text{th}}$, $3.2P_{\text{th}}$, $3.9P_{\text{th}}$, and $4.3P_{\text{th}}$. Circles represent experimental points, while solid lines show the correlation function $g^{(1)}(t)$ of Eq. 4.2 as obtained from the numerical simulations of the polariton (Eqs. 4.3 and 4.4), averaged over long integration times. Insets: Power spectrum $S(\omega)$ of the polariton field, as obtained via the Fourier transform of $g^{(1)}(t)$ obtained from the numerical simulations, illustrating the normal mode splitting by $\pm J$ around the central frequency $u(\bar{n}_1 + \bar{n}_2)$. In the simulations, for each pumping power P we used the phase-coherence time $\tau_{\text{ph}} = 1/\kappa$ shown in (b) and the oscillation period π/J shown in (c).

energy splitting $\Delta \simeq 2J$ of the two polariton eigenmodes [See Fig. 4.5(c)] decreases with an increase in the pumping power, and thereby the polariton intensity $\bar{n}$. Simulations using the Gross-Pitaevskii equations for the polariton condensate indicate that with increasing pumping power, the lateral size of the condensate in real space is progressively increased, while its in-plane k-space distribution is correspondingly reduced. This observation explains the reduction in the Josephson coupling between the two polariton components due to the spin-orbit interaction between the two bare polariton modes [330]. According to the arguments in Ref. [181], the exponential decay of polariton coherence has the rate $\kappa = 1/\tau_{\mathrm{ph}} \sim \gamma/2\bar{n}$, with γ being the decay rate of the polariton intensity. Therefore, the polariton coherence time is proportional to its intensity $\tau_{\mathrm{ph}} \propto \bar{n}$, and thereby the pumping power (stronger pumping-longer coherence time) consistent with the numerical simulations.

4.5 Condensate Nonlinearity

Optical confinement leads to linewidth narrowing of the condensate emission. This section investigates whether this narrowing is such that it approaches the single-polariton nonlinearity constant by comparing the number of polariton N that correspond to one linewidth shift in energy as:

$$Ng = \delta E \; A \,, \tag{4.5}$$

where g is polariton-polariton interaction strength, δE the condensate linewidth, and A the area of the condensate. The case of single polariton nonlinearity corresponds to $N = 1$, i.e. one polariton needs to be added to the system to shift the energy of the condensate by one linewidth.

The theoretical polariton-polariton interaction strength can be estimated as $g \approx 6E_b\alpha_B^2|X|^2$, with E_b is the excitonic binding energy, α_B the excitonic Bohr radius, and $|X|^2$ the exciton fraction as quantified by the Hopfield coefficient (Eq. 2.41). The latter is calculated by first fitting the LP polariton branch of Fig. 4.2(b) with Eq. 2.42 to extract the cavity-exciton detuning as ∼-7 meV, which is then inserted in Eq. 2.41 to estimate $|X|^2 \approx 0.2$ in this experiment. Assuming typical values for excitons in GaAs narrow quantum wells, namely $E_b \approx 10$ meV and $\alpha_B \approx 100$ Å, gives $g \approx 1.2$ μeVμm^2.

The condensate linewidth is calculated as $\delta E = \hbar/\tau_{\mathrm{ph}}$, where τ_{ph} is the phase-coherence time shown in Fig. 4.5(b). The condensate with the narrowest linewidth is realised for the highest pumping power $P = 4.3P_{\mathrm{th}}$, where $\tau_{\mathrm{ph}} \approx 1100$ ps yielding a linewidth $\delta E \approx 0.6$ μeV. Assuming a condensate diameter ∼7.5 μm from Fig. 4.1(b), the condensate area is calculated as $A \approx 44$ μm^2. Therefore, N is calculated from Eq. 4.5 as $N \approx$ 22. This result indicates that the system remains above the single polariton nonlinearity as 22 polaritons need to be added to shift the energy of the condensate by one linewidth, however it is not too far off either.

4.6 Polarisation-Resolved Measurements

The presence of the two orthogonal condensate modes can be verified through polarisation-resolved measurements. Specifically, the setup described in Section 3.2.2.1 is modified by adding a half-waveplate and a polariser before the interferometer and spectrometer, as shown in Fig. 4.6(a). The diffraction efficiency of the spectrometer's diffraction grating is polarisation-dependent. Therefore, the polariser is placed first and its polarisation axis is rotated so that the measured counts is maximised. The polariser then remains fixed, a practice which ensures that the polarisation of the detected light is fixed. The role of the half-waveplate is to rotate the plane of linearly polarised light. If a linearly polarised wave is normally incident on a waveplate with its plane of polarisation at an angle θ with respect to the waveplate's fast axis, the original polarisation direction will be rotated by an angle 2θ.

Therefore, the aim of this experiment is to rotate the waveplate so that the polarisation direction of one of the condensate modes gets aligned with the polariser's polarisation axis while the other mode's polarisation direction is perpendicular to the polariser's axis. In this case, one condensate mode will be eliminated from passing to the interferometer, and no beating will be expected in the temporal evolution of the temporal coherence from the condensate emission. The polarisation-revolved measurements are shown in Fig. 4.6(b). It is evident that a beating of the two modes is present in all three fast axis rotations (0°, 22.5°, and 45°), manifested by the existence of a peak after the initial decay of coherence to approximately zero. Even though these results are consistent with the developed theoretical model, the limited number of rotations measured in this work does not sample the whole polarisation sphere, e.g. condensate modes polarised at 22.5° and 90° + 22.5° to name an example. Unfortunately, when this theoretical model was developed, and the subsequent need for more elaborate polarisation-resolved measurements became obvious, the setup was deconstructed to facilitate measurements on Cu_2O oxide (See Chapters 5 and 6). Note that the different temporal decay compared to Fig. 4.5 is attributed to a different measurement location (See Section 4.7).

Despite the absence of complete polarisation-resolved measurements, the assumptions made by the theory are well founded. Apart from the previously measured energy splittings in the sample [300, 329], no other assumptions were made in the theory developed in this work. Additionally, the theoretical model has only two fitting parameters, i.e. the Josephson coupling

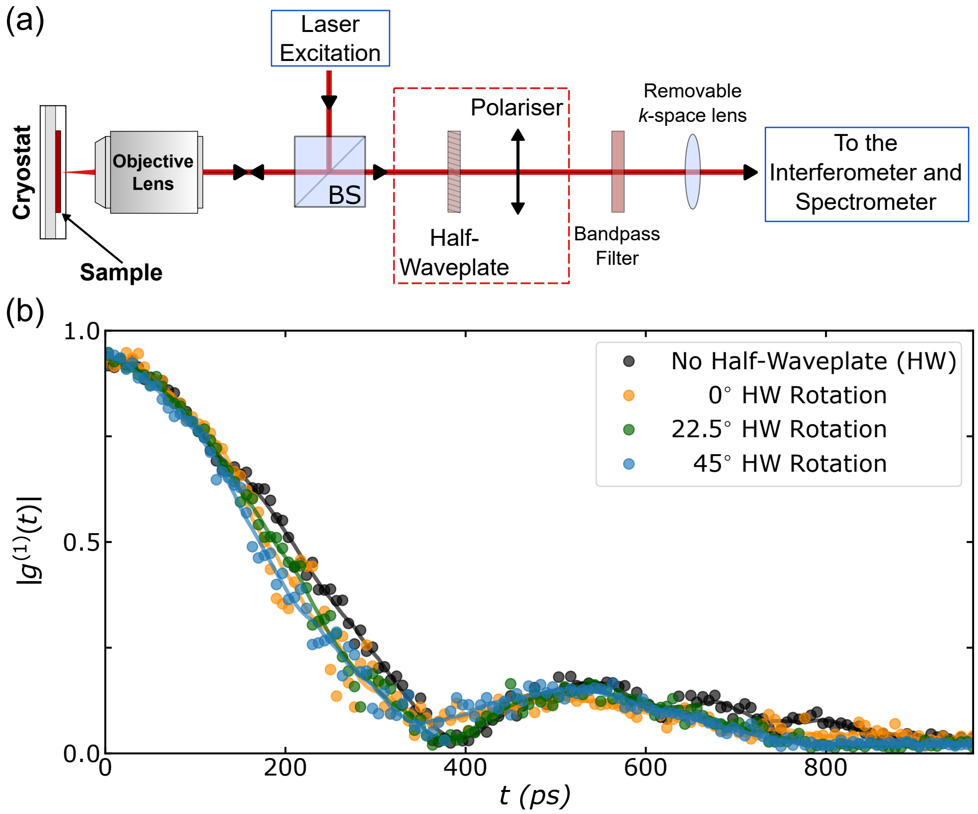

Figure 4.6: (a) The optical setup used to perform polarisation-resolved measurements. A half-waveplate and a polariser are placed before the interferometer and spectrometer, marked by the red dashed rectangle. (b) Temporal decay of fringe contrast measured for three different rotations of the half-waveplate's fast axis: 0° (yellow dots), 22.5° (green dots), and 45° (blue dots). The black dots correspond to the case without the presence of the half-waveplate in the setup. Solid lines are guides for the eye.

strength between the two polarisation modes and the coherence relaxation rate, yet it reproduces the experimental results exceptionally well. Given the remarkable agreement between experimental and theoretical data, the observed beating of the polariton field correlation function is attributed to the effective Josephson coupling between the circular modes due to the energy splitting of the linear polarisation modes. In the linear basis, the power dependence of the $g^{(1)}(t)$ correlation function is attributed to a power-dependent energy difference between the two polariton modes, which increases with power.

4.7 Dependence on Position

Apart from the excitation power, the temporal decay of the correlation function depends on the position of the sample where the pump laser excites. Different coherence times and beating periodicities are observed at different positions on the sample, as shown in Fig. 4.7. This discrepancy is attributed to local strain on the sample, which is known to be position dependent [300].

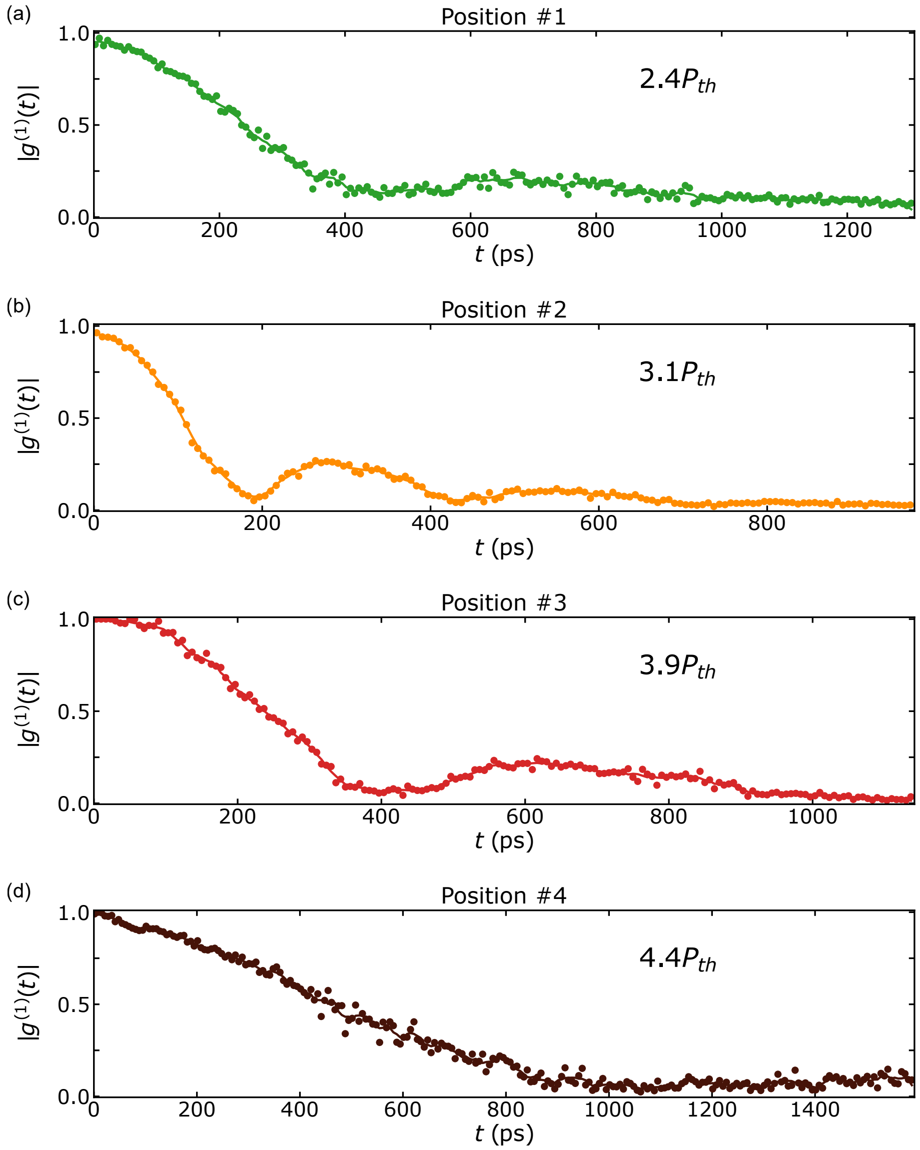

Figure 4.7: Temporal evolution of $|g^{(1)}|$ of a trapped condensate at four different locations, each with a different excitation power, similar to those used in Fig. 4.5. Solid lines are guides for the eye.

4.8 Summary and Outlook

In this chapter, the first-order temporal coherence of optically trapped polariton condensates was studied. Optical trapping increases the coherence time by more than an order of magnitude compared to that of an untrapped condensate. In the untrapped case, the condensate is formed on top of a sea of hot reservoir excitons that directly interacts with the condensate and induces strong decoherence. In the optically trapped condensate, however, this hot reservoir is mostly spatially decoupled from the condensate. This critical difference between the two cases permits the observations of ultralong coherence times in the trapped condensate. The highly prolonged coherence of the trapped polariton condensate allows for the observation of a temporal beating in the first-order correlation function of the emitted field. This beating originates from the fine structure in the condensate energy spectrum, resulting in two energy-degenerate modes of the polariton condensate. Measuring the first-order correlation function enables measuring the energy splitting of the two interacting polarisation modes of the condensate with unprecedented precision. The results presented in this work can thus be important for the characterising and controlling of spinor condensates in lattice potentials for realising analogue and digital polariton quantum simulators [332–335]. Despite the significant reduction in the linewidth, the system still cannot reach the single-polariton nonlinearity limit, highlighting the current limitations of GaAs-based microcavities towards this goal.

This page is intentionally left blank.

Chapter 5

Quantum Confined Rydberg Excitons in Cuprous Oxide Nanoparticles

This chapter studies Rydberg excitons in nanoparticles of cuprous oxide. Owing to their giant microscopic dimensions, Rydberg excitons in Cu_2O exhibit enhanced optical nonlinearities at much smaller densities compared with other traditional semiconductors [32, 34]. These nonlinearities can be harnessed by quantum confinement of the excitons in semiconductor low-dimensional structures such as quantum wells and quantum dots. Studying Rydberg excitons in confined dimensions is a crucial step towards harnessing their nonlinearities for applications. Nanoparticles are a suitable system for quantum confinement and an interesting platform for realising quantum technologies with Rydberg excitons, potentially underpinning future devices such as single-photon sources [275] and single-photon switches [336].

In Section 5.1, Rydberg excitons states are resolved up to principal quantum number $n = 6$ in the absorption spectrum of Cu_2O nanoparticles. The confinement of Rydberg excitons was found to have two major impacts: it reduces their oscillator strength, and it broadens the transitions, leading to a reduced number of exciton transitions compared to the bulk crystal. A theoretical framework for the description of these effects is developed in Section 5.2, encompassing the quantum confinement of the Rydberg states and the size distribution of nanoparticles. Section 5.3 investigates the contribution of other effects, such as the Rydberg blockade and the plasma effect previously observed in bulk Cu_2O, and also discusses the importance of considering the particle size distribution. Next, the results of probing single nanoparticles with DF reflection spectroscopy are presented in Section 5.4, followed by a discussion on the temperature dependence of the $n = 2$ transition of the bulk crystal and nanoparticle samples in Section 5.5. Finally, Section 5.6 gives a summary of the experimental and theoretical findings.

The experiments presented in this chapter were performed by the author under the supervision of Dr H. Ohadi and have been published in Ref. [249]. The theoretical model was developed by S. Zielińska-Raczyńska, G. Czajkowski, K. Karpiński, and D. Ziemkiewicz at the UTP University of Science and Technology in Bydgoszcz, Poland based on their earlier works [276, 337].

5.1 Absorption Spectroscopy of Bulk and Nanoparticles of Cu_2O

To measure and characterise the Rydberg series of Cu_2O samples, both bulk and nanoparticles, broadband LED absorption spectroscopy was performed. The input intensity of the LED was approximately 60 mW/cm^2 in the wavelength region of the yellow P excitons, i.e. between 571 and 580 nm. The spectrum of the light transmitted through the sample I, along with a reference spectrum of the LED I_0, were recorded. The reference spectrum was measured after moving the sample such that the LED light did not pass through the sample. The ratio of the transmitted intensity to the reference intensity quantifies the transmission through the sample $T = I/I_0$. The thickness of nanoparticle samples cannot be determined since it varies/fluctuates across the excitation spot as the particles redistribute during solvent evaporation. Consequently, the absorption coefficient cannot be defined accurately. Instead, the optical depth is used as a measure of absorption. It is a dimensionless quantity defined as Optical Depth $= -ln(T)$ and is proportional to the absorption coefficient and the thickness of the sample, as discussed in Section 3.2.1.1. The optical depth is also used for the bulk crystal to facilitate the comparison with nanoparticles, even though the bulk crystal's thickness can be measured (∼60µm). All spectra are corrected as outlined in Section 3.2.1.1.

The resulting absorption spectra at T = 4 K are shown in Fig. 5.1. The absorption spectrum of the bulk crystal (red line) exhibits a series of absorption lines corresponding to the excited Rydberg states of the yellow P exciton series. The series extends up to $n = 12$ (See inset in Fig. 5.1) and is overlaid on a continuous phonon background, originating from the virtual population of blue excitons, which subsequently decay into an optical phonon and the 1S orthoexciton (See Section 2.5.4). The absorption lines show an asymmetric lineshape with a steeper slope on the high-energy flank stemming from the Fano interference between the discrete excitonic states and the absorption background. The green 1S$_g$ appears as a weak peak between the 2P- and 3P-exciton lines. The smaller number of observed exciton lines compared with previous reports [32] can be attributed to several factors, mainly to the larger spectral resolution in our case (∼110 µeV compared to 5 neV in Ref. [32]). Other potential reasons for

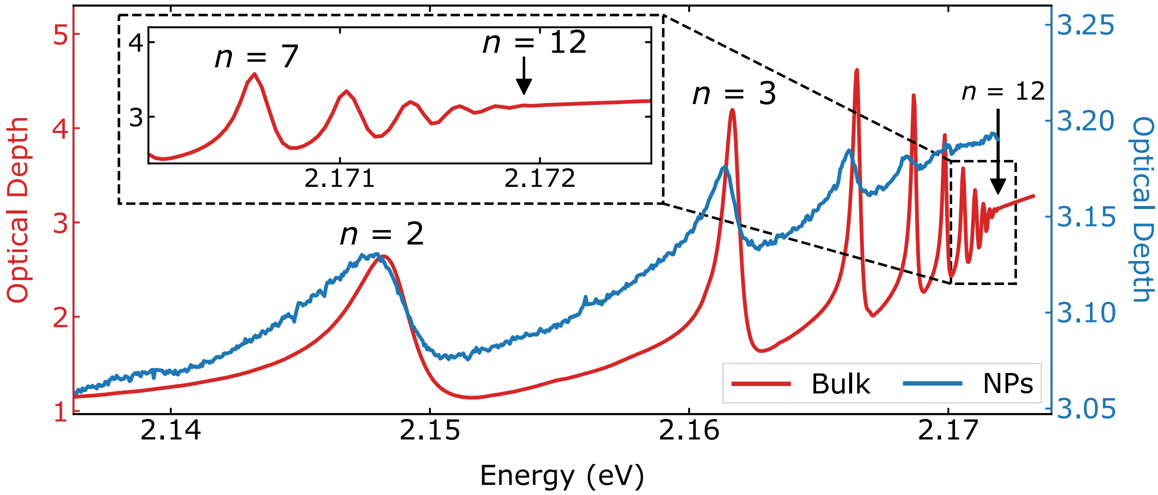

Figure 5.1: Absorption spectra of a natural thin crystal (red line) and natural nanoparticles (blue line) of Cu$_2$O at 4 K. The inset shows a zoomed-in version of the high-energy side of the spectrum where the highest principal quantum number of Rydberg exciton states of the bulk crystal, $n = 12$, is highlighted. The highest principal quantum number observed for nanoparticles is $n = 6$.

the reduced number of observed exciton lines in Fig. 5.1 include the higher temperature of the crystal (T = 4 K compared to 1.4 K), the potentially lower crystal quality, and a quenching of the higher-n excitons caused by the broadband spectrum of the excitation LED. Broadband light excites excitons from the other three series and free carriers, besides the excitation of P excitons from the yellow series, leading to multiple scattering interactions that potentially destroy higher-n states [32].

The absorption spectrum of a sample of NNPs covering a large area (∼100 µm diameter) on the substrate also shows clear exciton absorption lines (blue line in Fig. 5.1). The spectrum exhibits a higher amount of noise compared to the smoother spectrum of the bulk crystal. This discrepancy can be attributed to the morphology of the individual nanoparticles that the excitation spot covers, in addition to a modified phonon density of states in the nanoparticle system (See Section 5.4). Similar to the bulk case, exciton resonances are evident as discrete asymmetric peaks on top of the broad phonon background. However, the spectrum corresponding to the nanoparticle cluster shows a sharp decrease in the peak absorption of the excitons as n increases, such that only resonances up to $n = 6$ are resolvable. A possible explanation for the reduced number of exciton lines can be traced back to the polishing procedure. During polishing, the residual powder from the bulk crystal, i.e. the powder that is used for the fabrication of NNP samples, is also rubbed against the polishing grit, which, in turn, can cause damage to the nanoparticle lattice. To test this hypothesis, absorption spectroscopy was repeated using synthetic nanoparticles of comparable sizes. The absorption spectrum of SNPs exhibits the same number of resonances as the one for NNPs, as shown in Fig. 5.2. Therefore, polishing is not responsible for the reduced number of transitions. Note that resonances corresponding to the same n are slightly blueshifted both in Fig. 5.1 and Fig. 5.2 due to a different centre wavelength of the spectrometer's grating and a small temperature variation between the different experiments.

The exciton series of the bulk crystal and NNP samples are compared qualitatively in terms of the n-dependence of the resonance energy, linewidth, and area of each exciton peak. First, a curve describing the phonon background in each spectrum is defined by manually selecting individual the local minima between exciton peaks that define the range of each exciton peak. These points are subsequently connected by straight lines forming a curve that is subsequently subtracted from the absorption spectrum, thus setting the background of each peak to zero. To extract the corresponding resonance energy and linewidth, individual peaks are then fitted using an asymmetric Lorentzian (Eq. 2.61) convoluted with a Gaussian function f_G representing the spectrometer's response function:

$$\alpha_n(E) = \left(C_n \frac{\frac{\Gamma_n}{2} + 2q_n(E - E_n)}{(\frac{\Gamma_n}{2})^2 + (E - E_n)^2} \right) \circledast f_G(E)\,. \tag{5.1}$$

This practice enables filtering out the artificial broadening induced by the spectrometer, which becomes more relevant for the narrow high-n exciton peaks whose linewidths approach the spectrometer's resolution (0.03 nm or ~112 μeV). There is a noticeable difference for $n \geq 6$

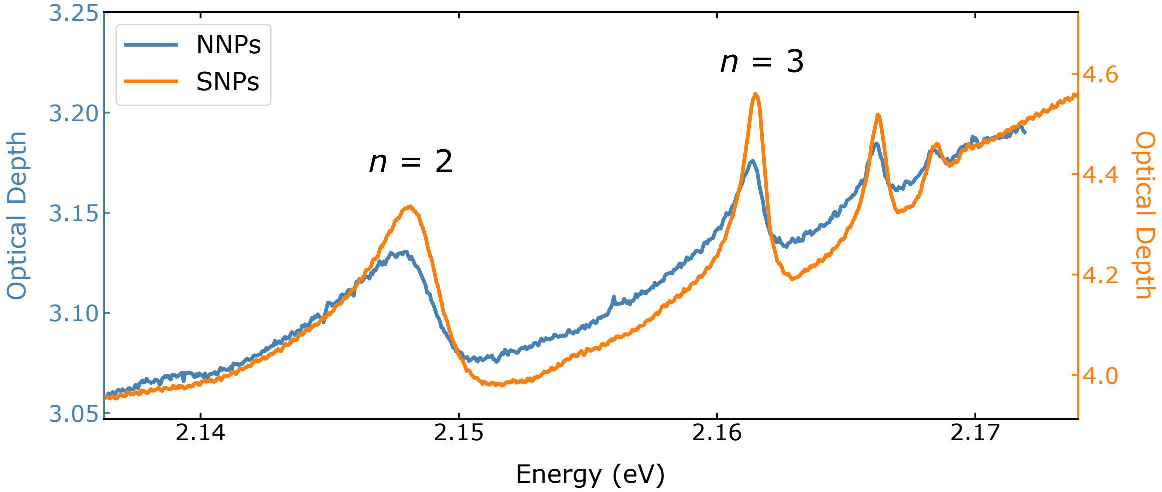

Figure 5.2: Absorption spectrum for natural (blue line) and synthetic (orange line) nanoparticles of Cu_2O at 4 K. The latter is produced from commercial synthetic powder (Nanografi) with an average size distribution of 0.6 μm. A comparison of the two spectra shows a similar number of transitions and peak broadening.

between the convolution corrected linewidths and the uncorrected ones. The new linewidths for nanoparticles are practically unchanged (the change for $n = 5$ is $\sim 1\%$) as they are much broader than our spectrometer resolution. Exciton states with $n \geq 10$ are excluded in the analysis of the bulk crystal since the linewidths are comparable to the spectrometer's resolution, and hence the corresponding exciton peaks consist of a small number of data points. The area under each exciton peak is calculated by numerically integrating along the energy axis using the composite trapezoidal rule. Note that the areas and hence the oscillator strengths are unaffected by the instrument broadening.

The P-exciton binding energies $E_g - E_n$ are shown in Fig. 5.3(a). The results from fitting the experimental data to the binding energy equation, without and with the quantum defect (Eq. 2.9 and Eq. 2.63, respectively), are summarised in Table 5.1. A fit to the experimental data with the standard equation for the exciton binding energy, shown as the lines in Fig. 5.3(a), yields $E_g = 2.17253 \pm 0.00002$ eV, $R_x^* = 96.4 \pm 0.2$ meV for the bulk crystal and $E_g = 2.17218 \pm 0.00004$ eV, $R_x^* = 95.7 \pm 0.2$ meV for the NNPs, values which agree well with those reported in the literature [32, 228, 248]. The errors quoted on these parameters are the errors returned from the fitting algorithm. Repeating the fits with the addition of the quantum defect yields similar results for the energy gap E_g but slightly larger Rydberg constants R_x^* compared to the case when it is not added (See Table 5.1). Interestingly, the quantum defect parameter $\delta_{n,P}$ is small compared to previous reports, which is expected as this correction is

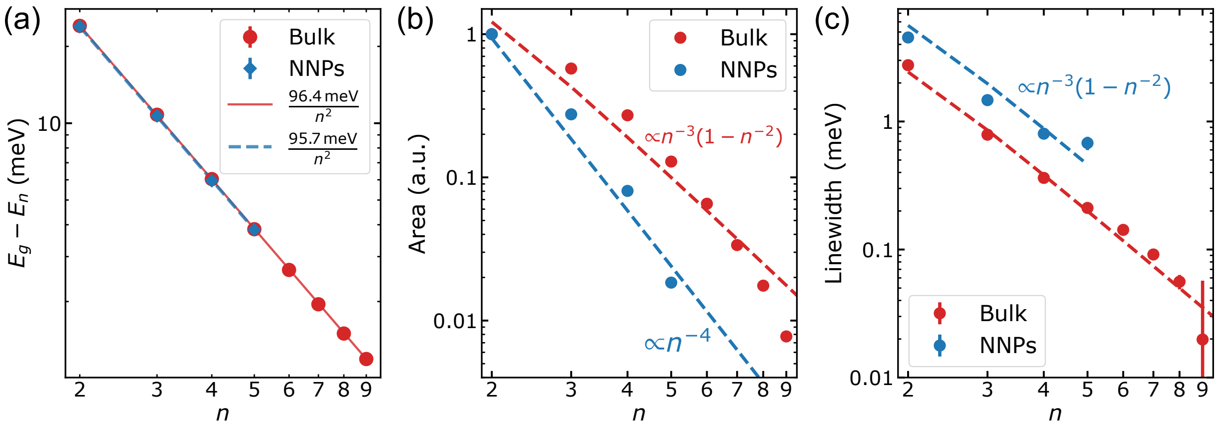

Figure 5.3: (a) Binding energies $E_g - E_n$, (b) peak areas, and (c) linewidths calculated from experimental (dots) results. The lines in (a) are the result of fitting the experimental data with Eq. 2.9. Peak areas in (b) are normalised to the value of $n = 2$ in each case, and the observed trends, which differ between the bulk crystal and the NNPs, are presented as dashed lines. The dashed lines in (c) show the theoretical n-dependence of linewidths. The error bars in panels (a) and (c) are smaller than the size of the data points for the majority of exciton states n.

Equation	Sample	E_g (eV)	R_x^* (meV)	$\delta_{n,P}$
Without QD (Eq. 2.9)	Bulk	2.17253 ± 0.00002	96.4 ± 0.2	-
	NNPs	2.17218 ± 0.00004	95.7 ± 0.2	-
With QD (Eq. 2.63)	Bulk	2.17258 ± 0.00002	98.9 ± 0.9	-0.025 ± 0.008
	NNPs	2.1723 ± 0.0001	99 ± 3	-0.03 ± 0.02

Table 5.1: Extracted bandgap energy E_g, Rydberg constant R_x^*, and quantum defect $\delta_{n,P}$ from the bulk crystal and the NNPs samples without and with the addition of the quantum defect.

more relevant for exciton states with $n > 10$ [32]. Also, it takes negative values for both the bulk crystal and the NNPs.

The area of each absorption peak corresponds to the absorption strength and is determined by the exciton oscillator strength. The areas of the peaks as a function of n are shown in Fig. 5.3(b), with the dashed lines approximating the observed trend. Both the bulk crystal and the NNPs exhibit a decrease in oscillator strength, i.e. peak area, as n is increased. The comparison of oscillator strength of the excitons in bulk and NNPs shows that the relative peak area of excitons in nanoparticles of Cu_2O decreases as $\propto n^{-4}$ compared to that in the bulk crystal, which decreases as $\propto n^{-3}$, which is the approximation of theoretical dependence for large n.

The trends in the linewidths Γ_n of the states with the principal quantum number are shown in Fig. 5.3(c) with the diagonal dashed lines representing the theoretical $n^{-3}(1 - n^{-2})$ scaling. The linewidths decrease with increasing n down to ~20 μeV for the $n = 9$ state of the bulk crystal. The linewidth of NNPs is approximately double the linewidth of the bulk crystal for the first three observed resonances. The broadening is more pronounced for $n = 5$ as the linewidth increases by more than three folds for NNPs.

Note that PL measurements were performed in multiple NP samples of varying thicknesses. However, no peaks were detected neither in the wavelength region of the yellow P exciton nor in the region of the 1S orthoexciton and the corresponding phonon-assisted lines (See Section 2.5.5). The reason behind the absence of PL peaks requires further investigation.

5.2 Modelling Quantum Confinement of Rydberg Excitons

As discussed in the previous section, the exciton transitions in nanoparticles of Cu_2O are broadened, and their oscillator strengths decrease as $\propto n^{-4}$ compared to those in the bulk crystal that decrease as $\propto n^{-3}$. Previously, the broadening of excitons in nanoparticles of CuCl (<15 nm diameter) was attributed to quantum confinement and the nanoparticle size distribution [338–

340]. In a similar process, the quantum confinement results in a broadening of the transitions in Cu_2O nanoparticles; however, due to the narrow linewidth of the transitions, the effect is visible for larger nanoparticle sizes.

From the point of view of the classification of low-dimensional semiconductor nanostructures, the considered nanocrystals can be classified as quantum dots (QDs). The SEM images suggest that the best model shape is a spherical quantum dot with a median diameter of $\sim$700 nm (See Fig. 3.2). The theoretical approach in this thesis assumes that the interaction between adjacent quantum dots is small enough. Under this assumption, interband transitions in an isolated QD are taken into account and then the results are averaged over a size distribution of QDs.

The optical properties of quantum-confined nanostructures, including QDs, can be studied using the real density matrix approach (RDMA) [341, 342]. In this method, the optical response (absorption, reflection, transmission) of the system is obtained by solving a set of equations for the excitonic amplitude $Y(\mathbf{r}_e, \mathbf{r}_h, t)$ and electric field vector $\mathbf{E}(\mathbf{R}, t)$ of the wave propagating in the nanostructure. The parameters $\mathbf{r}_e$ and $\mathbf{r}_h$ are the coordinates of the electron and the hole, and $\mathbf{R}$ is the center-of-mass coordinate of the electron-hole pair. The basic equations of RDMA have the general form:

$$-i(\hbar\partial_t + \mathit{\Gamma})Y(\mathbf{r}_e, \mathbf{r}_h, t) + H_{eh}Y(\mathbf{r}_e, \mathbf{r}_h) = \mathbf{M}(\mathbf{r})\mathbf{E}\,, \tag{5.2}$$

where $\mathit{\Gamma}$ is a phenomenological damping coefficient, $\mathbf{M}(\mathbf{r})$ is a smeared-out transition dipole density, which depends on the coherence radius $r_0 = (E_g/2\mu\hbar^2)^{-1/2}$, where E_g is the fundamental gap, μ is the reduced effective mass of the electron-hole pair, and $\mathbf{r} = \mathbf{r}_e - \mathbf{r}_h$ is the relative electron-hole distance. The operator H_{eh} corresponds to the two-band effective mass Hamiltonian, which includes the electron and hole kinetic energies, the electron-hole interaction potential, and the confinement potentials:

$$H_{eh} = E_g + \frac{\mathbf{p}_h^2}{2m_h} + \frac{\mathbf{p}_e^2}{2m_e} + V_{eh}(\mathbf{r}_e, \mathbf{r}_h) + V_h(\mathbf{r}_h) + V_e(\mathbf{r}_e)\,. \tag{5.3}$$

The second and the third terms are the electron and the hole kinetic energy operators with appropriate effective masses[1], the fourth term is the electron-hole attraction potential, and the two last terms are the surface confinement potentials for the electron and hole.

A third equation describes the total polarisation of the medium, which is related to the coherent amplitude Y and the transition dipole density $\mathbf{M}(\mathbf{r})$ as:

$$\mathbf{P}(\mathbf{R}) = 2\mathrm{Re}\int d^3r\, \mathbf{M}(\mathbf{r})Y(\mathbf{R}, \mathbf{r})\,. \tag{5.4}$$

---

[1] The asterisk * commonly used to describe effective masses is omitted for simplicity.

This equation, in turn, is used in Maxwell's field equation:

$$c^2\nabla^2\mathbf{E}(\mathbf{R}) - \epsilon_b\ddot{\mathbf{E}} = \frac{1}{\epsilon_0}\ddot{\mathbf{P}}(\mathbf{R})\,, \tag{5.5}$$

where ϵ_b is the dielectric constant (for Cu_2O $\epsilon_b = 7.5$ [267]). The equations 5.2 to 5.5 form a system of coupled integro-differential equations in six-dimensional configuration space $(\mathbf{r}_e, \mathbf{r}_h)$. The optical properties of spherical QDs can be described in terms of the exciton centre-of-mass quantisation method [276]. One assumes that the centre-of-mass is confined within a sphere of radius $R_{\max}$, which gives rise to the confinement states overlapping with the three-dimensional exciton states. The effective QD susceptibility in this limit is given by the formula:

$$\begin{aligned}
\overline{\chi}_{QD} &= \epsilon_b \sum_{n=2}^{n_{\max}} \sum_{N=1}^{N_{\max}} \frac{f_{n1} f_N \Delta_{LT}^{(2)}/R_y}{\left(E_{Tn} - E - i\Gamma_n\right)/R_y + \frac{\mu}{M_{tot}}\left(\frac{x_{\frac{3}{2},N}}{R}\right)^2},\\
f_N &= \frac{1}{6\pi}\left|j_2(x_{\frac{3}{2},N})\right|^{-2} x^2_{\frac{3}{2},N}\left[\int\limits_0^1 u^3 du \prod_{s=1}^{\infty}\left(1 - \frac{x^2_{\frac{3}{2},N}}{x^2_{\frac{3}{2},s}}u^2\right)\right]^2,\\
R &= \frac{R_{\max}}{a^*},\\
f_{n1} &= \frac{32(n^2-1)}{3n^5}\left[\frac{nr_0(r_0+2a^*)}{2r_0(r_0+na^*)}\right]^6,
\end{aligned} \tag{5.6}$$

where $j_N(x)$ are the spherical Bessel functions $(N = 1, 2, \ldots)$, $x_{N,s}$ are roots of the equation $j_N(x) = 0$, $s = 1, 2, \ldots$, $a^* = 1.1$ nm is the Rydberg radius, E_{Tn} are the energies of excitonic levels, and $r_0 = 1.1$ nm the coherence radius of Cu_2O [343]. The damping coefficients of the excitonic levels Γ_n are taken from the Ref. [337] and include phonon interactions [289, 344, 345]. Their values are consistent with experimental results from Ref. [32].

The absorption coefficient α is calculated from Eq. 2.61. The values of C_n are proportional to the area under the peaks of the imaginary part of susceptibility (Eq. 5.6) and normalised to obtain an exact match to the experimental value of α for the $n = 2$ resonance. The RDMA theory predicts symmetric lines; to account for the asymmetric exciton transition, the asymmetry is added phenomenologically via the q_n parameter of Eq. 2.61. Since the location of the asymmetric peak depends on the q_n parameter, the values of Ref. [32] were used and adjusted to fit the measured peak locations.

The experimental and calculated absorption spectra, after phonon background subtraction, are presented in Fig. 5.4. The background is removed as described in Section 5.1, i.e. by connecting the local minima between absorption peaks to define a background curve that is then subtracted from the original spectra. The spectrum corresponding to the bulk crystal [red curves in Figs. 5.4(b,d)] is also calculated from Eq. 5.6 by assuming a very large NP radius $R > 10$ µm.

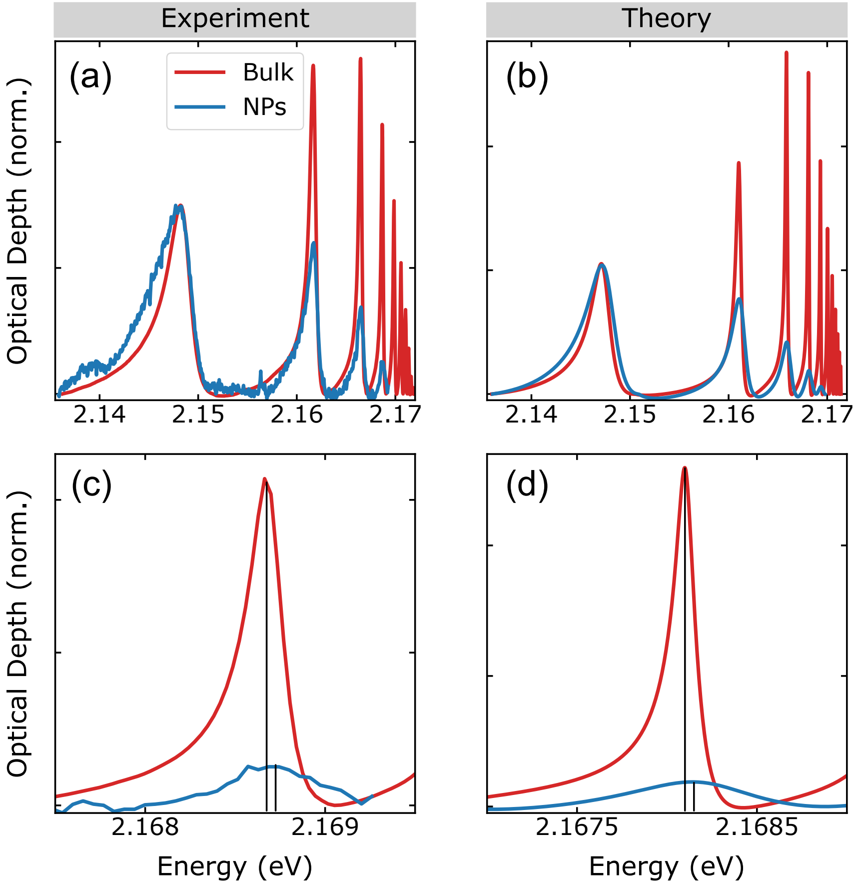

Figure 5.4: (a, c) Experimental and (b, d) theoretical absorption spectra of bulk (red lines) and NPs (blue lines) of Cu_2O in the full energy range and the vicinity of the $n = 5$ state. The theoretical absorption spectrum of NPs is calculated using the size distribution of nanoparticles and multiple confinement states N.

Due to the relatively large size of considered NPs and the corresponding confinement energy shifts on the order of ∼10 µeV, the direct observation of those energy shifts can be challenging. To acquire a clearer picture of the results, the absorption coefficient spectra obtained for the bulk and the nanoparticle systems were normalised so that the peak intensity matches the experimental $n = 2$ exciton resonance. Additionally, the NP spectrum was shifted in energy to obtain an exact match of the $n = 2$ lines, thus removing the influence of different experimental conditions such as temperature mentioned in Section 5.1. A difference of $\Delta E \approx 25$ µeV is observed between the bulk and NP line for the $n = 5$ exciton state [denoted by the vertical lines of Fig. 5.4(c, d)], both in the experimental spectra and calculation results. This amounts to the difference between the confinement energy of the $n = 5$ and $n = 2$ states, with the latter one being negligible. This result agrees with the theoretical predictions of Konzelmann et al. [245].

The exciton peaks of the theoretical absorption spectrum were fitted individually using

Eq. 2.61 and as described for the experimental spectrum. The results from the fits show an excellent match between the measured oscillator strength and the theoretical estimates when multiple confinement states and the size distribution of the nanoparticles are considered [blue line in Fig. 5.5(a)]. The calculation for a single NP size (R = 350 nm) fails to fully explain the oscillator strength reduction [green and orange lines in Fig. 5.5(a)], further confirming that quantum dot size distribution is crucial to the understanding of the observed effects. Upper confinement states ($N > 1$) contribute to the peak area, which explains why the orange line ($N = 1, 2, \ldots, 12$) is higher than the green line (one confined state $N = 1$) in Fig. 5.5(a). Specifically, upper confinement states contribute ~23% of the peak area for $n = 5$, with a smaller effect for $n < 5$.

The calculated linewidths match the experimental data for the $n = 3, 4, 5$ state, while slightly underestimating the linewidth of the $n = 2$ state [blue line in Fig. 5.5(b)]. Similar to the case of the oscillator strength, this observation highlights the effect of NP size and the importance of accounting for the size distribution of the NPs.

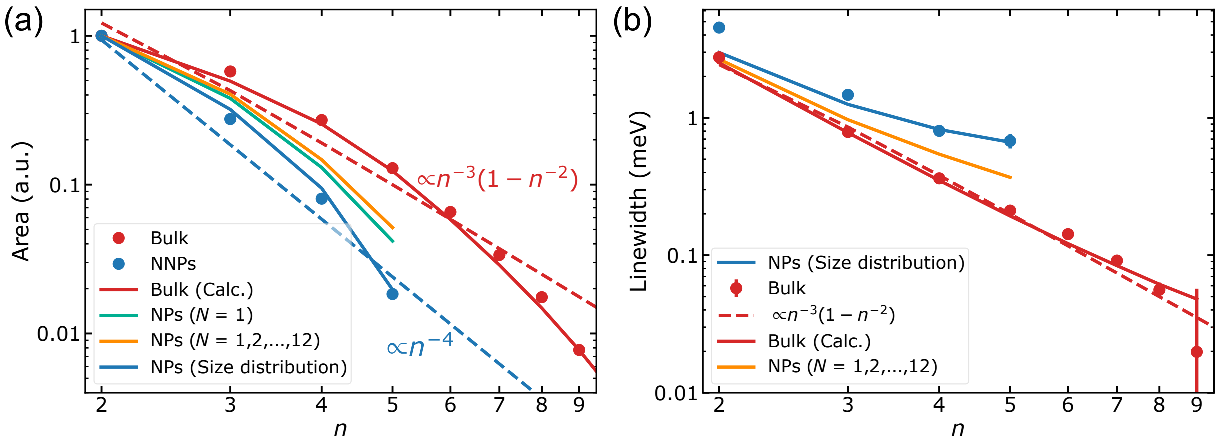

Figure 5.5: (a) Peak areas and (b) linewidths calculated from experimental (dots) and theoretical (lines) results. Calculations using multiple confinement states N and a size distribution (blue lines) match the experimental trends but fail when a single nanoparticle size is considered (orange and green lines). Peak areas in (a) are normalised to the value of $n = 2$ in each case.

5.3 The Importance of Particle Size Distribution

The theoretical approach introduced in the previous section attributes the line broadening and faster oscillator strength decrease in nanoparticles to quantum confinement of excitons in

Cu_2O particles of variable size. In this section, other potential reasons for these observations are discussed, and the effect of quantum confinement is further elucidated.

Previous studies reported that the absorption lines continuously decrease with increasing excitation power, with the higher-lying ones fading away first [32]. This power-dependent optical bleaching becomes visible for $n = 12$ for a pump intensity of $\sim$1 mW/mm^2. Additionally, the intensity required to induce optical bleaching was empirically estimated to scale as n^{10} [32]. Therefore, the laser power required to observe any nonlinearities at $n = 6$, the last exciton transition resolved in NPs, is on the order of 1 W/mm^2. The intensity of the illuminating light in the experiments of Section 5.1 is $\sim$1.5 mW/mm^2 in the spectral region of the $n = 6$ exciton state, hence sufficiently low so that the nonlinear effects observed in bulk can be neglected for the observed excitonic states.

In nanoparticle systems, the blockade diameter can become comparable to particle size even for small principal quantum numbers. Estimation of the dipole blockade volume, hence blockade radius and diameter, can be performed using the following equation [32]:

$$V_{\text{blockade}} = 3 \cdot 10^{-7} \mu\text{m}^3 n^7 \,. \tag{5.7}$$

For $n = 6$, the blockade diameter is $\sim$540 nm, i.e. approximately equal to the average diameter of the NPs. However, the intensities in this experiment are three orders of magnitude weaker than that required to reach the blockade effect [32].

The reduction in oscillator strength due to damage to crystal structure can be ruled out since a similar reduction is observed in synthetic NPs (See Fig. 5.2). Strain on Cu_2O crystals can cause a change in the absorption strength due to a change from isotropic to anisotropic nP states [228]. The substrate can exert stress on Cu_2O crystals and affect the exciton transition, especially when the crystal is glued onto the cold finger of the cryostat or when it is sandwiched between two substrates. However, none of these scenarios is applicable to NP samples, as nanoparticles are held in place only by the van der Waals forces between the substrate and the nanoparticles.

Moreover, electron-hole plasma injected by the incident broadband excitation can affect the absorption of Rydberg excitons. The collision of exciton with free carriers results in a reduction of exciton lifetime, broadening of the transitions, and a reduction of the exciton oscillatory strength. However, this effect is significant for Rydberg states with $n > 10$ [242], which is well above the highest n state observed for nanoparticles. It should be noted that the effect of electron-hole plasma on the absorption of Rydberg excitons could become enhanced in nanoparticles compared to the bulk crystal. In nanoparticles, the surface-to-volume ratio is much higher than in bulk materials, which could result in a stronger interaction between the electron-hole plasma and the surface plasmons. This stronger interaction could lead to an enhancement of the electron-hole plasma's effect on the absorption of Rydberg excitons, resulting in a more significant reduction of the exciton lifetime and broadening of the transitions [346, 347]. However, the role of surface effects in the absorption of Rydberg excitons is not well understood and requires further investigation. Additionally, the theoretical model developed in the remainder of this work explains the experimental findings very well without the addition of plasmonic effects.

Consequently, the reduction in oscillator strength is attributed to the quantum confinement effect present in nanoparticle samples. Theoretical calculations [245] for the $n = 5$ exciton state show that 3D confinement in a QD with a 700 µm diameter blueshifts the lowest confinement state ($N = 1$) by $\sim$20 µeV, which is an order of magnitude smaller than the linewidth of the $n = 5$ transition. However, the higher confinement states $N = 2, 3, 4, \dots$ provide a nontrivial contribution to the total area of the observed excitonic line, which is a measure of oscillator strength. This contribution to the overall exciton peak is shown in Fig. 5.6. There, the imaginary part of the susceptibility for the $n = 5$ exciton is depicted, along with the contributions from the $N = 1, 2, 3$ confinement states and different dot sizes. Since the energy shift of those states is proportional to N, it can reach values of over 200 µeV for $N > 2$. Additionally, the energy shift is proportional to R^{-2}, and a relatively large energy shift on the order of 0.5 meV can be expected at the lower end of the obtained NP sizes from the experiment. This is demonstrated in Fig. 5.6, where strongly blueshifted peaks corresponding to small NPs are visible. All these factors contribute to the shape of the total line (black curve in Fig. 5.6) and result in an apparent reduction of the oscillator strength as every observed excitonic line is essentially an overlap of the primary confinement state ($N = 1$) and multiple, blueshifted higher states which are too close to each other to discern them on the spectrum.

The contribution of these confinement states is twofold. First, they make the absorption peaks more symmetric. Since they have higher energy than the $N = 1$ state, their effect is more pronounced on the high-energy side of an absorption peak; this is visible in Figs. 5.4(c) and 5.4(d), where the asymmetric lineshape of the bulk crystal is transformed into a Gaussian shape for the nanoparticles. This effect is also manifested in Fig. 5.4(c) where the asymmetry parameter q_n reaches a value close to zero already at $n = 5$ for the nanoparticle sample as opposed to $n = 9$ for the bulk crystal.

Second, they significantly increase background absorption. Since the oscillator strength of the confinement states quickly decreases with increasing N, their contribution affects mostly the base of the absorption line. The widened bases overlap, forming a strong absorptive background, which, in turn, greatly reduces the area of the peak visible above that background resulting in an apparent reduction of the oscillator strengths. This observation explains why the calculated line based on the particle size distribution is below the other two calculated lines in Fig. 5.5(a). As the resonance energy of the confinement states depends on particle size (See Fig. 5.6), the

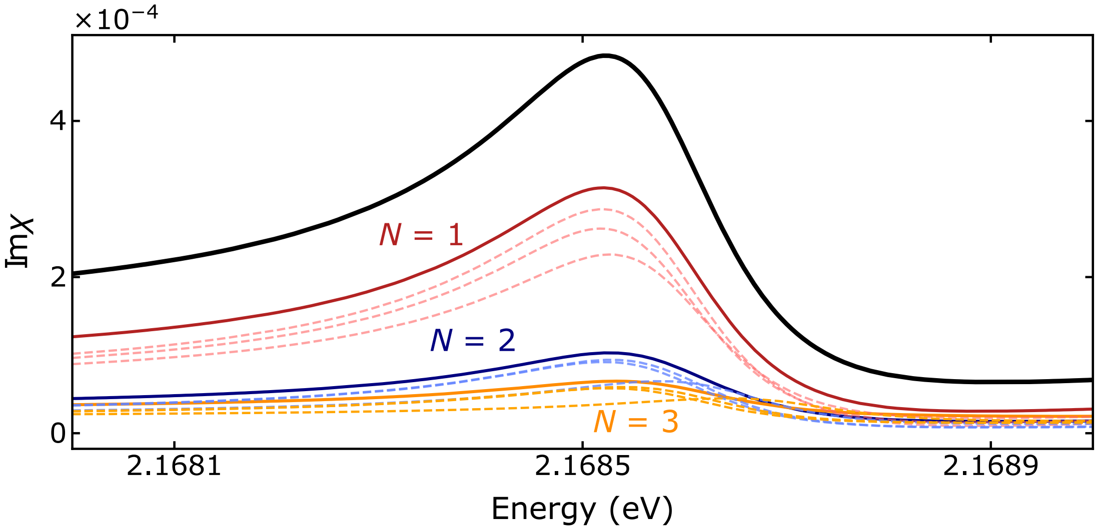

Figure 5.6: Imaginary part of susceptibility χ calculated for the $n = 5$ exciton state and various N values and dot sizes. For each N, a sample of three individual dot sizes (300, 700, and 1100 nm) is shown (dashed lines) along with an average (solid lines). The normalised sum over all confinement states and dot sizes is depicted as a solid black line. Even though only three dot sizes are included for each N in this figure, the solid lines are calculated using dot sizes from 100 to 2000 nm, in steps of 100 nm, for a total of 20 different dot sizes.

peaks coming from various nanoparticles are shifted to a various degree. The sum of many shifted peaks produces a wider peak for each n, with a much more pronounced base. Due to the presence of the absorption background, such broadened peaks “sink” into the background, and the part that sticks out of the background and is measured as peak area becomes smaller. The green and orange lines in Fig. 5.5(a) are calculated for one NP size, as opposed to a distribution of sizes (blue). Therefore, the effect of absorption background is less severe. Interestingly, the effect of adding up 12 confinement states slightly outweighs the increase in the background.

In general, there exists a delicate balance and the peak area may increase or decrease depending on the particle size distribution, background absorption, the number of confinement states considered and each peak is defined against the background. In particular, the high confinement states are very strongly shifted in very small particles. Therefore, a decrease in peak area is expected for a size distribution that contains small particles. On the other hand, for the case of a single, moderately large size, these states more or less coincide with the main peak and add to its area.

5.4 Optical Spectroscopy of Single Nanoparticles

The spectroscopy of single nanoparticles reveals the effect of particle shape on the spectra of Rydberg excitons. Owing to their small dimensionality, only a small fraction of the transmitted light can be absorbed, thus rendering absorption spectroscopy of single NPs impossible. This problem can be overcome by using DF reflection spectroscopy (See Section 3.2.4.1), as only the scattered light from a single NP is detected. The setup used for DF spectroscopy is schematically illustrated in Fig. 5.7(a). By using this setup, the zeroth order reflection is removed, and only the back-scattered light from the nanoparticles is collected. This practice enhances the signal

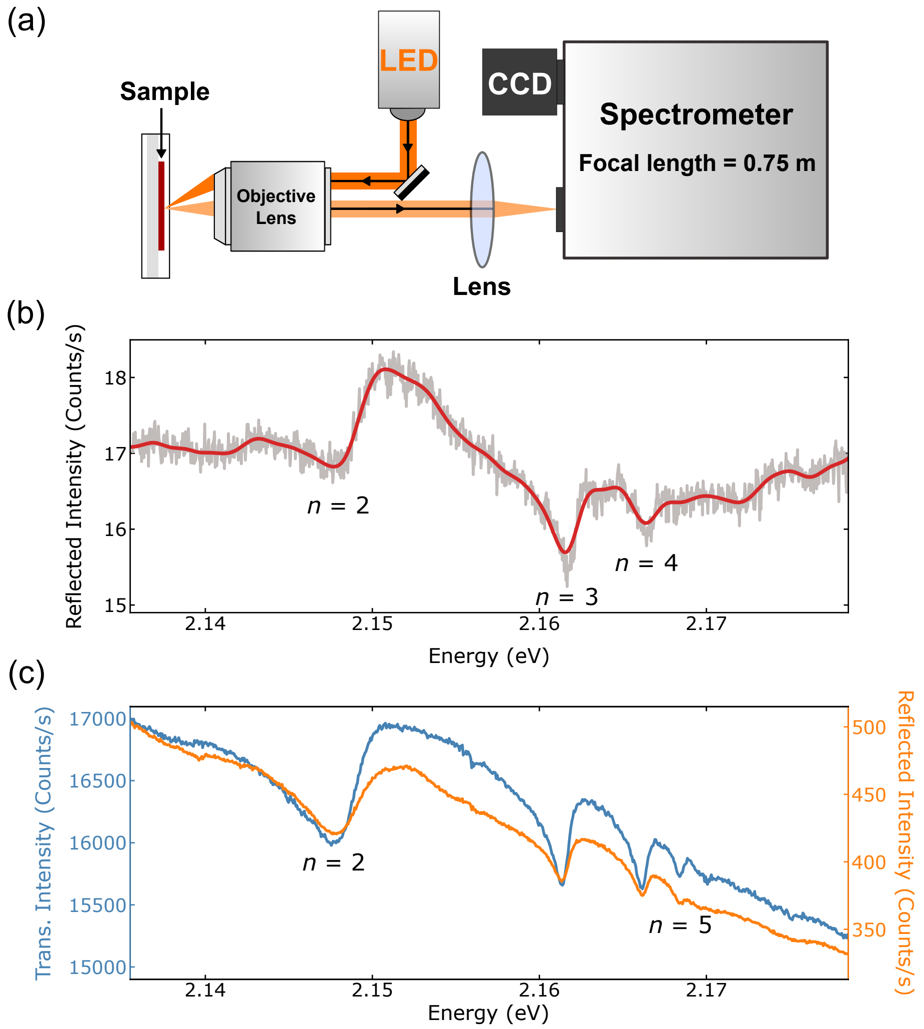

Figure 5.7: (a) Experimental setup for DF reflection spectroscopy. (b) DF reflection spectrum from a single nanoparticle. The solid line is a guide for the eye. (c) Absorption (blue line) and DF reflection (orange line) spectra for clusters of synthetic particles. The difference in the number of counts per second between the two experiments is due to a smaller light intensity as a significant fraction of the excitation is blocked by the dark-field stop.

contrast, thus allowing us to probe single particles which would otherwise be impossible to detect due to their small size. Fig. 5.7(b) displays a spectrum taken from the single nanoparticle depicted in Fig. 3.2(c). Morphology of the single NPs does affect the spectrum; however, the first three P excitons can be clearly resolved as dips in the spectrum. The smooth phonon absorption seen in the clusters is replaced by a flatter but much noisier background due to resonant Rayleigh scattering from the irregular surfaces of the nanoparticle. Several other dips are also observed in Fig. 5.7(b), which can be attributed to a modified phonon density of states (DOS) compared to the bulk crystal. Specifically, phonons are confined to dimensions comparable to the phonon wavelength in a nanoparticle, leading to discrete quantised energy levels for the phonons. This results in a discrete phonon DOS for a nanoparticle, which can give rise to additional peaks and dips in the reflection spectrum compared to the bulk material. For comparison, the absorption and DF reflection spectra from a cluster of NPs are superimposed in Fig. 5.7(c). The reflection spectrum reveals the same number of exciton transitions ($n = 5$) as the absorption one, which are overlaid on a similar phonon background.

The effect of nanoparticle morphology is shown in Fig. 5.8, where the DF reflection spectra from four different NPs of similar size are presented. Apart from the first three P-exciton resonances, which can be identified in all four cases, all spectra exhibit a different number of

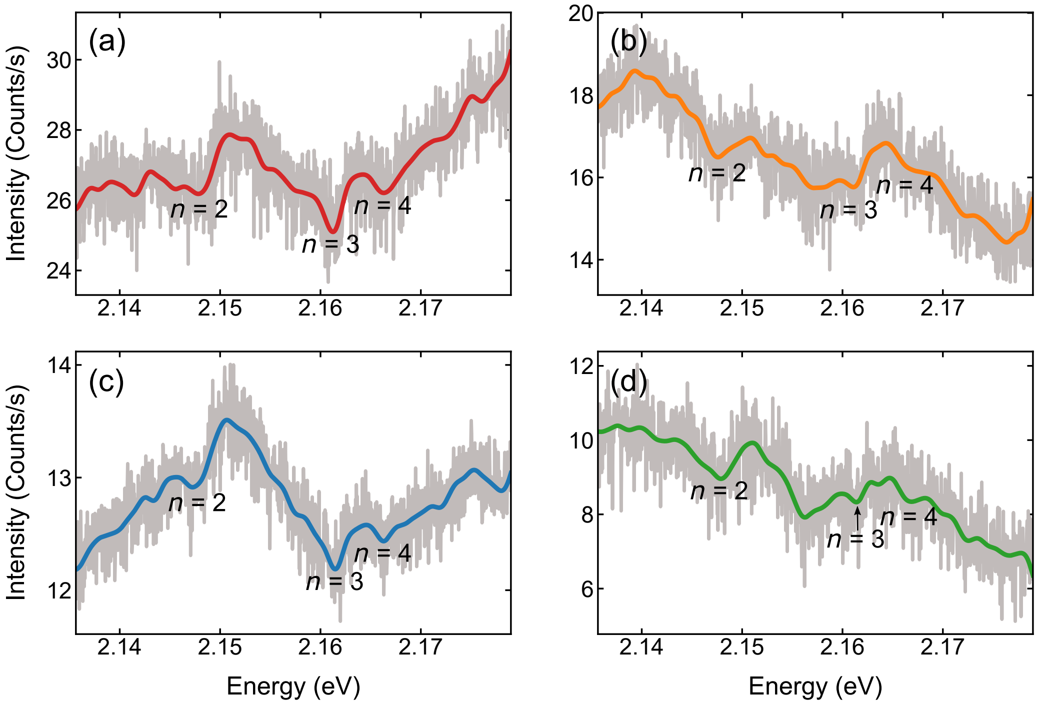

Figure 5.8: (a-d) DF reflection spectrum from different single synthetic nanoparticles of Cu_2O. The nanoparticles have an approximately circular shape, similar to the one shown in Fig. 3.2(c), with a diameter in the range of 500-800 nm. The solid line is a guide for the eye.

transitions, similar to the nanoparticle of Fig. 5.7(b). Moreover, the background is different in each single NP, reflecting differences in size, shape, and surface morphology. These peculiarities inherent to the nanoparticle system at a single particle level are currently hindering the characterisation of the single-exciton nonlinearities associated with this system.

Note that probing single nanoparticles is inherently difficult. Long exposure times of the CCD camera (over 1 hour) were required to detect the very weak signal from single NPs. Additionally, correcting slight misalignment of the focus, occurring naturally due to vibrations or temperature variations of the sample, becomes important owing to the small dimensionality of nanoparticles. To account for this misalignment, the optical focus needs to be readjusted periodically over the course of the long exposure.

5.5 Temperature Dependence of Bulk and Nanoparticles of Cu_2O

The temperature evolution of the exciton absorption line for both the bulk crystal and SNPs of Cu_2O is shown in Fig. 5.9. In both cases, the maximum of the $n = 2$ absorption exciton line are used as an approximation to the exciton resonance energy. The highest temperature where the exciton line can be resolved is 200 K for the bulk crystal and 160 K for the nanoparticle system. The increase of temperature results in a progressive redshift in the exciton transition energy, a behaviour characteristic of semiconductors. The variation of the bandgap of semiconductor can be described in terms of a hyperbolic cotangent relation [348]:

$$E_g(T) = E_g(0) - S\langle\hbar\omega\rangle\left[\coth(\langle\hbar\omega\rangle/2k_BT) - 1\right], \tag{5.8}$$

where $E_g(0)$ is the bandgap energy at 0 K, S is a dimensionless constant describing the strength of the electron-phonon coupling, k_B is the Boltzmann constant, and $\langle\hbar\omega\rangle$ is an average phonon energy. The results of the fits to the experimental data, summarised in Table 5.2, agree within the error bars for all three parameters, which indicates that the exciton absorption lines exhibit a similar temperature dependence for both the bulk crystal and SNPs.

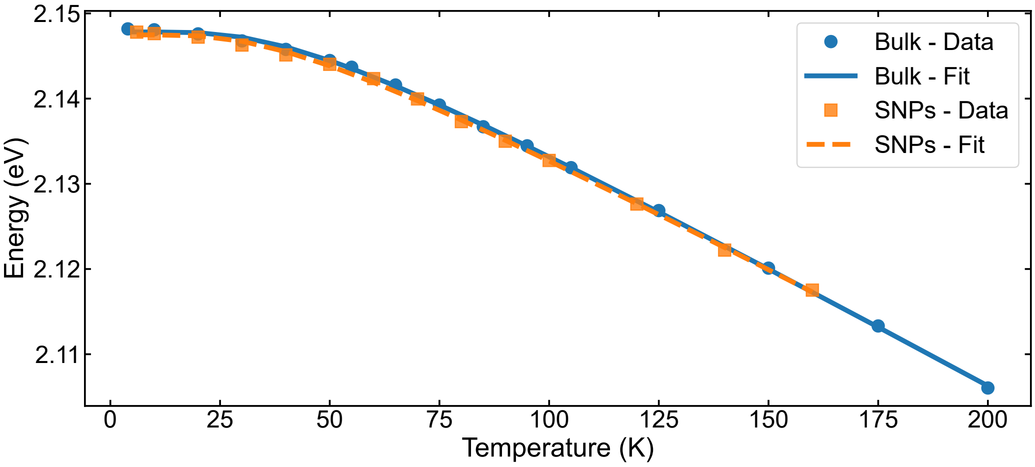

Figure 5.9: Temperature dependence of the $n = 2$ absorption exciton peak for the bulk crystal (blue dots) and SNPs (orange squares) of Cu_2O. Here, the maximum of the exciton peak is used as an approximation of the resonance energy. The corresponding fitted curves using Eq. 5.8 are shown as lines.

	NPs	Bulk
$E_g(0)$ (eV)	2.1475 ± 0.0002	2.1478 ± 0.0001
S	1.59 ± 0.03	1.66 ± 0.02
$\langle \hbar\omega \rangle$ (meV)	9.7 ± 0.4	10.5 ± 0.3

Table 5.2: Fitting parameters of temperature dependence of the exciton transitions in NPs and bulk using Eq. 5.8.

5.6 Summary and Outlook

In this chapter, quantum confined Rydberg excitons were observed for the first time in nanoparticles of Cu_2O. Exciton resonances were resolved and characterised via absorption spectroscopy by probing multiple nanoparticles simultaneously within the excitation spot. In the nanoparticles sample, the Rydberg exciton series was extended up to $n = 6$ in contrast to a thin bulk crystal where exciton up to $n = 12$ can be resolved. This discrepancy between the two samples stems from linewidth broadening accompanied by a simultaneous reduction of the oscillator strength of the excitonic peaks, as the crystal structure is reduced from bulk to nanoparticles. Several effects were considered to determine the origin of these two observations. One such effect is damage to the crystal structure during the extraction of natural nanoparticles after polishing a natural bulk crystal. However, this effect can be excluded as a similar reduction in the number of exciton transitions is observed for synthetic nanoparticles. Additionally, stress induced by the substrate is ruled out since nanoparticles are not mounted on the substrate but are held in place only by van der Waals forces. Additionally, the plasma and blockade effects, which have been previously observed in bulk Cu_2O, can be excluded for the excitation powers in this experiment in combination with the small principal quantum number of the studied transitions.

Consequently, the observed effects are described in terms of the quantum confinement of Rydberg excitons in conjunction with the particle size distribution. The confinement of the centre-of-mass motion of Rydberg excitons gives rise to confinement states, overlapping with the three-dimensional exciton states and modifying the exciton line profile. As these confinement states are affected by the particle size, including the particle size distribution is crucial.

Furthermore, single nanoparticles of Cu_2O can be isolated and probed by performing dark-field reflection spectroscopy. Their spectrum is significantly different compared to clusters of multiple NPs and is affected by the nanoparticle size, shape, and surface morphology. Specifically, the presence of multiple transitions in addition to the first three P excitons is attributed to a modified DOS in a nanoparticle, while the irregular background is attributed to resonant Rayleigh scattering from the irregular surfaces of the nanoparticle. These effects, i.e. the modified phonon DOS and the Rayleigh scattering, are hindering the characterisation of single nanoparticles and the corresponding single-exciton nonlinearities present in this system. Improving the means of probing these single nanoparticles is a crucial step towards characterising and utilising the nonlinearities inherent to the Cu_2O at the single nanoparticle level.

The results presented in this chapter are a first step towards understanding the interaction of Rydberg excitons in nanostructures and their application for quantum technologies.

Chapter 6

Rydberg Exciton-Polaritons in a Cuprous Oxide Microcavity

Exciton-polaritons in semiconductor microcavities have emerged as versatile light-matter interfaces whose unique properties, in combination with advanced semiconductor technology, can be exploited for future applications for scalable quantum simulations [332] and polaritonic devices [35], but also offer a platform for fundamental studies of many-body phenomena such as high-temperature Bose-Einstein condensation [135, 139], superfluidity [27, 119], quantized vorticity [28], and many others [35]. Previous studies were able to exploit exciton-exciton interactions to demonstrate optical nonlinearities [349, 350] and non-classical effects [351–354] at high light intensities. However, the realisation of strong and controllable interactions remains an important frontier that would bring applications deep into the quantum domain. A candidate system for such interactions is high-lying Rydberg exciton states, and cuprous oxide, in particular, has been identified as a well-suited material with giant Rydberg excitons as large as ~1 μm [32] leading to a strong blockade effect [246, 275]. The large Rydberg constant of Cu_2O ($R_x^* \approx 100$ meV) distinguishes it from other conventional semiconductors and has enabled the demonstration of a well-resolved P-exciton Rydberg series up to $n = 30$ [247]. In such highly excited states, Rydberg excitons become very sensitive to external fields [238] and exhibit mutual interactions that can be enhanced by more than ten orders of magnitude over that of the ground state [34, 246].

As discussed in Section 2.5.2, the lowest conduction band and the highest valence band in Cu_2O have the same parity, such that the direct dipole transition is parity forbidden, thus leading to a Rydberg series of long-lived P excitons. The narrow linewidths of the high-n Rydberg excitons imply lifetimes of 200-400 ps, an order of magnitude larger than exciton in GaAs quantum wells. The associated long coherence times [355] combined with the strong Rydberg-state interactions hold great promise for a broad range of applications. Yet, harnessing these interactions for applications has remained a challenge due to the weak light-matter coupling in this material. Specifically, the enhanced coherence comes at a cost as the forbidden dipole transition also implies a small oscillator strength and correspondingly weak coupling of light to Rydberg excitons in Cu_2O.

The present chapter discusses how the limitation mentioned above could be circumvented by embedding a Cu_2O crystal between two highly reflective DBR mirrors to form a microcavity and achieve strong coupling between light and Rydberg excitons. The transmission from the cavity is characterised in terms of its angle dependence in Section 6.1 and its sample position dependence in Section 6.2. Interestingly, the amplitude of the transmission peaks is not symmetric. This observation is theoretically modelled in Section 6.3 by considering the asymmetric line profile of the underlying Rydberg exciton transitions. Next, Section 6.4 discusses the reduction of the exciton-photon coupling strength in this system. This reduction is further studied using TMM simulations to reveal the effect of cavity thickness and phonon background in Section 6.5. Then, the origin of the reduced number of observed transitions in the cavity compared to the bulk is investigated in Section 6.6, by considering the effect of the blockade and plasma effects (Section 6.6.1) and the effect of strain on the sample (Section 6.6.2). Finally, Section 6.7 gives a summary of the experiment and an outlook for future studies.

The experiments presented in this chapter were performed by the author under the supervision of Dr H. Ohadi and have been published in Ref. [250]. The Cu_2O crystal that was used in the cavity was prepared by the author and Sai. K. Rajendran deposited the DBR mirrors. All TMM simulations were performed by Sai. K. Rajendran. The theoretical model was developed by V. Walther and T. Pohl.

6.1 Momentum-Resolved Cavity Transmission

To achieve strong coupling between photons and Rydberg excitons, a planar Fabry-Pérot microcavity is formed by placing a thin natural Cu_2O crystal between two highly reflective mirrors, as discussed in Section 3.1.3.2. Two DBRs form the top and bottom mirrors, with 13 and 10 pairs of SiO_2/Ta_2O_5 layers, respectively (See Fig. 3.5).

The coupling between cavity photons and Rydberg excitons is analysed by measuring the polaritonic energy dispersion as a function of the in-plane wavevector $k_{||}$ using a k-space imaging setup (See Section 3.2.1.4). As discussed in Section 2.2.3, the planar microcavity induces longitudinal confinement of the light at the resonant wavelength λ_c and corresponding frequency ω_c. For a single coupled longitudinal mode, the cavity photons acquire a quadratic energy dispersion $E_c \approx \hbar\omega_c + \hbar^2 k_{||}^2/2m_c^*$ (Eq. 2.31), akin to particles moving in the transverse plane of the cavity mirrors with an effective mass m_c^*. Due to the much larger mass of the excitons, the excitonic dispersion is virtually flat for relevant in-plane momenta $k_{||}$ and may cross the photon mode at the exciton energy. Strong light-matter coupling is manifested as an avoided crossing and two new modes (upper and lower exciton-polariton) that are separated by the vacuum Rabi splitting $\hbar\Omega$. To measure the k-dependent energy dispersion, transmission spectroscopy was performed. The excitation source was a top-hat resonant pulsed laser covering from 568 to 582 nm in wavelength [See Fig. 3.8(b)]. The angle-resolved transmission spectra at 4 K from the experiment and TMM simulations are shown in Fig. 6.1.

The spectrum from the transmission experiment exhibits a clear avoided crossing between the cavity modes and the Rydberg exciton states with $n = 3, \ldots, 6$, thus proving the successful exciton-photon hybridisation and the subsequent formation of Rydberg exciton-polaritons up to $n = 6$. While the linewidth of the P-exciton ground state ($n = 2$) is too large to reach the strong coupling regime, the increasingly shorter lifetime of the excited states makes it possible to form Rydberg polaritons under the conditions of our experiment in excellent agreement with the theoretical expectation based on TMM calculations [See Fig. 6.1(b)].

The experimental spectra can be used to characterise the cavity further and extract useful parameters such as the Q-factor, free spectral range, and cavity thickness. The experimental Q-factor of the microcavity is given by $Q = E_c/\delta E_c$ (Eq. 2.27), where δE_c denotes the cavity-

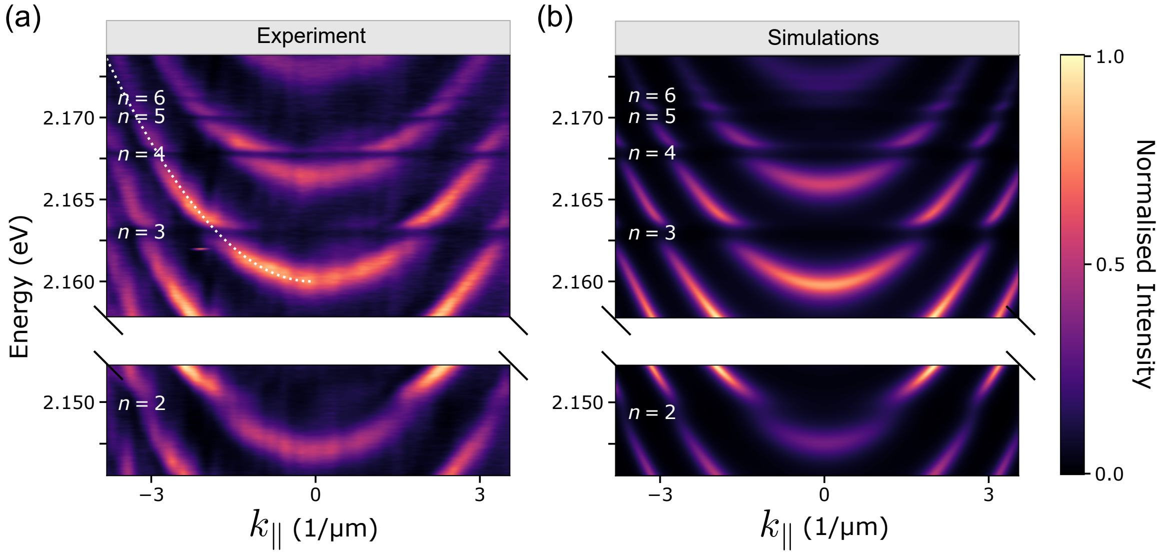

Figure 6.1: Momentum-resolved transmission spectra at $T = 4$ K in the vicinity of the $n = 2, \ldots, 6$ transitions from the experiment (a) and transfer matrix simulations (b). The dotted white line in (a) shows the cavity mode. The excitation source in (a) is a top-hat resonant pulsed laser [See Section 3.2.1.5 and Fig. 3.8(b)].

transmission linewidth of the nearly uncoupled cavity mode, away from any exciton resonance, at normal incidence. Selecting a cavity away from exciton resonances is important since, as soon as the interaction with an exciton transition is involved, the linewidth of the cavity mode will be limited by absorption events. In this case, the resonance energy of the first fully resolved cavity mode at the low energy side of the spectrum is $E_c \approx 2.135$ eV and the corresponding linewidth (FWHM) extracted from a Lorentzian fit is $\delta E_c \approx 1.26$ meV. The experiment thus yields a quality factor $Q \approx 1,700$ that is smaller than the predicted value from TMM simulations $Q \approx 2,300$. This discrepancy is attributed to the fact that TMM simulations do not include the inhomogeneous broadening due to local cavity thickness modulation caused by DBR deposition, polishing and the wedged structure of the cavity. From the experimental free spectral range of $FSR_{\mathrm{exp}} \approx 6.6$ eV, the active layer thickness is estimated as $l \approx 31$ µm, which matches with optical microscopy measurements.

6.2 Position-Resolved Cavity Transmission

The large size of the microcavity along the transverse direction permits scanning the photon dispersion through the exciton resonances. Crystal polishing induces a slight wedge (∼0.6°) in the Cu_2O active layer. By varying the excitation position of the incident field to control the relevant thickness of the microcavity's active layer, the energy of the cavity mode can thus be tuned. This is implemented by using a position scanner with a spatial resolution of 30 nm per step that enables the cavity transmission to be scanned with high precision (∼13 µeV per step). Using the same top-hat laser excitation as the k-space spectrum, the transmission spectrum at each position of the scanner can be recorded. By stacking all individual spectra one after the other, the real-space spectrum can be constructed as a function of position. The experimental and simulated real-space spectra at $T = 4$ K in the vicinity of the first five P-exciton states are shown in Fig. 6.2. Similar to the case of k-space, a cavity mode comes into resonance with each Rydberg exciton transition as the position is scanned and exhibits a clear avoided crossing of the polariton modes for $n = 3, \ldots, 6$. The $n = 2$ exciton shows signs of avoided crossing, but not as clear as the higher-n states. These observations are confirmed by the simulated spectra using the TMM calculations. Individual transmission intensity line profiles at different positions are shown in Fig. 6.2(c,d). The dispersion of the upper and lower polariton modes (red dashed lines) can be clearly seen here as the anticrossing occurs in the vicinity of the exciton resonance (dotted grey lines).

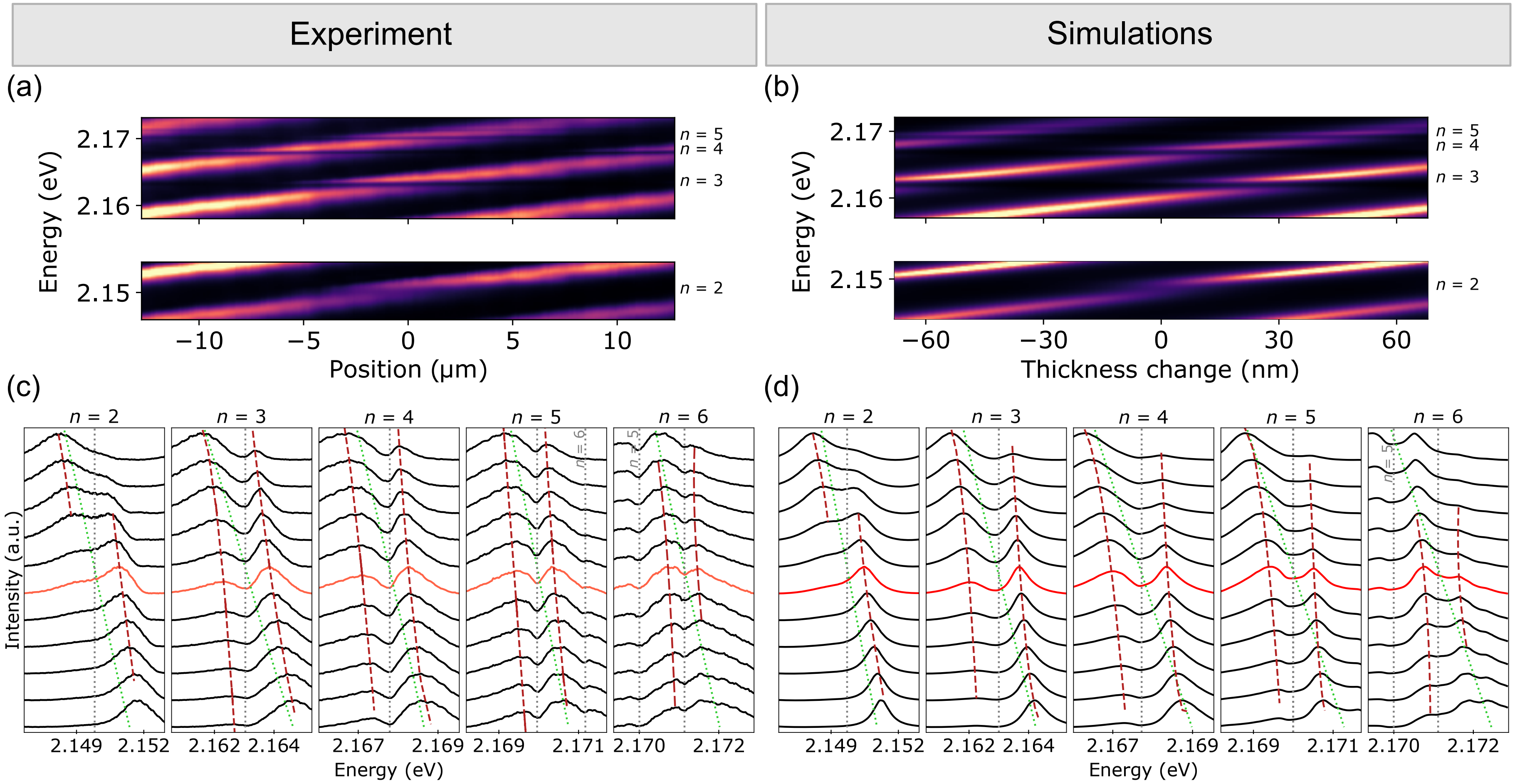

Figure 6.2: Experimental (a) and simulated (b) real-space position-resolved spectra at $T = 4$ K in the vicinity of the first five P-exciton states and the corresponding intensity line profiles (c,d). Dotted lines represent the exciton (grey) and cavity mode (green). Dashed lines trace the upper and lower polariton branches. The orange-lined spectrum is the line profile at zero detuning. The excitation source is a top-hat resonant pulsed laser [See Section 3.2.1.5 and Fig. 3.8(b)].

A careful examination of the transmission spectra is necessary to determine the zero cavity-exciton detuning for each Rydberg exciton state. The energy line profile of the resonance in a wedged planar Fabry-Pérot cavity is asymmetric (See Chapter 6 of Ref. [356]). For wedge angles such as the one in the present microcavity sample (∼0.6°) the asymmetry is such that the high energy slope of the cavity mode is steeper than the low energy side. The off-resonant cavity mode shows a slight asymmetry at the high energy side [orange dots in Fig. 6.3(a)] and a broadening compared to the k-space line profile due to the larger spot size of real-space measurements (nearly twice due to the lower NA of the excitation lens).

To determine the cavity-exciton detuning ($E_{\text{cav}} - E_n$) for each principal quantum number, the nearest cavity mode needs to be identified for each Rydberg state. Exciton absorption from multiple Rydberg exciton channels distorts the cavity modes, thus making it difficult to define them accurately. Therefore, a cavity mode at the low-energy side of the real-space transmission spectrum is selected as it is the furthest away from the exciton lines. Owing to small thickness variations in the microcavity sample, the cavity modes cannot be described with straight lines. Consequently, the cavity mode is fitted with an 8^{th} degree polynomial [yellow line in Fig. 6.3(b)]. A second cavity mode well away from the exciton transitions is also identified, and from these two modes, the spacing between adjacent modes is calculated. Subsequently, the cavity modes near the excitons can then be calculated by a simple energy translation since the cavity modes are equally spaced in energy by $hc/(2\bar{n}l)$, where c is the speed of light, h is

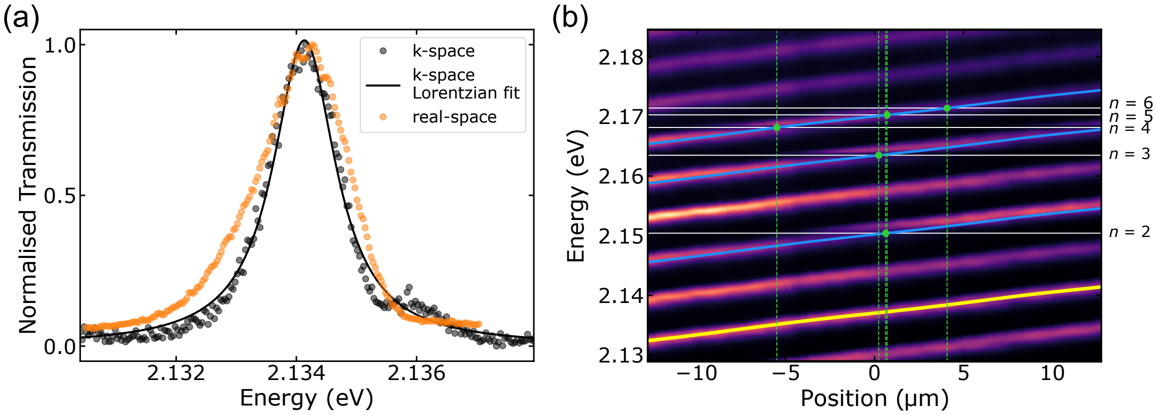

Figure 6.3: (a) Zoomed in cavity line profile at the low energy side of the transmission spectrum showing the asymmetric lineshape broadening (FWHM ≈ 1.74 meV) due to the wedged structure of the cavity (orange circles). The line profile of the cavity from k-space measurement in Fig. 6.1 (black circles) and the Lorentzian fit (FWHM ≈ 1.26 meV). (b) Experimental real-space spectrum at $T = 4$ K. Solid lines represent the exciton resonances (white) and cavity modes (blue and yellow). The point where each exciton line intersects with the corresponding cavity mode is denoted by a green dashed line.

the Planck constant, l is the cavity thickness, and $\bar{n}$ is the real refractive index of Cu_2O. This is achieved by translating one of the fitted cavity lines to find the modes in the vicinity of the first five exciton resonances [blue lines in Fig. 6.3(b)]. Zero detuning for each n can be accurately defined as the position where the exciton line intersects the corresponding cavity mode [green dashed lines in Fig. 6.3(b)]. The zero detuning spectrum is denoted by the orange-lined line profile for each n in Fig. 6.2. Interestingly, the amplitude of the transmission peaks of the upper and lower polaritons is not symmetric. This observation reflects the asymmetry of the exciton line, which originates from the continuous absorption background resulting in a Fano absorption profile, as discussed in Section 2.5.4. In the following section, the asymmetry in the transmission spectra is explained through a theoretical model based on the asymmetric absorption profile of the underlying Rydberg exciton transitions.

6.3 Theoretical Description of Transmission Spectra

The absorption lines of the yellow P-exciton series in Cu_2O have an asymmetric line shape, which here is attributed to interference with a spectrally broad, phonon-assisted background [240], giving rise to a Fano absorption profile $\alpha_n \propto \frac{\bar{\gamma}_n/2+2Q_n\Delta_n}{(\bar{\gamma}_n/2)^2+\Delta_n^2}$ with an asymmetry parameter $Q_n \neq 0$, a transition linewidth $\bar{\gamma}_n$, and a laser detuning $\Delta_n = \omega_{\text{in}} - E_n/\hbar$, where ω_{in} is the angular frequency of the laser. This asymmetry subsequently affects the shape of the cavity's transmission resonances, yielding asymmetry in the transmission peaks of the upper and lower polaritons.

In an excitation event, an incident photon can either excite any of the Rydberg exciton resonances n, described by the operator $\hat{X}_n$, or a phonon-assisted continuum of states, described by $\hat{Y}$, both at centre-of-mass momentum $\mathbf{k}$. The phonon-assisted states also possess an internal (relative) momentum $\mathbf{k}'$. The coupling of the Rydberg exciton states to the underlying phonon background provides an interfering excitation pathway, thus creating a Fano resonance [287]:

$$\begin{aligned}
\partial_t \hat{X}_n(\mathbf{k}) &= -\frac{\Gamma_n}{2}\hat{X}_n(\mathbf{k}) - i g_n \mathcal{E}(\mathbf{k}) - i\sum_{\mathbf{k}'} h_{n,\mathbf{k},\mathbf{k}'}\hat{Y}(\mathbf{k},\mathbf{k}')\,, \\
\partial_t \hat{Y}(\mathbf{k},\mathbf{k}') &= -\frac{\Gamma_{\mathbf{k},\mathbf{k}'}}{2}\hat{Y}(\mathbf{k},\mathbf{k}') - i g^{\text{bg}}_{\mathbf{k},\mathbf{k}'}\mathcal{E}(\mathbf{k}) - i\sum_{n} h_{n,\mathbf{k},\mathbf{k}'}\hat{X}_n(\mathbf{k})\,,
\end{aligned} \tag{6.1}$$

where $g^{\text{bg}}_{\mathbf{k},\mathbf{k}'}$ denotes the optical coupling rate to the phononic states of the background, $h_{n,\mathbf{k},\mathbf{k}'}$ the exciton-phonon coupling, $\Gamma_{\mathbf{k},\mathbf{k}'} = \gamma_{\mathbf{k},\mathbf{k}'} - 2i\Delta_{\mathbf{k},\mathbf{k}'}$ the complex phonon linewidth with linewidth $\gamma_{\mathbf{k},\mathbf{k}'}$ and detuning $\Delta_{\mathbf{k},\mathbf{k}'} = \omega_{\text{in}} - \omega_{\mathbf{k},\mathbf{k}'}$, and Γ_n is equivalently defined for the n_{th} exciton. The variables associated with the Rydberg resonance are defined equivalently. The field $\mathscr{E}$ can be understood to give rise to a photon density $\langle \mathscr{E}^\dagger(\mathbf{k})\mathscr{E}(\mathbf{k})\rangle$ in mode $\mathbf{k}$. In the above description, small contributions from scattering processes involving multiple different phonons are neglected. In the steady state, we can solve for the continuum operators:

$$\langle \hat{Y}(\mathbf{k},\mathbf{k}')\rangle = \frac{2}{\Gamma_{\mathbf{k},\mathbf{k}'}}\left[-ig^{\mathrm{bg}}_{\mathbf{k},\mathbf{k}'}\mathscr{E}(\mathbf{k}) - i\sum_n h_{n,\mathbf{k},\mathbf{k}'}\langle \hat{X}_n(\mathbf{k})\rangle\right]. \tag{6.2}$$

The phonon states can be assumed as flat ($g^{\mathrm{bg}}_{\mathbf{k},\mathbf{k}'} = g^{\mathrm{bg}}_{\mathbf{k}}$ and $h_{n,\mathbf{k},\mathbf{k}'} = h_{n,\mathbf{k}}$) and dense in the relative momentum quantum number, allowing the sums to be evaluated as:

$$\begin{aligned}\sum_{\mathbf{k}'} h_{n,\mathbf{k},\mathbf{k}'}\langle \hat{Y}(\mathbf{k},\mathbf{k}')\rangle &\approx \left[-ih_{n,\mathbf{k}}g^{\mathrm{bg}}_{\mathbf{k}}\mathscr{E}(\mathbf{k}) - ih^2_{n,\mathbf{k}}\langle \hat{X}_n(\mathbf{k})\rangle\right]\tau_{\mathbf{k},n} \\ &= -i\bar{h}_{n,\mathbf{k}}\bar{g}^{\mathrm{bg}}_{n,\mathbf{k}}\mathscr{E}(\mathbf{k}) - i\bar{h}^2_{n,\mathbf{k}}\langle \hat{X}_n(\mathbf{k})\rangle,\end{aligned} \tag{6.3}$$

where $\tau_{\mathbf{k},n}$ was defined as $\tau_{\mathbf{k},n} \equiv \tau_{\mathbf{k}}(\omega_{\mathrm{in}} = \omega_n)$ from $\tau_{\mathbf{k}}(\omega_{\mathrm{in}}) = \sum_{\mathbf{k}'}\frac{2}{\Gamma_{\mathbf{k},\mathbf{k}'}}$ and was absorbed into $\bar{h}_{n,\mathbf{k}} \equiv \sqrt{\tau_{\mathbf{k},n}}h_{n,\mathbf{k}}$ and, similarly, $\bar{g}^{\mathrm{bg}}_{n,\mathbf{k}}$ (that have units $\sim \sqrt{\mathrm{energy}}$). Small contributions from off-resonant Rydberg states are also neglected. While $\bar{h}_{n,\mathbf{k}}$ and $\bar{g}^{\mathrm{bg}}_{n,\mathbf{k}}$ can, in general, carry complex signatures of the underlying decay rates, here, they are assumed to be real and constant across each exciton resonance. The polarisation $\mathscr{P}(\mathbf{k}) = \chi_{\mathbf{k}}\mathscr{E}(\mathbf{k})$ can be solved explicitly and it defines $\chi_{\mathbf{k}}$ via:

$$\begin{aligned}\mathscr{P}(\mathbf{k}) &= \sum_n g_n\langle \hat{X}_n(\mathbf{k})\rangle + \sum_{\mathbf{k}'} g^{\mathrm{bg}}_{\mathbf{k},\mathbf{k}'}\langle \hat{Y}(\mathbf{k},\mathbf{k}')\rangle \\ &= -i\sum_n \frac{(g_n - i\bar{g}^{\mathrm{bg}}_{n,\mathbf{k}}\bar{h}_{n,\mathbf{k}})^2}{\frac{\Gamma_n}{2} + \bar{h}^2_{n,\mathbf{k}}}\mathscr{E}(\mathbf{k}) - i(\bar{g}^{\mathrm{bg}}_{\mathbf{k}}(\omega_{\mathrm{in}}))^2\mathscr{E}(\mathbf{k}) \\ &= -i\sum_n g_n^2\frac{(1 - iQ_{n,\mathbf{k}})^2}{\frac{\bar{\gamma}_n}{2} - i\Delta_n}\mathscr{E}(\mathbf{k}) - i(\bar{g}^{\mathrm{bg}}_{\mathbf{k}}(\omega_{\mathrm{in}}))^2\mathscr{E}(\mathbf{k}),\end{aligned} \tag{6.4}$$

where $\bar{\gamma}_n/2 = \gamma_n/2 + \bar{h}^2_n$ and the asymmetry parameter $Q_{n,\mathbf{k}} = \frac{\bar{g}^{\mathrm{bg}}_{n,\mathbf{k}}\bar{h}_{n,\mathbf{k}}}{g_n}$. The free-space absorption is given through the imaginary part of $\chi_{\mathbf{k}}$ as:

$$\alpha_{\mathbf{k}} = -\frac{2}{c\bar{n}}\Im(\chi_{\mathbf{k}}) = \sum_n \frac{4g_n^2}{c\bar{n}}\frac{\bar{\gamma}_n + 4Q_{n,\mathbf{k}}\Delta_n}{\bar{\gamma}_n^2 + 4\Delta_n^2} + \alpha^{\mathrm{bg}}_{\mathbf{k}}(\omega^{\mathrm{in}}), \tag{6.5}$$

where $\bar{n}$ is the refractive index. The terms $\sim Q^2_{n,\mathbf{k}}$ were dropped under the assumption that $Q^2_{n,\mathbf{k}} \ll 1$. Plain exciton absorption corresponds to the case when $Q_{n,\mathbf{k}} = 0$. The cross-term originates from the interference between direct and indirect excitation of the background and produces an asymmetric lineshape. The standard in-cavity field equation for transverse momentum $\mathbf{k}_{||}$ [175] is modified as follows:

$$\partial_t \tilde{\mathcal{E}}(\mathbf{k}_{||}) = -\frac{\Gamma_{\text{cav}}}{2}\tilde{\mathcal{E}}(\mathbf{k}_{||}) - \frac{i}{\bar{n}^2}\mathcal{P}(\mathbf{k}_{||}) + \eta_{\text{in}} E^{\text{in}}(\mathbf{k}_{||})\,, \tag{6.6}$$

with $\Gamma_{\text{cav}} = \kappa - 2i(\omega_{\text{in}} - (\omega_{\text{cav}} + \hbar k_{||}^2/(2m_{\text{ph}})))$, κ the cavity linewidth, m_{ph} the effective transverse photon mass and E^{in} the external driving field with corresponding coupling η. Transmission through the cavity at fixed $\mathbf{k}_{||}$ is proportional to the in-cavity intensity $T = C_{\text{out}}|\mathcal{E}|^2$ and is given by:

$$\begin{aligned} T_n = \Bigg[& \left(\frac{\kappa}{2} + \sum_n \left(\frac{g_n}{\bar{n}}\right)^2 \frac{[1-Q_n^2]\frac{\bar{\gamma}_n}{2} + 2\Delta_n \cdot Q_n}{(\bar{\gamma}_n/2)^2 + \Delta_n^2} + \left(\frac{\bar{g}^{\text{bg}}(\omega_{\text{in}})}{\bar{n}}\right)^2 \right)^2 \\ & + \left(\Delta_{\text{cav}} - \sum_n \left(\frac{g_n}{\bar{n}}\right)^2 \frac{[1-Q_n^2]\Delta_n - Q_n\bar{\gamma}_n}{(\bar{\gamma}/2)^2 + \Delta_n^2} \right)^2 \Bigg]^{-1}, \end{aligned} \tag{6.7}$$

where the parameter $G_n \equiv g_n/\bar{n}$ is the effective coupling strength. Note that for comparison with Eq. 6.5, terms $\sim Q_n^2$ should be dropped. For the case of a single exciton transition, while neglecting the adjucent transitions, the resonant cavity transmission spectrum (Eq. 6.7) can be approximated as:

$$T_n \approx \left[\left(\frac{\tilde{\kappa}}{2} + G_n^2 \frac{\bar{\gamma}_n/2 + 2Q_n\Delta_n}{(\bar{\gamma}_n/2)^2 + \Delta_n^2} \right)^2 + \left(\Delta_n - G_n^2 \frac{\Delta_n - Q_n\bar{\gamma}_n}{(\bar{\gamma}_n/2)^2 + \Delta_n^2} \right)^2 \right]^{-1}. \tag{6.8}$$

Here $\tilde{\kappa} \equiv \kappa + 2\left(\frac{\bar{g}^{\text{bg}}(\omega_{\text{in}})}{\bar{n}}\right)^2$ is the cavity linewidth far off-resonance, which includes losses from the phonon background. This equation yields transmission maxima at the expected polariton resonances as a function of the laser detuning $\Delta_n = \omega_{\text{in}} - E_n/\hbar$.

The experimental zero-detuning spectra presented in Fig. 6.2 are fitted using Eq. 6.7, which quantitatively explains the asymmetric transmission peaks observed in the experiments [See Fig. 6.4(a)]. Including adjacent transitions is particularly important for $n = 4, \ldots, 6$ transitions, where the exciton energy spacing becomes comparable to the cavity linewidth. The fittings using Eq. 6.7 are implemented by varying the effective exciton-coupling coupling strength G_n and a normalising amplitude while fixing other independently measured parameters such as $\tilde{\kappa}$, Q_n, and $\bar{\gamma}_n$. Considering that there is essentially only one fitting parameter (i.e. the G_n), the theory yields a remarkably good agreement with the measurements. The fitting parameters and the extracted G_n values are summarised in Table 6.1.

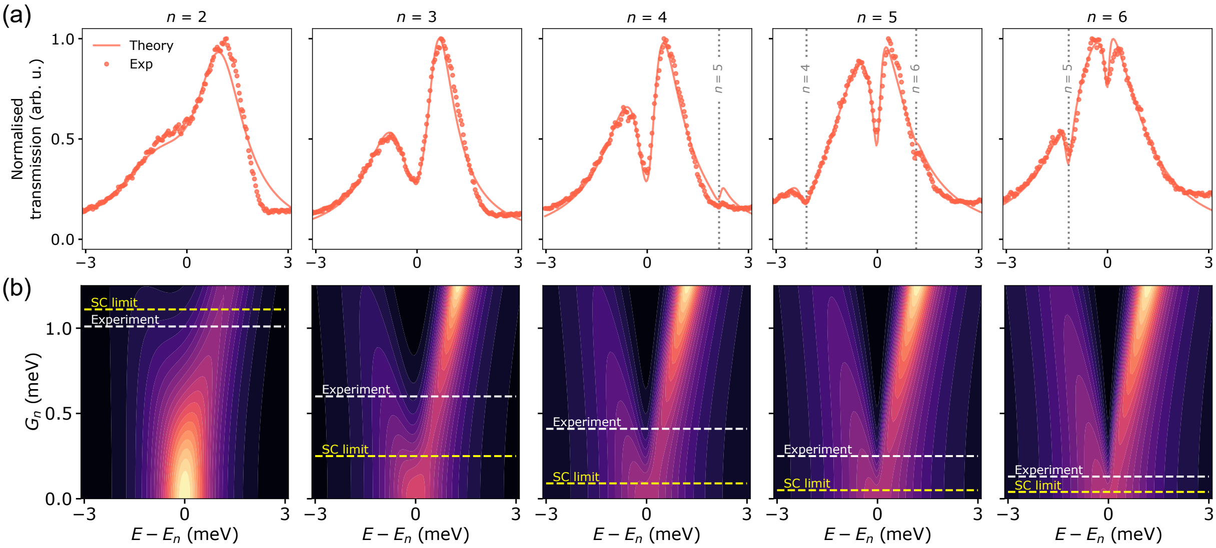

Figure 6.4: (a) Experimental data and fitted lines for the lower and upper polariton branches at zero detuning (cavity resonant with exciton) for the $n = 2, \ldots, 6$ exciton states. The excitation source in panel is a top-hat resonant pulsed laser [See Section 3.2.1.5 and Fig. 3.8(b)]. The small mismatch between the theory fits and the experiment at positive energies is due to a wedge in the microcavity, which gives rise to an asymmetric cavity line profile, as discussed in Section 6.2. (b) Theoretical contour plots of the effective coupling strength G_n as a function of detuning for the $n = 2, \ldots, 6$ exciton states. The theoretical strong coupling transition (See Section 6.4) is depicted as a yellow dashed line, while the experimentally obtained coupling strength is shown as a white dashed line.

n	κ (meV)	γ (meV)	γ_{pol} (meV)	Q_n	$\hbar\Omega_R$ (meV)	$\hbar\Omega_R/\gamma_{\mathrm{pol}}$	min(G_n) for SC (meV)	G_n (meV)
2	1.44 ± 0.03	2.75 ± 0.02	2.09 ± 0.02	-0.251 ± 0.005	–	–	1.11 ± 0.01	1.01 ± 0.01
3	1.90 ± 0.03	0.789 ± 0.007	1.34 ± 0.02	-0.241 ± 0.005	1.50 ± 0.03	1.12 ± 0.03	0.25 ± 0.01	0.60 ± 0.01
4	2.37 ± 0.06	0.363 ± 0.005	1.36 ± 0.03	-0.212 ± 0.007	1.13 ± 0.03	0.83 ± 0.03	0.09 ± 0.01	0.41 ± 0.01
5	2.66 ± 0.05	0.211 ± 0.005	1.43 ± 0.03	-0.20 ± 0.01	0.89 ± 0.04	0.62 ± 0.03	0.05 ± 0.01	0.25 ± 0.01
6	2.64 ± 0.04	0.142 ± 0.005	1.39 ± 0.02	-0.17 ± 0.01	0.67 ± 0.04	0.48 ± 0.03	0.04 ± 0.01	0.13 ± 0.01

Table 6.1: Cavity linewidth κ, exciton linewidth γ, asymmetry parameter Q_n, vacuum Rabi splitting $\hbar\Omega_R$, minimum effective exciton-photon coupling G_n for strong coupling, and the fitted G_n at zero detuning for each Rydberg exciton transition n. γ_{pol} is the average exciton (γ) and cavity linewidth (κ). min(G_n) for strong coupling is theoretically calculated when two clear peaks in spectra are observed (that is when two local maxima are observed).

6.4 Exciton-Photon Coupling Strength

The theoretical line profiles can be used to obtain the minimum value of G_n required to observe clearly separated polariton resonances for each n and determine whether an exciton transition is strongly coupled [See Fig. 6.4(b)]. Specifically, Eq. 6.8 is used to plot the theoretical transmission spectrum for a broad range of G_n values for each exciton transition individually. As an example, Fig. 6.5(a) shows seven theoretical spectra for the $n = 3$ transition with G_n values ranging from 0.1 to 0.4. A clear dip between the two polariton modes starts forming for a G_n value between 0.2 and 0.3. To accurately determine the exact value, the derivative of the transmission spectrum for this range of values is plotted [See Fig. 6.5(b)]. The minimum G_n is calculated as the first value where the derivative near resonance crosses zero [red dashed line in Fig. 6.5(b)]. The corresponding spectrum describes the case where the transmission flattens near the resonance. For $n = 3$ in particular, this is $G_n = 0.25$. For a greater G_n value, there is a local minimum in the transmission function with two separate peaks on either side. A similar routine is implemented for the other exciton transitions. The minimum values of G_n for operation in the strong coupling regime are summarised in Table 6.1.

The experimental coupling strength along with the minimum value required for strong coupling are overlaid on the theoretical contour plot of the effective coupling strength G_n as a function of detuning for each of the $n = 2, \ldots, 6$ exciton states [See Fig. 6.4(b)]. The depicted comparison between the measured values (white dashed lines) and the theoretical minimum of G_n (yellow dashed lines) demonstrates that the microcavity just reaches the onset of the strong coupling regime for $n = 2$ and shows Rydberg polaritons well within the strong coupling regime for $n = 3, \ldots, 6$.

The effective exciton-photon coupling strength G_n decreases with n, in a similar manner to the Rydberg scaling of the oscillator strength, as shown in Fig. 6.6. This observation implies that the strong coupling condition is ultimately limited by the competition with the linewidth

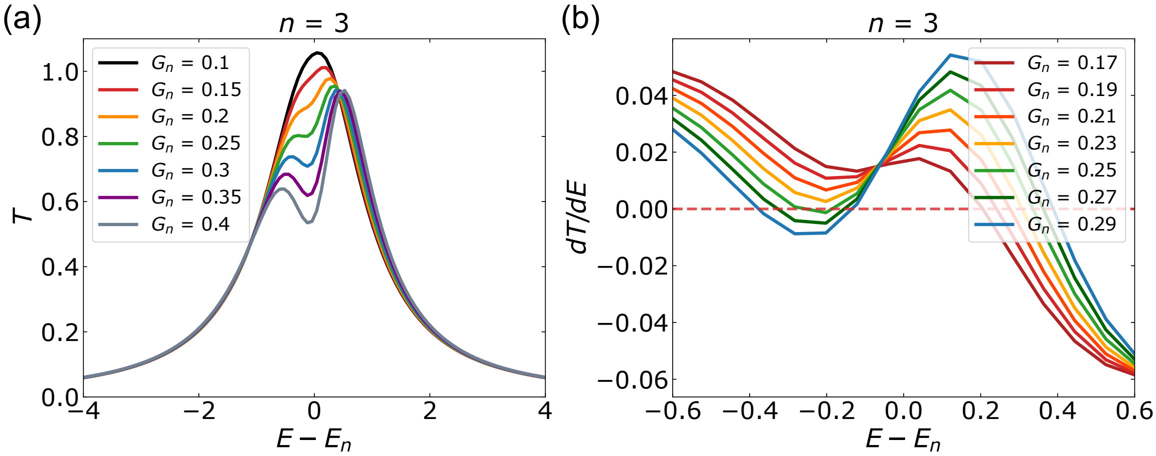

Figure 6.5: (a) Theoretical transmission spectra for the $n = 3$ transition for different values of G_n. The spectra were calculated using Eq. 6.8. (b) Derivative of the transmission spectra ($\mathrm{d}E/\mathrm{d}T$) with respect to energy for $n = 3$ for different values of G_n.

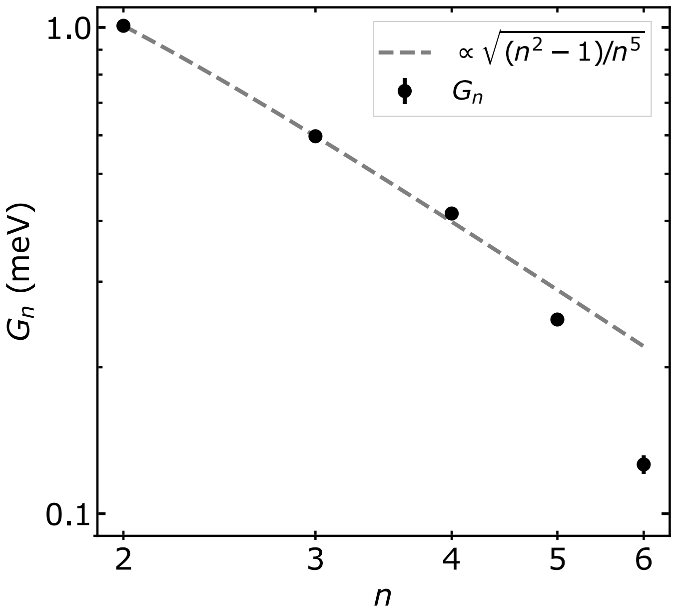

Figure 6.6: Effective coupling strength parameter G_n versus quantum number n in the experiment (circles), and the square root of the theoretical oscillator strength (dashed line) show agreement with each other. The error bars (vertical lines) represent fitting errors.

of the formed polaritons. The exciton-photon coupling can, in principle, be made stronger by increasing the cavity thickness because a larger volume of the active medium collectively enhances the exciton-photon coupling. However, the phonon-induced absorption background of Cu_2O represents a competitive photon-loss mechanism that adds to the linewidth of the cavity. The role of each one of these two competitive mechanisms is further studied using TMM simulations in the following section.

6.5 Transfer Matrix Simulations

The aim of this section is to use the transfer matrix method to investigate the strength of coupling between the yellow nP-exciton transitions and the cavity mode. Additionally, TMM simulations can further elucidate the contribution of the phonon background to strong coupling in Cu_2O microcavities. The cavities in all TMM calculations consist of 13 and 10 pairs of alternating Ta_2O_5 and SiO_2 layers for the top and bottom DBRs as in the experiment.

6.5.1 Refractive Indices

A key challenge in calculating the coupling strength of Rydberg exciton transitions to cavity modes involves obtaining the correct optical response of Cu_2O. The complete excitonic picture is only observed at cryogenic temperatures (See Section 2.1.1). Hence, the refractive index of Cu_2O ($\tilde{n} - ik$) must also be obtained at the same temperature, making it difficult to use standard techniques such as ellipsometry. Furthermore, to determine the contribution of the phonon background to the strong coupled Rydberg states, the optical response of Cu_2O must be accurately determined both in the presence and absence of the phonon background. This analysis requires estimating the complex refractive index of Cu_2O when the absorption spectrum arises from only P excitons, without any phonon background, in addition to case where the background is present.

The imaginary part of the refractive index can be extracted by recording the absorption coefficient of Cu_2O at $T = 4$ K. The complex refractive index, following the Kramers-Kronig relations, is then obtained using a Hilbert transformation of the imaginary part [37] [See Fig. 6.7(d)]. A constant real value of 3 was then added to the refractive index of Cu_2O to obtain a dispersion similar to that of the crystal [357].

The k values shown in Fig. 6.7(b) were obtained by extracting values from the optical response of Cu_2O in Ref. [240]. This figure shows two broad absorption bands corresponding to the phonon-assisted absorption of the yellow $1S_y$ excitons for wavelengths shorter than 606 nm and of the green $1S_g$ excitons for wavelengths shorter than 572 nm, respectively. After removing the phonon-assisted $1S_g$ component, the optical response of only yellow P and $1S_y$ excitons remain [See Fig. 6.7(c)]. When both the phonon-assisted absorption into $1S_y$ and $1S_g$ are removed, the optical response of only nP excitons can be isolated [See Fig. 6.7(a)]. Here, while k demonstrates the narrow nP resonances, a residual background absorption exists near the band edge and is assigned to the Urbach tail (See Section 2.5.4). The real parts of the corresponding refractive indices ($\tilde{n}$) are also shown in the plots of Fig. 6.7. These refractive indices can then be used to calculate the effect of such exciton transitions on the resultant polariton modes.

6.5.2 The Effect of Cavity Thickness

Using the estimated refractive index of Cu_2O ($\tilde{n} - ik$), the thickness of the crystal can be varied to tune the cavity mode into resonance with each of the exciton transitions, which occurs for thicknesses at integer multiples of $\lambda/2\tilde{n}$. The calculated transmission spectra of a microcavity with different Cu_2O thicknesses are shown in Fig. 6.8. The energy of the P-exciton transitions is denoted by the white dashed lines. For the case of a $\lambda/2\tilde{n}$ cavity with a crystal thickness

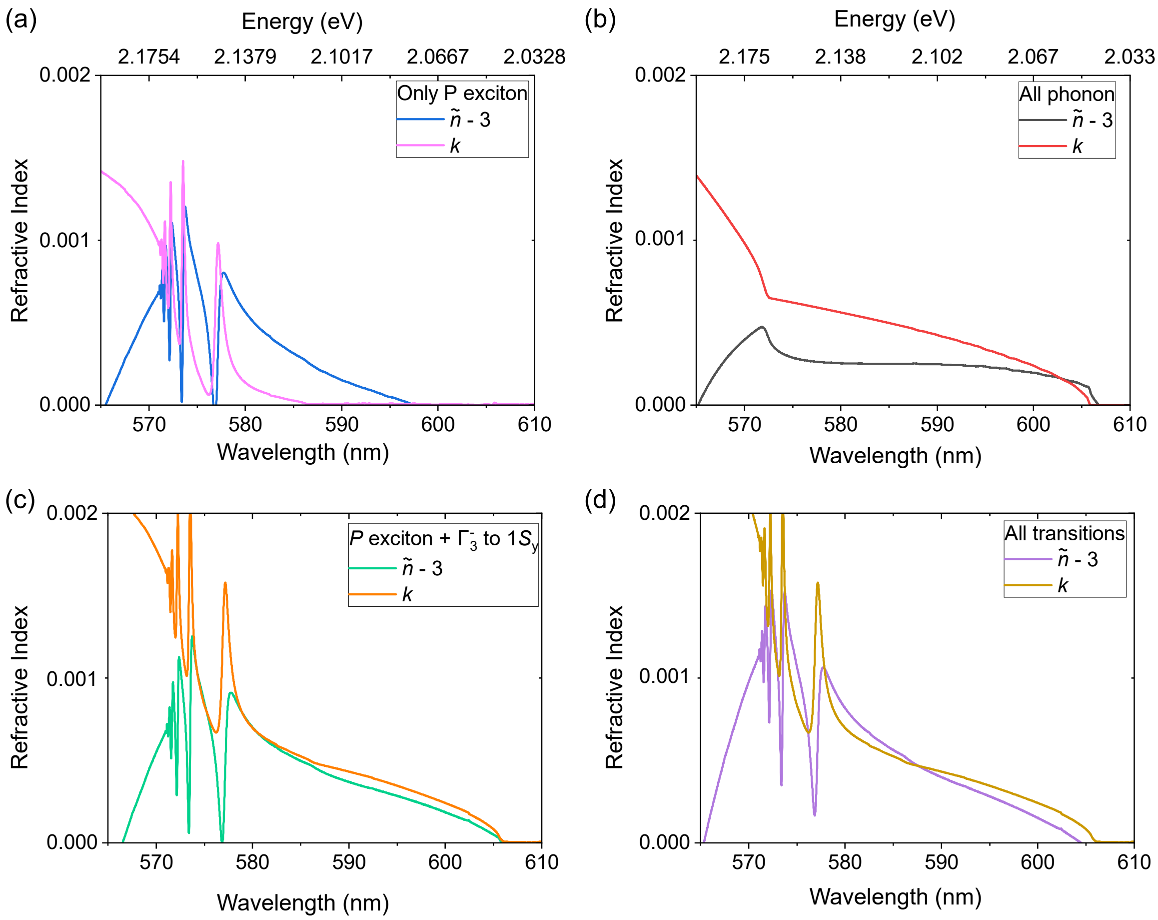

Figure 6.7: The complex refractive index of cuprous oxide at $T = 4$ K estimated when the absorption spectrum arises from (a) P excitons, (b) only phonon-assisted 1S transitions, (c) only yellow series excitons and (d) all exciton transitions.

~96 nm, a broadening of the normal modes is observed when the cavity mode is resonant to the exciton modes; however, no clear splitting is obtained [See Fig. 6.8(a)]. On the contrary, a much thicker $21\lambda/2\tilde{n}$ cavity with a thickness ~2 µm exhibits clear splitting for the $n = 3, \ldots, 7$ exciton transitions, visible, demonstrating strong coupling of the resonant modes [See Fig. 6.8(b)]. For the $n = 2$ transition, the coupling strength to the cavity mode results in a small broadening and splitting, still below the onset of strong coupling, similar to the experiment.

When varying the cavity thickness, the minima in normal mode splitting energy occurs when the cavity mode is in resonance with the exciton transition. Fig. 6.8(c) shows the Rabi splitting energy of the $n = 3, \ldots, 7$ exciton transitions as a function of cavity thickness, expressed in integer multiples of $\lambda/2\tilde{n}$. The noise in the estimated Rabi splitting energy trend arises from the spectral resolution of 0.03 nm used to experimentally measure the absorption spectrum of Cu_2O crystal for the TMM calculations. All P-exciton transitions display an increase in

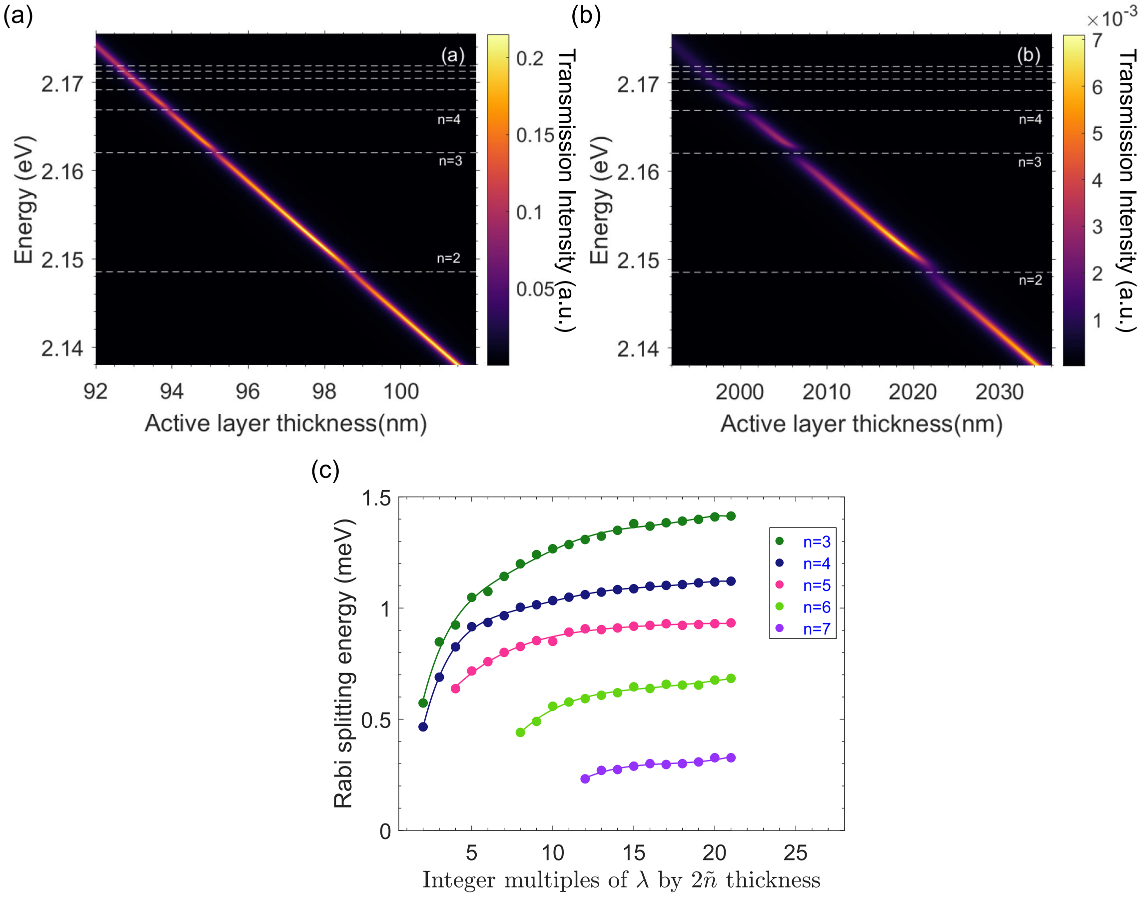

Figure 6.8: The calculated transmission through a microcavity with different cuprous oxide crystal thicknesses of (a) $\lambda/2\tilde{n}$ and (b) 21 $\lambda/2\tilde{n}$. (c) The calculated Rabi splitting energies of different cuprous oxide yellow transitions as a function of crystal thickness in the cavity.

Rabi splitting energy with increasing cavity thickness due to the accompanying enhancement of the absorption strength before slowly saturating to a constant value. The highest splitting is obtained for the $n = 3$ transition, followed by the $n = 4$, 5 and 6 transitions. The increase in thickness of Cu_2O crystal required to observe the onset of strong coupling for increasing principal quantum number is explained in the next section.

6.5.3 The Effect of Phonon Background

To exploit the giant nonlinearities inherent to Rydberg excitons, achieving strong coupling in as high a principal quantum number n is necessary. The reduction of oscillator strength as well as spectral linewidth (FWHM) by the same scaling factor of n^{-3} implies that transitions of all principal quantum numbers should be equally strongly coupled. To better understand the origin of strong coupling in Cu_2O, the Rabi splitting was calculated for two cases: first, for exciton transitions when the Cu_2O optical response consists of only P excitons, and second when phonon-assisted 1S excitons are calculated.

The polariton linewidth depends on the averaged exciton and cavity linewidths weighted by their Hopfield coefficients (See Section 2.3.2). When the cavity mode is in resonance with the exciton transition, the exciton and photon components of the emerging polariton mode have equal magnitude and affect the polariton linewidth in equal weights. The polariton linewidths determine the lifetime of the polaritons, and the Rabi splitting energies determine the time period of oscillation between the hybrid states within those polariton lifetimes. The exciton linewidths extracted from fitting the exciton absorption lines with an asymmetric Lorentzian formula are shown in Fig. 6.9(b). Note that a new thin Cu_2O crystal was used, extracted from the same mother crystal as the one used in the experiments in this chapter. The TMM calculated cavity linewidth is extracted for two different optical responses. First, a cavity with a transparent spacer, given by a constant refractive index of 3, is considered. The cavity spectral FWHM at wavelengths resonant with the nP-exciton transitions shows the expected 1/thickness reduction due to the increase of cavity round-trip time [See Fig. 6.9(b)]. Conversely, a cavity with phonon-assisted $1S_y$ and $1S_g$ transitions shows a broadening of the cavity mode with increasing active layer thickness [See Fig. 6.9(a)]. This observation highlights that the resonant $1S_y$ absorption offers an additional decay channel for the photons. Cavity modes resonant with transitions of $n >= 5$ are relatively broader due to additional absorption by the $1S_g$ excitons in addition to the $1S_y$ excitons. A secondary broadening is also caused by the background Urbach tail resonant with high-n Rydberg states (See Section 2.5.4). The former effect can be eliminated

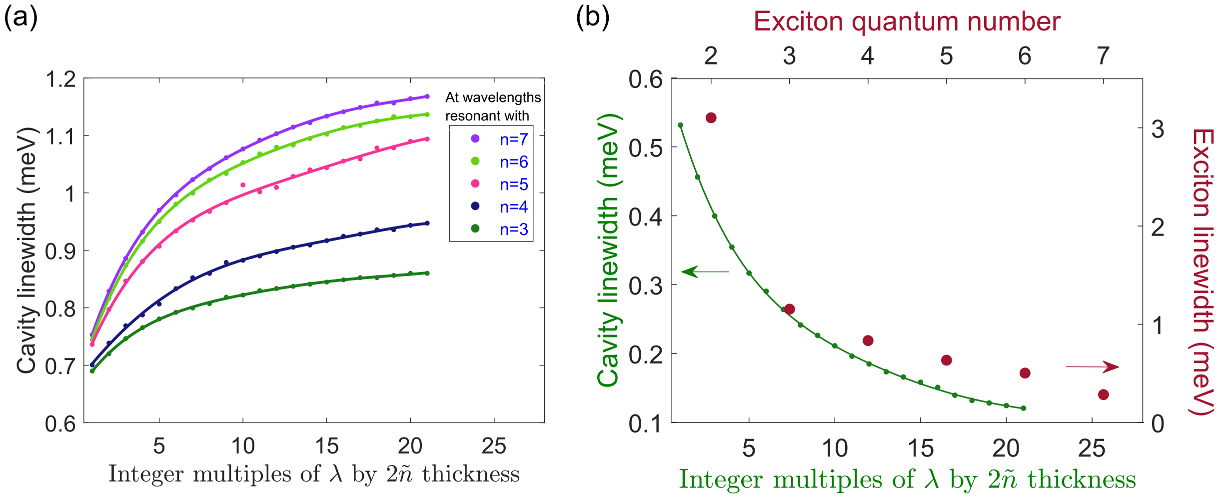

Figure 6.9: The extracted linewidths of the calculated cavity modes in the (a) presence and (b) absence of phonon-assisted transitions from TMM simulations. The P-exciton linewidths are also shown as scatter plots (b).

by two-photon absorption [34, 358], first to a low-lying S exciton followed by a transition to a higher P exciton.

A so-called strong coupling factor $\hbar\Omega/\gamma_{\text{pol}}$ can be defined by dividing the Rabi splitting energy [See Fig. 6.8(c)] with the corresponding polariton linewidth. The system is in the strong coupling regime when there is a clear Rabi splitting present. Therefore, a nonzero strong coupling factor indicates operation in the strong coupling regime. Figure 6.10(a) presents the strong coupling factor calculated using the polariton linewidth obtained from a cavity mode broadened by the phonon-assisted transitions, i.e. when the phonon background is included in the absorption. The strong coupling factor $\hbar\Omega/\gamma_{\text{pol}}$ plateaus quickly as the cavity thickness increases as the additional decay channel into the phonon-assisted $1S_g$ hinders the observation of strong coupling for high-n. On the other hand, if the polariton linewidth is calculated for the case where the P excitons can emit light only into the cavity mode, i.e. when the phonon background is removed, the coupling factor increases continuously with increasing cavity thickness and no plateau is observed [See Fig. 6.10(b)].

Therefore, it is evident that additional phonon-assisted absorption of the 1S excitons resonant with the P excitons is the main reason for the saturation of Rabi splitting with thickness. This limitation, in turn, poses a challenge towards the observation of strong coupling in high n giant Rydberg excitons. Note that the estimation of Rabi splitting in the TMM simulations is limited up to $n = 7$ due to the same limit on nP transitions observed in the absorption spectrum of the Cu_2O crystal sample used. This particular crystal sample was taken from the same natural

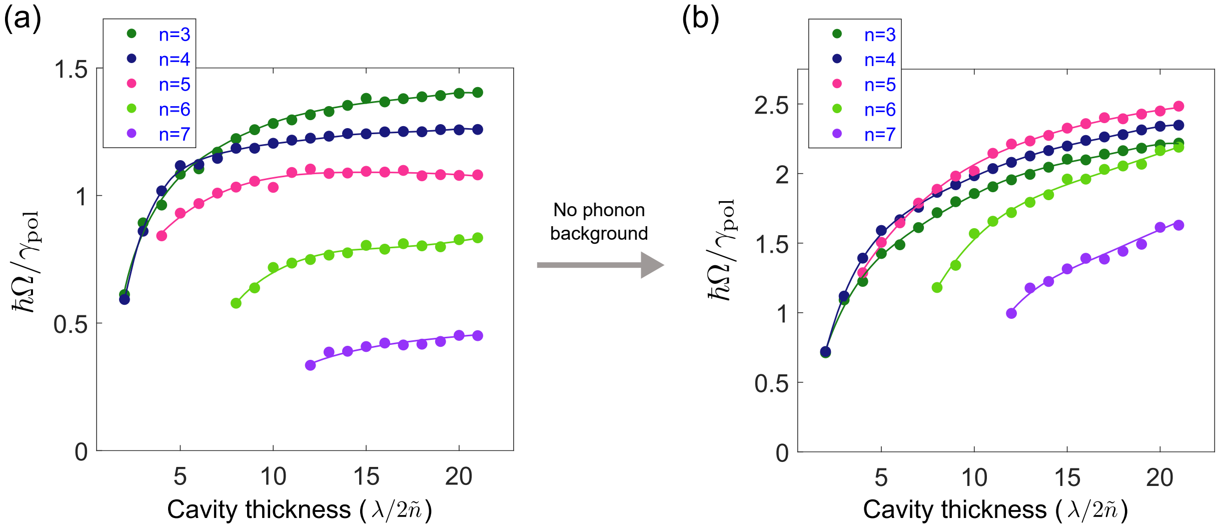

Figure 6.10: Transfer matrix calculations of the strong coupling factor ($\hbar\Omega/\gamma_{\text{pol}}$) for the yellow P excitons in the (a) presence and (b) absence of phonon-assisted 1S transitions. The solid lines are a guide to the eye.

stone used in the cavity, thus allowing a better comparison with the experimental spectra. The decision to use it for the TMM simulations in this work and Ref. [250] was based on the fact that it shows a more representative spectrum for the thin Cu_2O samples extracted from the mother crystal, and hence the one used in the cavity. This comparison highlights a mistake in our judgement when assuming that all samples would yield exciton resonances up to $n = 12$ as the sample of Fig. 5.1, which was the first Cu_2O sample ever prepared in our research group. When using the experimental absorption spectrum obtained from this Cu_2O crystal that exhibits clear resonances up to $n = 12$, TMM calculations were able to exhibit Rabi splitting up to $n = 12$. Hence Cu_2O presents a potential for observation of high-n strong coupling of ground state transitions.

An alternative route to enhanced strong coupling and hence enhanced single-particle nonlinearity may be achieved using electromagnetic induced transparency schemes [34, 358]. However, the interaction strength of the $n = 3, \ldots, 6$ P-exciton ground state transitions are sufficiently large to present an interesting opportunity to explore additional non-linearity effects induced when these polaritons interact with each other through cavity-mediated Rydberg blockade.

6.6 Limiting Factors to Strong Coupling

The calculations based on the transfer matrix method indicate that the competition between the cavity thickness and the phonon-induced absorption background leads to a finite ratio of the vacuum Rabi splitting to the linewidth of the polaritons as the cavity thickness is increased. In the absence of the phonon background, the calculations yield a steadily increasing ratio of the Rabi splitting to the polariton linewidth with increasing crystal thickness. On the other hand, with the phonon absorption background, the calculations also predict strong coupling for all Rydberg states observed in the bulk crystal, but the coupling strength plateaus as cavity thickness increases.

The question then arises as to why the experiment is limited to $n = 6$ for strong coupling when the exciton series is extended up to $n = 12$ in the bulk crystal. This limitation could be due to several reasons: the plasma effect, the blockade effect, external strain or charged defects in the crystal.

6.6.1 Photon Number and In-cavity Intensity

To investigate whether the plasma and blockade effects are responsible for the reduced number of strongly coupled Rydberg exciton transitions, the photon number and the in-cavity intensity are calculated.

The in-cavity photon number per cavity mode n_{cav} can be estimated from the spatially and wavelength-integrated CCD count rate R_{2D} of the transmission spectrum within a cavity mode energy range [for instance, see Fig. 6.3(a)], which is calculated as $R_{\mathrm{2D}} = 4.2 \times 10^6$ counts/s in this experiment. To associate this quantity to n_{cav}, the microcavity is modelled as Fabry-Pérot cavity with transmission coefficients β_1 for the back mirror on the excitation side and β_0 for the front mirror on the collection side. The pulsed laser excitation creates a photon population n_{cav} inside the cavity. On a time scale of the order of the round trip time given by $\tau_{RT} = 2Ln_{ref}/c \approx 0.62$ ps (Eq. 2.28), a fraction $\sim\beta_1 n_{\mathrm{cav}}$ of the cavity photons leaks out of the back mirror, leaving a population of $n_{\mathrm{cav}} - n_{\mathrm{cav}}\beta_1$ photons inside the cavity. The leakage through the front mirror is thus $\beta_0(n_{\mathrm{cav}} - n_{\mathrm{cav}}\beta_1) \approx n_{\mathrm{cav}}\beta_0$. The photon leakage rate is given by $n_{\mathrm{cav}}\beta_0/\tau_{RT}$. R_{2D} is related to n_{cav} by:

$$R_{\mathrm{2D}} = \frac{\beta_0 n_{\mathrm{cav}}}{\tau_{RT}} \eta \tau_p \times \mathrm{PRF} \times \frac{\mathrm{QE}}{\alpha}, \tag{6.9}$$

where $\beta_0 = 3 \times 10^{-4}$ is the transmission of the out-coupling DBR mirror (See Section 3.1.3.2), $\eta = 0.208$ is the total optical collection efficiency, $\tau_p = 5$ ps is the laser pulse duration, PRF = 78 MHz is the pulsed laser repetition frequency, QE = 0.97 is the CCD's quantum efficiency and $\alpha = 1.5$ e^-/count is the CCD's sensitivity. The total optical collection efficiency is estimated as by considering the transmission/reflection coefficient of all optical components the light encounters after being transmitted from the cavity and until it reaches the spectrometer's CCD camera [See Fig. 3.8(a)]. Substituting $R_{\mathrm{2D}} = 4.2 \times 10^6$ counts/s to Eq. 6.9 yields $n_{\mathrm{cav}} = 160 \pm 100$.

The peak in-cavity intensity can be estimated from the multiplication of the photon flux Φ with the incident photon energy E_{ph} as:

$$I_{\mathrm{in-cavity-peak}} = \Phi \cdot E_{\mathrm{ph}} = 2n_{\mathrm{cav}}hc/(\tau_{\mathrm{RT}}A\lambda) \approx 26\ \mathrm{\mu W/\mu m^2}\,, \tag{6.10}$$

where A is the area of the laser spot with diameter $\sim$3 µm and $\lambda \approx 575$ nm as the middle of the top-hat excitation [See Fig. 3.8(b)]. The in-cavity intensity is sufficiently low that the plasma effect and the blockade effect can be neglected [242].

By considering a mean laser power of $P_{\mathrm{laser-mean}} \approx 40\mathrm{\mu W/nm}$, the peak laser intensity incident can be estimated as:

$$I_{\text{laser-peak}} = \frac{P_{\text{laser-peak}}}{A} = \frac{P_{\text{laser-mean}}}{\tau_p \times \text{PRF} \times A} \approx 15\ \frac{\text{mW}}{\mu\text{m}^2}\,. \tag{6.11}$$

Comparing the peak in-cavity intensity with the peak laser intensity incident on the sample yields a cavity throughput of ∼0.2%.

The Rydberg blockade effect can result in non-classical light. The blockade effect arises from the competition of the interaction-induced level shift and the width of the exciton line at a given principal quantum number n (See Section 2.5.2). For P excitons, several potential curves with degenerate asymptotes contribute to the nonlinearity. However, one approach includes using the range of the resulting non-local nonlinear response (see, e.g. Ref. [47]) to estimate the blockade radius. This approach yields a blockade radius of 1 µm at $n = 15$, as obtained from the measured nonlinear absorption without a cavity. This length scale is known to scale as $n^{7/3}$ with the principal quantum number n, yielding a blockade radius r_{Ry} above 100 nm for $n = 6$.

The threshold particle number for non-linearity n_{th} is simply the mode volume of the cavity $V_{\text{cav}} = A \cdot L$ divided by the Rydberg volume $V_{\text{Ry}} = 4/3\pi r_{\text{Ry}}^3$. Assuming a blockade radius of ∼100 nm for $n = 6$ and given the excitation spot diameter of 3 µm and cavity length $L = 31$ µm, the particle density for non-linearity in the cavity is $n_{th} \simeq 5 \times 10^4$, which is two orders of magnitude larger than our cavity photon number n_{cav}. However, this threshold could be improved by reducing the thickness of the crystal and the spot size. For an experimentally achievable mode volume of 1 µm^3, the cavity would saturate already at a level of ∼200 photons and generate non-classical light at such low photon numbers for $n = 6$. Therefore, it is possible to reach the regime of a few strongly interacting polaritons for cavity-mode volumes achievable in future experiments, although higher-n polaritons are more desirable.

6.6.2 Strain Effect in the Cavity

Another potential reason behind the reduced number of observed strongly coupled transitions is the strain in the microcavity. This hypothesis is tested by first investigating the amount of strain present in the current sample by performing PL measurements. Then, a new sample is prepared to further investigate the induced strain due to the cavity fabrication process implemented in this work.

The cavity PL spectra at different two different locations are shown in Fig. 6.11. The lower signal-to-noise ratio is attributed to the fact that the wavelength region of the 1S orthoexciton is inside the stopband (See Fig. 3.6). The spectrum labelled “Centre” (blue line in Fig. 6.11) corresponds to a location in the middle of the cavity sample and coincides with

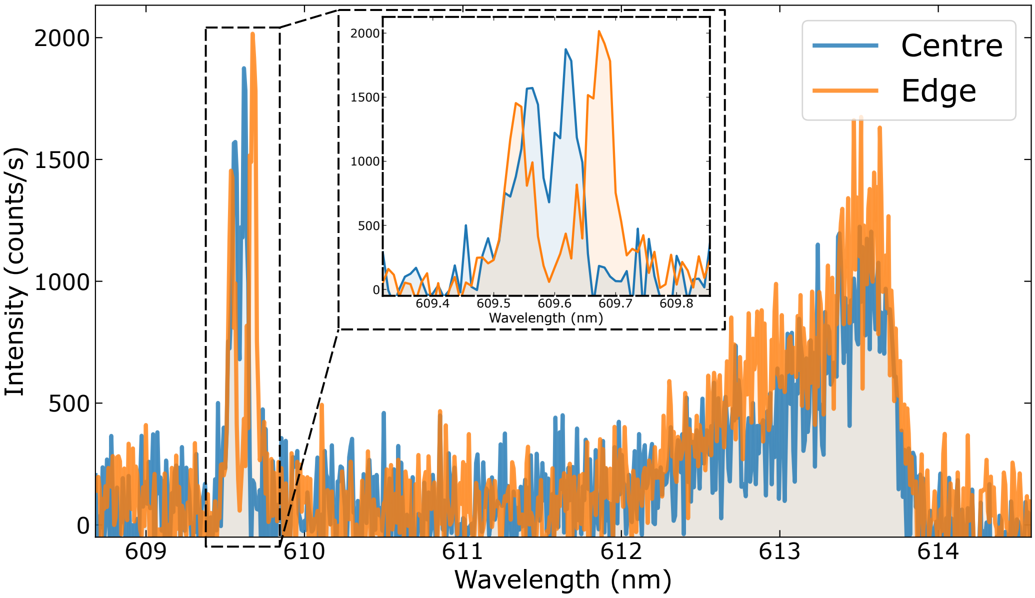

Figure 6.11: Photoluminescence spectra recorded from the centre (blue line) and from an edge of the cavity (orange line). Inset displays the spectral region around the 1S orthoexciton.

the area where Figs. 6.1 and 6.2 were recorded. The spectrum consists of the 1S orthoexciton peak circa 609.6 nm and two broad features at ∼612.6 nm and ∼613.5 nm, corresponding to the phonon-assisted transition involving the Γ_5^- and Γ_3^- phonon, respectively [243, 248], as discussed in Section 2.5.5. Interestingly, the 1S state is split by ∼67 pm. This splitting is attributed to strain along the [100] crystallographic direction, which is known to cause the triply-degenerate 1S state to split into a singlet and a doublet with the singlet energy increasing, and the doublet energy decreasing with strain [230, 359].

A positional scanner was used to scan the sample in order to find the position with the largest splitting for the 1S state. The second spectrum labelled “Edge” (orange line in Fig. 6.11), corresponds to the spectrum with the highest observed splitting and was recorded at a location close to the edge of the cavity sample. In this case, the splitting is approximately double (∼135 pm) to that observed at the centre of the sample. In both cases, the observed splitting can be explained by a small amount of strain ($\ll 0.5$ kbar) [230, 359].

The strain present in the microcavity sample can be attributed to the fabrication process, namely glueing the Cu_2O crystal to the bottom DBR and depositing a second DBR mirror on top of the crystal (See Section 3.1.3.2). To investigate the validity of this claim, a new Cu_2O crystal was prepared, and the two fabrication steps mentioned above were repeated while optically characterising the sample before and after each step.

Following the procedure outlined in Section 3.1.3.2, a new Cu_2O crystal was thinned down to ~30 μm. The sample was placed between two CaF_2 substrates (See Section 3.1.1), and the absorption and PL spectra were recorded at $T = 4$ K (See blue lines Fig. 6.12). The exciton series extends up to $n = 9$ in the absorption spectrum, while the PL spectrum is dominated by the narrow (FWHM ~0.04 nm) 1S orthoexciton peak at ~609.7 nm, accompanied by the Γ_5^- and Γ_3^- phonon-assisted peaks.

Subsequently, a thin epoxy layer, similar to the one used for fabricating the microcavity sample, was spin-coated onto a new CaF_2 substrate, and the new Cu_2O crystal was transferred onto the substrate and cured with UV light. The epoxy layer, after UV curing, has a thickness of ~4 μm. Absorption and PL measurements were repeated on the same region of the crystal as before (orange lines in Fig. 6.12). The absorption spectrum exhibits the same number of exciton resonances (i.e. up to $n = 9$) in addition to a consistent blue shift of ~0.2 nm for all

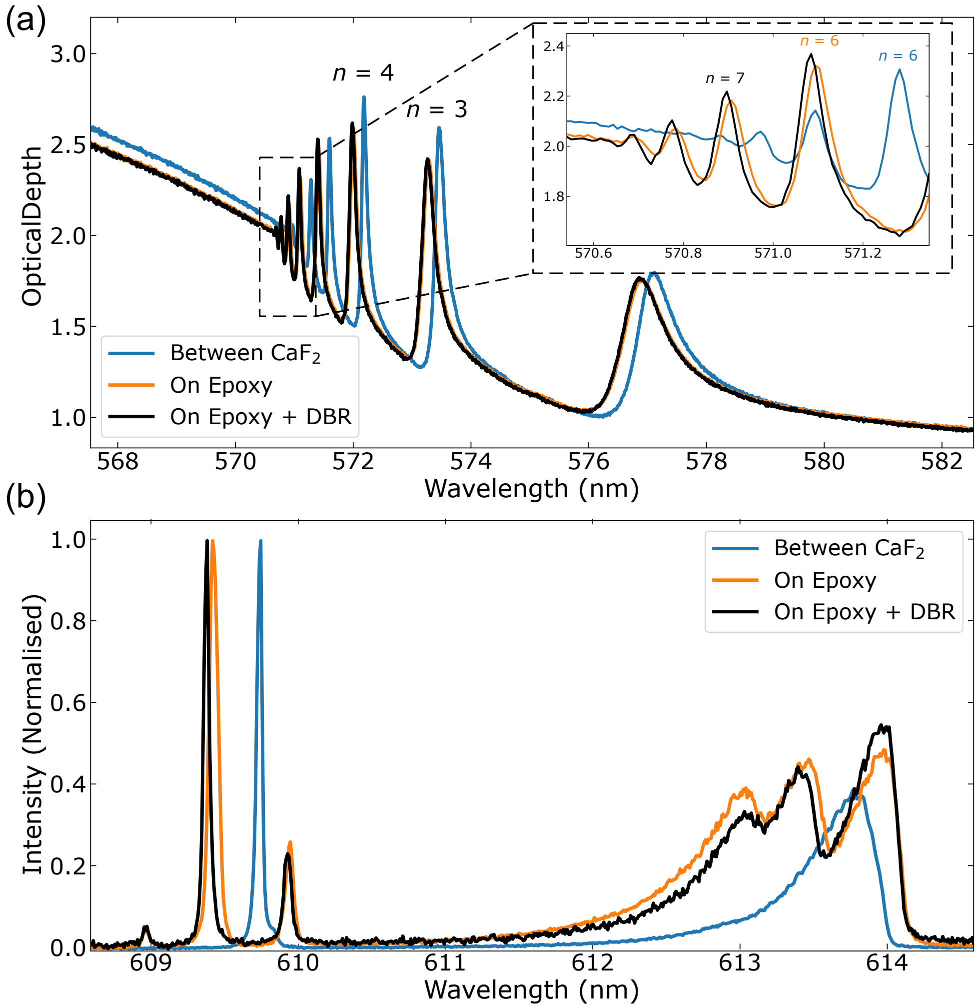

Figure 6.12: (a) Absorption and (b) PL spectra from a thin Cu_2O crystal between two transparent substrates (blue line), the same crystal mounted on a UV cured epoxy (orange line) and when a DBR is deposited on top of the crystal (black line).

peaks, compared to the sample sandwiched between the CaF_2 substrates. This shift could be due to better thermal contact between the crystal and the substrate in the presence of epoxy. In the PL spectrum [orange line in Fig. 6.12(b)], the 1S orthoexciton degeneracy is totally lifted, and the peak splits into three energy levels. This observation is consistent with strain applied across the [110] direction [231]. The splitting between the two extreme peaks is ~1 nm, or equivalently ~3 meV in energy. This splitting amounts to an applied strain of 1-1.5 kbar, which is significantly larger than the strain on the microcavity sample.

The final step includes depositing a DBR on top of the bulk crystal mounted on the epoxy (black lines in Fig. 6.12). For the purpose of this section, only a pair of SiO_2 and Ta_2O_5 layers is sufficient to reproduce any possible strain but is still transparent enough for transmission measurements. The absorption spectrum exhibits the same number of exciton transitions as the bare crystal before but is slightly blue-shifted by only ~0.01 nm compared to the glued sample, or equivalently, by ~0.21 nm, from the sample sandwiched between the CaF_2 substrates. Similar to the glued sample, a blue shift and triple splitting are present in the PL spectrum.

In conclusion, careful step-by-step spectroscopy during the fabrication process on a different sample shows that strain originating from the fabrication process, i.e. glueing the sample on the substrate and depositing a DBR mirror on top of it, is present. However, it does not affect the number of exciton transitions present in the absorption spectrum at least up to $n = 9$. The question remains as to what the reason is for the reduced number of exciton transitions observed in the microcavity compared to that of the bulk. Given that our fabrication process is not responsible, the reduced number of exciton transitions in the microcavity is limited by the quality of the natural crystal used as the active material, which was not as high as the one used in the experiments in Chapter 5 (See Fig. 5.1). Even though all our samples originate from the same mother mineral stone, different parts can yield a slightly different number of exciton transitions due to the varying defect composition and internal stress from location to location.

6.7 Summary and Outlook

In this chapter, the strong coupling of Rydberg excitons to cavity photons was demonstrated using an optical microcavity with the semiconductor Cu_2O as its active layer. The microcavity reaches the strong light-matter coupling regime for Rydberg excitons with principal quantum numbers up to $n = 6$, which, in turn, makes it possible to form Rydberg exciton-polaritons, as evidenced by transmission spectroscopy with high spectral and spatial resolution. After considering the underlying phonon-assisted absorption processes present in Cu_2O, a simple model was developed to describe the resonant cavity transmission spectrum. The smaller number of strongly coupled exciton transitions in this microcavity (up $n = 6$, compared to $n = 12$ observed in the bare bulk Cu_2O crystal) was attributed to the quality of the Cu_2O sample used.

Owing to their greatly enhanced nonlinearities arising from strong and long-range exciton interactions [246] , Rydberg exciton-polaritons in Cu_2O microcavities provide a versatile platform for exploring quantum many-body phenomena, extending the physics of weakly interacting photon fluids achievable with low-lying exciton states [175, 353, 354]. Previous measurements [32] report a blockade diameter of ∼0.5 µm for $n = 6$, but this value can be extended up to ∼2 µm for $n = 10$. The associated polariton blockade under strong cavity coupling conditions thus offers a promising approach for generating and manipulating non-classical states of light [360]. Additionally, synthetic Cu_2O microcrystals [225, 226] and microscale patterning [24, 187] would yield configurable lattices of strongly interacting individual polaritons.

The exploration of Rydberg exciton-polariton physics has not been limited to Cu_2O. Recent studies have achieved strong coupling between photon and excited exciton states in monolayers of WSe_2 [361] and ReS_2 [362] and in a perovskite cavity containing single-crystal $CsPbBr_3$ microplates [363]. Whereas these observations of polaritons have been limited to $n = 2$, Cu_2O offers the advantage that narrow exciton lines with principal quantum numbers up to $n = 12$ can be routinely detected, making it possible to realise Rydberg polaritons with $n = 6$ in the presence of phonon coupling in this work. Calculations show that with experimentally feasible cavity thicknesses and excitation spot diameters, non-classical light can be observed even for $n = 6$ polaritons.

This page is intentionally left blank.

Chapter 7

Conclusion and Outlook

This thesis explored three routes towards achieving single-particle nonlinearities using semiconductor systems. First, a state-of-the-art GaAs-based microcavity with a high quality factor was used to realise a polariton condensate in optically induced potential traps. A laser pattern consisting of multiple laser spots was generated using a spatial light modulator and used to excite polaritons in the microcavity non-resonantly. The blue-shift potential arising from repulsive exciton-polariton and polariton-polariton interactions supports the formation of trapped condensates confined to the centre of the excitation geometry. The spatial separation between condensate and the decoherence-inducing reservoir has been shown to result in strong reductions of the condensation threshold, as well as narrowing of the emission linewidth, as demonstrated by Askitopoulos et al. in ef. [84]. Here, the ultranarrow condensate linewidth was probed through interferometry by means of measuring the evolution of the temporal coherence of condensate emission.

Due to the reduction of the spatial overlap with the thermal reservoir of excitons, the coherence time of the trapped condensate is more than an order of magnitude longer than that of an untrapped condensate. This ultralong coherence enables high-precision spectroscopy of the trapped condensate, revealing an ultranarrow linewidth of ∼1 μeV. Additionally, the field correlation function exhibits periodic beats attributed to a fine energy splitting of two polarisation modes of the condensate. Our result thus enables high-resolution spectroscopy of polariton condensates, which can be applied to the precision tuning of the condensates energies in optical lattices and polariton simulators.

Following this attempt, instead of improving the GaAs microcavity system, the goal of achieving single-polariton nonlinearity was approached by studying a material with a greater potential for larger interactions. Recently, cuprous oxide has attracted renewed attention as a semiconductor material for quantum optics. Cu_2O can host large excitation, named Rydberg excitons, with potentially orders of magnitude larger interaction strengths than classic semiconductors such as GaAs, accompanied with large dimensions that would make tailoring and networking of these particles realisable. The unique properties of Rydberg exciton in Cu_2O offer the opportunity for harnessing the strong Rydberg interactions for generating significant nonlinearities at the single-photon level in a solid-state system.

There is growing interest in quantum-confined Rydberg excitons in nanostructures with regard to how their energies change and how this affects their quantum statistics. This is a crucial step for making new quantum devices and quantum simulators in solid-state using Cu_2O. In this work, Rydberg excitons were resolved for the first time in nanoparticles of Cu_2O up to the principal quantum number $n = 6$. Quantum confinement of Rydberg excitons has two major impacts on the transmission lines: it reduces their oscillator strength while simultaneously broadening the transitions. These two observed effects were described in terms of the quantum confinement of Rydberg excitons in conjunction with the particle size distribution. Such results are the first step towards understanding the interaction of Rydberg excitons in nanostructures and their application for quantum technologies.

Moreover, the hybridisation of cavity photons with Rydberg excitons to form highly nonlinear polaritons was explored as another route towards single-polariton nonlinearities. Despite the unique properties of Rydberg excitons, their potential for semiconductor quantum photonic applications has remained untapped for many years due to the weak light-matter coupling strength in cuprous oxide. Embedding a thin Cu_2O crystal into a Fabry-Pérot microcavity overcomes this hurdle by demonstrating the formation of Rydberg exciton-polaritons up to $n = 6$ in a strongly coupled cuprous-oxide microcavity. The Rydberg excitons in Cu_2O have much larger coherence (∼0.1 meV), much larger blockade diameters (∼0.5 µm) and orders of magnitude larger dimensions (∼120 nm) than more traditional excitons in GaAs. They also have unique phonon interactions that result in asymmetric polariton modes, demonstrated for the first time in this work. The microcavity system studied in this work is still below the threshold particle number for nonlinearity; however, reducing the thickness of the Cu_2O crystal and the spot size to experimentally achievable values would put the system well into the nonlinear regime.

The effects and techniques developed in this thesis pave the way for several interesting research directions. Our findings establish the cuprous oxide material platform as a strong contender for quantum polaritonics - an emerging field that holds great promise for technology applications. While the onset of the polaritonic quantum regime was recently demonstrated with GaAs exciton-polaritons [353, 354], the achievable exciton-exciton interactions in conventional semiconductors are rather limited and pose a strong roadblock to reaching the deep quantum regime. Strongly coupling cuprous oxide Rydberg excitons to light, as demonstrated in this thesis, removes this roadblock, and constitutes a major milestone in the realisation of strongly interacting quantum fluids of light.

Future work on Rydberg polaritons should be directed towards achieving single-polariton nonlinearities in high-quality microcavities with Rydberg states with as high-n as possible. Using a high-quality Cu_2O sample as the active material is essential as it will enable strong exciton-photon coupling for high-n Rydberg states, thus overcoming the limitation present in our sample. Additionally, reducing the Cu_2O active layer thickness in conjunction with using a smaller spot size will reduce the cavity-mode volume, and the system could reach the regime of a few strongly interacting Rydberg polaritons for even low-n states, such as $n = 6$ observed in this work. Alternatively, fibre microcavities can be exploited because of their small mode volumes, exceptional quality factors, and the ability to tune the active layer thickness [364, 365]. Moreover, fibre microcavities can be used to strongly couple Rydberg excitons to photons in nanocrystals, such as Cu_2O nanoparticles, down to a single particle level. The nanocrystals can be deposited on a DBR substrate, and coupling of the cavity photons to Rydberg excitons will be investigated by scanning the fibre DBR position so that it coincides with the nanocrystal of interest. The emission of non-classical light from future microcavities can be probed by measuring the intensity autocorrelation function $g^{(2)}(t)$, which characterises the photon statistics of a state of light and can be used to distinguish between its classical or quantum nature. Observing $g^{(2)}(t = 0) < 1$ is a signature of the nonclassical nature of light, often referred to as anti-bunched light, and has significant applications in quantum technologies [366].

One route towards of achieving and enhancing the strong coupling between Rydberg excitons and photons is by suppressing the photon-induced background of Cu_2O, which represents an additional excitation channel that inevitably competes with the Rydberg exciton series. The absorption background can be experimentally eliminated via an electromagnetically induced transparency (EIT) scheme involving two-photon coupling to Rydberg S-state excitons, which will thus make it possible to achieve strong cavity coupling with even higher-lying Rydberg states. Additionally, the demonstrated possibility to generate multiple excited levels in semiconductor microcavities will permit the realisation of electromagnetically induced transparency, whereby a low-lying P exciton can be strongly coupled to cavity photons, and the transition to a highly excited S-state exciton is driven by an external control field [34, 358]. These Rydberg EIT settings, which exploit the strong van der Waals interaction between high-lying Cu_2O Rydberg excitons, suggest exciting possibilities when combined with semiconductor microcavities [367].

An alternative route towards eliminating the background is through optical second harmonic generation (SHG), which has been established as a versatile tool for spectroscopy of Rydberg excitons [368–371]. SHG is a coherent process in which two incoming photons are converted to one outgoing photon at twice the energy of the incoming photon. Unlike one-photon absorption, the SHG spectrum is dominated by excitonic resonances and does not exhibit the large phonon-assisted absorption background. Additionally, resonances of even-parity (S/D) as well as odd-parity P excitons can be detected [370, 371]. Eliminating the phonon background in addition to strongly coupled high-n Rydberg excitons in high-quality microcavities will pave the way towards achieving Rydberg polariton condensation.

Bibliography

[1] Darrick E. Chang, Anders S. Sørensen, Eugene A. Demler, and Mikhail D. Lukin. A single-photon transistor using nanoscale surface plasmons. *Nature Physics*, 3(11):807–812, November 2007. ISSN 1745-2473, 1745-2481. doi: 10.1038/nphys708. URL `http://www.nature.com/articles/nphys708`.

[2] Dario Gerace, Hakan E. Türeci, Atac Imamoglu, Vittorio Giovannetti, and Rosario Fazio. The quantum-optical Josephson interferometer. *Nature Physics*, 5(4):281–284, April 2009. ISSN 1745-2473, 1745-2481. doi: 10.1038/nphys1223. URL `http://www.nature.com/articles/nphys1223`.

[3] Darrick E. Chang, Vladan Vuletić, and Mikhail D. Lukin. Quantum nonlinear optics — photon by photon. *Nature Photonics*, 8(9):685–694, September 2014. ISSN 1749-4885, 1749-4893. doi: 10.1038/nphoton.2014.192. URL `http://www.nature.com/articles/nphoton.2014.192`.

[4] Yasuhiko Arakawa and Mark J. Holmes. Progress in quantum-dot single photon sources for quantum information technologies: A broad spectrum overview. *Applied Physics Reviews*, 7(2):021309, June 2020. ISSN 1931-9401. doi: 10.1063/5.0010193. URL `http://aip.scitation.org/doi/10.1063/5.0010193`.

[5] Davide Nigro, Marco Clementi, Camille-Sophie Brés, Marco Liscidini, and Dario Gerace. Single-photon nonlinearities and blockade from a strongly driven photonic molecule. *Optics Letters*, 47(20):5348, October 2022. ISSN 0146-9592, 1539-4794. doi: 10.1364/OL.468546. URL `https://opg.optica.org/abstract.cfm?URI=ol-47-20-5348`.

[6] Michael Förtsch, Josef U. Fürst, Christoffer Wittmann, Dmitry Strekalov, Andrea Aiello, Maria V. Chekhova, Christine Silberhorn, Gerd Leuchs, and Christoph Marquardt. A versatile source of single photons for quantum information processing. *Nature Communications*, 4(1):1818, October 2013. ISSN 2041-1723. doi: 10.1038/ncomms2838. URL `http://www.nature.com/articles/ncomms2838`.

[7] H. J. Kimble. The quantum internet. *Nature*, 453(7198):1023–1030, June 2008. ISSN 0028-0836, 1476-4687. doi: 10.1038/nature07127. URL `http://www.nature.com/articles/nature07127`.

[8] Michael J Hartmann. Quantum simulation with interacting photons. *Journal of Optics*, 18(10):104005, October 2016. ISSN 2040-8978, 2040-8986. doi: 10.1088/2040-8978/18/10/104005. URL `https://iopscience.iop.org/article/10.1088/2040-8978/18/10/104005`.

[9] A. Reiserer, S. Ritter, and G. Rempe. Nondestructive Detection of an Optical Photon. *Science*, 342(6164):1349–1351, December 2013. ISSN 0036-8075, 1095-9203. doi: 10.1126/science.1246164. URL `https://www.sciencemag.org/lookup/doi/10.1126/science.1246164`.

[10] T. G. Tiecke, J. D. Thompson, N. P. de Leon, L. R. Liu, V. Vuletić, and M. D. Lukin. Nanophotonic quantum phase switch with a single atom. *Nature*, 508(7495):241–244, April 2014. ISSN 0028-0836, 1476-4687. doi: 10.1038/nature13188. URL `http://www.nature.com/articles/nature13188`.

[11] Bastian Hacker, Stephan Welte, Gerhard Rempe, and Stephan Ritter. A photon–photon quantum gate based on a single atom in an optical resonator. *Nature*, 536(7615):193–196, August 2016. ISSN 0028-0836, 1476-4687. doi: 10.1038/nature18592. URL `http://www.nature.com/articles/nature18592`.

[12] Luigi Giannelli, Tom Schmit, Tommaso Calarco, Christiane P Koch, Stephan Ritter, and Giovanna Morigi. Optimal storage of a single photon by a single intra-cavity atom. *New Journal of Physics*, 20(10):105009, October 2018. ISSN 1367-2630. doi: 10.1088/1367-2630/aae725. URL `https://iopscience.iop.org/article/10.1088/1367-2630/aae725`.

[13] Thibault Peyronel, Ofer Firstenberg, Qi-Yu Liang, Sebastian Hofferberth, Alexey V. Gorshkov, Thomas Pohl, Mikhail D. Lukin, and Vladan Vuletić. Quantum nonlinear optics with single photons enabled by strongly interacting atoms. *Nature*, 488(7409):57–60, August 2012. ISSN 0028-0836, 1476-4687. doi: 10.1038/nature11361. URL `http://www.nature.com/articles/nature11361`.

[14] Jonathan D. Pritchard, Kevin J. Weatherill, and Charles S. Adams. Nonlinear Optics Using Cold Rydberg Atoms. In *Annual Review of Cold Atoms and Molecules*, volume 1, pages 301–350. World Scientific, February 2013. ISBN 978-981-4440-39-4 978-981-4440-40-0. doi: 10.1142/9789814440400_0008. URL `http://www.worldscientific.com/doi/abs/10.1142/9789814440400_0008`.

[15] Callum R. Murray and Thomas Pohl. Coherent Photon Manipulation in Interacting Atomic Ensembles. *Physical Review X*, 7(3):031007, July 2017. ISSN 2160-3308. doi: 10.1103/PhysRevX.7.031007. URL `http://link.aps.org/doi/10.1103/PhysRevX.7.031007`.

[16] P. Michler, A. Kiraz, C. Becher, W. V. Schoenfeld, P. M. Petroff, Lidong Zhang, E. Hu, and A. Imamoglu. A Quantum Dot Single-Photon Turnstile Device. *Science*, 290(5500):2282–2285, December 2000. ISSN 0036-8075, 1095-9203. doi: 10.1126/science.290.5500.2282. URL `https://www.science.org/doi/10.1126/science.290.5500.2282`.

[17] Ilya Fushman, Dirk Englund, Andrei Faraon, Nick Stoltz, Pierre Petroff, and Jelena Vučković. Controlled Phase Shifts with a Single Quantum Dot. *Science*, 320(5877):769–772, May 2008. ISSN 0036-8075, 1095-9203. doi: 10.1126/science.1154643. URL `https://www.science.org/doi/10.1126/science.1154643`.

[18] Chao-Yang Lu and Jian-Wei Pan. Quantum-dot single-photon sources for the quantum internet. *Nature Nanotechnology*, 16(12):1294–1296, December 2021. ISSN 1748-3387, 1748-3395. doi: 10.1038/s41565-021-01033-9. URL `https://www.nature.com/articles/s41565-021-01033-9`.

[19] A. Beveratos, S. Kühn, R. Brouri, T. Gacoin, J.-P. Poizat, and P. Grangier. Room temperature stable single-photon source. *The European Physical Journal D - Atomic, Molecular and Optical Physics*, 18(2):191–196, February 2002. ISSN 1434-6060, 1434-6079. doi: 10.1140/epjd/e20020023. URL `http://link.springer.com/10.1140/epjd/e20020023`.

[20] Andrei Faraon, Paul E. Barclay, Charles Santori, Kai-Mei C. Fu, and Raymond G. Beausoleil. Resonant enhancement of the zero-phonon emission from a colour centre in a diamond cavity. *Nature Photonics*, 5(5):301–305, May 2011. ISSN 1749-4885, 1749-4893. doi: 10.1038/nphoton.2011.52. URL `http://www.nature.com/articles/nphoton.2011.52`.

[21] Birgit J. M. Hausmann, Brendan Shields, Qimin Quan, Patrick Maletinsky, Murray McCutcheon, Jennifer T. Choy, Tom M. Babinec, Alexander Kubanek, Amir Yacoby, Mikhail D. Lukin, and Marko Loncar. Integrated Diamond Networks for Quantum Nanophotonics. *Nano Letters*, 12(3):1578–1582, March 2012. ISSN 1530-6984, 1530-6992. doi: 10.1021/nl204449n. URL `https://pubs.acs.org/doi/10.1021/nl204449n`.

[22] C. E. Whittaker, E. Cancellieri, P. M. Walker, D. R. Gulevich, H. Schomerus, D. Vaitiekus, B. Royall, D. M. Whittaker, E. Clarke, I. V. Iorsh, I. A. Shelykh, M. S. Skolnick, and D. N. Krizhanovskii. Exciton Polaritons in a Two-Dimensional Lieb Lattice with Spin-Orbit Coupling. *Physical Review Letters*, 120(9):097401, March 2018. ISSN 0031-9007,

1079-7114. doi: 10.1103/PhysRevLett.120.097401. URL `https://link.aps.org/doi/10.1103/PhysRevLett.120.097401`.

[23] H. Ohadi, A. J. Ramsay, H. Sigurdsson, Y. del Valle-Inclan Redondo, S. I. Tsintzos, Z. Hatzopoulos, T. C. H. Liew, I. A. Shelykh, Y. G. Rubo, P. G. Savvidis, and J. J. Baumberg. Spin Order and Phase Transitions in Chains of Polariton Condensates. *Physical Review Letters*, 119(6):067401, August 2017. ISSN 0031-9007, 1079-7114. doi: 10.1103/PhysRevLett.119.067401. URL `http://link.aps.org/doi/10.1103/PhysRevLett.119.067401`.

[24] H. Ohadi, Y. del Valle-Inclan Redondo, A. J. Ramsay, Z. Hatzopoulos, T. C. H. Liew, P. R. Eastham, P. G. Savvidis, and J. J. Baumberg. Synchronization crossover of polariton condensates in weakly disordered lattices. *Physical Review B*, 97(19):195109, May 2018. ISSN 2469-9950, 2469-9969. doi: 10.1103/PhysRevB.97.195109. URL `https://link.aps.org/doi/10.1103/PhysRevB.97.195109`.

[25] J. D. Töpfer, I. Chatzopoulos, H. Sigurdsson, T. Cookson, Y. G. Rubo, and P. G. Lagoudakis. Engineering spatial coherence in lattices of polariton condensates. *Optica*, 8(1):106, January 2021. ISSN 2334-2536. doi: 10.1364/OPTICA.409976. URL `https://opg.optica.org/abstract.cfm?URI=optica-8-1-106`.

[26] Benoit Deveaud-Plédran. On the condensation of polaritons. *Journal of the Optical Society of America B*, 29(2):A138, February 2012. ISSN 0740-3224, 1520-8540. doi: 10.1364/JOSAB.29.00A138. URL `https://opg.optica.org/abstract.cfm?URI=josab-29-2-A138`.

[27] A. Amo, D. Sanvitto, F. P. Laussy, D. Ballarini, E. del Valle, M. D. Martin, A. Lemaître, J. Bloch, D. N. Krizhanovskii, M. S. Skolnick, C. Tejedor, and L. Viña. Collective fluid dynamics of a polariton condensate in a semiconductor microcavity. *Nature*, 457(7227): 291–295, January 2009. ISSN 0028-0836, 1476-4687. doi: 10.1038/nature07640. URL `http://www.nature.com/articles/nature07640`.

[28] K. G. Lagoudakis, M. Wouters, M. Richard, A. Baas, I. Carusotto, R. André, Le Si Dang, and B. Deveaud-Plédran. Quantized vortices in an exciton-polariton condensate. *Nature Physics*, 4(9):706–710, September 2008. ISSN 1745-2473, 1745-2481. doi: 10.1038/nphys1051. URL `http://www.nature.com/articles/nphys1051`.

[29] Xuekai Ma, Oleg A. Egorov, and Stefan Schumacher. Creation and Manipulation of Stable Dark Solitons and Vortices in Microcavity Polariton Condensates. *Physical Review Letters*, 118(15):157401, April 2017. ISSN 0031-9007, 1079-7114. doi: 10.1103/PhysRevLett.118.157401. URL `http://link.aps.org/doi/10.1103/PhysRevLett.118.157401`.

[30] E. F. Gross and N. A. Karryev. Pogloshchenie sveta kristallom zakisi medi v infrakrasnoi i vidimoi chasti spektra. 84(Nr. 2):261–264, 1952.

[31] Masakazu Hayashi and Kiichirô Katsuki. Hydrogen-Like Absorption Spectrum of Cuprous Oxide. *Journal of the Physical Society of Japan*, 7(6):599–603, November 1952. ISSN 0031-9015, 1347-4073. doi: 10.1143/JPSJ.7.599. URL `https://journals.jps.jp/doi/10.1143/JPSJ.7.599`.

[32] T. Kazimierczuk, D. Fröhlich, S. Scheel, H. Stolz, and M. Bayer. Giant Rydberg excitons in the copper oxide Cu_2O. *Nature*, 514(7522):343–347, October 2014. ISSN 0028-0836, 1476-4687. doi: 10.1038/nature13832. URL `http://www.nature.com/articles/nature13832`.

[33] Svetlana G. Lukishova and Luke J. Bissell. Nanophotonic Advances for Room-Temperature Single-Photon Sources. In Robert W. Boyd, Svetlana G. Lukishova, and Victor N. Zadkov, editors, *Quantum Photonics: Pioneering Advances and Emerging Applications*, volume 217, pages 103–178. Springer International Publishing, Cham, 2019. ISBN 978-3-319-98400-1 978-3-319-98402-5. doi: 10.1007/978-3-319-98402-5_4. URL `http://link.springer.com/10.1007/978-3-319-98402-5_4`. Series Title: Springer Series in Optical Sciences.

[34] Valentin Walther, Robert Johne, and Thomas Pohl. Giant optical nonlinearities from Rydberg excitons in semiconductor microcavities. *Nature Communications*, 9(1):1309, April 2018. ISSN 2041-1723. doi: 10.1038/s41467-018-03742-7. URL `https://www.nature.com/articles/s41467-018-03742-7`. Number: 1 Publisher: Nature Publishing Group.

[35] Daniele Sanvitto and Stéphane Kéna-Cohen. The road towards polaritonic devices. *Nature Materials*, 15(10):1061–1073, October 2016. ISSN 1476-1122, 1476-4660. doi: 10.1038/nmat4668. URL `https://www.nature.com/articles/nmat4668`.

[36] Mark Fox. *Optical properties of solids.* Number v. 3 in Oxford master series in condensed matter physics. Oxford University Press, Oxford ; New York, 2nd ed edition, 2010. ISBN 978-0-19-957336-3 978-0-19-957337-0.

[37] Peter Y. Yu and Manuel Cardona. *Fundamentals of Semiconductors.* Graduate Texts in Physics. Springer Berlin Heidelberg, Berlin, Heidelberg, 2010. ISBN 978-3-642-00709-5 978-3-642-00710-1. doi: 10.1007/978-3-642-00710-1. URL `http://link.springer.com/10.1007/978-3-642-00710-1`.

[38] M. D. Sturge. Optical Absorption of Gallium Arsenide between 0.6 and 2.75 eV. *Physical*

Review, 127(3):768–773, August 1962. ISSN 0031-899X. doi: 10.1103/PhysRev.127.768. URL https://link.aps.org/doi/10.1103/PhysRev.127.768.

[39] S. Brahms, S. Nikitine, and J.P. Dahl. On the band structure and the absorption spectrum of Cu_2O. *Physics Letters*, 22(1):31–33, July 1966. ISSN 00319163. doi: 10.1016/0031-9163(66)90044-8. URL https://linkinghub.elsevier.com/retrieve/pii/0031916366900448.

[40] Hui Deng, Hartmut Haug, and Yoshihisa Yamamoto. Exciton-polariton Bose-Einstein condensation. *Reviews of Modern Physics*, 82(2):1489–1537, May 2010. ISSN 0034-6861, 1539-0756. doi: 10.1103/RevModPhys.82.1489. URL https://link.aps.org/doi/10.1103/RevModPhys.82.1489.

[41] V M Agranovich, D M Basko, G C La Rocca, and F Bassani. Excitons and optical nonlinearities in hybrid organic-inorganic nanostructures. *Journal of Physics: Condensed Matter*, 10(42):9369–9400, October 1998. ISSN 0953-8984, 1361-648X. doi: 10.1088/0953-8984/10/42/005. URL https://iopscience.iop.org/article/10.1088/0953-8984/10/42/005.

[42] Gregory H. Wannier. The Structure of Electronic Excitation Levels in Insulating Crystals. *Physical Review*, 52(3):191–197, August 1937. ISSN 0031-899X. doi: 10.1103/PhysRev.52.191. URL https://link.aps.org/doi/10.1103/PhysRev.52.191.

[43] N. F. Mott. Conduction in polar crystals. II. The conduction band and ultra-violet absorption of alkali-halide crystals. *Transactions of the Faraday Society*, 34:500, 1938. ISSN 0014-7672. doi: 10.1039/tf9383400500. URL http://xlink.rsc.org/?DOI=tf9383400500.

[44] Robert S. Knox. *Theory of excitons*. Number 5 in Solid state physics Supplement. Academic Pr, New York, 2. print edition, 1972. ISBN 978-0-12-607765-0.

[45] G. Dresselhaus. Effective mass approximation for excitons. *Journal of Physics and Chemistry of Solids*, 1(1-2):14–22, September 1956. ISSN 00223697. doi: 10.1016/0022-3697(56)90004-X. URL https://linkinghub.elsevier.com/retrieve/pii/002236975690004X.

[46] Kikuo Cho. *Excitons*. Springer Berlin Heidelberg, Berlin, Heidelberg, 1979. ISBN 978-3-642-81368-9 978-3-642-81370-2. URL https://doi.org/10.1007/978-3-642-81368-9. OCLC: 858930892.

[47] Alexey V. Kavokin, Jeremy J. Baumberg, Guillaume Malpuech, and Fabrice P. Laussy. *Microcavities*. Oxford University PressOxford, 2 edition, May 2017. ISBN 978-0-19-878299-5 978-0-19-182622-1. doi: 10.1093/oso/9780198782995.001.0001. URL https://academic.oup.com/book/26123.

[48] Ivan Pelant and Jan Valenta. *Luminescence spectroscopy of semiconductors.* Oxford University Press, Oxford ; New York, 2012. ISBN 978-0-19-875754-2 978-0-19-958833-6. OCLC: ocn757147121.

[49] Sjard Ole Krüger, Heinrich Stolz, and Stefan Scheel. Interaction of charged impurities and Rydberg excitons in cuprous oxide. *Physical Review B*, 101(23):235204, June 2020. ISSN 2469-9950, 2469-9969. doi: 10.1103/PhysRevB.101.235204. URL `https://link.aps.org/doi/10.1103/PhysRevB.101.235204`.

[50] Nevill Mott. *Metal-Insulator Transitions.* CRC Press, 0 edition, January 2004. ISBN 978-0-429-09488-0. doi: 10.1201/b12795. URL `https://www.taylorfrancis.com/books/9781466576452`.

[51] L. Kappei, J. Szczytko, F. Morier-Genoud, and B. Deveaud. Direct Observation of the Mott Transition in an Optically Excited Semiconductor Quantum Well. *Physical Review Letters*, 94(14):147403, April 2005. ISSN 0031-9007, 1079-7114. doi: 10.1103/PhysRevLett.94.147403. URL `https://link.aps.org/doi/10.1103/PhysRevLett.94.147403`.

[52] G Manzke, D Semkat, F Richter, D Kremp, and K Henneberger. Mott transition versus Bose-Einstein condensation of excitons. *Journal of Physics: Conference Series*, 210:012020, February 2010. ISSN 1742-6596. doi: 10.1088/1742-6596/210/1/012020. URL `https://iopscience.iop.org/article/10.1088/1742-6596/210/1/012020`.

[53] Kerry J. Vahala. Optical microcavities. *Nature*, 424(6950):839–846, August 2003. ISSN 0028-0836, 1476-4687. doi: 10.1038/nature01939. URL `http://www.nature.com/articles/nature01939`.

[54] G. Khitrova, H. M. Gibbs, M. Kira, S. W. Koch, and A. Scherer. Vacuum Rabi splitting in semiconductors. *Nature Physics*, 2(2):81–90, February 2006. ISSN 1745-2473, 1745-2481. doi: 10.1038/nphys227. URL `http://www.nature.com/articles/nphys227`.

[55] Geoffrey Brooker. *Modern classical optics.* Number 8 in Oxford master series in physics. Oxford University Press, Oxford ; New York, 2003. ISBN 978-0-19-859965-4 978-0-19-859964-7. OCLC: ocm52829216.

[56] Alexey Kavokin. Exciton-polaritons in microcavities: Recent discoveries and perspectives: Exciton-polaritons in microcavities. *physica status solidi (b)*, 247(8):1898–1906, August 2010. ISSN 03701972. doi: 10.1002/pssb.200983955. URL `https://onlinelibrary.wiley.com/doi/10.1002/pssb.200983955`.

[57] K.D. Choquette. Vertical cavity surface emitting lasers (VCSELs). In *Semiconductor Lasers*, pages 316–340. Elsevier, 2013. ISBN 978-0-85709-121-5. doi: 10.1533/9780857096401.2.316. URL `https://linkinghub.elsevier.com/retrieve/pii/B9780857091215500084`.

[58] Shijie Fu, Wei Shi, Yan Feng, Lei Zhang, Zhongmin Yang, Shanhui Xu, Xiushan Zhu, R. A. Norwood, and N. Peyghambarian. Review of recent progress on single-frequency fiber lasers. *Journal of the Optical Society of America B*, 34(3):A49, March 2017. ISSN 0740-3224, 1520-8540. doi: 10.1364/JOSAB.34.000A49. URL `https://opg.optica.org/abstract.cfm?URI=josab-34-3-A49`.

[59] Bilal Janjua, Meng Lon Iu, Zhizhong Yan, Paul Charles, Eric Chen, and Amr S. Helmy. Distributed feedback lasers using surface gratings in Bragg waveguides. *Optics Letters*, 46(15):3689, August 2021. ISSN 0146-9592, 1539-4794. doi: 10.1364/OL.431292. URL `https://opg.optica.org/abstract.cfm?URI=ol-46-15-3689`.

[60] A. Weisshaar and J. Li. Generalised impedance boundary method of moments for multilayer graded-index dielectric waveguide structures. *IEE Proceedings - Optoelectronics*, 143(3):167–172, June 1996. ISSN 1350-2433, 1359-7078. doi: 10.1049/ip-opt:19960508. URL `https://digital-library.theiet.org/content/journals/10.1049/ip-opt_19960508`.

[61] F. Jahnke, M. Kira, and S.W. Koch. Linear and nonlinear optical properties of excitons in semiconductor quantum wells and microcavities. *Zeitschrift für Physik B Condensed Matter*, 104(3):559–572, March 1997. ISSN 0722-3277, 1431-584X. doi: 10.1007/s002570050490. URL `http://link.springer.com/10.1007/s002570050490`.

[62] C J R Sheppard. Approximate calculation of the reflection coefficient from a stratified medium. *Pure and Applied Optics: Journal of the European Optical Society Part A*, 4(5):665–669, September 1995. ISSN 0963-9659, 1361-6617. doi: 10.1088/0963-9659/4/5/018. URL `https://iopscience.iop.org/article/10.1088/0963-9659/4/5/018`.

[63] Cheng Zhang, Rami ElAfandy, and Jung Han. Distributed Bragg Reflectors for GaN-Based Vertical-Cavity Surface-Emitting Lasers. *Applied Sciences*, 9(8):1593, April 2019. ISSN 2076-3417. doi: 10.3390/app9081593. URL `https://www.mdpi.com/2076-3417/9/8/1593`.

[64] Steven Byrnes. tmm: Simulate light propagation in multilayer thin and/or thick films using the fresnel equations and transfer matrix method. URL `http://pypi.python.org/pypi/tmm`.

[65] V. Savona, L.C. Andreani, P. Schwendimann, and A. Quattropani. Quantum well excitons in semiconductor microcavities: Unified treatment of weak and strong coupling regimes. *Solid State Communications*, 93(9):733–739, March 1995. ISSN 00381098. doi: 10.1016/0038-1098(94)00865-5. URL `https://linkinghub.elsevier.com/retrieve/pii/0038109894008655`.

[66] M S Skolnick, T A Fisher, and D M Whittaker. Strong coupling phenomena in quantum microcavity structures. *Semiconductor Science and Technology*, 13(7):645–669, July 1998. ISSN 0268-1242, 1361-6641. doi: 10.1088/0268-1242/13/7/003. URL `https://iopscience.iop.org/article/10.1088/0268-1242/13/7/003`.

[67] R. Houdré, C. Weisbuch, R. P. Stanley, U. Oesterle, P. Pellandini, and M. Ilegems. Measurement of Cavity-Polariton Dispersion Curve from Angle-Resolved Photoluminescence Experiments. *Physical Review Letters*, 73(15):2043–2046, October 1994. ISSN 0031-9007. doi: 10.1103/PhysRevLett.73.2043. URL `https://link.aps.org/doi/10.1103/PhysRevLett.73.2043`.

[68] Tim Byrnes, Na Young Kim, and Yoshihisa Yamamoto. Exciton-polariton condensates. *Nature Physics*, 10(11):803–813, November 2014. ISSN 1745-2473, 1745-2481. doi: 10.1038/nphys3143. URL `http://www.nature.com/articles/nphys3143`.

[69] Mark Fox. *Quantum optics: an introduction.* Number 15 in Oxford master series in physics. Oxford University Press, Oxford ; New York, 2006. ISBN 978-0-19-856672-4 978-0-19-856673-1.

[70] E. M. Purcell, H. C. Torrey, and R. V. Pound. Resonance Absorption by Nuclear Magnetic Moments in a Solid. *Physical Review*, 69(1-2):37–38, January 1946. ISSN 0031-899X. doi: 10.1103/PhysRev.69.37. URL `https://link.aps.org/doi/10.1103/PhysRev.69.37`.

[71] Michael C. Munnix, Anatol Lochmann, Dieter Bimberg, and Vladimir A. Haisler. Modeling Highly Efficient RCLED-Type Quantum-Dot-Based Single Photon Emitters. *IEEE Journal of Quantum Electronics*, 45(9):1084–1088, September 2009. ISSN 0018-9197. doi: 10.1109/JQE.2009.2020995. URL `http://ieeexplore.ieee.org/document/5191277/`.

[72] D. Bimberg, E. Stock, A. Lochmann, A. Schliwa, J.A. Tofflinger, W. Unrau, M. Munnix, S. Rodt, V.A. Haisler, A.I. Toropov, A. Bakarov, and A.K. Kalagin. Quantum Dots for Single- and Entangled-Photon Emitters. *IEEE Photonics Journal*, 1(1):58–68, June 2009. ISSN 1943-0655. doi: 10.1109/JPHOT.2009.2025329. URL `http://ieeexplore.ieee.org/document/5075634/`.

[73] J. J. Hopfield. Theory of the Contribution of Excitons to the Complex Dielectric Constant of Crystals. *Physical Review*, 112(5):1555–1567, December 1958. ISSN 0031-899X. doi: 10.1103/PhysRev.112.1555. URL `https://link.aps.org/doi/10.1103/PhysRev.112.1555`.

[74] Y. Kaluzny, P. Goy, M. Gross, J. M. Raimond, and S. Haroche. Observation of Self-Induced Rabi Oscillations in Two-Level Atoms Excited Inside a Resonant Cavity: The Ringing Regime of Superradiance. *Physical Review Letters*, 51(13):1175–1178, September 1983. ISSN 0031-9007. doi: 10.1103/PhysRevLett.51.1175. URL `https://link.aps.org/doi/10.1103/PhysRevLett.51.1175`.

[75] R. J. Thompson, G. Rempe, and H. J. Kimble. Observation of normal-mode splitting for an atom in an optical cavity. *Physical Review Letters*, 68(8):1132–1135, February 1992. ISSN 0031-9007. doi: 10.1103/PhysRevLett.68.1132. URL `https://link.aps.org/doi/10.1103/PhysRevLett.68.1132`.

[76] C. Weisbuch, M. Nishioka, A. Ishikawa, and Y. Arakawa. Observation of the coupled exciton-photon mode splitting in a semiconductor quantum microcavity. *Physical Review Letters*, 69(23):3314–3317, December 1992. ISSN 0031-9007. doi: 10.1103/PhysRevLett.69.3314. URL `https://link.aps.org/doi/10.1103/PhysRevLett.69.3314`.

[77] Stanley Pau, Gunnar Björk, Joseph Jacobson, Hui Cao, and Yoshihisa Yamamoto. Microcavity exciton-polariton splitting in the linear regime. *Physical Review B*, 51(20):14437–14447, May 1995. ISSN 0163-1829, 1095-3795. doi: 10.1103/PhysRevB.51.14437. URL `https://link.aps.org/doi/10.1103/PhysRevB.51.14437`.

[78] Alexander Dreismann. *Controlling the spin of trapped polariton condensates with light and electric fields*. PhD thesis, University of Cambridge, September 2015.

[79] Arash Rahimi-Iman. Fundamentals of Polariton Physics. In *Polariton Physics*, volume 229, pages 33–64. Springer International Publishing, Cham, 2020. ISBN 978-3-030-39331-1 978-3-030-39333-5. doi: 10.1007/978-3-030-39333-5_2. URL `http://link.springer.com/10.1007/978-3-030-39333-5_2`. Series Title: Springer Series in Optical Sciences.

[80] Peter Cristofolini. Optical control of polariton condensation and dipolaritons in coupled quantum wells. March 2015. doi: 10.17863/CAM.16617. URL `https://www.repository.cam.ac.uk/handle/1810/247219`. Publisher: Apollo - University of Cambridge Repository.

[81] Yongbao Sun, Yoseob Yoon, Mark Steger, Gangqiang Liu, Loren N. Pfeiffer, Ken West, David W. Snoke, and Keith A. Nelson. Direct measurement of polariton-polariton interac-

tion strength. *Nature Physics*, 13(9):870–875, September 2017. ISSN 1745-2473, 1745-2481. doi: 10.1038/nphys4148. URL `http://www.nature.com/articles/nphys4148`.

[82] D. Sanvitto, S. Pigeon, A. Amo, D. Ballarini, M. De Giorgi, I. Carusotto, R. Hivet, F. Pisanello, V. G. Sala, P. S. S. Guimaraes, R. Houdré, E. Giacobino, C. Ciuti, A. Bramati, and G. Gigli. All-optical control of the quantum flow of a polariton condensate. *Nature Photonics*, 5(10):610–614, October 2011. ISSN 1749-4885, 1749-4893. doi: 10.1038/nphoton.2011.211. URL `http://www.nature.com/articles/nphoton.2011.211`.

[83] J. Kasprzak, M. Richard, S. Kundermann, A. Baas, P. Jeambrun, J. M. J. Keeling, F. M. Marchetti, M. H. Szymańska, R. André, J. L. Staehli, V. Savona, P. B. Littlewood, B. Deveaud, and Le Si Dang. Bose-Einstein condensation of exciton polaritons. *Nature*, 443 (7110):409–414, September 2006. ISSN 0028-0836, 1476-4687. doi: 10.1038/nature05131. URL `http://www.nature.com/articles/nature05131`.

[84] A. Askitopoulos, H. Ohadi, A. V. Kavokin, Z. Hatzopoulos, P. G. Savvidis, and P. G. Lagoudakis. Polariton condensation in an optically induced two-dimensional potential. *Physical Review B*, 88(4):041308, July 2013. ISSN 1098-0121, 1550-235X. doi: 10.1103/PhysRevB.88.041308. URL `https://link.aps.org/doi/10.1103/PhysRevB.88.041308`.

[85] S. I. Tsintzos, N. T. Pelekanos, G. Konstantinidis, Z. Hatzopoulos, and P. G. Savvidis. A GaAs polariton light-emitting diode operating near room temperature. *Nature*, 453 (7193):372–375, May 2008. ISSN 0028-0836, 1476-4687. doi: 10.1038/nature06979. URL `http://www.nature.com/articles/nature06979`.

[86] Daniele Bajoni, Elizaveta Semenova, Aristide Lemaître, Sophie Bouchoule, Esther Wertz, Pascale Senellart, and Jacqueline Bloch. Polariton light-emitting diode in a GaAs-based microcavity. *Physical Review B*, 77(11):113303, March 2008. ISSN 1098-0121, 1550-235X. doi: 10.1103/PhysRevB.77.113303. URL `https://link.aps.org/doi/10.1103/PhysRevB.77.113303`.

[87] F. Tassone, C. Piermarocchi, V. Savona, A. Quattropani, and P. Schwendimann. Bottleneck effects in the relaxation and photoluminescence of microcavity polaritons. *Physical Review B*, 56(12):7554–7563, September 1997. ISSN 0163-1829, 1095-3795. doi: 10.1103/PhysRevB.56.7554. URL `https://link.aps.org/doi/10.1103/PhysRevB.56.7554`.

[88] A. I. Tartakovskii, M. Emam-Ismail, R. M. Stevenson, M. S. Skolnick, V. N. Astratov, D. M. Whittaker, J. J. Baumberg, and J. S. Roberts. Relaxation bottleneck and its suppression in semiconductor microcavities. *Physical Review B*, 62(4):R2283–R2286, July

2000. ISSN 0163-1829, 1095-3795. doi: 10.1103/PhysRevB.62.R2283. URL https://link.aps.org/doi/10.1103/PhysRevB.62.R2283.

[89] F. Stokker-Cheregi, A. Vinattieri, F. Semond, M. Leroux, I. R. Sellers, J. Massies, D. Solnyshkov, G. Malpuech, M. Colocci, and M. Gurioli. Polariton relaxation bottleneck and its thermal suppression in bulk GaN microcavities. *Applied Physics Letters*, 92 (4):042119, January 2008. ISSN 0003-6951, 1077-3118. doi: 10.1063/1.2839380. URL http://aip.scitation.org/doi/10.1063/1.2839380.

[90] F. Tassone and Y. Yamamoto. Exciton-exciton scattering dynamics in a semiconductor microcavity and stimulated scattering into polaritons. *Physical Review B*, 59(16):10830–10842, April 1999. ISSN 0163-1829, 1095-3795. doi: 10.1103/PhysRevB.59.10830. URL https://link.aps.org/doi/10.1103/PhysRevB.59.10830.

[91] P. G. Savvidis, J. J. Baumberg, R. M. Stevenson, M. S. Skolnick, D. M. Whittaker, and J. S. Roberts. Angle-Resonant Stimulated Polariton Amplifier. *Physical Review Letters*, 84(7):1547–1550, February 2000. ISSN 0031-9007, 1079-7114. doi: 10.1103/PhysRevLett.84.1547. URL https://link.aps.org/doi/10.1103/PhysRevLett.84.1547.

[92] H. Ohadi, E. Kammann, T. C. H. Liew, K. G. Lagoudakis, A. V. Kavokin, and P. G. Lagoudakis. Spontaneous Symmetry Breaking in a Polariton and Photon Laser. *Physical Review Letters*, 109(1):016404, July 2012. ISSN 0031-9007, 1079-7114. doi: 10.1103/PhysRevLett.109.016404. URL https://link.aps.org/doi/10.1103/PhysRevLett.109.016404.

[93] R. Huang, F. Tassone, and Y. Yamamoto. Experimental evidence of stimulated scattering of excitons into microcavity polaritons. *Physical Review B*, 61(12):R7854–R7857, March 2000. ISSN 0163-1829, 1095-3795. doi: 10.1103/PhysRevB.61.R7854. URL https://link.aps.org/doi/10.1103/PhysRevB.61.R7854.

[94] Dallin S. Durfee and Wolfgang Ketterle. Experimental studies of Bose-Einstein condensation. *Optics Express*, 2(8):299, April 1998. ISSN 1094-4087. doi: 10.1364/OE.2.000299. URL https://opg.optica.org/abstract.cfm?URI=oe-2-8-299.

[95] Bose. Plancks Gesetz und Lichtquantenhypothese. *Zeitschrift für Physik*, 26(1):178–181, December 1924. ISSN 1434-6001, 1434-601X. doi: 10.1007/BF01327326. URL http://link.springer.com/10.1007/BF01327326.

[96] A. Einstein. Quantentheorie des einatomigen idealen Gases. In Dieter Simon, editor, *Albert Einstein: Akademie-Vorträge*, pages 237–244. Wiley, 1 edition, December 2005.

ISBN 978-3-527-40609-8 978-3-527-60895-9. doi: 10.1002/3527608958.ch27. URL https://onlinelibrary.wiley.com/doi/10.1002/3527608958.ch27.

[97] James F. Annett. *Superconductivity, superfluids, and condensates.* Oxford master series in condensed matter physics. Oxford University Press, Oxford ; New York, 2004. ISBN 978-0-19-850755-0 978-0-19-850756-7.

[98] L. P. Pitaevskiĭ and S. Stringari. *Bose-Einstein condensation.* Number 116 in Oxford science publications. Clarendon Press, Oxford ; New York, 2003. ISBN 978-0-19-850719-2. OCLC: ocm52145831.

[99] M. H. Anderson, J. R. Ensher, M. R. Matthews, C. E. Wieman, and E. A. Cornell. Observation of Bose-Einstein Condensation in a Dilute Atomic Vapor. *Science*, 269(5221): 198–201, July 1995. ISSN 0036-8075, 1095-9203. doi: 10.1126/science.269.5221.198. URL https://www.science.org/doi/10.1126/science.269.5221.198.

[100] K. B. Davis, M. O. Mewes, M. R. Andrews, N. J. van Druten, D. S. Durfee, D. M. Kurn, and W. Ketterle. Bose-Einstein Condensation in a Gas of Sodium Atoms. *Physical Review Letters*, 75(22):3969–3973, November 1995. ISSN 0031-9007, 1079-7114. doi: 10.1103/PhysRevLett.75.3969. URL https://link.aps.org/doi/10.1103/PhysRevLett.75.3969.

[101] Iulia Georgescu. 25 years of BEC. *Nature Reviews Physics*, 2(8):396–396, August 2020. ISSN 2522-5820. doi: 10.1038/s42254-020-0211-7. URL http://www.nature.com/articles/s42254-020-0211-7.

[102] Dirk van Delft and Peter Kes. The discovery of superconductivity. *Physics Today*, 63 (9):38–43, September 2010. ISSN 0031-9228, 1945-0699. doi: 10.1063/1.3490499. URL http://physicstoday.scitation.org/doi/10.1063/1.3490499.

[103] J. Bardeen, L. N. Cooper, and J. R. Schrieffer. Theory of Superconductivity. *Physical Review*, 108(5):1175–1204, December 1957. ISSN 0031-899X. doi: 10.1103/PhysRev.108.1175. URL https://link.aps.org/doi/10.1103/PhysRev.108.1175.

[104] P. Kapitza. Viscosity of Liquid Helium below the λ-Point. *Nature*, 141(3558):74–74, January 1938. ISSN 0028-0836, 1476-4687. doi: 10.1038/141074a0. URL https://www.nature.com/articles/141074a0.

[105] F. London. The λ-Phenomenon of Liquid Helium and the Bose-Einstein Degeneracy. *Nature*, 141(3571):643–644, April 1938. ISSN 0028-0836, 1476-4687. doi: 10.1038/141643a0. URL https://www.nature.com/articles/141643a0.

[106] S. A. Moskalenko and D. W. Snoke. *Bose-Einstein Condensation of Excitons and Biexcitons: And Coherent Nonlinear Optics with Excitons.* Cambridge University Press, 1 edition, February 2000. ISBN 978-0-521-58099-1 978-0-521-02235-4 978-0-511-72168-7. doi: 10.1017/CBO9780511721687. URL https://www.cambridge.org/core/product/identifier/9780511721687/type/book.

[107] John M. Blatt, K. W. Böer, and Werner Brandt. Bose-Einstein Condensation of Excitons. *Physical Review*, 126(5):1691–1692, June 1962. ISSN 0031-899X. doi: 10.1103/PhysRev.126.1691. URL https://link.aps.org/doi/10.1103/PhysRev.126.1691.

[108] L. L. Chase, N. Peyghambarian, G. Grynberg, and A. Mysyrowicz. Evidence for Bose-Einstein Condensation of Biexcitons in CuCl. *Physical Review Letters*, 42(18):1231–1234, April 1979. ISSN 0031-9007. doi: 10.1103/PhysRevLett.42.1231. URL https://link.aps.org/doi/10.1103/PhysRevLett.42.1231.

[109] Masahiro Hasuo, Nobukata Nagasawa, Tadashi Itoh, and André Mysyrowicz. Progress in the Bose-Einstein condensation of biexcitons in CuCl. *Physical Review Letters*, 70 (9):1303–1306, March 1993. ISSN 0031-9007. doi: 10.1103/PhysRevLett.70.1303. URL https://link.aps.org/doi/10.1103/PhysRevLett.70.1303.

[110] J. B. Grun, R. Levy, E. Ostertag, H. Vu Duy Phach, and H. Port. Biexciton luminescence in CuCl and CuBr. In *Physics of Highly Excited States in Solids*, volume 57, pages 49–56. Springer Berlin Heidelberg, Berlin, Heidelberg, 1976. ISBN 978-3-540-07991-0. doi: 10.1007/3-540-07991-2_75. URL http://link.springer.com/10.1007/3-540-07991-2_75. Series Title: Lecture Notes in Physics.

[111] D. Hulin, A. Mysyrowicz, and C. Benoît à la Guillaume. Evidence for Bose-Einstein Statistics in an Exciton Gas. *Physical Review Letters*, 45(24):1970–1973, December 1980. ISSN 0031-9007. doi: 10.1103/PhysRevLett.45.1970. URL https://link.aps.org/doi/10.1103/PhysRevLett.45.1970.

[112] Jia Ling Lin and J. P. Wolfe. Bose-Einstein condensation of paraexcitons in stressed Cu_2O. *Physical Review Letters*, 71(8):1222–1225, August 1993. ISSN 0031-9007. doi: 10.1103/PhysRevLett.71.1222. URL https://link.aps.org/doi/10.1103/PhysRevLett.71.1222.

[113] M. Y. Shen, T. Yokouchi, S. Koyama, and T. Goto. Dynamics associated with Bose-Einstein statistics of orthoexcitons generated by resonant excitations in cuprous oxide. *Physical Review B*, 56(20):13066–13072, November 1997. ISSN 0163-1829, 1095-3795. doi: 10.1103/PhysRevB.56.13066. URL https://link.aps.org/doi/10.1103/PhysRevB.56.13066.

[114] L. V. Butov, A. Zrenner, G. Abstreiter, G. Böhm, and G. Weimann. Condensation of Indirect Excitons in Coupled AlAs/GaAs Quantum Wells. *Physical Review Letters*, 73 (2):304–307, July 1994. ISSN 0031-9007. doi: 10.1103/PhysRevLett.73.304. URL `https://link.aps.org/doi/10.1103/PhysRevLett.73.304`.

[115] L. V. Butov, C. W. Lai, A. L. Ivanov, A. C. Gossard, and D. S. Chemla. Towards Bose-Einstein condensation of excitons in potential traps. *Nature*, 417(6884):47–52, May 2002. ISSN 0028-0836, 1476-4687. doi: 10.1038/417047a. URL `http://www.nature.com/articles/417047a`.

[116] D. W. Snoke. When should we say we have observed Bose condensation of excitons? *physica status solidi (b)*, 238(3):389–396, August 2003. ISSN 03701972, 15213951. doi: 10.1002/pssb.200303151. URL `https://onlinelibrary.wiley.com/doi/10.1002/pssb.200303151`.

[117] David Snoke and G M Kavoulakis. Bose-Einstein condensation of excitons in $\mathrm{Cu_2O}$: progress over 30 years. *Reports on Progress in Physics*, 77(11):116501, November 2014. ISSN 0034-4885, 1361-6633. doi: 10.1088/0034-4885/77/11/116501. URL `https://iopscience.iop.org/article/10.1088/0034-4885/77/11/116501`.

[118] A. Imamoğlu, R. J. Ram, S. Pau, and Y. Yamamoto. Nonequilibrium condensates and lasers without inversion: Exciton-polariton lasers. *Physical Review A*, 53(6):4250–4253, June 1996. ISSN 1050-2947, 1094-1622. doi: 10.1103/PhysRevA.53.4250. URL `https://link.aps.org/doi/10.1103/PhysRevA.53.4250`.

[119] Alberto Amo, Jérôme Lefrère, Simon Pigeon, Claire Adrados, Cristiano Ciuti, Iacopo Carusotto, Romuald Houdré, Elisabeth Giacobino, and Alberto Bramati. Superfluidity of polaritons in semiconductor microcavities. *Nature Physics*, 5(11):805–810, November 2009. ISSN 1745-2473, 1745-2481. doi: 10.1038/nphys1364. URL `http://www.nature.com/articles/nphys1364`.

[120] Georgios Roumpos, Michael D. Fraser, Andreas Löffler, Sven Höfling, Alfred Forchel, and Yoshihisa Yamamoto. Single vortex-antivortex pair in an exciton-polariton condensate. *Nature Physics*, 7(2):129–133, February 2011. ISSN 1745-2473, 1745-2481. doi: 10.1038/nphys1841. URL `http://www.nature.com/articles/nphys1841`.

[121] A. Amo, S. Pigeon, D. Sanvitto, V. G. Sala, R. Hivet, I. Carusotto, F. Pisanello, G. Leménager, R. Houdré, E Giacobino, C. Ciuti, and A. Bramati. Polariton Superfluids Reveal Quantum Hydrodynamic Solitons. *Science*, 332(6034):1167–1170, June 2011. ISSN 0036-8075, 1095-9203. doi: 10.1126/science.1202307. URL `https://www.science.org/doi/10.1126/science.1202307`.

[122] M. Sich, D. N. Krizhanovskii, M. S. Skolnick, A. V. Gorbach, R. Hartley, D. V. Skryabin, E. A. Cerda-Méndez, K. Biermann, R. Hey, and P. V. Santos. Observation of bright polariton solitons in a semiconductor microcavity. *Nature Photonics*, 6(1):50–55, January 2012. ISSN 1749-4885, 1749-4893. doi: 10.1038/nphoton.2011.267. URL `http://www.nature.com/articles/nphoton.2011.267`.

[123] A. S. Abdalla, Bingsuo Zou, and Yongyou Zhang. Optical Josephson oscillation achieved by two coupled exciton-polariton condensates. *Optics Express*, 28(7):9136, March 2020. ISSN 1094-4087. doi: 10.1364/OE.389486. URL `https://opg.optica.org/abstract.cfm?URI=oe-28-7-9136`.

[124] K. Orfanakis, A. F. Tzortzakakis, D. Petrosyan, P. G. Savvidis, and H. Ohadi. Ultralong temporal coherence in optically trapped exciton-polariton condensates. *Physical Review B*, 103(23):235313, June 2021. ISSN 2469-9950, 2469-9969. doi: 10.1103/PhysRevB.103.235313. URL `https://link.aps.org/doi/10.1103/PhysRevB.103.235313`.

[125] C. W. Lai, N. Y. Kim, S. Utsunomiya, G. Roumpos, H. Deng, M. D. Fraser, T. Byrnes, P. Recher, N. Kumada, T. Fujisawa, and Y. Yamamoto. Coherent zero-state and π-state in an exciton-polariton condensate array. *Nature*, 450(7169):529–532, November 2007. ISSN 0028-0836, 1476-4687. doi: 10.1038/nature06334. URL `http://www.nature.com/articles/nature06334`.

[126] Fabio Scafirimuto, Darius Urbonas, Michael A. Becker, Ullrich Scherf, Rainer F. Mahrt, and Thilo Stöferle. Tunable exciton-polariton condensation in a two-dimensional Lieb lattice at room temperature. *Communications Physics*, 4(1):39, December 2021. ISSN 2399-3650. doi: 10.1038/s42005-021-00548-w. URL `http://www.nature.com/articles/s42005-021-00548-w`.

[127] R. Balili, V. Hartwell, D. Snoke, L. Pfeiffer, and K. West. Bose-Einstein Condensation of Microcavity Polaritons in a Trap. *Science*, 316(5827):1007–1010, May 2007. ISSN 0036-8075, 1095-9203. doi: 10.1126/science.1140990. URL `https://www.science.org/doi/10.1126/science.1140990`.

[128] Esther Wertz, Lydie Ferrier, Dmitry D. Solnyshkov, Pascale Senellart, Daniele Bajoni, Audrey Miard, Aristide Lemaître, Guillaume Malpuech, and Jacqueline Bloch. Spontaneous formation of a polariton condensate in a planar GaAs microcavity. *Applied Physics Letters*, 95(5):051108, August 2009. ISSN 0003-6951, 1077-3118. doi: 10.1063/1.3192408. URL `http://aip.scitation.org/doi/10.1063/1.3192408`.

[129] Daniele Bajoni, Pascale Senellart, Aristide Lemaître, and Jacqueline Bloch. Photon lasing in GaAs microcavity: Similarities with a polariton condensate. *Physical Review B*, 76(20):

201305, November 2007. ISSN 1098-0121, 1550-235X. doi: 10.1103/PhysRevB.76.201305. URL https://link.aps.org/doi/10.1103/PhysRevB.76.201305.

[130] Gabriel Christmann, Raphaël Butté, Eric Feltin, Jean-François Carlin, and Nicolas Grandjean. Room temperature polariton lasing in a GaN-AlGaN multiple quantum well microcavity. *Applied Physics Letters*, 93(5):051102, August 2008. ISSN 0003-6951, 1077-3118. doi: 10.1063/1.2966369. URL http://aip.scitation.org/doi/10.1063/1.2966369.

[131] J. J. Baumberg, A. V. Kavokin, S. Christopoulos, A. J. D. Grundy, R. Butté, G. Christmann, D. D. Solnyshkov, G. Malpuech, G. Baldassarri Höger von Högersthal, E. Feltin, J.-F. Carlin, and N. Grandjean. Spontaneous Polarization Buildup in a Room-Temperature Polariton Laser. *Physical Review Letters*, 101(13):136409, September 2008. ISSN 0031-9007, 1079-7114. doi: 10.1103/PhysRevLett.101.136409. URL https://link.aps.org/doi/10.1103/PhysRevLett.101.136409.

[132] Jacques Levrat, Raphaël Butté, Eric Feltin, Jean-François Carlin, Nicolas Grandjean, Dmitry Solnyshkov, and Guillaume Malpuech. Condensation phase diagram of cavity polaritons in GaN-based microcavities: Experiment and theory. *Physical Review B*, 81 (12):125305, March 2010. ISSN 1098-0121, 1550-235X. doi: 10.1103/PhysRevB.81.125305. URL https://link.aps.org/doi/10.1103/PhysRevB.81.125305.

[133] T. Guillet, M. Mexis, J. Levrat, G. Rossbach, C. Brimont, T. Bretagnon, B. Gil, R. Butté, N. Grandjean, L. Orosz, F. Réveret, J. Leymarie, J. Zúñiga-Pérez, M. Leroux, F. Semond, and S. Bouchoule. Polariton lasing in a hybrid bulk ZnO microcavity. *Applied Physics Letters*, 99(16):161104, October 2011. ISSN 0003-6951, 1077-3118. doi: 10.1063/1.3650268. URL http://aip.scitation.org/doi/10.1063/1.3650268.

[134] Feng Li, L. Orosz, O. Kamoun, S. Bouchoule, C. Brimont, P. Disseix, T. Guillet, X. Lafosse, M. Leroux, J. Leymarie, M. Mexis, M. Mihailovic, G. Patriarche, F. Réveret, D. Solnyshkov, J. Zuniga-Perez, and G. Malpuech. From Excitonic to Photonic Polariton Condensate in a ZnO-Based Microcavity. *Physical Review Letters*, 110(19):196406, May 2013. ISSN 0031-9007, 1079-7114. doi: 10.1103/PhysRevLett.110.196406. URL https://link.aps.org/doi/10.1103/PhysRevLett.110.196406.

[135] Johannes D. Plumhof, Thilo Stöferle, Lijian Mai, Ullrich Scherf, and Rainer F. Mahrt. Room-temperature Bose–Einstein condensation of cavity exciton–polaritons in a polymer. *Nature Materials*, 13(3):247–252, March 2014. ISSN 1476-1122, 1476-4660. doi: 10.1038/nmat3825. URL https://www.nature.com/articles/nmat3825.

[136] Christof P. Dietrich, Anja Steude, Laura Tropf, Marcel Schubert, Nils M. Kronenberg, Kai Ostermann, Sven Höfling, and Malte C. Gather. An exciton-polariton laser based on

biologically produced fluorescent protein. *Science Advances*, 2(8):e1600666, August 2016. ISSN 2375-2548. doi: 10.1126/sciadv.1600666. URL `https://www.science.org/doi/10.1126/sciadv.1600666`.

[137] Tamsin Cookson, Kyriacos Georgiou, Anton Zasedatelev, Richard T. Grant, Tersilla Virgili, Marco Cavazzini, Francesco Galeotti, Caspar Clark, Natalia G. Berloff, David G. Lidzey, and Pavlos G. Lagoudakis. A Yellow Polariton Condensate in a Dye Filled Microcavity. *Advanced Optical Materials*, 5(18):1700203, September 2017. ISSN 21951071. doi: 10.1002/adom.201700203. URL `https://onlinelibrary.wiley.com/doi/10.1002/adom.201700203`.

[138] Jiaxin Zhao, Rui Su, Antonio Fieramosca, Weijie Zhao, Wei Du, Xue Liu, Carole Diederichs, Daniele Sanvitto, Timothy C. H. Liew, and Qihua Xiong. Ultralow Threshold Polariton Condensate in a Monolayer Semiconductor Microcavity at Room Temperature. *Nano Letters*, 21(7):3331–3339, April 2021. ISSN 1530-6984, 1530-6992. doi: 10.1021/acs.nanolett.1c01162. URL `https://pubs.acs.org/doi/10.1021/acs.nanolett.1c01162`.

[139] Rui Su, Sanjib Ghosh, Jun Wang, Sheng Liu, Carole Diederichs, Timothy C. H. Liew, and Qihua Xiong. Observation of exciton polariton condensation in a perovskite lattice at room temperature. *Nature Physics*, 16(3):301–306, March 2020. ISSN 1745-2473, 1745-2481. doi: 10.1038/s41567-019-0764-5. URL `http://www.nature.com/articles/s41567-019-0764-5`.

[140] Thierry Guillet and Christelle Brimont. Polariton condensates at room temperature. *Comptes Rendus Physique*, 17(8):946–956, October 2016. ISSN 16310705. doi: 10.1016/j.crhy.2016.07.002. URL `https://linkinghub.elsevier.com/retrieve/pii/S1631070516300494`.

[141] Jan Klaers, Julian Schmitt, Frank Vewinger, and Martin Weitz. Bose-Einstein condensation of photons in an optical microcavity. *Nature*, 468(7323):545–548, November 2010. ISSN 0028-0836, 1476-4687. doi: 10.1038/nature09567. URL `http://www.nature.com/articles/nature09567`.

[142] S. O. Demokritov, V. E. Demidov, O. Dzyapko, G. A. Melkov, A. A. Serga, B. Hillebrands, and A. N. Slavin. Bose–Einstein condensation of quasi-equilibrium magnons at room temperature under pumping. *Nature*, 443(7110):430–433, September 2006. ISSN 0028-0836, 1476-4687. doi: 10.1038/nature05117. URL `http://www.nature.com/articles/nature05117`.

[143] V. E. Demidov, O. Dzyapko, M. Buchmeier, T. Stockhoff, G. Schmitz, G. A. Melkov, and S. O. Demokritov. Magnon Kinetics and Bose-Einstein Condensation Studied in

Phase Space. *Physical Review Letters*, 101(25):257201, December 2008. ISSN 0031-9007, 1079-7114. doi: 10.1103/PhysRevLett.101.257201. URL https://link.aps.org/doi/10.1103/PhysRevLett.101.257201.

[144] A. V. Chumak, G. A. Melkov, V. E. Demidov, O. Dzyapko, V. L. Safonov, and S. O. Demokritov. Bose-Einstein Condensation of Magnons under Incoherent Pumping. *Physical Review Letters*, 102(18):187205, May 2009. ISSN 0031-9007, 1079-7114. doi: 10.1103/PhysRevLett.102.187205. URL https://link.aps.org/doi/10.1103/PhysRevLett.102.187205.

[145] Oliver Penrose and Lars Onsager. Bose-Einstein Condensation and Liquid Helium. *Physical Review*, 104(3):576–584, November 1956. ISSN 0031-899X. doi: 10.1103/PhysRev.104.576. URL https://link.aps.org/doi/10.1103/PhysRev.104.576.

[146] Hui Deng, Glenn S. Solomon, Rudolf Hey, Klaus H. Ploog, and Yoshihisa Yamamoto. Spatial Coherence of a Polariton Condensate. *Physical Review Letters*, 99(12):126403, September 2007. ISSN 0031-9007, 1079-7114. doi: 10.1103/PhysRevLett.99.126403. URL https://link.aps.org/doi/10.1103/PhysRevLett.99.126403.

[147] Daniele Bajoni, Pascale Senellart, Esther Wertz, Isabelle Sagnes, Audrey Miard, Aristide Lemaître, and Jacqueline Bloch. Polariton Laser Using Single Micropillar GaAs - GaAlAs Semiconductor Cavities. *Physical Review Letters*, 100(4):047401, January 2008. ISSN 0031-9007, 1079-7114. doi: 10.1103/PhysRevLett.100.047401. URL https://link.aps.org/doi/10.1103/PhysRevLett.100.047401.

[148] B. Nelsen, R. Balili, D. W. Snoke, L. Pfeiffer, and K. West. Lasing and polariton condensation: Two distinct transitions in GaAs microcavities with stress traps. *Journal of Applied Physics*, 105(12):122414, June 2009. ISSN 0021-8979, 1089-7550. doi: 10.1063/1.3140822. URL http://aip.scitation.org/doi/10.1063/1.3140822.

[149] Stefano Azzini, Dario Gerace, Matteo Galli, Isabelle Sagnes, Rémy Braive, Aristide Lemaître, Jacqueline Bloch, and D. Bajoni. Ultra-low threshold polariton lasing in photonic crystal cavities. *Applied Physics Letters*, 99(11):111106, September 2011. ISSN 0003-6951, 1077-3118. doi: 10.1063/1.3638469. URL http://aip.scitation.org/doi/10.1063/1.3638469.

[150] P Tsotsis, P S Eldridge, T Gao, S I Tsintzos, Z Hatzopoulos, and P G Savvidis. Lasing threshold doubling at the crossover from strong to weak coupling regime in GaAs microcavity. *New Journal of Physics*, 14(2):023060, February 2012. ISSN 1367-2630. doi: 10.1088/1367-2630/14/2/023060. URL https://iopscience.iop.org/article/10.1088/1367-2630/14/2/023060.

[151] D. Sarchi and V. Savona. Towards thermal equilibrium in the Bose-Einstein condensation of microcavity polaritons. *Solid State Communications*, 144(9):371–377, December 2007. ISSN 00381098. doi: 10.1016/j.ssc.2007.07.039. URL `https://linkinghub.elsevier.com/retrieve/pii/S0038109807005789`.

[152] Fei Xue, Fengcheng Wu, Ming Xie, Jung-Jung Su, and A. H. MacDonald. Microscopic theory of equilibrium polariton condensates. *Physical Review B*, 94(23):235302, December 2016. ISSN 2469-9950, 2469-9969. doi: 10.1103/PhysRevB.94.235302. URL `https://link.aps.org/doi/10.1103/PhysRevB.94.235302`.

[153] A. P. D. Love, D. N. Krizhanovskii, D. M. Whittaker, R. Bouchekioua, D. Sanvitto, S. Al Rizeiqi, R. Bradley, M. S. Skolnick, P. R. Eastham, R. André, and Le Si Dang. Intrinsic Decoherence Mechanisms in the Microcavity Polariton Condensate. *Physical Review Letters*, 101(6):067404, August 2008. ISSN 0031-9007, 1079-7114. doi: 10.1103/PhysRevLett.101.067404. URL `https://link.aps.org/doi/10.1103/PhysRevLett.101.067404`.

[154] P. C. Hohenberg. Existence of Long-Range Order in One and Two Dimensions. *Physical Review*, 158(2):383–386, June 1967. ISSN 0031-899X. doi: 10.1103/PhysRev.158.383. URL `https://link.aps.org/doi/10.1103/PhysRev.158.383`.

[155] Vanderlei Bagnato, David E. Pritchard, and Daniel Kleppner. Bose-Einstein condensation in an external potential. *Physical Review A*, 35(10):4354–4358, May 1987. ISSN 0556-2791. doi: 10.1103/PhysRevA.35.4354. URL `https://link.aps.org/doi/10.1103/PhysRevA.35.4354`.

[156] Michael D Fraser. Coherent exciton-polariton devices. *Semiconductor Science and Technology*, 32(9):093003, September 2017. ISSN 0268-1242, 1361-6641. doi: 10.1088/1361-6641/aa730c. URL `https://iopscience.iop.org/article/10.1088/1361-6641/aa730c`.

[157] V D Kulakovskii, A I Tartakovskii, D N Krizhanovskii, N A Gippius, M S Skolnick, and J S Roberts. Nonlinear effects in a dense two-dimensional exciton-polariton system in semiconductor microcavities. *Nanotechnology*, 12(4):475–479, December 2001. ISSN 0957-4484, 1361-6528. doi: 10.1088/0957-4484/12/4/319. URL `https://iopscience.iop.org/article/10.1088/0957-4484/12/4/319`.

[158] J. M. Ménard, C. Poellmann, M. Porer, U. Leierseder, E. Galopin, A. Lemaître, A. Amo, J. Bloch, and R. Huber. Revealing the dark side of a bright exciton-polariton condensate. *Nature Communications*, 5(1):4648, December 2014. ISSN 2041-1723. doi: 10.1038/ncomms5648. URL `http://www.nature.com/articles/ncomms5648`.

[159] R. Houdré, J. L. Gibernon, P. Pellandini, R. P. Stanley, U. Oesterle, C. Weisbuch, J. O'Gorman, B. Roycroft, and M. Ilegems. Saturation of the strong-coupling regime in a semiconductor microcavity: Free-carrier bleaching of cavity polaritons. *Physical Review B*, 52(11):7810–7813, September 1995. ISSN 0163-1829, 1095-3795. doi: 10.1103/PhysRevB.52.7810. URL `https://link.aps.org/doi/10.1103/PhysRevB.52.7810`.

[160] G. Tosi, G. Christmann, N. G. Berloff, P. Tsotsis, T. Gao, Z. Hatzopoulos, P. G. Savvidis, and J. J. Baumberg. Sculpting oscillators with light within a nonlinear quantum fluid. *Nature Physics*, 8(3):190–194, March 2012. ISSN 1745-2473, 1745-2481. doi: 10.1038/nphys2182. URL `http://www.nature.com/articles/nphys2182`.

[161] P. Cristofolini, A. Dreismann, G. Christmann, G. Franchetti, N. G. Berloff, P. Tsotsis, Z. Hatzopoulos, P. G. Savvidis, and J. J. Baumberg. Optical Superfluid Phase Transitions and Trapping of Polariton Condensates. *Physical Review Letters*, 110(18):186403, May 2013. ISSN 0031-9007, 1079-7114. doi: 10.1103/PhysRevLett.110.186403. URL `https://link.aps.org/doi/10.1103/PhysRevLett.110.186403`.

[162] P. R. Eastham. Mode locking and mode competition in a nonequilibrium solid-state condensate. *Physical Review B*, 78(3):035319, July 2008. ISSN 1098-0121, 1550-235X. doi: 10.1103/PhysRevB.78.035319. URL `https://link.aps.org/doi/10.1103/PhysRevB.78.035319`.

[163] David Racine and P. R. Eastham. Quantum theory of multimode polariton condensation. *Physical Review B*, 90(8):085308, August 2014. ISSN 1098-0121, 1550-235X. doi: 10.1103/PhysRevB.90.085308. URL `https://link.aps.org/doi/10.1103/PhysRevB.90.085308`.

[164] C. Antón, G. Tosi, M. D. Martín, Z. Hatzopoulos, G. Konstantinidis, P. S. Eldridge, P. G. Savvidis, C. Tejedor, and L. Viña. Quantum coherence in momentum space of light-matter condensates. *Physical Review B*, 90(8):081407, August 2014. ISSN 1098-0121, 1550-235X. doi: 10.1103/PhysRevB.90.081407. URL `https://link.aps.org/doi/10.1103/PhysRevB.90.081407`.

[165] Maurice G. A. Bernard and Georges Duraffourg. Laser Conditions in Semiconductors. *physica status solidi (b)*, 1(7):699–703, 1961. ISSN 03701972, 15213951. doi: 10.1002/pssb.19610010703. URL `https://onlinelibrary.wiley.com/doi/10.1002/pssb.19610010703`.

[166] Long Zhang, Jiaqi Hu, Jinqi Wu, Rui Su, Zhanghai Chen, Qihua Xiong, and Hui Deng. Recent developments on polariton lasers. *Progress in Quantum Electronics*,

83:100399, May 2022. ISSN 00796727. doi: 10.1016/j.pquantelec.2022.100399. URL https://linkinghub.elsevier.com/retrieve/pii/S0079672722000258.

[167] Michiel Wouters and Iacopo Carusotto. Excitations in a Nonequilibrium Bose-Einstein Condensate of Exciton Polaritons. *Physical Review Letters*, 99(14):140402, October 2007. ISSN 0031-9007, 1079-7114. doi: 10.1103/PhysRevLett.99.140402. URL https://link.aps.org/doi/10.1103/PhysRevLett.99.140402.

[168] Michiel Wouters. Synchronized and desynchronized phases of coupled nonequilibrium exciton-polariton condensates. *Physical Review B*, 77(12):121302, March 2008. ISSN 1098-0121, 1550-235X. doi: 10.1103/PhysRevB.77.121302. URL https://link.aps.org/doi/10.1103/PhysRevB.77.121302.

[169] Michiel Wouters and Iacopo Carusotto. Superfluidity and Critical Velocities in Nonequilibrium Bose-Einstein Condensates. *Physical Review Letters*, 105(2):020602, July 2010. ISSN 0031-9007, 1079-7114. doi: 10.1103/PhysRevLett.105.020602. URL https://link.aps.org/doi/10.1103/PhysRevLett.105.020602.

[170] M. Wouters, T. C. H. Liew, and V. Savona. Energy relaxation in one-dimensional polariton condensates. *Physical Review B*, 82(24):245315, December 2010. ISSN 1098-0121, 1550-235X. doi: 10.1103/PhysRevB.82.245315. URL https://link.aps.org/doi/10.1103/PhysRevB.82.245315.

[171] P.-É. Larré, N. Pavloff, and A. M. Kamchatnov. Wave pattern induced by a localized obstacle in the flow of a one-dimensional polariton condensate. *Physical Review B*, 86(16):165304, October 2012. ISSN 1098-0121, 1550-235X. doi: 10.1103/PhysRevB.86.165304. URL https://link.aps.org/doi/10.1103/PhysRevB.86.165304.

[172] Lydie Ferrier, Esther Wertz, Robert Johne, Dmitry D. Solnyshkov, Pascale Senellart, Isabelle Sagnes, Aristide Lemaître, Guillaume Malpuech, and Jacqueline Bloch. Interactions in Confined Polariton Condensates. *Physical Review Letters*, 106(12):126401, March 2011. ISSN 0031-9007, 1079-7114. doi: 10.1103/PhysRevLett.106.126401. URL https://link.aps.org/doi/10.1103/PhysRevLett.106.126401.

[173] Georgios Roumpos, Michael Lohse, Wolfgang H. Nitsche, Jonathan Keeling, Marzena Hanna Szymańska, Peter B. Littlewood, Andreas Löffler, Sven Höfling, Lukas Worschech, Alfred Forchel, and Yoshihisa Yamamoto. Power-law decay of the spatial correlation function in exciton-polariton condensates. *Proceedings of the National Academy of Sciences*, 109(17):6467–6472, April 2012. ISSN 0027-8424, 1091-6490. doi: 10.1073/pnas.1107970109. URL https://pnas.org/doi/full/10.1073/pnas.1107970109.

[174] Jonathan Keeling and Natalia G. Berloff. Spontaneous Rotating Vortex Lattices in a Pumped Decaying Condensate. *Physical Review Letters*, 100(25):250401, June 2008. doi: 10.1103/PhysRevLett.100.250401. URL `https://link.aps.org/doi/10.1103/PhysRevLett.100.250401`. Publisher: American Physical Society.

[175] Iacopo Carusotto and Cristiano Ciuti. Quantum fluids of light. *Reviews of Modern Physics*, 85(1):299–366, February 2013. ISSN 0034-6861, 1539-0756. doi: 10.1103/RevModPhys.85.299. URL `https://link.aps.org/doi/10.1103/RevModPhys.85.299`.

[176] Roy J. Glauber. The Quantum Theory of Optical Coherence. *Physical Review*, 130(6): 2529–2539, June 1963. ISSN 0031-899X. doi: 10.1103/PhysRev.130.2529. URL `https://link.aps.org/doi/10.1103/PhysRev.130.2529`.

[177] J. Fischer, I. G. Savenko, M. D. Fraser, S. Holzinger, S. Brodbeck, M. Kamp, I. A. Shelykh, C. Schneider, and S. Höfling. Spatial Coherence Properties of One Dimensional Exciton-Polariton Condensates. *Physical Review Letters*, 113(20):203902, November 2014. ISSN 0031-9007, 1079-7114. doi: 10.1103/PhysRevLett.113.203902. URL `https://link.aps.org/doi/10.1103/PhysRevLett.113.203902`.

[178] Jonathan Keeling and Stéphane Kéna-Cohen. Bose-Einstein Condensation of Exciton-Polaritons in Organic Microcavities. *Annual Review of Physical Chemistry*, 71(1):435–459, April 2020. ISSN 0066-426X, 1545-1593. doi: 10.1146/annurev-physchem-010920-102509. URL `https://www.annualreviews.org/doi/10.1146/annurev-physchem-010920-102509`.

[179] F. Manni, K. G. Lagoudakis, T. C. H. Liew, R. André, and B. Deveaud-Plédran. Spontaneous Pattern Formation in a Polariton Condensate. *Physical Review Letters*, 107(10): 106401, September 2011. ISSN 0031-9007, 1079-7114. doi: 10.1103/PhysRevLett.107.106401. URL `https://link.aps.org/doi/10.1103/PhysRevLett.107.106401`.

[180] C. Sturm, D. Tanese, H.S. Nguyen, H. Flayac, E. Galopin, A. Lemaître, I. Sagnes, D. Solnyshkov, A. Amo, G. Malpuech, and J. Bloch. All-optical phase modulation in a cavity-polariton Mach-Zehnder interferometer. *Nature Communications*, 5(1):3278, May 2014. ISSN 2041-1723. doi: 10.1038/ncomms4278. URL `http://www.nature.com/articles/ncomms4278`.

[181] Seonghoon Kim, Bo Zhang, Zhaorong Wang, Julian Fischer, Sebastian Brodbeck, Martin Kamp, Christian Schneider, Sven Höfling, and Hui Deng. Coherent Polariton Laser. *Physical Review X*, 6(1):011026, March 2016. ISSN 2160-3308. doi: 10.1103/PhysRevX.6.011026. URL `https://link.aps.org/doi/10.1103/PhysRevX.6.011026`.

[182] Aurélien Trichet, Emilien Durupt, François Médard, Sanjoy Datta, Anna Minguzzi, and Maxime Richard. Long-range correlations in a 97% excitonic one-dimensional polariton condensate. *Physical Review B*, 88(12):121407, September 2013. ISSN 1098-0121, 1550-235X. doi: 10.1103/PhysRevB.88.121407. URL `https://link.aps.org/doi/10.1103/PhysRevB.88.121407`.

[183] T. C. H. Liew, A. V. Kavokin, and I. A. Shelykh. Optical Circuits Based on Polariton Neurons in Semiconductor Microcavities. *Physical Review Letters*, 101(1):016402, July 2008. ISSN 0031-9007, 1079-7114. doi: 10.1103/PhysRevLett.101.016402. URL `https://link.aps.org/doi/10.1103/PhysRevLett.101.016402`.

[184] T. C. H. Liew, A. V. Kavokin, T. Ostatnický, M. Kaliteevski, I. A. Shelykh, and R. A. Abram. Exciton-polariton integrated circuits. *Physical Review B*, 82(3):033302, July 2010. ISSN 1098-0121, 1550-235X. doi: 10.1103/PhysRevB.82.033302. URL `https://link.aps.org/doi/10.1103/PhysRevB.82.033302`.

[185] Na Young Kim, Kenichiro Kusudo, Congjun Wu, Naoyuki Masumoto, Andreas Löffler, Sven Höfling, Norio Kumada, Lukas Worschech, Alfred Forchel, and Yoshihisa Yamamoto. Dynamical d-wave condensation of exciton-polaritons in a two-dimensional square-lattice potential. *Nature Physics*, 7(9):681–686, September 2011. ISSN 1745-2473, 1745-2481. doi: 10.1038/nphys2012. URL `http://www.nature.com/articles/nphys2012`.

[186] Naoyuki Masumoto, Na Young Kim, Tim Byrnes, Kenichiro Kusudo, Andreas Löffler, Sven Höfling, Alfred Forchel, and Yoshihisa Yamamoto. Exciton-polariton condensates with flat bands in a two-dimensional kagome lattice. *New Journal of Physics*, 14(6):065002, June 2012. ISSN 1367-2630. doi: 10.1088/1367-2630/14/6/065002. URL `https://iopscience.iop.org/article/10.1088/1367-2630/14/6/065002`.

[187] T. Jacqmin, I. Carusotto, I. Sagnes, M. Abbarchi, D. D. Solnyshkov, G. Malpuech, E. Galopin, A. Lemaître, J. Bloch, and A. Amo. Direct Observation of Dirac Cones and a Flatband in a Honeycomb Lattice for Polaritons. *Physical Review Letters*, 112(11):116402, March 2014. ISSN 0031-9007, 1079-7114. doi: 10.1103/PhysRevLett.112.116402. URL `https://link.aps.org/doi/10.1103/PhysRevLett.112.116402`.

[188] C Schneider, K Winkler, M D Fraser, M Kamp, Y Yamamoto, E A Ostrovskaya, and S Höfling. Exciton-polariton trapping and potential landscape engineering. *Reports on Progress in Physics*, 80(1):016503, January 2017. ISSN 0034-4885, 1361-6633. doi: 10.1088/0034-4885/80/1/016503. URL `https://iopscience.iop.org/article/10.1088/0034-4885/80/1/016503`.

[189] R. B. Balili, D. W. Snoke, L. Pfeiffer, and K. West. Actively tuned and spatially trapped polaritons. *Applied Physics Letters*, 88(3):031110, January 2006. ISSN 0003-6951, 1077-3118. doi: 10.1063/1.2164431. URL `http://aip.scitation.org/doi/10.1063/1.2164431`.

[190] M. M. de Lima, M. van der Poel, P. V. Santos, and J. M. Hvam. Phonon-Induced Polariton Superlattices. *Physical Review Letters*, 97(4):045501, July 2006. ISSN 0031-9007, 1079-7114. doi: 10.1103/PhysRevLett.97.045501. URL `https://link.aps.org/doi/10.1103/PhysRevLett.97.045501`.

[191] E. A. Cerda-Méndez, D. N. Krizhanovskii, M. Wouters, R. Bradley, K. Biermann, K. Guda, R. Hey, P. V. Santos, D. Sarkar, and M. S. Skolnick. Polariton Condensation in Dynamic Acoustic Lattices. *Physical Review Letters*, 105(11):116402, September 2010. ISSN 0031-9007, 1079-7114. doi: 10.1103/PhysRevLett.105.116402. URL `https://link.aps.org/doi/10.1103/PhysRevLett.105.116402`.

[192] E. A. Cerda-Méndez, D. Sarkar, D. N. Krizhanovskii, S. S. Gavrilov, K. Biermann, M. S. Skolnick, and P. V. Santos. Exciton-Polariton Gap Solitons in Two-Dimensional Lattices. *Physical Review Letters*, 111(14):146401, October 2013. ISSN 0031-9007, 1079-7114. doi: 10.1103/PhysRevLett.111.146401. URL `https://link.aps.org/doi/10.1103/PhysRevLett.111.146401`.

[193] P. Tsotsis, S. I. Tsintzos, G. Christmann, P. G. Lagoudakis, O. Kyriienko, I. A. Shelykh, J. J. Baumberg, A. V. Kavokin, Z. Hatzopoulos, P. S. Eldridge, and P. G. Savvidis. Tuning the Energy of a Polariton Condensate via Bias-Controlled Rabi Splitting. *Physical Review Applied*, 2(1):014002, July 2014. ISSN 2331-7019. doi: 10.1103/PhysRevApplied.2.014002. URL `https://link.aps.org/doi/10.1103/PhysRevApplied.2.014002`.

[194] E. Wertz, L. Ferrier, D. D. Solnyshkov, R. Johne, D. Sanvitto, A. Lemaître, I. Sagnes, R. Grousson, A. V. Kavokin, P. Senellart, G. Malpuech, and J. Bloch. Spontaneous formation and optical manipulation of extended polariton condensates. *Nature Physics*, 6 (11):860–864, November 2010. ISSN 1745-2473, 1745-2481. doi: 10.1038/nphys1750. URL `http://www.nature.com/articles/nphys1750`.

[195] T. Gao, P. S. Eldridge, T. C. H. Liew, S. I. Tsintzos, G. Stavrinidis, G. Deligeorgis, Z. Hatzopoulos, and P. G. Savvidis. Polariton condensate transistor switch. *Physical Review B*, 85(23):235102, June 2012. ISSN 1098-0121, 1550-235X. doi: 10.1103/PhysRevB.85.235102. URL `https://link.aps.org/doi/10.1103/PhysRevB.85.235102`.

[196] Na Young Kim, Chih-Wei Lai, Shoko Utsunomiya, Georgios Roumpos, Michael Fraser, Hui Deng, Tim Byrnes, Patrik Recher, Norio Kumada, Toshimasa Fujisawa, and Yoshihisa

Yamamoto. GaAs microcavity exciton-polaritons in a trap. *physica status solidi (b)*, 245 (6):1076–1080, June 2008. ISSN 03701972, 15213951. doi: 10.1002/pssb.200777610. URL https://onlinelibrary.wiley.com/doi/10.1002/pssb.200777610.

[197] A. Gärtner, L. Prechtel, D. Schuh, A. W. Holleitner, and J. P. Kotthaus. Micropatterned electrostatic traps for indirect excitons in coupled GaAs quantum wells. *Physical Review B*, 76(8):085304, August 2007. ISSN 1098-0121, 1550-235X. doi: 10.1103/PhysRevB.76.085304. URL https://link.aps.org/doi/10.1103/PhysRevB.76.085304.

[198] M. D. Fraser, H. H. Tan, and C. Jagadish. Selective confinement of macroscopic long-lifetime exciton and trion populations. *Physical Review B*, 84(24):245318, December 2011. ISSN 1098-0121, 1550-235X. doi: 10.1103/PhysRevB.84.245318. URL https://link.aps.org/doi/10.1103/PhysRevB.84.245318.

[199] N Y Kim, K Kusudo, A Löffler, S Höfling, A Forchel, and Y Yamamoto. Exciton–polariton condensates near the Dirac point in a triangular lattice. *New Journal of Physics*, 15 (3):035032, March 2013. ISSN 1367-2630. doi: 10.1088/1367-2630/15/3/035032. URL https://iopscience.iop.org/article/10.1088/1367-2630/15/3/035032.

[200] R. Idrissi Kaitouni, O. El Daïf, A. Baas, M. Richard, T. Paraiso, P. Lugan, T. Guillet, F. Morier-Genoud, J. D. Ganière, J. L. Staehli, V. Savona, and B. Deveaud. Engineering the spatial confinement of exciton polaritons in semiconductors. *Physical Review B*, 74(15): 155311, October 2006. ISSN 1098-0121, 1550-235X. doi: 10.1103/PhysRevB.74.155311. URL https://link.aps.org/doi/10.1103/PhysRevB.74.155311.

[201] O. El Daïf, A. Baas, T. Guillet, J.-P. Brantut, R. Idrissi Kaitouni, J. L. Staehli, F. Morier-Genoud, and B. Deveaud. Polariton quantum boxes in semiconductor microcavities. *Applied Physics Letters*, 88(6):061105, February 2006. ISSN 0003-6951, 1077-3118. doi: 10.1063/1.2172409. URL http://aip.scitation.org/doi/10.1063/1.2172409.

[202] R. Cerna, D. Sarchi, T. K. Paraïso, G. Nardin, Y. Léger, M. Richard, B. Pietka, O. El Daif, F. Morier-Genoud, V. Savona, M. T. Portella-Oberli, and B. Deveaud-Plédran. Coherent optical control of the wave function of zero-dimensional exciton polaritons. *Physical Review B*, 80(12):121309, September 2009. ISSN 1098-0121, 1550-235X. doi: 10.1103/PhysRevB.80.121309. URL https://link.aps.org/doi/10.1103/PhysRevB.80.121309.

[203] Karol Winkler, Julian Fischer, Anne Schade, Matthias Amthor, Robert Dall, Jonas Geßler, Monika Emmerling, Elena A Ostrovskaya, Martin Kamp, Christian Schneider, and Sven Höfling. A polariton condensate in a photonic crystal potential landscape. *New Journal of Physics*, 17(2):023001, January 2015. ISSN 1367-2630. doi: 10.1088/1367-2630/

17/2/023001. URL https://iopscience.iop.org/article/10.1088/1367-2630/17/2/023001.

[204] M. Bayer, T. Gutbrod, A. Forchel, T. L. Reinecke, P. A. Knipp, R. Werner, and J. P. Reithmaier. Optical Demonstration of a Crystal Band Structure Formation. *Physical Review Letters*, 83(25):5374–5377, December 1999. ISSN 0031-9007, 1079-7114. doi: 10.1103/PhysRevLett.83.5374. URL https://link.aps.org/doi/10.1103/PhysRevLett.83.5374.

[205] S. Michaelis de Vasconcellos, A. Calvar, A. Dousse, J. Suffczyński, N. Dupuis, A. Lemaître, I. Sagnes, J. Bloch, P. Voisin, and P. Senellart. Spatial, spectral, and polarization properties of coupled micropillar cavities. *Applied Physics Letters*, 99(10):101103, September 2011. ISSN 0003-6951, 1077-3118. doi: 10.1063/1.3632111. URL http://aip.scitation.org/doi/10.1063/1.3632111.

[206] H. S. Nguyen, D. Vishnevsky, C. Sturm, D. Tanese, D. Solnyshkov, E. Galopin, A. Lemaître, I. Sagnes, A. Amo, G. Malpuech, and J. Bloch. Realization of a Double-Barrier Resonant Tunneling Diode for Cavity Polaritons. *Physical Review Letters*, 110(23):236601, June 2013. ISSN 0031-9007, 1079-7114. doi: 10.1103/PhysRevLett.110.236601. URL https://link.aps.org/doi/10.1103/PhysRevLett.110.236601.

[207] Bo Zhang, Zhaorong Wang, Sebastian Brodbeck, Christian Schneider, Martin Kamp, Sven Höfling, and Hui Deng. Zero-dimensional polariton laser in a subwavelength grating-based vertical microcavity. *Light: Science & Applications*, 3(1):e135–e135, January 2014. ISSN 2047-7538. doi: 10.1038/lsa.2014.16. URL http://www.nature.com/articles/lsa201416.

[208] S. Dufferwiel, F. Fras, A. Trichet, P. M. Walker, F. Li, L. Giriunas, M. N. Makhonin, L. R. Wilson, J. M. Smith, E. Clarke, M. S. Skolnick, and D. N. Krizhanovskii. Strong exciton-photon coupling in open semiconductor microcavities. *Applied Physics Letters*, 104(19):192107, May 2014. ISSN 0003-6951, 1077-3118. doi: 10.1063/1.4878504. URL http://aip.scitation.org/doi/10.1063/1.4878504.

[209] M. Vladimirova, S. Cronenberger, D. Scalbert, K. V. Kavokin, A. Miard, A. Lemaître, J. Bloch, D. Solnyshkov, G. Malpuech, and A. V. Kavokin. Polariton-polariton interaction constants in microcavities. *Physical Review B*, 82(7):075301, August 2010. ISSN 1098-0121, 1550-235X. doi: 10.1103/PhysRevB.82.075301. URL https://link.aps.org/doi/10.1103/PhysRevB.82.075301.

[210] N. Takemura, S. Trebaol, M. Wouters, M. T. Portella-Oberli, and B. Deveaud. Heterodyne spectroscopy of polariton spinor interactions. *Physical Review B*, 90(19):195307, November

2014. ISSN 1098-0121, 1550-235X. doi: 10.1103/PhysRevB.90.195307. URL https://link.aps.org/doi/10.1103/PhysRevB.90.195307.

[211] Gabriel Christmann, Guilherme Tosi, Natalia G. Berloff, Panos Tsotsis, Peter S. Eldridge, Zacharias Hatzopoulos, Pavlos G. Savvidis, and Jeremy J. Baumberg. Polariton ring condensates and sunflower ripples in an expanding quantum liquid. *Physical Review B*, 85 (23):235303, June 2012. ISSN 1098-0121, 1550-235X. doi: 10.1103/PhysRevB.85.235303. URL https://link.aps.org/doi/10.1103/PhysRevB.85.235303.

[212] Mengjie Wei, Wouter Verstraelen, Konstantinos Orfanakis, Arvydas Ruseckas, Timothy C. H. Liew, Ifor D. W. Samuel, Graham A. Turnbull, and Hamid Ohadi. Optically trapped room temperature polariton condensate in an organic semiconductor. *Nature Communications*, 13(1):7191, November 2022. ISSN 2041-1723. doi: 10.1038/s41467-022-34440-0. URL https://www.nature.com/articles/s41467-022-34440-0.

[213] Michiel Wouters, Iacopo Carusotto, and Cristiano Ciuti. Spatial and spectral shape of inhomogeneous nonequilibrium exciton-polariton condensates. *Physical Review B*, 77(11): 115340, March 2008. ISSN 1098-0121, 1550-235X. doi: 10.1103/PhysRevB.77.115340. URL https://link.aps.org/doi/10.1103/PhysRevB.77.115340.

[214] N. Peyghambarian, H. M. Gibbs, J. L. Jewell, A. Antonetti, A. Migus, D. Hulin, and A. Mysyrowicz. Blue Shift of the Exciton Resonance due to Exciton-Exciton Interactions in a Multiple-Quantum-Well Structure. *Physical Review Letters*, 53(25):2433–2436, December 1984. ISSN 0031-9007. doi: 10.1103/PhysRevLett.53.2433. URL https://link.aps.org/doi/10.1103/PhysRevLett.53.2433.

[215] Alexander Dreismann, Peter Cristofolini, Ryan Balili, Gabriel Christmann, Florian Pinsker, Natasha G. Berloff, Zacharias Hatzopoulos, Pavlos G. Savvidis, and Jeremy J. Baumberg. Coupled counterrotating polariton condensates in optically defined annular potentials. *Proceedings of the National Academy of Sciences*, 111(24):8770–8775, June 2014. ISSN 0027-8424, 1091-6490. doi: 10.1073/pnas.1401988111. URL https://pnas.org/doi/full/10.1073/pnas.1401988111.

[216] G. Tosi, G. Christmann, N.G. Berloff, P. Tsotsis, T. Gao, Z. Hatzopoulos, P.G. Savvidis, and J.J. Baumberg. Geometrically locked vortex lattices in semiconductor quantum fluids. *Nature Communications*, 3(1):1243, January 2012. ISSN 2041-1723. doi: 10.1038/ncomms2255. URL http://www.nature.com/articles/ncomms2255.

[217] H. Ohadi, Y. del Valle-Inclan Redondo, A. Dreismann, Y. G. Rubo, F. Pinsker, S. I. Tsintzos, Z. Hatzopoulos, P. G. Savvidis, and J. J. Baumberg. Tunable Magnetic Alignment between Trapped Exciton-Polariton Condensates. *Physical Review Letters*, 116(10):106403,

March 2016. ISSN 0031-9007, 1079-7114. doi: 10.1103/PhysRevLett.116.106403. URL https://link.aps.org/doi/10.1103/PhysRevLett.116.106403.

[218] Johannes Schmutzler, Przemyslaw Lewandowski, Marc Aßmann, Dominik Niemietz, Stefan Schumacher, Martin Kamp, Christian Schneider, Sven Höfling, and Manfred Bayer. All-optical flow control of a polariton condensate using nonresonant excitation. *Physical Review B*, 91(19):195308, May 2015. ISSN 1098-0121, 1550-235X. doi: 10.1103/PhysRevB.91.195308. URL https://link.aps.org/doi/10.1103/PhysRevB.91.195308.

[219] A. H. Pfund. The Light Sensitiveness of Copper Oxide. *Physical Review*, 7(3):289–301, March 1916. doi: 10.1103/PhysRev.7.289. URL https://link.aps.org/doi/10.1103/PhysRev.7.289. Publisher: American Physical Society.

[220] L. O. Grondahl and P. H. Geiger. A new electronic rectifier. *Journal of the A.I.E.E.*, 46(3):215–222, March 1927. ISSN 0095-9804. doi: 10.1109/JAIEE.1927.6534186. URL http://ieeexplore.ieee.org/document/6534186/.

[221] L. O. Grondahl. The Copper-Cuprous-Oxide Rectifier and Photoelectric Cell. *Reviews of Modern Physics*, 5(2):141–168, April 1933. ISSN 0034-6861. doi: 10.1103/RevModPhys.5.141. URL https://link.aps.org/doi/10.1103/RevModPhys.5.141.

[222] A.E. Rakhshani. Preparation, characteristics and photovoltaic properties of cuprous oxide—a review. *Solid-State Electronics*, 29(1):7–17, January 1986. ISSN 00381101. doi: 10.1016/0038-1101(86)90191-7. URL https://linkinghub.elsevier.com/retrieve/pii/0038110186901917.

[223] K. Akimoto, S. Ishizuka, M. Yanagita, Y. Nawa, Goutam K. Paul, and T. Sakurai. Thin film deposition of Cu_2O and application for solar cells. *Solar Energy*, 80(6):715–722, June 2006. ISSN 0038092X. doi: 10.1016/j.solener.2005.10.012. URL https://linkinghub.elsevier.com/retrieve/pii/S0038092X0500366X.

[224] Lung-Chien Chen. Review of preparation and optoelectronic characteristics of Cu_2O-based solar cells with nanostructure. *Materials Science in Semiconductor Processing*, 16(5):1172–1185, October 2013. ISSN 13698001. doi: 10.1016/j.mssp.2012.12.028. URL https://linkinghub.elsevier.com/retrieve/pii/S1369800113000097.

[225] Stephan Steinhauer, Marijn A. M. Versteegh, Samuel Gyger, Ali W. Elshaari, Birgit Kunert, André Mysyrowicz, and Val Zwiller. Rydberg excitons in Cu_2O microcrystals grown on a silicon platform. *Communications Materials*, 1(1):11, December 2020. ISSN 2662-4443. doi: 10.1038/s43246-020-0013-6. URL http://www.nature.com/articles/s43246-020-0013-6.

[226] Stephen A. Lynch, Chris Hodges, Soumen Mandal, Wolfgang Langbein, Ravi P. Singh, Liam A. P. Gallagher, Jon D. Pritchett, Danielle Pizzey, Joshua P. Rogers, Charles S. Adams, and Matthew P. A. Jones. Rydberg excitons in synthetic cuprous oxide Cu_2O. *Physical Review Materials*, 5(8):084602, August 2021. ISSN 2475-9953. doi: 10.1103/PhysRevMaterials.5.084602. URL https://link.aps.org/doi/10.1103/PhysRevMaterials.5.084602.

[227] E. F. Gross. Optical spectrum of excitons in the crystal lattice. *Il Nuovo Cimento*, 3 (S4):672–701, April 1956. ISSN 0029-6341, 1827-6121. doi: 10.1007/BF02746069. URL http://link.springer.com/10.1007/BF02746069.

[228] V. T. Agekyan. Spectroscopic properties of semiconductor crystals with direct forbidden energy gap. *Physica Status Solidi (a)*, 43(1):11–42, September 1977. ISSN 00318965, 1521396X. doi: 10.1002/pssa.2210430102. URL https://onlinelibrary.wiley.com/doi/10.1002/pssa.2210430102.

[229] S. Nikitine. Excitons. In Sol Nudelman and S. S. Mitra, editors, *Optical Properties of Solids*, pages 197–237. Springer US, Boston, MA, 1969. ISBN 978-1-4757-1125-7 978-1-4757-1123-3. doi: 10.1007/978-1-4757-1123-3_9. URL http://link.springer.com/10.1007/978-1-4757-1123-3_9.

[230] R. G. Waters, Fred H. Pollak, R. H. Bruce, and H. Z. Cummins. Effects of uniaxial stress on excitons in Cu_2O. *Physical Review B*, 21(4):1665–1675, February 1980. ISSN 0163-1829. doi: 10.1103/PhysRevB.21.1665. URL https://link.aps.org/doi/10.1103/PhysRevB.21.1665.

[231] H. R. Trebin, H. Z. Cummins, and J. L. Birman. Excitons in cuprous oxide under uniaxial stress. *Physical Review B*, 23(2):597–606, January 1981. ISSN 0163-1829. doi: 10.1103/PhysRevB.23.597. URL https://link.aps.org/doi/10.1103/PhysRevB.23.597.

[232] D. Snoke, J. P. Wolfe, and A. Mysyrowicz. Quantum saturation of a Bose gas: Excitons in Cu_2O. *Physical Review Letters*, 59(7):827–830, August 1987. ISSN 0031-9007. doi: 10.1103/PhysRevLett.59.827. URL https://link.aps.org/doi/10.1103/PhysRevLett.59.827.

[233] G. M. Kavoulakis. Bose-Einstein condensation of excitons in Cu_2O. *Physical Review B*, 65(3):035204, December 2001. ISSN 0163-1829, 1095-3795. doi: 10.1103/PhysRevB.65.035204. URL https://link.aps.org/doi/10.1103/PhysRevB.65.035204.

[234] J. Thewes, J. Heckötter, T. Kazimierczuk, M. Aßmann, D. Fröhlich, M. Bayer, M. A. Semina, and M. M. Glazov. Observation of High Angular Momentum Excitons in Cuprous

Oxide. *Physical Review Letters*, 115(2):027402, July 2015. ISSN 0031-9007, 1079-7114. doi: 10.1103/PhysRevLett.115.027402. URL `https://link.aps.org/doi/10.1103/PhysRevLett.115.027402`.

[235] Marc Aßmann, Johannes Thewes, Dietmar Fröhlich, and Manfred Bayer. Quantum chaos and breaking of all anti-unitary symmetries in Rydberg excitons. *Nature Materials*, 15(7): 741–745, July 2016. ISSN 1476-1122, 1476-4660. doi: 10.1038/nmat4622. URL `https://www.nature.com/articles/nmat4622`.

[236] P. Grünwald, M. Aßmann, J. Heckötter, D. Fröhlich, M. Bayer, H. Stolz, and S. Scheel. Signatures of Quantum Coherences in Rydberg Excitons. *Physical Review Letters*, 117 (13):133003, September 2016. ISSN 0031-9007, 1079-7114. doi: 10.1103/PhysRevLett.117.133003. URL `https://link.aps.org/doi/10.1103/PhysRevLett.117.133003`.

[237] F. Schöne, S.-O. Krüger, P. Grünwald, H. Stolz, S. Scheel, M. Aßmann, J. Heckötter, J. Thewes, D. Fröhlich, and M. Bayer. Deviations of the exciton level spectrum in Cu_2O from the hydrogen series. *Physical Review B*, 93(7):075203, February 2016. ISSN 2469-9950, 2469-9969. doi: 10.1103/PhysRevB.93.075203. URL `https://link.aps.org/doi/10.1103/PhysRevB.93.075203`.

[238] J. Heckötter, M. Freitag, D. Fröhlich, M. Aßmann, M. Bayer, M. A. Semina, and M. M. Glazov. High-resolution study of the yellow excitons in Cu_2O subject to an electric field. *Physical Review B*, 95(3):035210, January 2017. ISSN 2469-9950, 2469-9969. doi: 10.1103/PhysRevB.95.035210. URL `https://link.aps.org/doi/10.1103/PhysRevB.95.035210`.

[239] Frank Schweiner, Jörg Main, Günter Wunner, and Christoph Uihlein. Even exciton series in Cu_2O. *Physical Review B*, 95(19):195201, May 2017. ISSN 2469-9950, 2469-9969. doi: 10.1103/PhysRevB.95.195201. URL `http://link.aps.org/doi/10.1103/PhysRevB.95.195201`.

[240] Florian Schöne, Heinrich Stolz, and Nobuko Naka. Phonon-assisted absorption of excitons in Cu_2O. *Physical Review B*, 96(11):115207, September 2017. ISSN 2469-9950, 2469-9969. doi: 10.1103/PhysRevB.96.115207. URL `https://link.aps.org/doi/10.1103/PhysRevB.96.115207`.

[241] J. Heckötter, M. Freitag, D. Fröhlich, M. Aßmann, M. Bayer, M. A. Semina, and M. M. Glazov. Scaling laws of Rydberg excitons. *Physical Review B*, 96(12):125142, September 2017. ISSN 2469-9950, 2469-9969. doi: 10.1103/PhysRevB.96.125142. URL `https://link.aps.org/doi/10.1103/PhysRevB.96.125142`.

[242] J. Heckötter, M. Freitag, D. Fröhlich, M. Aßmann, M. Bayer, P. Grünwald, F. Schöne, D. Semkat, H. Stolz, and S. Scheel. Rydberg Excitons in the Presence of an Ultralow-Density Electron-Hole Plasma. *Physical Review Letters*, 121(9):097401, August 2018. ISSN 0031-9007, 1079-7114. doi: 10.1103/PhysRevLett.121.097401. URL `https://link.aps.org/doi/10.1103/PhysRevLett.121.097401`.

[243] Mitsuyoshi Takahata and Nobuko Naka. Photoluminescence properties of the entire excitonic series in Cu_2O. *Physical Review B*, 98(19):195205, November 2018. ISSN 2469-9950, 2469-9969. doi: 10.1103/PhysRevB.98.195205. URL `https://link.aps.org/doi/10.1103/PhysRevB.98.195205`.

[244] Sjard Ole Krüger and Stefan Scheel. Interseries transitions between Rydberg excitons in Cu_2O. *Physical Review B*, 100(8):085201, August 2019. ISSN 2469-9950, 2469-9969. doi: 10.1103/PhysRevB.100.085201. URL `https://link.aps.org/doi/10.1103/PhysRevB.100.085201`.

[245] Annika Konzelmann, Bettina Frank, and Harald Giessen. Quantum confined Rydberg excitons in reduced dimensions. *Journal of Physics B: Atomic, Molecular and Optical Physics*, 53(2):024001, January 2020. ISSN 0953-4075, 1361-6455. doi: 10.1088/1361-6455/ab56a9. URL `https://iopscience.iop.org/article/10.1088/1361-6455/ab56a9`.

[246] Julian Heckötter, Valentin Walther, Stefan Scheel, Manfred Bayer, Thomas Pohl, and Marc Aßmann. Asymmetric Rydberg blockade of giant excitons in Cuprous Oxide. *Nature Communications*, 12(1):3556, December 2021. ISSN 2041-1723. doi: 10.1038/s41467-021-23852-z. URL `http://www.nature.com/articles/s41467-021-23852-z`.

[247] Marijn A. M. Versteegh, Stephan Steinhauer, Josip Bajo, Thomas Lettner, Ariadna Soro, Alena Romanova, Samuel Gyger, Lucas Schweickert, André Mysyrowicz, and Val Zwiller. Giant Rydberg excitons in Cu_2O probed by photoluminescence excitation spectroscopy. *Physical Review B*, 104(24):245206, December 2021. ISSN 2469-9950, 2469-9969. doi: 10.1103/PhysRevB.104.245206. URL `https://link.aps.org/doi/10.1103/PhysRevB.104.245206`.

[248] Dongyeon Daniel Kang, Aaron Gross, HeeBong Yang, Yusuke Morita, Kyung Soo Choi, Kosuke Yoshioka, and Na Young Kim. Temperature study of Rydberg exciton optical properties in Cu_2O. *Physical Review B*, 103(20):205203, May 2021. ISSN 2469-9950, 2469-9969. doi: 10.1103/PhysRevB.103.205203. URL `https://link.aps.org/doi/10.1103/PhysRevB.103.205203`.

[249] Konstantinos Orfanakis, Sai Kiran Rajendran, Hamid Ohadi, Sylwia Zielińska-Raczyńska, Gerard Czajkowski, Karol Karpiński, and David Ziemkiewicz. Quantum confined Rydberg

excitons in Cu_2O nanoparticles. *Physical Review B*, 103(24):245426, June 2021. ISSN 2469-9950, 2469-9969. doi: 10.1103/PhysRevB.103.245426. URL `https://link.aps.org/doi/10.1103/PhysRevB.103.245426`.

[250] Konstantinos Orfanakis, Sai Kiran Rajendran, Valentin Walther, Thomas Volz, Thomas Pohl, and Hamid Ohadi. Rydberg exciton-polaritons in a Cu_2O microcavity. *Nature Materials*, 21(7):767–772, July 2022. ISSN 1476-1122, 1476-4660. doi: 10.1038/s41563-022-01230-4. URL `https://www.nature.com/articles/s41563-022-01230-4`.

[251] Bruno K. Meyer, Angelika Polity, Daniel Reppin, Martin Becker, Philipp Hering, Benedikt Kramm, Peter J. Klar, Thomas Sander, Christian Reindl, Christian Heiliger, Markus Heinemann, Christian Müller, and Carsten Ronning. The Physics of Copper Oxide (Cu_2O). In *Semiconductors and Semimetals*, volume 88, pages 201–226. Elsevier, 2013. ISBN 978-0-12-396489-2. doi: 10.1016/B978-0-12-396489-2.00006-0. URL `https://linkinghub.elsevier.com/retrieve/pii/B9780123964892000060`.

[252] Takayuki Ito, Hiroyuki Yamaguchi, Katsuya Okabe, and Taizo Masumi. Single-crystal growth and characterization of Cu_2O and CuO. *Journal of Materials Science*, 33(14):3555–3566, 1998. ISSN 00222461. doi: 10.1023/A:1004690809547. URL `http://link.springer.com/10.1023/A:1004690809547`.

[253] J.P. Dahl and A.C. Switendick. Energy bands in cuprous oxide. *Journal of Physics and Chemistry of Solids*, 27(6-7):931–942, June 1966. ISSN 00223697. doi: 10.1016/0022-3697(66)90064-3. URL `https://linkinghub.elsevier.com/retrieve/pii/0022369766900643`.

[254] A. Werner and H. D. Hochheimer. High-pressure x-ray study of Cu_2O and Ag_2O. *Physical Review B*, 25(9):5929–5934, May 1982. ISSN 0163-1829. doi: 10.1103/PhysRevB.25.5929. URL `https://link.aps.org/doi/10.1103/PhysRevB.25.5929`.

[255] R. J. Elliott. Symmetry of Excitons in Cu_2O. *Physical Review*, 124(2):340–345, October 1961. ISSN 0031-899X. doi: 10.1103/PhysRev.124.340. URL `https://link.aps.org/doi/10.1103/PhysRev.124.340`.

[256] Leonard Kleinman and Kenneth Mednick. Self-consistent energy bands of Cu_2O. *Physical Review B*, 21(4):1549–1553, February 1980. ISSN 0163-1829. doi: 10.1103/PhysRevB.21.1549. URL `https://link.aps.org/doi/10.1103/PhysRevB.21.1549`.

[257] John Robertson. Electronic structure and x-ray near-edge core spectra of Cu_2O. *Physical Review B*, 28(6):3378–3385, September 1983. ISSN 0163-1829. doi: 10.1103/PhysRevB.28.3378. URL `https://link.aps.org/doi/10.1103/PhysRevB.28.3378`.

[258] M French, R Schwartz, H Stolz, and R Redmer. Electronic band structure of Cu_2O by spin density functional theory. *Journal of Physics: Condensed Matter*, 21(1):015502, January 2009. ISSN 0953-8984, 1361-648X. doi: 10.1088/0953-8984/21/1/015502. URL `https://iopscience.iop.org/article/10.1088/0953-8984/21/1/015502`.

[259] Y. Wang, S. Lany, J. Ghanbaja, Y. Fagot-Revurat, Y. P. Chen, F. Soldera, D. Horwat, F. Mücklich, and J. F. Pierson. Electronic structures of Cu_2O, Cu_4O_3, and CuO: A joint experimental and theoretical study. *Physical Review B*, 94(24):245418, December 2016. ISSN 2469-9950, 2469-9969. doi: 10.1103/PhysRevB.94.245418. URL `https://link.aps.org/doi/10.1103/PhysRevB.94.245418`.

[260] George F. Koster, editor. *Properties of the thirty-two point groups*. M.I.T. Pr, Cambridge, Mass, 3. printing edition, 1969. ISBN 978-0-262-11010-5.

[261] Ch. Uihlein, D. Fröhlich, and R. Kenklies. Investigation of exciton fine structure in Cu_2O. *Physical Review B*, 23(6):2731–2740, March 1981. ISSN 0163-1829. doi: 10.1103/PhysRevB.23.2731. URL `https://link.aps.org/doi/10.1103/PhysRevB.23.2731`.

[262] S. Brahms and S. Nikitine. Intrinsic absorption and reflection of cuprous oxide in the 2.5 to 6.5 eV region. *Solid State Communications*, 3(8):209–212, August 1965. ISSN 00381098. doi: 10.1016/0038-1098(65)90293-0. URL `https://linkinghub.elsevier.com/retrieve/pii/0038109865902930`.

[263] R.A. Forman, W.S. Brower, and H.S. Parker. Phonons and the green exciton series in cuprous oxide, Cu_2O. *Physics Letters A*, 36(5):395–396, September 1971. ISSN 03759601. doi: 10.1016/0375-9601(71)90276-3. URL `https://linkinghub.elsevier.com/retrieve/pii/0375960171902763`.

[264] Patric Rommel, Patrik Zielinski, and Jörg Main. Green exciton series in cuprous oxide. *Physical Review B*, 101(7):075208, February 2020. ISSN 2469-9950, 2469-9969. doi: 10.1103/PhysRevB.101.075208. URL `https://link.aps.org/doi/10.1103/PhysRevB.101.075208`.

[265] A. Farenbruch, D. Fröhlich, H. Stolz, D. R. Yakovlev, and M. Bayer. Second-harmonic generation of blue series excitons and magnetoexcitons in Cu_2O. *Physical Review B*, 104 (7):075203, August 2021. ISSN 2469-9950, 2469-9969. doi: 10.1103/PhysRevB.104.075203. URL `https://link.aps.org/doi/10.1103/PhysRevB.104.075203`.

[266] A. Daunois, J.L. Deiss, and B. Meyer. Étude spectrophotométrique de l'absorption bleue et violette de Cu_2O. *Journal de Physique*, 27(3-4):142–146, 1966. ISSN 0368-3842. doi: 10.

1051/jphys:01966002703-4014200. URL http://www.edpsciences.org/10.1051/jphys:01966002703-4014200.

[267] J W Hodby, T E Jenkins, C Schwab, H Tamura, and D Trivich. Cyclotron resonance of electrons and of holes in cuprous oxide, Cu_2O. *Journal of Physics C: Solid State Physics*, 9(8):1429–1439, April 1976. ISSN 0022-3719. doi: 10.1088/0022-3719/9/8/014. URL https://iopscience.iop.org/article/10.1088/0022-3719/9/8/014.

[268] Nobuko Naka, Ikuko Akimoto, Masanobu Shirai, and Ken-ichi Kan'no. Time-resolved cyclotron resonance in cuprous oxide. *Physical Review B*, 85(3):035209, January 2012. ISSN 1098-0121, 1550-235X. doi: 10.1103/PhysRevB.85.035209. URL https://link.aps.org/doi/10.1103/PhysRevB.85.035209.

[269] H. Matsumoto, K. Saito, M. Hasuo, S. Kono, and N. Nagasawa. Revived interest on yellow-exciton series in Cu_2O: An experimental aspect. *Solid State Communications*, 97 (2):125–129, January 1996. ISSN 00381098. doi: 10.1016/0038-1098(95)00601-X. URL https://linkinghub.elsevier.com/retrieve/pii/003810989500601X.

[270] S. B. Nam, D. C. Reynolds, C. W. Litton, R. J. Almassy, T. C. Collins, and C. M. Wolfe. Free-exciton energy spectrum in GaAs. *Physical Review B*, 13(2):761–767, January 1976. ISSN 0556-2805. doi: 10.1103/PhysRevB.13.761. URL https://link.aps.org/doi/10.1103/PhysRevB.13.761.

[271] G. M. Kavoulakis, Yia-Chung Chang, and Gordon Baym. Fine structure of excitons in Cu_2O. *Physical Review B*, 55(12):7593–7599, March 1997. ISSN 0163-1829, 1095-3795. doi: 10.1103/PhysRevB.55.7593. URL https://link.aps.org/doi/10.1103/PhysRevB.55.7593.

[272] Jongseok Lim, Han-gyeol Lee, and Jaewook Ahn. Review of cold Rydberg atoms and their applications. *Journal of the Korean Physical Society*, 63(4):867–876, August 2013. ISSN 0374-4884, 1976-8524. doi: 10.3938/jkps.63.867. URL http://link.springer.com/10.3938/jkps.63.867.

[273] Marc Aßmann and Manfred Bayer. Semiconductor Rydberg Physics. *Advanced Quantum Technologies*, 3(11):1900134, November 2020. ISSN 2511-9044, 2511-9044. doi: 10.1002/qute.201900134. URL https://onlinelibrary.wiley.com/doi/10.1002/qute.201900134.

[274] M. Saffman, T. G. Walker, and K. Mølmer. Quantum information with Rydberg atoms. *Reviews of Modern Physics*, 82(3):2313–2363, August 2010. ISSN 0034-6861, 1539-

0756. doi: 10.1103/RevModPhys.82.2313. URL https://link.aps.org/doi/10.1103/RevModPhys.82.2313.

[275] Mohammadsadegh Khazali, Khabat Heshami, and Christoph Simon. Single-photon source based on Rydberg exciton blockade. *Journal of Physics B: Atomic, Molecular and Optical Physics*, 50(21):215301, October 2017. ISSN 0953-4075. doi: 10.1088/1361-6455/aa8d7c. URL https://iopscience.iop.org/article/10.1088/1361-6455/aa8d7c/meta. Publisher: IOP Publishing.

[276] David Ziemkiewicz, Karol Karpiński, Gerard Czajkowski, and Sylwia Zielińska-Raczyńska. Excitons in Cu_2O: From quantum dots to bulk crystals and additional boundary conditions for Rydberg exciton-polaritons. *Physical Review B*, 101(20):205202, May 2020. ISSN 2469-9950, 2469-9969. doi: 10.1103/PhysRevB.101.205202. URL https://link.aps.org/doi/10.1103/PhysRevB.101.205202.

[277] G. Kuwabara, M. Tanaka, and H. Fukutani. Optical absorption due to paraexciton of Cu_2O. *Solid State Communications*, 21(6):599–601, February 1977. ISSN 00381098. doi: 10.1016/0038-1098(77)90042-4. URL https://linkinghub.elsevier.com/retrieve/pii/0038109877900424.

[278] P. D. Bloch and C. Schwab. Direct Evidence for Phonon-Assisted Transitions to the 1 s Paraexciton Level of the Yellow Exciton Series in Cu_2O. *Physical Review Letters*, 41 (7):514–517, August 1978. ISSN 0031-9007. doi: 10.1103/PhysRevLett.41.514. URL https://link.aps.org/doi/10.1103/PhysRevLett.41.514.

[279] A. Mysyrowicz, D. Hulin, and A. Antonetti. Long Exciton Lifetime in Cu_2O. *Physical Review Letters*, 43(15):1123–1126, October 1979. ISSN 0031-9007. doi: 10.1103/PhysRevLett.43.1123. URL https://link.aps.org/doi/10.1103/PhysRevLett.43.1123.

[280] J.S. Weiner, N. Caswell, P.Y. Yu, and A. Mysyrowicz. Ortho- to para-exciton conversion in Cu_2O: A subnanosecond time-resolved photoluminescence study. *Solid State Communications*, 46(2):105–108, April 1983. ISSN 00381098. doi: 10.1016/0038-1098(83)90588-4. URL https://linkinghub.elsevier.com/retrieve/pii/0038109883905884.

[281] K. E. O'Hara and J. P. Wolfe. Relaxation kinetics of excitons in cuprous oxide. *Physical Review B*, 62(19):12909–12922, November 2000. ISSN 0163-1829, 1095-3795. doi: 10.1103/PhysRevB.62.12909. URL https://link.aps.org/doi/10.1103/PhysRevB.62.12909.

[282] K. E. O'Hara, L. Ó Súilleabháin, and J. P. Wolfe. Strong nonradiative recombination of excitons in Cu_2O and its impact on Bose-Einstein statistics. *Physical Review B*, 60

(15):10565–10568, October 1999. ISSN 0163-1829, 1095-3795. doi: 10.1103/PhysRevB.60.10565. URL `https://link.aps.org/doi/10.1103/PhysRevB.60.10565`.

[283] Julian Heckötter. Strongly interacting Rydberg excitons in Cu_2O. 2020. doi: 10.17877/DE290R-21696. URL `https://eldorado.tu-dortmund.de/handle/2003/39805`. Publisher: Technische Universität Dortmund.

[284] Yutaka Toyozawa. Theory of Line-Shapes of the Exciton Absorption Bands. *Progress of Theoretical Physics*, 20(1):53–81, July 1958. ISSN 0033-068X. doi: 10.1143/PTP.20.53. URL `https://academic.oup.com/ptp/article-lookup/doi/10.1143/PTP.20.53`.

[285] Y. Toyozawa. Interband effect of lattice vibrations in the exciton absorption spectra. *Journal of Physics and Chemistry of Solids*, 25(1):59–71, January 1964. ISSN 00223697. doi: 10.1016/0022-3697(64)90162-3. URL `https://linkinghub.elsevier.com/retrieve/pii/0022369764901623`.

[286] Frank Schweiner, Jörg Main, and Günter Wunner. Linewidths in excitonic absorption spectra of cuprous oxide. *Physical Review B*, 93(8):085203, February 2016. ISSN 2469-9950, 2469-9969. doi: 10.1103/PhysRevB.93.085203. URL `https://link.aps.org/doi/10.1103/PhysRevB.93.085203`.

[287] U. Fano. Effects of Configuration Interaction on Intensities and Phase Shifts. *Physical Review*, 124(6):1866–1878, December 1961. ISSN 0031-899X. doi: 10.1103/PhysRev.124.1866. URL `https://link.aps.org/doi/10.1103/PhysRev.124.1866`.

[288] Jakob Gollwitzer, Lars Bocklage, Ralf Röhlsberger, and Guido Meier. Connecting Fano interference and the Jaynes-Cummings model in cavity magnonics. *npj Quantum Information*, 7(1):114, December 2021. ISSN 2056-6387. doi: 10.1038/s41534-021-00445-8. URL `http://www.nature.com/articles/s41534-021-00445-8`.

[289] Heinrich Stolz, Florian Schöne, and Dirk Semkat. Interaction of Rydberg excitons in cuprous oxide with phonons and photons: optical linewidth and polariton effect. *New Journal of Physics*, 20(2):023019, February 2018. ISSN 1367-2630. doi: 10.1088/1367-2630/aaa396. URL `https://iopscience.iop.org/article/10.1088/1367-2630/aaa396`.

[290] Florian Schöne, Sjard-Ole Krüger, Peter Grünwald, Marc Aßmann, Julian Heckötter, Johannes Thewes, Heinrich Stolz, Dietmar Fröhlich, Manfred Bayer, and Stefan Scheel. Coupled valence band dispersions and the quantum defect of excitons in Cu_2O. *Journal of Physics B: Atomic, Molecular and Optical Physics*, 49(13):134003, July 2016. ISSN 0953-4075, 1361-6455. doi: 10.1088/0953-4075/49/13/134003. URL `https://iopscience.iop.org/article/10.1088/0953-4075/49/13/134003`.

[291] Thomas F. Gallagher. *Rydberg Atoms*. Cambridge University Press, 1 edition, September 1994. ISBN 978-0-521-38531-2 978-0-521-02166-1 978-0-511-52453-0. doi: 10.1017/CBO9780511524530. URL https://www.cambridge.org/core/product/identifier/9780511524530/type/book.

[292] Sjard Ole Krüger. Rydberg excitons in external fields. 2020. doi: 10.18453/ROSDOK_ID00002996. URL http://rosdok.uni-rostock.de/resolve/id/rosdok_disshab_0000002490. Publisher: Universität Rostock.

[293] J. I. Jang, Y. Sun, B. Watkins, and J. B. Ketterson. Bound excitons in Cu_2O: Efficient internal free exciton detector. *Physical Review B*, 74(23):235204, December 2006. ISSN 1098-0121, 1550-235X. doi: 10.1103/PhysRevB.74.235204. URL https://link.aps.org/doi/10.1103/PhysRevB.74.235204.

[294] Sandhaya Koirala, Nobuko Naka, and Koichiro Tanaka. Correlated lifetimes of free paraexcitons and excitons trapped at oxygen vacancies in cuprous oxide. *Journal of Luminescence*, 134:524–527, February 2013. ISSN 00222313. doi: 10.1016/j.jlumin.2012.07.035. URL https://linkinghub.elsevier.com/retrieve/pii/S0022231312004450.

[295] Sandhaya Koirala, Mitsuyoshi Takahata, Yuji Hazama, Nobuko Naka, and Koichiro Tanaka. Relaxation of localized excitons by phonon emission at oxygen vacancies in Cu_2O. *Journal of Luminescence*, 155:65–69, November 2014. ISSN 00222313. doi: 10.1016/j.jlumin.2014.06.027. URL https://linkinghub.elsevier.com/retrieve/pii/S0022231314003615.

[296] Laszlo Frazer, Erik J. Lenferink, Kelvin B. Chang, Kenneth R. Poeppelmeier, Nathaniel P. Stern, and John B. Ketterson. Evaluation of defects in cuprous oxide through exciton luminescence imaging. *Journal of Luminescence*, 159:294–302, March 2015. ISSN 00222313. doi: 10.1016/j.jlumin.2014.11.035. URL https://linkinghub.elsevier.com/retrieve/pii/S0022231314006851.

[297] G. G. Macfarlane, T. P. McLean, J. E. Quarrington, and V. Roberts. Some Effects of Strain in thin Specimens on Absorption Measurements at Low Temperature. *Physical Review Letters*, 2(6):252–254, March 1959. ISSN 0031-9007. doi: 10.1103/PhysRevLett.2.252. URL https://link.aps.org/doi/10.1103/PhysRevLett.2.252.

[298] Philip W. Baumeister. Optical Absorption of Cuprous Oxide. *Physical Review*, 121(2):359–362, January 1961. ISSN 0031-899X. doi: 10.1103/PhysRev.121.359. URL https://link.aps.org/doi/10.1103/PhysRev.121.359.

[299] Glen A. Slack. Thermal Conductivity of CaF_2 , MnF_2, CoF_2, and ZnF_2 Crystals. *Physical Review*, 122(5):1451–1464, June 1961. ISSN 0031-899X. doi: 10.1103/PhysRev.122.1451. URL https://link.aps.org/doi/10.1103/PhysRev.122.1451.

[300] H. Ohadi, A. Dreismann, Y. G. Rubo, F. Pinsker, Y. del Valle-Inclan Redondo, S. I. Tsintzos, Z. Hatzopoulos, P. G. Savvidis, and J. J. Baumberg. Spontaneous Spin Bifurcations and Ferromagnetic Phase Transitions in a Spinor Exciton-Polariton Condensate. *Physical Review X*, 5(3):031002, July 2015. ISSN 2160-3308. doi: 10.1103/PhysRevX.5.031002. URL https://link.aps.org/doi/10.1103/PhysRevX.5.031002.

[301] Ichiro Shibasaki and Naohiro Kuze. Mass production of sensors grown by MBE. In *Molecular Beam Epitaxy*, pages 697–720. Elsevier, 2013. ISBN 978-0-12-387839-7. doi: 10.1016/B978-0-12-387839-7.00031-2. URL https://linkinghub.elsevier.com/retrieve/pii/B9780123878397000312.

[302] Secondo Franchi. Molecular beam epitaxy. In *Molecular Beam Epitaxy*, pages 1–46. Elsevier, 2013. ISBN 978-0-12-387839-7. doi: 10.1016/B978-0-12-387839-7.00001-4. URL https://linkinghub.elsevier.com/retrieve/pii/B9780123878397000014.

[303] John R. Arthur. Molecular beam epitaxy. *Surface Science*, 500(1-3):189–217, March 2002. ISSN 00396028. doi: 10.1016/S0039-6028(01)01525-4. URL https://linkinghub.elsevier.com/retrieve/pii/S0039602801015254.

[304] Jan Brandt, Dietmar Fröhlich, Christian Sandfort, Manfred Bayer, Heinrich Stolz, and Nobuko Naka. Ultranarrow Optical Absorption and Two-Phonon Excitation Spectroscopy of Cu_2O Paraexcitons in a High Magnetic Field. *Physical Review Letters*, 99(21):217403, November 2007. ISSN 0031-9007, 1079-7114. doi: 10.1103/PhysRevLett.99.217403. URL https://link.aps.org/doi/10.1103/PhysRevLett.99.217403.

[305] Materials Data on Cu_2O by Materials Project, 2020. URL https://www.osti.gov/servlets/purl/1207131/. Type: dataset.

[306] Wei Lu and Ying Fu. Reflection and Transmission. In *Spectroscopy of Semiconductors*, volume 215, pages 73–106. Springer International Publishing, Cham, 2018. ISBN 978-3-319-94952-9 978-3-319-94953-6. doi: 10.1007/978-3-319-94953-6_3. URL http://link.springer.com/10.1007/978-3-319-94953-6_3. Series Title: Springer Series in Optical Sciences.

[307] Jayampathi C. B. Kangara, Andrew J. Hachtel, Matthew C. Gillette, Jason T. Barkeloo, Ethan R. Clements, Samir Bali, Brett E. Unks, Nicholas A. Proite, Deniz D. Yavuz, Paul J. Martin, Jeremy J. Thorn, and Daniel A. Steck. Design and construction of cost-effective

tapered amplifier systems for laser cooling and trapping experiments. *American Journal of Physics*, 82(8):805–817, August 2014. ISSN 0002-9505, 1943-2909. doi: 10.1119/1.4867376. URL `http://aapt.scitation.org/doi/10.1119/1.4867376`.

[308] A. S. Arnold, J. S. Wilson, and M. G. Boshier. A simple extended-cavity diode laser. *Review of Scientific Instruments*, 69(3):1236–1239, March 1998. ISSN 0034-6748, 1089-7623. doi: 10.1063/1.1148756. URL `http://aip.scitation.org/doi/10.1063/1.1148756`.

[309] R. A. Nyman, G. Varoquaux, B. Villier, D. Sacchet, F. Moron, Y. Le Coq, A. Aspect, and P. Bouyer. Tapered-amplified antireflection-coated laser diodes for potassium and rubidium atomic-physics experiments. *Review of Scientific Instruments*, 77(3):033105, March 2006. ISSN 0034-6748, 1089-7623. doi: 10.1063/1.2186809. URL `http://aip.scitation.org/doi/10.1063/1.2186809`.

[310] Pasquale Maddaloni, Marco Bellini, and Paolo De Natale. *Laser-based measurements for time and frequency domain applications: a handbook*. Series in optics and optoelectronics. Taylor & Francis, Boca Raton, FL, 2013. ISBN 978-1-4398-4151-8.

[311] B. Mroziewicz. External cavity wavelength tunable semiconductor lasers - a review. *Opto-Electronics Review*, 16(4), January 2008. ISSN 1896-3757. doi: 10.2478/s11772-008-0045-9. URL `http://www.degruyter.com/view/j/oere.2008.16.issue-4/s11772-008-0045-9/s11772-008-0045-9.xml`.

[312] Stephen R. Wells, Masabumi Miyabe, and Shuichi Hasegawa. Design, construction and characterization of a single unit external cavity diode laser coupled tapered amplifier system for atomic physics. *Optics & Laser Technology*, 126:106118, June 2020. ISSN 00303992. doi: 10.1016/j.optlastec.2020.106118. URL `https://linkinghub.elsevier.com/retrieve/pii/S0030399219315403`.

[313] F. J. Duarte. *Tunable laser optics*. CRC Press, Boca Raton London New York, second edition, first issued in paperback edition, 2017. ISBN 978-1-138-89375-7 978-1-4822-4529-5.

[314] J. N. Walpole. Semiconductor amplifiers and lasers with tapered gain regions. *Optical and Quantum Electronics*, 28(6):623–645, June 1996. ISSN 0306-8919, 1572-817X. doi: 10.1007/BF00411298. URL `http://link.springer.com/10.1007/BF00411298`.

[315] Tomoyuki Horikiri, Tim Byrnes, Kenichiro Kusudo, Natsuko Ishida, Yasuhiro Matsuo, Yutaka Shikano, Andreas Löffler, Sven Höfling, Alfred Forchel, and Yoshihisa Yamamoto. Highly excited exciton-polariton condensates. *Physical Review B*, 95(24):245122, June 2017. ISSN 2469-9950, 2469-9969. doi: 10.1103/PhysRevB.95.245122. URL `https://link.aps.org/doi/10.1103/PhysRevB.95.245122`.

[316] Timur Yagafarov, Denis Sannikov, Anton Zasedatelev, Kyriacos Georgiou, Anton Baranikov, Oleksandr Kyriienko, Ivan Shelykh, Lizhi Gai, Zhen Shen, David Lidzey, and Pavlos Lagoudakis. Mechanisms of blueshifts in organic polariton condensates. *Communications Physics*, 3(1):18, December 2020. ISSN 2399-3650. doi: 10.1038/s42005-019-0278-6. URL http://www.nature.com/articles/s42005-019-0278-6.

[317] William T. Silfvast. *Laser Fundamentals*. Cambridge University Press, 2 edition, January 2004. ISBN 978-0-521-54105-3 978-0-521-83345-5 978-0-511-61642-6. doi: 10.1017/CBO9780511616426. URL https://www.cambridge.org/core/product/identifier/9780511616426/type/book.

[318] Jia-ming Liu. *Photonic Devices*. Cambridge University Press, 1 edition, April 2005. ISBN 978-0-521-55195-3 978-0-521-55859-4 978-0-511-61425-5. doi: 10.1017/CBO9780511614255. URL https://www.cambridge.org/core/product/identifier/9780511614255/type/book.

[319] Robert G. Hunsperger. Acousto-Optic Modulators. In *Integrated Optics*, pages 175–191. Springer Berlin Heidelberg, Berlin, Heidelberg, 2002. ISBN 978-3-662-12096-5 978-3-540-38843-2. doi: 10.1007/978-3-540-38843-2_10. URL http://link.springer.com/10.1007/978-3-540-38843-2_10. Series Title: Advanced Texts in Physics.

[320] Zichen Zhang, Zheng You, and Daping Chu. Fundamentals of phase-only liquid crystal on silicon (LCOS) devices. *Light: Science & Applications*, 3(10):e213–e213, October 2014. ISSN 2047-7538. doi: 10.1038/lsa.2014.94. URL http://www.nature.com/articles/lsa201494.

[321] Matthew Pasienski and Brian DeMarco. A high-accuracy algorithm for designing arbitrary holographic atom traps. *Optics Express*, 16(3):2176, 2008. ISSN 1094-4087. doi: 10.1364/OE.16.002176. URL https://opg.optica.org/oe/abstract.cfm?uri=oe-16-3-2176.

[322] Jerome Mertz. *Introduction to Optical Microscopy*. Cambridge University Press, 2 edition, July 2019. ISBN 978-1-108-55266-0 978-1-108-42830-9. doi: 10.1017/9781108552660. URL https://www.cambridge.org/highereducation/books/introduction-to-optical-microscopy/F6C6318C87732519D7E07BA7A03F0B81#contents.

[323] David C Joy. Scanning electron microscopy for materials characterization. *Current Opinion in Solid State and Materials Science*, 2(4):465–468, August 1997. ISSN 13590286. doi: 10.1016/S1359-0286(97)80091-5. URL https://linkinghub.elsevier.com/retrieve/pii/S1359028697800915.

[324] Ludwig Reimer. *Scanning Electron Microscopy*, volume 45 of *Springer Series in Optical Sciences*. Springer Berlin Heidelberg, Berlin, Heidelberg, 1998. ISBN 978-3-642-08372-3 978-3-540-38967-5. doi: 10.1007/978-3-540-38967-5. URL `http://link.springer.com/10.1007/978-3-540-38967-5`.

[325] Bernard D. Cullity. *Elements of x-ray diffraction*. Addison-Wesley series in metallurgy and materials. Addison-Wesley, Reading, Mass., 3. printing edition, 1967. ISBN 978-0-201-01230-9.

[326] Thiago Matheus Guimarães Selva, Jéssica Soares Guimarães Selva, and Raphael Bacil Prata. Sensing Materials: Diamond-Based Materials. In *Reference Module in Biomedical Sciences*, page B9780128225486000819. Elsevier, 2021. ISBN 978-0-12-801238-3. doi: 10.1016/B978-0-12-822548-6.00081-9. URL `https://linkinghub.elsevier.com/retrieve/pii/B9780128225486000819`.

[327] C. J. Hwang. Lifetimes of Free and Bound Excitons in High-Purity GaAs. *Physical Review B*, 8(2):646–652, July 1973. ISSN 0556-2805. doi: 10.1103/PhysRevB.8.646. URL `https://link.aps.org/doi/10.1103/PhysRevB.8.646`.

[328] J. Feldmann, G. Peter, E. O. Göbel, P. Dawson, K. Moore, C. Foxon, and R. J. Elliott. Linewidth dependence of radiative exciton lifetimes in quantum wells. *Physical Review Letters*, 59(20):2337–2340, November 1987. ISSN 0031-9007. doi: 10.1103/PhysRevLett.59.2337. URL `https://link.aps.org/doi/10.1103/PhysRevLett.59.2337`.

[329] Alexander Dreismann, Hamid Ohadi, Yago del Valle-Inclan Redondo, Ryan Balili, Yuri G. Rubo, Simeon I. Tsintzos, George Deligeorgis, Zacharias Hatzopoulos, Pavlos G. Savvidis, and Jeremy J. Baumberg. A sub-femtojoule electrical spin-switch based on optically trapped polariton condensates. *Nature Materials*, 15(10):1074–1078, October 2016. ISSN 1476-1122, 1476-4660. doi: 10.1038/nmat4722. URL `https://www.nature.com/articles/nmat4722`.

[330] E. Kammann, T. C. H. Liew, H. Ohadi, P. Cilibrizzi, P. Tsotsis, Z. Hatzopoulos, P. G. Savvidis, A. V. Kavokin, and P. G. Lagoudakis. Nonlinear Optical Spin Hall Effect and Long-Range Spin Transport in Polariton Lasers. *Physical Review Letters*, 109(3):036404, July 2012. ISSN 0031-9007, 1079-7114. doi: 10.1103/PhysRevLett.109.036404. URL `https://link.aps.org/doi/10.1103/PhysRevLett.109.036404`.

[331] A.M. Cockroft and R.L. Hudson. Quantum mechanical Wiener processes. *Journal of Multivariate Analysis*, 7(1):107–124, March 1977. ISSN 0047259X. doi: 10.1016/0047-259X(77)90035-5. URL `https://linkinghub.elsevier.com/retrieve/pii/0047259X77900355`.

[332] Alberto Amo and Jacqueline Bloch. Exciton-polaritons in lattices: A non-linear photonic simulator. *Comptes Rendus Physique*, 17(8):934–945, October 2016. ISSN 16310705. doi: 10.1016/j.crhy.2016.08.007. URL `https://linkinghub.elsevier.com/retrieve/pii/S163107051630086X`.

[333] Pavlos G Lagoudakis and Natalia G Berloff. A polariton graph simulator. *New Journal of Physics*, 19(12):125008, December 2017. ISSN 1367-2630. doi: 10.1088/1367-2630/aa924b. URL `https://iopscience.iop.org/article/10.1088/1367-2630/aa924b`.

[334] Natalia G. Berloff, Matteo Silva, Kirill Kalinin, Alexis Askitopoulos, Julian D. Töpfer, Pasquale Cilibrizzi, Wolfgang Langbein, and Pavlos G. Lagoudakis. Realizing the classical XY Hamiltonian in polariton simulators. *Nature Materials*, 16(11):1120–1126, November 2017. ISSN 1476-1122, 1476-4660. doi: 10.1038/nmat4971. URL `https://www.nature.com/articles/nmat4971`.

[335] P. A. Kalozoumis, G. M. Nikolopoulos, and D. Petrosyan. Coherent population oscillations and an effective spin-exchange interaction in a $\mathcal{PT}$ symmetric polariton mixture. *EPL (Europhysics Letters)*, 129(3):37003, February 2020. ISSN 1286-4854. doi: 10.1209/0295-5075/129/37003. URL `https://iopscience.iop.org/article/10.1209/0295-5075/129/37003`.

[336] Simon Baur, Daniel Tiarks, Gerhard Rempe, and Stephan Dürr. Single-Photon Switch Based on Rydberg Blockade. *Physical Review Letters*, 112(7):073901, February 2014. ISSN 0031-9007, 1079-7114. doi: 10.1103/PhysRevLett.112.073901. URL `https://link.aps.org/doi/10.1103/PhysRevLett.112.073901`.

[337] D. Ziemkiewicz and S. Zielińska-Raczyńska. Solid-state pulsed microwave emitter based on Rydberg excitons. *Optics Express*, 27(12):16983, June 2019. ISSN 1094-4087. doi: 10.1364/OE.27.016983. URL `https://opg.optica.org/abstract.cfm?URI=oe-27-12-16983`.

[338] A.I. Ekimov, A.A. Onushchenko, A.G. Plyukhin, and Al.L. Efros. Size quantization of excitons and determination of the parameters of their energy spectrum in CuCl. 61(4): 891, 1985.

[339] A.I. Ekimov, Al.L. Efros, and A.A. Onushchenko. Quantum size effect in semiconductor microcrystals. *Solid State Communications*, 56(11):921–924, December 1985. ISSN 00381098. doi: 10.1016/S0038-1098(85)80025-9. URL `https://linkinghub.elsevier.com/retrieve/pii/S0038109885800259`.

[340] A.I. Ekimov, A.A. Onushchenko, M.E. Raikh, and Al. L. Efros. Size quantization of excitons in microcrystals with large longitudinal-transverse splitting. 63(5):1054, 1986.

[341] G. Czajkowski, F. Bassani, and L. Silvestri. Excitonic optical properties of nanostructures: real density matrix approach. *La Rivista del Nuovo Cimento*, 26(5):1–150, May 2003. ISSN 1826-9850. doi: 10.1393/ncr/i2003-10002-2. URL `https://doi.org/10.1393/ncr/i2003-10002-2`.

[342] Sylwia Zielińska-Raczyńska, David Ziemkiewicz, and Gerard Czajkowski. Electro-optical properties of Rydberg excitons. *Physical Review B*, 94(4):045205, July 2016. ISSN 2469-9950, 2469-9969. doi: 10.1103/PhysRevB.94.045205. URL `https://link.aps.org/doi/10.1103/PhysRevB.94.045205`.

[343] Sylwia Zielińska-Raczyńska, Gerard Czajkowski, and David Ziemkiewicz. Optical properties of Rydberg excitons and polaritons. *Physical Review B*, 93(7):075206, February 2016. ISSN 2469-9950, 2469-9969. doi: 10.1103/PhysRevB.93.075206. URL `https://link.aps.org/doi/10.1103/PhysRevB.93.075206`.

[344] Hui Zhao, Sven Wachter, and Heinz Kalt. Effect of quantum confinement on exciton-phonon interactions. *Physical Review B*, 66(8):085337, August 2002. ISSN 0163-1829, 1095-3795. doi: 10.1103/PhysRevB.66.085337. URL `https://link.aps.org/doi/10.1103/PhysRevB.66.085337`.

[345] S. Rudin and T. L. Reinecke. Temperature-dependent exciton linewidths in semiconductor quantum wells. *Physical Review B*, 41(5):3017–3027, February 1990. ISSN 0163-1829, 1095-3795. doi: 10.1103/PhysRevB.41.3017. URL `https://link.aps.org/doi/10.1103/PhysRevB.41.3017`.

[346] Jianxun Liu, Huilin He, Dong Xiao, Shengtao Yin, Wei Ji, Shouzhen Jiang, Dan Luo, Bing Wang, and Yanjun Liu. Recent Advances of Plasmonic Nanoparticles and their Applications. *Materials*, 11(10):1833, September 2018. ISSN 1996-1944. doi: 10.3390/ma11101833. URL `http://www.mdpi.com/1996-1944/11/10/1833`.

[347] Marco Notarianni, Kristy Vernon, Alison Chou, Muhsen Aljada, Jinzhang Liu, and Nunzio Motta. Plasmonic effect of gold nanoparticles in organic solar cells. *Solar Energy*, 106:23–37, August 2014. ISSN 0038092X. doi: 10.1016/j.solener.2013.09.026. URL `https://linkinghub.elsevier.com/retrieve/pii/S0038092X13003885`.

[348] K. P. O'Donnell and X. Chen. Temperature dependence of semiconductor band gaps. *Applied Physics Letters*, 58(25):2924–2926, June 1991. ISSN 0003-6951, 1077-3118. doi: 10.1063/1.104723. URL `http://aip.scitation.org/doi/10.1063/1.104723`.

[349] D. Ballarini, M. De Giorgi, E. Cancellieri, R. Houdré, E. Giacobino, R. Cingolani, A. Bramati, G. Gigli, and D. Sanvitto. All-optical polariton transistor. *Nature Com-*

munications, 4(1):1778, June 2013. ISSN 2041-1723. doi: 10.1038/ncomms2734. URL http://www.nature.com/articles/ncomms2734.

[350] Anton V. Zasedatelev, Anton V. Baranikov, Darius Urbonas, Fabio Scafirimuto, Ullrich Scherf, Thilo Stöferle, Rainer F. Mahrt, and Pavlos G. Lagoudakis. A room-temperature organic polariton transistor. *Nature Photonics*, 13(6):378–383, June 2019. ISSN 1749-4885, 1749-4893. doi: 10.1038/s41566-019-0392-8. URL http://www.nature.com/articles/s41566-019-0392-8.

[351] T. Boulier, M. Bamba, A. Amo, C. Adrados, A. Lemaitre, E. Galopin, I. Sagnes, J. Bloch, C. Ciuti, E. Giacobino, and A. Bramati. Polariton-generated intensity squeezing in semiconductor micropillars. *Nature Communications*, 5(1):3260, May 2014. ISSN 2041-1723. doi: 10.1038/ncomms4260. URL http://www.nature.com/articles/ncomms4260.

[352] Álvaro Cuevas, Juan Camilo López Carreño, Blanca Silva, Milena De Giorgi, Daniel G. Suárez-Forero, Carlos Sánchez Muñoz, Antonio Fieramosca, Filippo Cardano, Lorenzo Marrucci, Vittorianna Tasco, Giorgio Biasiol, Elena del Valle, Lorenzo Dominici, Dario Ballarini, Giuseppe Gigli, Paolo Mataloni, Fabrice P. Laussy, Fabio Sciarrino, and Daniele Sanvitto. First observation of the quantized exciton-polariton field and effect of interactions on a single polariton. *Science Advances*, 4(4):eaao6814, April 2018. ISSN 2375-2548. doi: 10.1126/sciadv.aao6814. URL https://www.science.org/doi/10.1126/sciadv.aao6814.

[353] Guillermo Muñoz-Matutano, Andrew Wood, Mattias Johnsson, Xavier Vidal, Ben Q. Baragiola, Andreas Reinhard, Aristide Lemaître, Jacqueline Bloch, Alberto Amo, Gilles Nogues, Benjamin Besga, Maxime Richard, and Thomas Volz. Emergence of quantum correlations from interacting fibre-cavity polaritons. *Nature Materials*, 18(3):213–218, March 2019. ISSN 1476-1122, 1476-4660. doi: 10.1038/s41563-019-0281-z. URL https://www.nature.com/articles/s41563-019-0281-z.

[354] Aymeric Delteil, Thomas Fink, Anne Schade, Sven Höfling, Christian Schneider, and Ataç İmamoğlu. Towards polariton blockade of confined exciton–polaritons. *Nature Materials*, 18(3):219–222, March 2019. ISSN 1476-1122, 1476-4660. doi: 10.1038/s41563-019-0282-y. URL https://www.nature.com/articles/s41563-019-0282-y.

[355] Tatsuya Kitamura, Mitsuyoshi Takahata, and Nobuko Naka. Quantum number dependence of the photoluminescence broadening of excitonic Rydberg states in cuprous oxide. *Journal of Luminescence*, 192:808–813, December 2017. ISSN 00222313. doi: 10.1016/j.jlumin.2017.07.060. URL https://linkinghub.elsevier.com/retrieve/pii/S0022231317301448.

[356] H. S. Varu. *The optical modelling and design of Fabry Perot Interferometer sensors for ultrasound detection*. Doctoral, UCL (University College London), September 2014. URL https://discovery.ucl.ac.uk/id/eprint/1447253/. Pages: ?-? Publication Title: Doctoral thesis, UCL (University College London).

[357] M. E. Abu-Zeid, A. E. Rakhshani, A. A. Al-Jassar, and Y. A. Youssef. Determination of the Thickness and Refractive Index of Cu_2O Thin Film Using Thermal and Optical Interferometry. *physica status solidi (a)*, 93(2):613–620, February 1986. ISSN 00318965, 1521396X. doi: 10.1002/pssa.2210930226. URL https://onlinelibrary.wiley.com/doi/10.1002/pssa.2210930226.

[358] V. Walther, P. Grünwald, and T. Pohl. Controlling Exciton-Phonon Interactions via Electromagnetically Induced Transparency. *Physical Review Letters*, 125(17):173601, October 2020. ISSN 0031-9007, 1079-7114. doi: 10.1103/PhysRevLett.125.173601. URL https://link.aps.org/doi/10.1103/PhysRevLett.125.173601.

[359] J. I. Jang and J. P. Wolfe. Relaxation of stress-split orthoexcitons in Cu_2O. *Physical Review B*, 73(7):075207, February 2006. ISSN 1098-0121, 1550-235X. doi: 10.1103/PhysRevB.73.075207. URL https://link.aps.org/doi/10.1103/PhysRevB.73.075207.

[360] Alexey V. Gorshkov, Johannes Otterbach, Michael Fleischhauer, Thomas Pohl, and Mikhail D. Lukin. Photon-Photon Interactions via Rydberg Blockade. *Physical Review Letters*, 107(13):133602, September 2011. ISSN 0031-9007, 1079-7114. doi: 10.1103/PhysRevLett.107.133602. URL https://link.aps.org/doi/10.1103/PhysRevLett.107.133602.

[361] Jie Gu, Valentin Walther, Lutz Waldecker, Daniel Rhodes, Archana Raja, James C. Hone, Tony F. Heinz, Stéphane Kéna-Cohen, Thomas Pohl, and Vinod M. Menon. Enhanced nonlinear interaction of polaritons via excitonic Rydberg states in monolayer WSe_2. *Nature Communications*, 12(1):2269, December 2021. ISSN 2041-1723. doi: 10.1038/s41467-021-22537-x. URL http://www.nature.com/articles/s41467-021-22537-x.

[362] A. Coriolano, L. Polimeno, M. Pugliese, A. Cannavale1, D. Trypogeorgos, A. Di Renzo, V. Ardizzone, A. Rizzo1, D. Ballarini, G. Gigli1, V. Maiorano, A. S. Rosyadi, C. A. Chuang, C. H. Ho, L. De Marco, D. Sanvitto, and M. De Giorgi. Rydberg polaritons in ReS_2 crystals, August 2022. URL http://arxiv.org/abs/2208.03035. arXiv:2208.03035 [physics].

[363] Wei Bao, Xiaoze Liu, Fei Xue, Fan Zheng, Renjie Tao, Siqi Wang, Yang Xia, Mervin Zhao, Jeongmin Kim, Sui Yang, Quanwei Li, Ying Wang, Yuan Wang, Lin-Wang Wang, Allan H.

MacDonald, and Xiang Zhang. Observation of Rydberg exciton polaritons and their condensate in a perovskite cavity. *Proceedings of the National Academy of Sciences*, 116(41): 20274–20279, October 2019. ISSN 0027-8424, 1091-6490. doi: 10.1073/pnas.1909948116. URL https://pnas.org/doi/full/10.1073/pnas.1909948116.

[364] D Hunger, T Steinmetz, Y Colombe, C Deutsch, T W Hänsch, and J Reichel. A fiber Fabry-Perot cavity with high finesse. *New Journal of Physics*, 12(6):065038, June 2010. ISSN 1367-2630. doi: 10.1088/1367-2630/12/6/065038. URL https://iopscience.iop.org/article/10.1088/1367-2630/12/6/065038.

[365] Peng Qing, Jue Gong, Xing Lin, Ni Yao, Weidong Shen, Arash Rahimi-Iman, Wei Fang, and Limin Tong. A simple approach to fiber-based tunable microcavity with high coupling efficiency. *Applied Physics Letters*, 114(2):021106, January 2019. ISSN 0003-6951, 1077-3118. doi: 10.1063/1.5083011. URL http://aip.scitation.org/doi/10.1063/1.5083011.

[366] Rajiv Boddeda, Quentin Glorieux, Alberto Bramati, and Simon Pigeon. Generating strong anti-bunching by interfering nonclassical and classical states of light. *Journal of Physics B: Atomic, Molecular and Optical Physics*, 52(21):215401, oct 2019. doi: 10.1088/1361-6455/ab3e98. URL https://dx.doi.org/10.1088/1361-6455/ab3e98.

[367] Valentin Walther, Sjard Ole Krüger, Stefan Scheel, and Thomas Pohl. Interactions between Rydberg excitons in Cu_2O. *Physical Review B*, 98(16):165201, October 2018. ISSN 2469-9950, 2469-9969. doi: 10.1103/PhysRevB.98.165201. URL https://link.aps.org/doi/10.1103/PhysRevB.98.165201.

[368] Johannes Mund, Dietmar Fröhlich, Dmitri R. Yakovlev, and Manfred Bayer. High-resolution second harmonic generation spectroscopy with femtosecond laser pulses on excitons in Cu_2O. *Physical Review B*, 98(8):085203, August 2018. ISSN 2469-9950, 2469-9969. doi: 10.1103/PhysRevB.98.085203. URL https://link.aps.org/doi/10.1103/PhysRevB.98.085203.

[369] Johannes Mund, Christoph Uihlein, Dietmar Fröhlich, Dmitri R. Yakovlev, and Manfred Bayer. Second harmonic generation on the yellow 1S exciton in Cu_2O in symmetry-forbidden geometries. *Physical Review B*, 99(19):195204, May 2019. ISSN 2469-9950, 2469-9969. doi: 10.1103/PhysRevB.99.195204. URL https://link.aps.org/doi/10.1103/PhysRevB.99.195204.

[370] Joshua P. Rogers, Liam A. P. Gallagher, Danielle Pizzey, Jon D. Pritchett, Charles S. Adams, Matthew P. A. Jones, Chris Hodges, Wolfgang Langbein, and Stephen A.

Lynch. High-resolution nanosecond spectroscopy of even-parity Rydberg excitons in Cu_2O. *Physical Review B*, 105(11):115206, March 2022. ISSN 2469-9950, 2469-9969. doi: 10.1103/PhysRevB.105.115206. URL https://link.aps.org/doi/10.1103/PhysRevB.105.115206.

[371] Liam A. P. Gallagher, Joshua P. Rogers, Jon D. Pritchett, Rajan A. Mistry, Danielle Pizzey, Charles S. Adams, Matthew P. A. Jones, Peter Grünwald, Valentin Walther, Chris Hodges, Wolfgang Langbein, and Stephen A. Lynch. Microwave-optical coupling via Rydberg excitons in cuprous oxide. *Physical Review Research*, 4(1):013031, January 2022. ISSN 2643-1564. doi: 10.1103/PhysRevResearch.4.013031. URL https://link.aps.org/doi/10.1103/PhysRevResearch.4.013031.